

LL

Theoretical modeling and experimental investigation of the thermal performance of the LHC prototype lattice cryostats

[REDACTED]
CERN LIBRARIES, GENEVA



CM-P00069602

Thesis-1997-Riddone

Germana Riddone

POLITECNICO DI TORINO
FACOLTA' DI INGEGNERIA

TESI DI DOTTORATO
Dipartimento di Energetica

**Theoretical modeling and experimental
investigation of the thermal performance
of the LHC prototype lattice cryostats**

Germana Riddone

Tutori

Prof. Giovanni Del Tin (Politecnico di Torino)
Philippe Lebrun (CERN)

Coordinatore del dottorato di ricerca in Energetica

Prof. Michele Cali' Quaglia

Gennaio 1997

Acknowledgements

My thesis has been carried out in the LHC/ACR group at CERN in the framework of a collaboration with the “Politecnico di Torino” and the Italian association “Associazione per lo Sviluppo scientifico e tecnologico del Piemonte” (ASP).

I wish to thank Professor G. Del Tin, my supervisor at “Politecnico di Torino”, for the interest he has shown for my work.

I would like to express my gratitude and appreciation to my supervisor at CERN, Philippe Lebrun, head of the ACR group, for his support, advice and many useful comments on the concept text.

I wish to thank the “Politecnico di Torino” for the grant I received to carry out my doctoral thesis.

Thank also to the “Fellows and Associates Service”, Personnel Division of CERN, for supporting financially my work, and CERN for giving me the opportunity to perform this thesis.

I appreciated the help of the following persons:

B. Szeless, L. Tavian and L. Williams for their advice, interest and many fruitful discussions

M. Blin, L. Dufay, G. Ferlin and J.-M. Rieubland for their support in the construction of cryostats and the measurements of their thermal performance

Finally I would like to express my thanks to my family and friends for their help and encouragement.

Geneva, January 1997

Germana Riddone

Foreword

This thesis presents the thermal performance of the LHC (Large Hadron Collider) prototype cryostats both in steady-state and in transient conditions. LHC will be built in the 27 km LEP tunnel and will provide proton-proton collisions. It will make use of superconducting magnets operating in static bath of superfluid helium at 1.9 K.

The thesis is mainly divided in three parts. The first part contains three chapters which present a brief overview of the LHC project. Part 1-Chapter 1 gives a short introduction to the LHC design, layout and performance. Part 1-Chapter 2 refers to LHC cryogenic system and describes the general architecture of the cryogenic plants, the temperature levels and the heat loads. The 50 m long LHC prototype half-cell contains one twin-bore quadrupole and four twin-aperture dipoles. In Part 1-Chapter 3 the design and construction of the prototype dipole and quadrupole cryostats are presented. The LHC prototype cryostats have integrated cryogenic lines, while the final LHC cryostats have separate distribution lines.

The second part of the thesis illustrates the steady-state cryostat thermal performance beginning with a short description of the heat transfer processes involved in the cryostat thermal budget (Part 2-Chapter 1). An overview of material and helium properties is given in Annexes 2 and 3. The mathematical model used to simulate the cryostat thermal performance has been validated and the experimental tools used to accomplish this aim are presented in Part 2-Chapter 2. Full-scale prototype cryostats have been designed, constructed and used to assess the cryogenic behaviour. The thermal performance of the cryostats has been investigated both in nominal and in degraded operating conditions and is presented in Part 2-Chapter 3. Screen temperature and residual gas pressure have been varied in order to investigate their influence on the total thermal budget. The heat load due to resistive heating in the non-superconducting cable splices has been analysed and results from electrical measurements have been compared with those from calorimetric measurements. The list of detailed heat loads for the CTM and the string test is given in Annex 1. The heat interceptions play a very important role in the cryostat thermal performance, since low heat inleaks can be maintained only with a very efficient thermalisation. The main components which need to be cooled at intermediate temperatures are the screens, the support posts, the cryogenic valves and the vacuum barrier. The thermal contacts between these components and the cooling pipes have been studied in different cryostats and results of their thermal impedances are presented. Annex 4 describes the basic concept of thermal contacts and gives a few empirical correlations which may be applied in specific cases. The last chapter in Part 2 presents the potential of an actively cooled “soft” screen with respect to the “floating” insulation system. The efficiency of

a soft screen depends on the quality of the heat interception and the insulation to the cold mass. Dedicated test set-ups have been constructed to measure the thermal impedance of shrink-fitted type thermal contacts and the conduction through net-type insulating spacers. Test set-up and measurements results are described.

The third part explains the cryostat thermal performance in transient modes. Forced flow cooldown and warmup have been tested in the LHC prototype magnet string and calculated and experimental results are exposed in Part 3-Chapter 1. Natural warmup with and without active pumping on the insulation system is described in Part 3-Chapter 2 as well as the simulation of accidental loss of insulation vacuum. For each case a one-dimensional non-linear mathematical model has been developed and validated against measured data.

CONTENTS

ACKNOWLEDGEMENT	i
FOREWORD	ii
LIST OF FIGURES	viii
LIST OF TABLES	xii
LIST OF SYMBOLS	xiv

PART 1 THE LHC PROJECT AND ITS CRYOGENIC SYSTEM ***1***

1 INTRODUCTION TO THE LHC PROJECT	2
1.1 BASIC DESIGN	2
1.2 PERFORMANCE	3
1.2.1 Performance for proton-proton collisions	3
1.2.2 Performance as an ion-ion collider	5
1.3 SYSTEMS	5
1.3.1 Layout	5
1.3.2 Injectors and injections	7
1.3.3 Magnets	7
1.3.4 Protection against beam losses	9
1.3.5 Vacuum	9
1.3.7 The RF system	9
2 THE LHC CRYOGENIC SYSTEM	10
2.1 GENERAL ARCHITECTURE	10
2.2 TEMPERATURE LEVELS AND HEAT LOADS	10
2.3 RING COOLING SYSTEM	12
2.4 CRYOGENIC PLANTS	12
2.5 HELIUM INVENTORY	14

3	THE LHC PROTOTYPE MAGNET CRYOSTATS	15
3.1	PROTOTYPE DIPOLE CRYOSTAT	15
3.1.1	Introduction	15
3.1.2	Design and construction	15
3.2	PROTOTYPE SHORT STRAIGHT SECTION CRYOSTAT	17
3.2.1	Introduction	17
3.2.2	Design and construction	18
	 <i><u>PART 2</u> STEADY-STATE THERMAL PERFORMANCE OF THE LHC PROTOTYPE CRYOSTATS</i>	 20
1	MODELING CRYOSTAT THERMAL PERFORMANCE	21
1.1	HEAT TRANSFER PROCESSES	21
1.1.1	Solid conduction	21
1.1.2	Conduction in residual gas	23
1.1.3	Radiation	24
1.1.4	Convection	26
1.1.5	Multilayer systems	26
1.1.6	Heat transfer in HeII	31
1.2	THERMAL NETWORK MODEL	33
2	EXPERIMENTAL TOOLS AND METHODS FOR ASSESSING THERMAL PERFORMANCE OF CRYOSTATS	38
2.1	THE CRYOSTAT THERMAL MODEL (CTM)	38
2.1.1	Specifications	40
2.1.2	Cryogenics	41
2.1.3	Supply and return end boxes	43
2.1.4	Methods for measuring steady-state heat inleaks	44
2.1.5	Instrumentation	49
2.1.6	Control and data acquisition	52
2.2	LHC PROTOTYPE MAGNET STRING	53
2.2.1	System layout	53
2.2.2	Cryogenics	53
2.2.3	Instrumentation, data acquisition and process control	55
2.3	SINGLE MAGNET TEST	55
2.3.1	System layout	55
2.3.2	Instrumentation and process control	57
3	CALCULATED AND MEASURED THERMAL PERFORMANCE OF CRYOSTATS	58

3.1	HEAT LOAD ASSESSMENT	58
3.1.1	Heat loads under nominal steady-state conditions	58
3.1.2	Influence of cryogenic line temperatures	61
3.1.3	Influence of insulation vacuum	69
3.1.4	Resistive dissipation in non-superconducting cable splices	70
3.2	EXPERIMENTAL INVESTIGATION OF HEAT INTERCEPTIONS	72
3.2.1	Prototype magnet support posts	73
3.2.2	Prototype magnet thermal shield	79
3.2.3	Prototype magnet vacuum barrier	81
3.2.2	Prototype cryogenic valves	81
4	POTENTIAL OF AN ACTIVELY COOLED SCREEN AT 4.5-20 K	83
4.1	ACTIVELY COOLED SCREEN AT 4.5-20 K	83
4.1.1	Thermal design	85
4.1.2	Potential of a thermalised multilayer insulation system	87
4.1.3	Thermal contact to cooling pipe and net-type insulating spacers	89
4.1.4	Comparison of thermal performance	90
4.2	IMPROVEMENT OF THERMAL CONTACTS	93
4.2.1	Test set-up	93
4.2.2	Instrumentation	95
4.2.3	Results	95
4.2.4	Summary of tests	99
<u>PART 3</u> TRANSIENT THERMAL PERFORMANCE OF THE LHC PROTOTYPE CRYOSTATS		100
1	FORCED-FLOW COOLDOWN AND WARMUP	101
1.1	SHORT DESCRIPTION OF THE COLD MASS	101
1.2	MATHEMATICAL MODEL	103
1.3	RESULTS	106
2	NATURAL WARMUP AND ACCIDENTAL LOSS OF INSULATION VACUUM	110
2.1	MATHEMATICAL MODEL	110
2.2	TEST PROCEDURE AND RESULTS	114
CONCLUSION		118

ANNEX 1 DETAILED HEAT INLEAKS	120
A1.1 HEAT INLEAKS OF THE LHC PROTOTYPE MAGNET STRING	120
A1.2 HEAT INLEAKS OF THE CRYOSTAT THERMAL MODEL	122
ANNEX 2 MATERIAL PROPERTIES AT LOW TEMPERATURES	125
A2.1 SPECIFIC HEAT	125
A2.2 ELECTRICAL RESISTIVITY	125
A2.3 THERMAL CONDUCTIVITY	127
A2.4 THERMAL CONTRACTION	128
A2.5 MECHANICAL PROPERTIES	130
ANNEX 3 HELIUM PROPERTIES	132
ANNEX 4 THERMAL CONTACTS	137
A4.1 MODEL FOR SOLID-TO-SOLID CONTACTS	137
A4.2 EMPIRICAL CORRELATIONS	139
A4.3 METHODS TO IMPROVE THE THERMAL CONTACT	140
REFERENCES	142

LIST OF FIGURES

Figure I-1.1:	LHC in the LEP tunnel	3
Figure I-1.2:	Schematic layout of the LHC	5
Figure I-1.3:	Layout of the half-cell of the LHC	6
Figure I-1.4:	Schematic layout of the LHC injection	7
Figure I-1.5:	Phase-transition surface of Niobium-Titanium	8
Figure I-2.1:	General architecture of the LHC cryogenic scheme	11
Figure I-2.2:	Cryogenic flow-scheme of an LHC half-cell	13
Figure I-3.1:	Cross-section of the LHC prototype dipole cryostat	16
Figure I-3.2:	Longitudinal section of the LHC prototype short straight section	17
Figure I-3.3:	Cross-section of the LHC prototype short straight section cryostat, showing quadrupole	19
Figure II-1.1:	Measured heat flux for varying layer densities of MLI between 77 K and 4.2 K	27
Figure II-1.2:	Calculated heat flux through 30 layers of MLI from 300 K to T_1 at 10^{-4} Pa	28
Figure II-1.3:	Calculated heat flux through 10 layers of MLI from T_2 to 4.5 K at 10^{-4} Pa	29
Figure II-1.4:	Measured heat flux from 80 K to 4.5 K versus residual helium pressure	30
Figure II-1.5:	Measured heat flux from 300 K to 80 K versus residual gas pressure	30
Figure II-1.6:	Heat transfer from a copper surface to liquid helium I and II	31
Figure II-1.7:	Heat conductivity function for HeII in turbulent regime	32
Figure II-1.8:	Thermal conductivity integral of pressurised superfluid helium ($m=3.4$, l in cm and \dot{q} in W/cm^2)	33
Figure II-1.9:	Thermal network of the LHC prototype dipole cryostat	34
Figure II-1.10:	Thermal network of the LHC prototype short straight section cryostat	35

Figure II-2.1:	Longitudinal view of the CTM with end boxes.	39
Figure II-2.2:	Cross-section of the CTM	39
Figure II-2.3:	Simplified layout of the dummy cold mass	40
Figure II-2.4:	Process and instrumentation diagram of the CTM	42
Figure II-2.5:	Supply end box of the CTM	43
Figure II-2.6:	Return end box of the CTM	44
Figure II-2.7:	Exchange of heat, work and mass in a thermodynamic system	45
Figure II-2.8:	Heat leak in a steady-state open system	46
Figure II-2.9:	Measurement of heat leak at 1.9 K by helium boil-off	47
Figure II-2.10:	Measurement of heat leak at 1.9 K by temperature drift	48
Figure II-2.11:	Schematic layout of acquisition and control system	52
Figure II-2.12:	Simplified process and instrumentation diagram of the LHC prototype magnet string	54
Figure II-2.13:	Simplified process and instrumentation diagram of the single magnet test bench	56
Figure II-3.1:	Heat leak at 1.9 K versus line C temperature (residual gas pressure= 10^{-3} Pa, Lines E-F=50-75 K)	63
Figure II-3.2:	Heat leak at 1.9 K versus thermal shield temperature (residual gas pressure= 10^{-3} Pa, Lines C-D=4.5-20 K)	63
Figure II-3.3:	Measured heat leak at 4.5-20 K versus thermal shield temperature (residual gas pressure= 10^{-3} Pa)	64
Figure II-3.4:	Heat leak at 4.5-20 K versus thermal shield temperature (residual gas pressure= 10^{-3} Pa)	64
Figure II-3.5:	Measured heat leak at 4.5-20 K versus line C temperature (residual gas pressure= 10^{-3} Pa, Lines E-F = 50-75 K)	65
Figure II-3.6:	Heat leak at 4.5-20 K versus line C temperature (residual gas pressure= 10^{-3} Pa, Lines E-F = 50-75 K)	65
Figure II-3.7:	Measured heat leak at 50-75 K versus thermal shield temperature (residual gas pressure= 10^{-3} Pa, Lines C-D = 4.5-20 K)	66
Figure II-3.8:	Heat leak at 50-75 K versus thermal shield temperature (residual gas pressure= 10^{-3} Pa, Lines C-D = 4.5-20 K)	66
Figure II-3.9:	Heat flux from the thermal shield to 1.9 K through 10 layers of type-B MLI (residual gas pressure= 10^{-3} Pa)	68
Figure II-3.10:	Heat flux from 300 K to the thermal shield through 30 layers of type-B MLI (residual gas pressure= 10^{-3} Pa)	68
Figure II-3.11:	Heat leak at 1.9 K versus residual helium pressure (Lines C-D=4.5-20 K, Lines E-F=50-75 K)	69
Figure II-3.12:	Electrical scheme of LHC prototype magnet string in RUN 2	71
Figure II-3.13:	Magnet current ramping procedure for contact resistance measurement	71
Figure II-3.14:	Heat interception between the magnet support post and line C	73
Figure II-3.15:	Heat interception between the magnet support post and line E	74
Figure II-3.16:	Thermal network of support post	74
Figure II-3.17:	Instrumentation scheme of support post	75

Figure II-3.18: Calculated heat leak at 1.9 K versus the temperature of the flange cooled by line C	77
Figure II-3.19: Calculated heat leak at 4.5-20 K versus the temperature of the flange cooled by line E (CF=temperature of the flange cooled by line C)	78
Figure II-3.20: Calculated heat leak at 50-75 K versus the temperature of the flange cooled by line E (CF=temperature of the flange cooled by line C)	78
Figure II-3.21: Instrumentation scheme of the thermal shield of the LHC prototype magnet String (Run 2)	80
Figure II-3.22: Temperature sensors on vacuum barrier and cryogenic valves	82
Figure II-4.1: LHC dipole cryostat, reference design	84
Figure II-4.2: Heat leak at 1.9 K	84
Figure II-4.3: Principle schemes for “floating” (1) and “thermalised” (2) multilayer systems	85
Figure II-4.4: Thermal network of “floating” and thermalised multilayer systems	86
Figure II-4.5: Thermal impedance between the thermal shield and the soft screen	88
Figure II-4.6: Break-even lines for thermalized versus “floating” systems, in terms of R_{cp} and r_{cm}	88
Figure II-4.7: Experimental measurements of thermal impedance of net-type insulating spacers under variable applied pressure	89
Figure II-4.8: Temperature of the screen at 4.5-20 K versus residual helium pressure ($R_{cp}=4$ K/W; $r_{cm}=482$ K·m ² /W at 10^{-4} Pa)	90
Figure II-4.9: Comparison of heat leak at 1.9 K between “floating” and thermalized systems ($R_{cp}=4$ K/W; $r_{cm}=482$ K·m ² /W at 10^{-4} Pa)	91
Figure II-4.10: Heat leak at 4.5-20 K versus residual helium pressure ($R_{cp}=4$ K/W; $r_{cm}=482$ K·m ² /W at 10^{-4} Pa)	91
Figure II-4.11: Heat leak at 1.9 K with “hard” screen at 4.5-20 K ($R_{cp}=4$ K/W; $r_{cm}=0$ at 10^{-4} Pa)	93
Figure II-4.12: Test set-up for measuring thermal impedance of thermal contacts	94
Figure II-4.13: Experimental measurement of thermal impedance of thermal contacts	95
Figure II-4.14: Thermal impedance of the shrink-fitted contact versus helium temperature (sample 1)	96
Figure II-4.15: Temperature difference across the shrink-fitted contact versus heating power (sample 1)	96
Figure II-4.16: Breakdown of thermal impedance (sample 1)	97
Figure II-4.17: Temperature difference across the shrink-fitted contact versus electrical power (sample 2)	97
Figure III-1.1: Transverse cross-section of the LHC prototype dipole magnet	102

Figure III-1.2:	Heat capacity of the cold mass of the LHC prototype magnet string (1 quadrupole and 3 dipoles)	103
Figure III-1.3:	Scheme of the mathematical model for forced-flow cooldown and warmup	103
Figure III-1.4:	Calculated heat transfer coefficient between magnet and helium	105
Figure III-1.5:	Forced-flow cooldown of LHC prototype magnet string (Run 2A)	107
Figure III-1.6:	Forced-flow warmup of LHC prototype magnet string (Run 1)	107
Figure III-1.7:	Simulation of the fast forced-flow cooldown of LHC prototype magnet string (Run 2; He mass-flow=65 g/s)	108
Figure III-1. 8:	Simulation of the fast forced-flow warmup of LHC prototype magnet string (Run 2; He mass-flow=65 g/s)	109
Figure III-2.1:	Thermal network of natural warmup	113
Figure III-2.2:	Thermal network of accelerated warmup	113
Figure III-2.3:	Evolution of the residual gas pressure respect to the cold mass temperature measured during natural warmup without active pumping of the insulation vacuum (Run 2A)	115
Figure III-2.4:	LHC prototype magnet string temperatures during natural and accelerated warmup (Run 2A)	116
Figure III-2.5:	Heat flux evolution over time during accelerated warmup (Run 2A)	116
Figure III-2.6:	LHC prototype magnet String temperatures during natural warmup with pumping on the insulation vacuum (Run 2B)	117
Figure III-2.7:	Simulation of the cold mass temperature during natural warmup	117
Figure A2.1:	Specific heat of selected materials at low temperature	126
Figure A2.2:	Electrical resistivity of selected materials at low temperature	126
Figure A2.3:	Thermal conductivity of selected materials at low temperature	127
Figure A2.4:	Thermal conductivity of selected gases at low temperature	128
Figure A2.5:	Thermal contraction of selected materials at low temperature	129
Figure A2.6:	Yield stress of selected materials at low temperature	130
Figure A2.7:	Ultimate stress of selected materials at low temperature	131
Figure A3.3:	Density of helium at saturation	134
Figure A3.4:	Density of liquid helium at saturation	134
Figure A3.5:	Latent heat of vaporisation of helium	135
Figure A3.6:	Specific heat of liquid helium at saturation	135
Figure A3.7:	Entropy of liquid helium at saturation	136
Figure A4.1:	Physical situation (a) and temperature profile (b) of the thermal contact	137
Figure A4.2:	Joint-roughness model for modeling thermal contact impedance	139

LIST OF TABLES

Table I-1.1:	LHC performance parameters	4
Table I-2.1:	Distributed heat loads in LHC arcs [W/m]	12
Table I-2.2:	Refrigeration capacity demands of LHC sector cryoplants	13
Table I-3.1:	Main dimensions of the prototype dipole cryostat	16
Table I-3.2:	Operational conditions for the cryogenic piping (in nominal operation)	17
Table II-1.1:	Thermal conductivity integrals for selected materials ($T_1 = 4$ K)	22
Table II-1.2:	Accommodation coefficient for different gases	24
Table II-1.3:	Thermal emissivity of technical materials at cryogenic temperatures	25
Table II-1.4:	Characteristics of insulation systems	29
Table II-2.1:	Helium inventory in the CTM	41
Table II-2.2:	Precision of Allen-Bradley carbon sensor calibration	50
Table II-2.3:	CTM flowmeters	51
Table II-3.1:	CTM parameters in nominal steady state condition	59
Table II-3.2:	CTM heat inleaks under steady-state conditions	59
Table II-3.3:	Heat inleaks to support posts	60
Table II-3.4:	Main differences between LHC design and LHC prototype magnet string	60
Table II-3.5:	Heat inleaks of the LHC prototype magnet string under steady-state conditions [W]	61
Table II-3.6:	Heat loads of the single-magnet test under steady-state conditions [W]	61
Table II-3.7:	Range of cryoline temperatures investigated in the CTM	62

Table II-3.8:	Measured heat flux through multilayer reflective insulation systems (type B)	67
Table II-3.9:	Heat inleak at 1.9 K under degraded insulation vacuum (LHC prototype String test)	70
Table II-3.10:	Summary of contact resistance measurements	72
Table II-3.11:	Main dimensions of support post heat interceptions	73
Table II-3.12:	Measurements on instrumented prototype cryostat	76
Table II-3.13:	Calculated heat inleaks of prototype magnet support system (2 posts)	77
Table II-3.14:	Summary of measurements on prototype cryostats	79
Table II-3.15:	Measured temperatures on the thermal shield	80
Table II-3.16:	Measured temperature on the vacuum barrier heat intercepts	81
Table II-3.17:	Measured temperatures on the valve heat intercepts	82
Table II-4.1:	Heat inleaks under steady-state conditions	92
Table II-4.2:	Test program of the cryostat to measure the impedance of thermal contacts	94
Table III-1.1:	Mass of the LHC prototype main lattice magnets	102
Table III-1.2:	Helium-to-magnet heat transfer coefficient (forced-flow cooldown)	105
Table III-1.3:	Main parameters of the string forced-flow cooldown and warmup	106
Table III-2.1:	Masses and main dimensions of the string test	114
Table A1.1:	Calculated heat inleaks in short straight section cryostat in steady-state conditions	120
Table A1.2:	Calculated heat inleaks in dipole cryostat in steady-state conditions	121
Table A1.3:	Calculated heat inleaks in the LHC prototype magnet string in steady-state conditions	121
Table A1.4:	Measured steady-state heat inleaks for different temperatures of the circuit E-F (precision= $\pm 5\%$)	122
Table A1.5:	Measured steady-state heat inleaks for different temperatures of the circuit C-D (precision= $\pm 5\%$)	123
Table A1.6:	Measured steady-state heat inleaks at 1.9 K under varying residual He pressure (precision= $\pm 5\%$)	124
Table A1.7:	Comparison between CTM1 and CTM2 heat inleak measurements in nominal steady-state condition	124
Table A3.1:	Helium characteristics	136

LIST OF SYMBOLS

A	Cross-section	[m ²]
A	Gorter-Mellink mutual friction parameter	[cm·s/g]
\bar{A}	Surface	[m ²]
A _a	Apparent section	[m ²]
A _C	Contact are	[m ²]
A _V	Void area	[m ²]
B	Magnetic field	[T]
c	Constant for thermal conductivity	Dimensionless
C	Thermal conductance	[W/m ² ·K]
C _p	Specific heat at constant pressure	[J/kg·K]
C _v	Specific heat at constant volume	[J/m ³ ·K]
d	Distance between two surfaces	[m]
D	Diameter	[m]
D _h	Hydraulic diameter	[m]
e	Material thickness	[m]
e _g	Thickness of the void space	[m]
E	Emissivity factor	Dimensionless
E	Elastic module	[Pa]
f	Revolution frequency	[1/s]
f _c	Convection factor	Dimensionless
F	Reduction factor	Dimensionless
F	Applied force	[N]
h	Specific enthalpy	[J/kg]
h _c	Heat transfer coefficient	[W/m ² ·K]
h _C	Contact coefficient	[W/m ² ·K]
h _l	Heat transfer coefficient per unit length	[W/m·K]
H	Enthalpy	[J]
I	Current	[A]
J	Current density	[A/mm ²]

k	Number of bunches	Dimensionless
K	Thermal conductivity	[W/m·K]
K ₀	Thermal conductivity of reference	[W/m·K]
l	Length	[m]
L	Luminosity	[1/cm ² ·s]
L _p	Mean free path	[cm]
m	Coefficient for conduction in superfluid helium	Dimensionless
m	Mass	[kg]
\dot{m}	Mass-flow	[kg/s]
M	Molecular weight	[kg/mol]
n	Number of irregularities	[1/m ²]
N	Number of protons	Dimensionless
N _S	Number of aluminised reflective films	Dimensionless
P	Pressure	[Pa]
\dot{q}	Heat flux	[W/m ²]
Q	Heat quantity	[J]
\dot{Q}	Heat (power)	[W]
r	Radius	[m]
r	Specific thermal impedance	[K·m ² /W]
r _c	Contact radius	[m]
R	Universal gas constant	[J/mol·K]
R	Electrical resistance	[Ω]
R	Thermal impedance	[K/W]
R _e	Yield stress	[Pa]
R _r	Ultimate tensile stress	[Pa]
s	Specific entropy	[J/kg·K]
S	Entropy	[J/K]
t	Time	[s]
T	Temperature	[K]
u	Specific internal energy	[J/kg]
U	Internal energy	[J]
v	Specific volume	[m ³ /kg]
v	Velocity	[m/s]
V	Voltage	[V]
V	Volume	[m ³]
W	Total work	[J]
W _f	Flow work	[J]
W _m	Mechanical work	[J]
x	Longitudinal co-ordinate	[m]

Z	Potential energy	[J]
α	Accommodation factor for conduction in residual gas	Dimensionless
α_S	Conductive (solid conduction) factor for heat transfer through MLI	[W/m ² ·K ²]
α_T	Linear thermal expansion coefficient	[1/K]
β	Betatron function	[m]
β_S	Radiative factor for heat transfer through MLI	[W/m ² ·K ⁴]
β_T	Volume thermal expansion coefficient	[1/K]
γ	Lorentz factor	Dimensionless
γ_c	Ratio of specific heats	Dimensionless
γ_S	Conductive (conduction in residual gas) factor for heat transfer through MLI	[W/Pa·m ² ·K]
Δ	Roughness	[m]
ε	Porosity	Dimensionless
ε	Emissivity	Dimensionless
ε_n	Emittance	[m ²]
η	Dynamic viscosity	[Pa·s]
θ	Temperature ratio=T/T _λ	Dimensionless
σ	Stefan-Boltzmann constant	[W/m ² ·K ⁴]
λ	Wavelength	[μm]
λ_c	Contact factor	Dimensionless
ρ	Density	[kg/m ³]
ρ	Resistivity	[μΩ·cm]
ρ_0	Constant term of the resistivity	[μΩ·cm]
σ	Applied pressure	[Pa]

Dimensionless numbers

Nusselt number	$Nu = \frac{hD_h}{K}$
Grashof number	$Gr = \frac{\rho g \beta_T (T - T_{fluid}) l^3}{\eta^2}$
Prandtl number	$Pr = \frac{C_p \eta}{K}$
Reynolds number	$Re = \frac{\rho v D_h}{\eta}$

Subscripts***General***

c	Refers to critical conditions
C	Refers to contact region
e	Refers to emitted molecules
g	Refers to gas
i	Refers to incident molecules
l	Refers to liquid
s	General fluid
s	Spacer
t	Total
w	Evaluated at wall condition
λ	Evaluated at Lambda point
∞	Evaluated at free-stream condition

Components

cm	Cold mass
cp	Cooling pipe
sp	Support post
ss	Screen at 4.5-20 K
S	MLI
S1	MLI wrapped around the thermal shield
S2	MLI wrapped around the cold mass
ts	Thermal shield
vv	Vacuum vessel

Temperature

amb	Ambient temperature
m	Average temperature
1	Cold boundary temperature
2	Warm boundary temperature
S1	Outer layer of MLI wrapped around the thermal shield
S2	Outer layer of MLI wrapped around the thermal shield

Time

0	time t
1	t+dt
n	t+n·dt

Other symbols***Materials***

Al	Aluminum
Cu	Copper
He	Helium

M Magnet
 StSt Stainless steel

Heat transfer processes

cv Convection
 gc Conduction in residual gas
 r Radiation
 sc Solid conduction

PART 1

THE LHC PROJECT

AND ITS CRYOGENIC SYSTEM

CHAPTER 1

Introduction to the LHC project

The Large Hadron Collider (LHC) project [1-3] was approved by the CERN Council in December 1994. It will provide proton-proton collisions with a centre-of-mass energy of up to 14 TeV, and an unprecedented nominal luminosity of $10^{34} \text{ cm}^{-2}\text{s}^{-1}$, as well as heavy ion (Pb-Pb) collisions with a luminosity of up to $10^{27} \text{ cm}^{-2}\text{s}^{-1}$. It will be installed in the existing Large Electron-Positron storage ring (LEP) tunnel (figure I-1.1) at the end of LEP operation [4, 5]. Space will be kept above the LHC for the possible reinstallation of a LEP-like electron ring to provide future e-p collisions.

This machine will permit to investigate the fine structure of the matter at the scale of 10^{-19} m , by recreating the conditions which prevailed in the very early universe.

In order to achieve the design energy, the superconducting magnet system will operate in superfluid helium below 2 K, with a dipole field of 8.36 T. Space limitations and cost considerations impose a two-in-one magnet design, where the two rings are incorporated in the same cryostat.

1.1 Basic design

Both LEP and LHC machines are synchrotrons in which beams of particles are accelerated, held in a circular orbit by thousands of electromagnets and brought into collision at a few points around the circumference, where large physics detectors observe and analyse the outcoming reaction products. LEP collides electrons with positrons (leptons), while in the LHC both beams of particle are protons (hadrons). The maximum energy of the leptons which collide in LEP is limited to about 100 GeV by synchrotron radiation. In view of their much larger rest mass, the LHC protons will circulate in the same tunnel as the LEP electrons radiating much less synchrotron radiation. Therefore, the ultimate energy attained by LHC beams will only be limited by the bending field produced in the superconducting magnets. The LHC will be installed in the 27 km LEP tunnel after removing LEP. It will allow proton beams to be stored at an energy of 7 TeV per beam using superconducting magnets with a field of 8.36 T, about twice as high as the current state-of-the-art for accelerators magnets.

To collide two beams of equally charged particles, two separate magnetic channels are needed. LHC will make use of twin-aperture magnets which consists of two sets of coils and beam channels within the same mechanical structure and cryostat.

The two beam channels lie in the same plane and the beams pass from one ring to the other in four crossing points where the physics experiments are installed.

It is also planned to use the LHC to collide ions. The two separate beam channels of the LHC can also store relativistic ion beams. The energy per ion is the energy per proton multiplied by the number of charges of the fully stripped ion. For heavy ions, such as lead, the total collision energy of the nuclei would reach 1148 TeV.

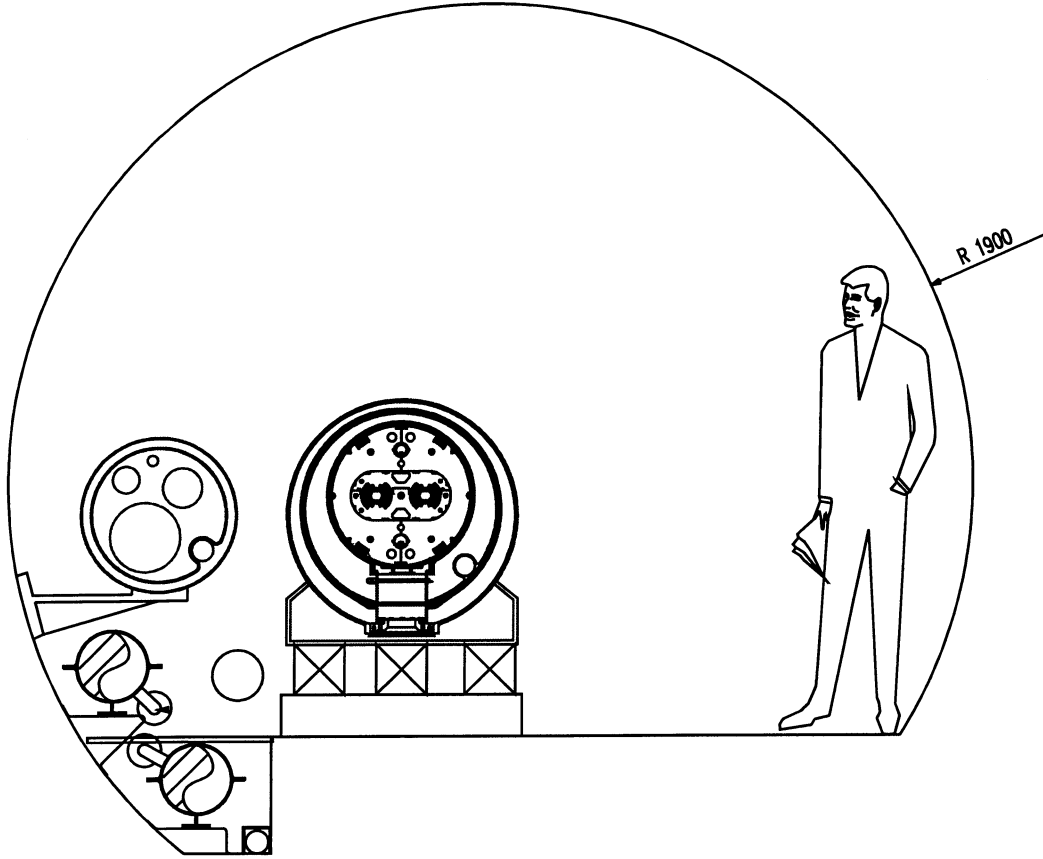


Figure I-1.1: LHC in the LEP tunnel

1.2 Performance

1.2.1 Performance for proton-proton collisions

Table I-1.1 shows the main performance parameters for the proton-proton operation. In the design of LHC an important parameter is luminosity since it determines the number of events per second for a given particle interaction. As a consequence of the decrease of interaction cross-section with increasing energy, the luminosity should increase at least as E^2 in order to maintain an equally effective physics programme at a higher beam energy. The LHC should reach the highest usable luminosity which will be in the range of $10^{34} \text{ cm}^{-2} \text{ s}^{-1}$. Luminosity is given by the following formula:

$$L = \frac{N^2 \cdot k \cdot f \cdot \gamma}{4 \cdot \pi \cdot \epsilon_n \cdot \beta^*} \cdot F \quad (\text{I-1.1})$$

where N is the number of protons in each of the k circulating bunches, f is the revolution frequency, β^* is the value of the betatron function at the crossing point, ε_n is the emittance corresponding to the contour of the beam, normalised by multiplying by the Lorentz factor $\gamma = (E/m_0c^2)$, and F is the reduction factor caused by the crossing angle, which is about 0.9 in the LHC.

The main limit to luminosity comes from the beam-beam effect which tends to scatter the periphery of the beam due to the influence of non-linear fields seen by the particles of one beam as it passes through the oncoming bunches of the other. As a result of this effect high-energy colliders tend to have a luminosity which scales in proportion with energy, and not the square of energy as one would like. Luminosity can also be maximised by making β^* as small as possible. The number of bunches, k , has to be chosen in order to maximise luminosity for a given total current and to be acceptable for the data-taking capacity of the experiments. The chosen bunch interval is 25 ns, or 40 MHz bunch frequency.

Another limit comes from the total power delivered to the cold bore of the magnets by synchrotron radiation. It must be absorbed at a temperature of a few kelvin and it will be one of the main heat inputs to the cryogenic system.

Table I-1.1: LHC performance parameters

Energy	[TeV]	7.0
Dipole field	[T]	8.36
Coil aperture	[mm]	56
Distance between apertures	[mm]	194
Luminosity	[cm ⁻² s ⁻¹]	10 ³⁴
Beam-beam parameter		0.0034
Injection energy	[GeV]	450
Circulating current/beam	[A]	0.54
Bunch spacing	[ns]	25
Particles per bunch		10 ¹¹
Stored beam energy	[MJ]	334
Normalised transverse emittance	[μ m.rad]	3.75
r.m.s. bunch length	[m]	0.075
β -values at I.P. in collision	[m]	0.5
Full crossing angle	[μ rad]	200
Beam lifetime	[h]	22
Luminosity lifetime	[h]	10
Energy loss per turn	[keV]	6.7
Critical photon energy	[eV]	44.1
Total radiated power per beam	[kW]	3.6

The design luminosity of $10^{34} \text{cm}^{-2} \text{s}^{-1}$ has been selected well below the beam-beam limited value which is $2.5 \cdot 10^{34} \text{cm}^{-2} \text{s}^{-1}$ in order to reduce the particle loss rate dangerous for superconducting elements.

A classical beam absorber is employed to safely absorb the total energy stored in the beam at the end of each run or in case of malfunction or an emergency. At the maximum luminosity of the LHC the stored beam energy is approximately 550 MJ.

1.2.2 Performance as an ion-ion collider

CERN has built a lead-ion source together with a new pre-accelerated stage. The LHC would be able to collide heavy nuclei (Pb-Pb) with a centre-of-mass energy of 2.76 TeV/u and 7.0 TeV per charge. By modifying the existing antiproton ring (LEAR) into an ion accumulator in which strong electron cooling is applied, the peak luminosity can reach more than $10^{27} \text{cm}^{-2} \text{s}^{-1}$.

1.3 Systems

1.3.1 Layout

The basic layout of the machine (figure I-1.2) follows that of LEP.

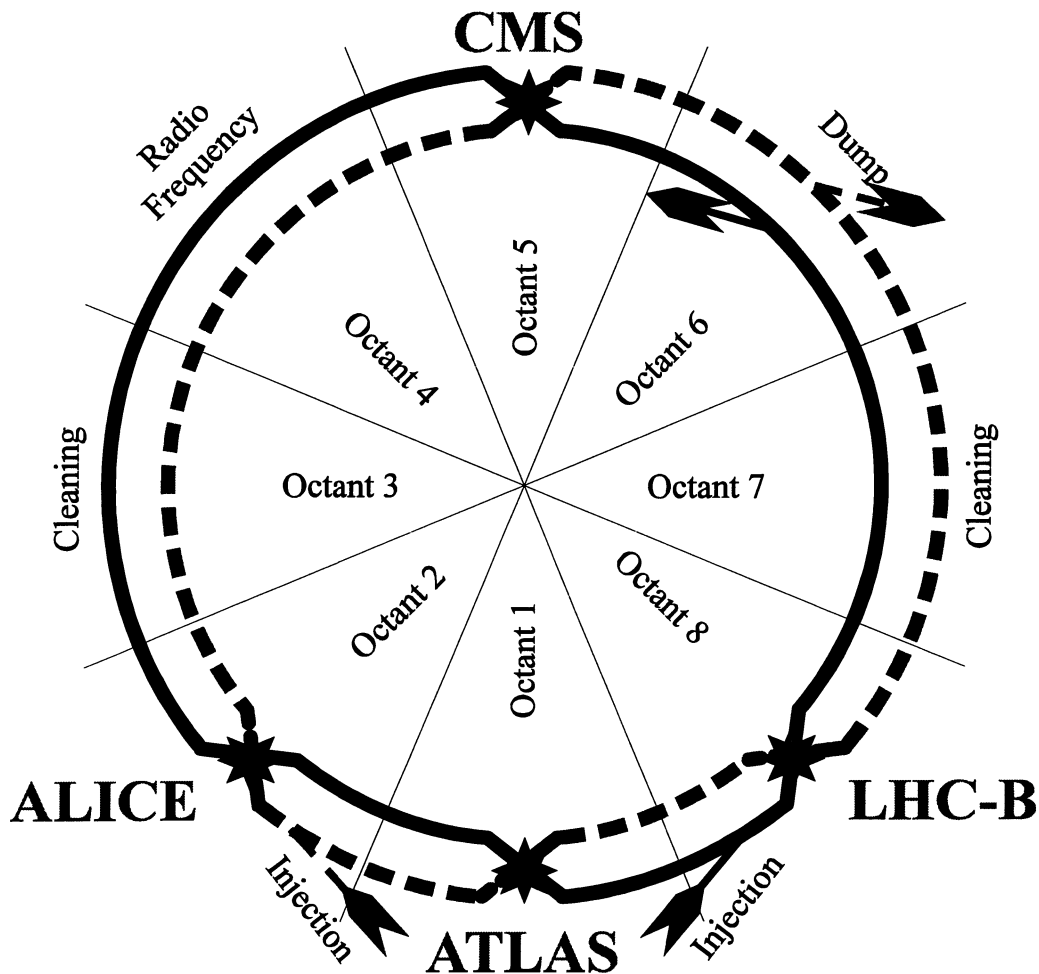
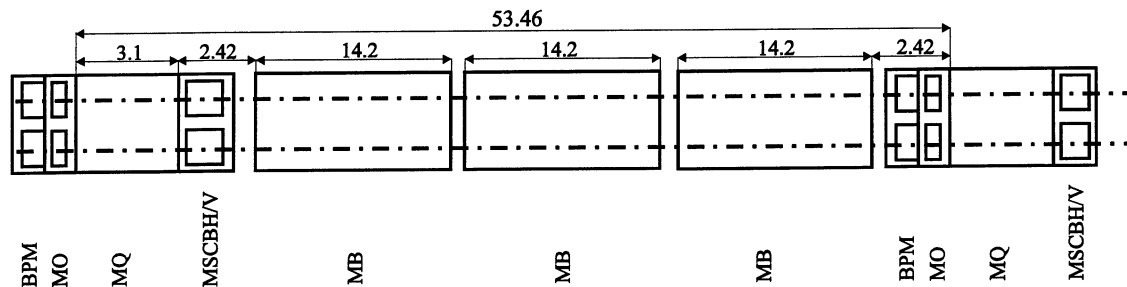


Figure I-1.2: Schematic layout of the LHC

Almost 24 km of the LHC ring will be filled with superconducting magnets of various types. The LHC circumference is composed of eight arcs 2459.16 m long each, sixteen dispersion suppressor cells 174 m long each and eight straight sections approximately 528 m long each, available for experimental insertions or utilities.

Two high-luminosity proton-proton experiments are located at diametrically opposite straight sections, point 1 (ATLAS) and point 5 (CMS). Two other experimental sections are located at point 2 (ALICE) and point 8 (B-physics), which also contains the injection system. The beams cross from one ring to the other only at these four locations. The remaining four straight sections do not have beam crossings. Points 3 and 7 are used for beam “cleaning”. The cleaning insertion must allow for collimation and cleaning of the beam halo in order to minimise the background in the detectors as well as the beam losses in the cryogenic part of the machine. Point 6 contains the beam abort system which has the purpose to dump the beams in a safe way at the end of physics runs and to protect the machine in case of hardware failure or beam instability. Point 4 contains the RF systems.

Each arc contains 23 regular lattice periods. Each lattice period, 106.9 m in length (figure I-1.3), contains six 14.2 m twin-aperture dipole magnets and two 3.10 m twin-bore quadrupoles. The separation between the dipole is 1.46 m, which includes 0.52 m for connections between the cryostats. Each dipole contains short sextupole and decapole correctors in order to compensate for undesired field harmonics. The lattice quadrupoles are powered separately from the dipoles for adjusting the betatron tune of the machine. The quadrupoles are integrated into “short straight sections” which also contain a beam position monitor (BPM), an octupole and a combined sextupole/dipole corrector.



MB= arc dipole

MQ= arc quadrupole

MO= arc octupole

MSCBH/V= arc sextupole-dipole corrector horizontal/vertical

BPM= beam position monitor

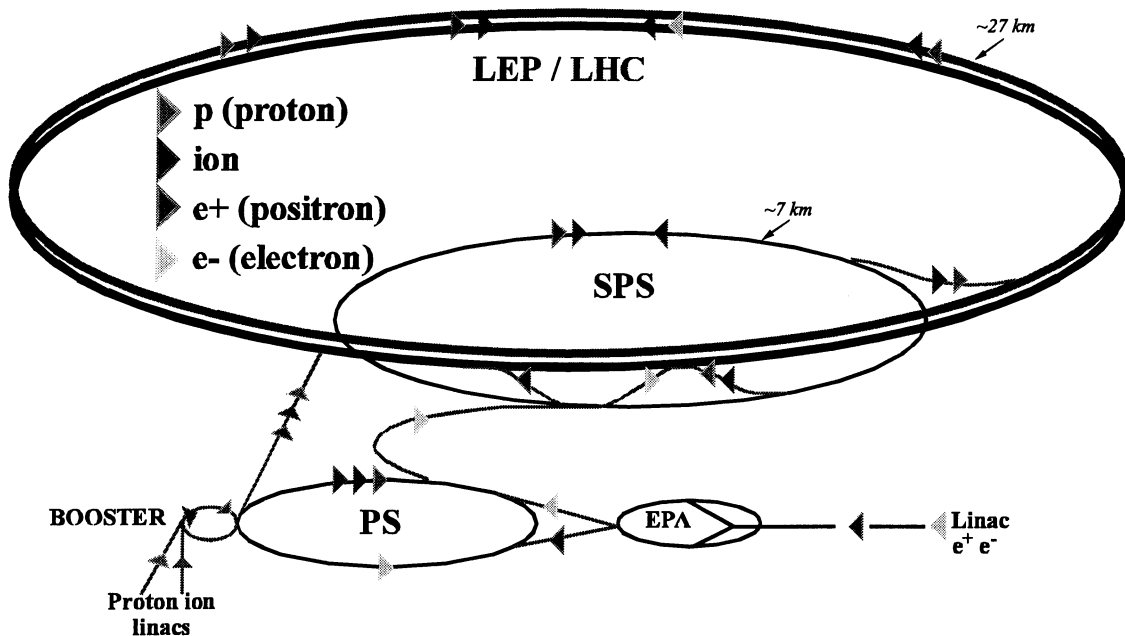
Figure I-1.3: Layout of the half-cell of the LHC

At the end of each arc there are the dispersion suppressors which bring the beam “dispersion”, i.e. the variation of trajectory with momentum spread, to zero before entering the collision regions. Each dispersion suppressor consists of two lattice periods with four dipoles per period and four independently powered quadrupole units.

The low-beta insertion is antisymmetric and consists of a matching section (outer triplets) for detuning the optics and an inner triplet for focusing the beams to the interaction point. Between the outer and inner triplets a pair of recombination dipoles brings the beams into a common channel with a small residual crossing angle at the interaction point.

1.3.2 Injectors and injections

The existing accelerator chain shown in figure I-1.4 (Linac/Booster/PS/SPS) will be used for LHC injection.



PS= Proton synchrotron

SPS= Super Proton Synchrotron

EPA= Electron-Positron Accumulator

Linacs= Linear Accelerators

Figure I-1.4: Schematic layout of the LHC injection

In order to achieve the emittance, intensity, and bunch spacing required, some modifications to the PS, SPS and Booster are necessary. The filling sequence starts with the injection of three bunch trains into the SPS on three successive PS cycles each separated by 3.6 s, filling one third of the SPS circumference. The SPS then accelerates the beam to 450 GeV and transfers each batch (each containing $2.4 \cdot 10^{13}$ protons) to one or the other of the LHC rings. This is repeated 12 times per ring with a cycle time of 16.8 s. Once both rings are filled, the beams are accelerated to the nominal collision energy in about 20 min.

1.3.3 Magnets

The superconducting magnets are the most challenging components of the LHC. Superconductivity is a property that some materials acquire when they are cooled to a low temperature: their resistance to the passage of electrical current virtually disappears. The superconducting state only exists when materials are maintained

below the critical temperature that depends on the amount of current carried by the conductors and the magnetic field to which the conductor is subjected. The *critical surface*, as shown in figure I-1.5 is defined by the boundaries of critical temperature T_c , critical magnetic flux density B_c , and critical current density J_c . The resistive transition from the superconducting to the normal state (quench) occurs if one of the three parameters exceeds its critical value.

Using Nb-Ti based conductor, the superconducting magnets operate in superfluid helium in order to achieve the high guide field (8.36 T) required. Magnets can be compact since large current can pass through superconductors of small cross-sections. The basic structure of both dipoles and quadrupoles is the twin-aperture design.

In order to retain the large electromagnetic bursting forces (more than 500 tons per meter length) the coils must be firmly clamped in a rigid mechanical structure. Combined aluminium collars have been chosen instead of stainless steel in order to minimise the pre-stress required at room temperature and ensure the best parallelism between the dipole fields in the two channels.

The regular lattice and dispersion suppressors will require 1232 dipoles and 368 normal quadrupoles as well as special quadrupoles in the matching sections and insertion regions.

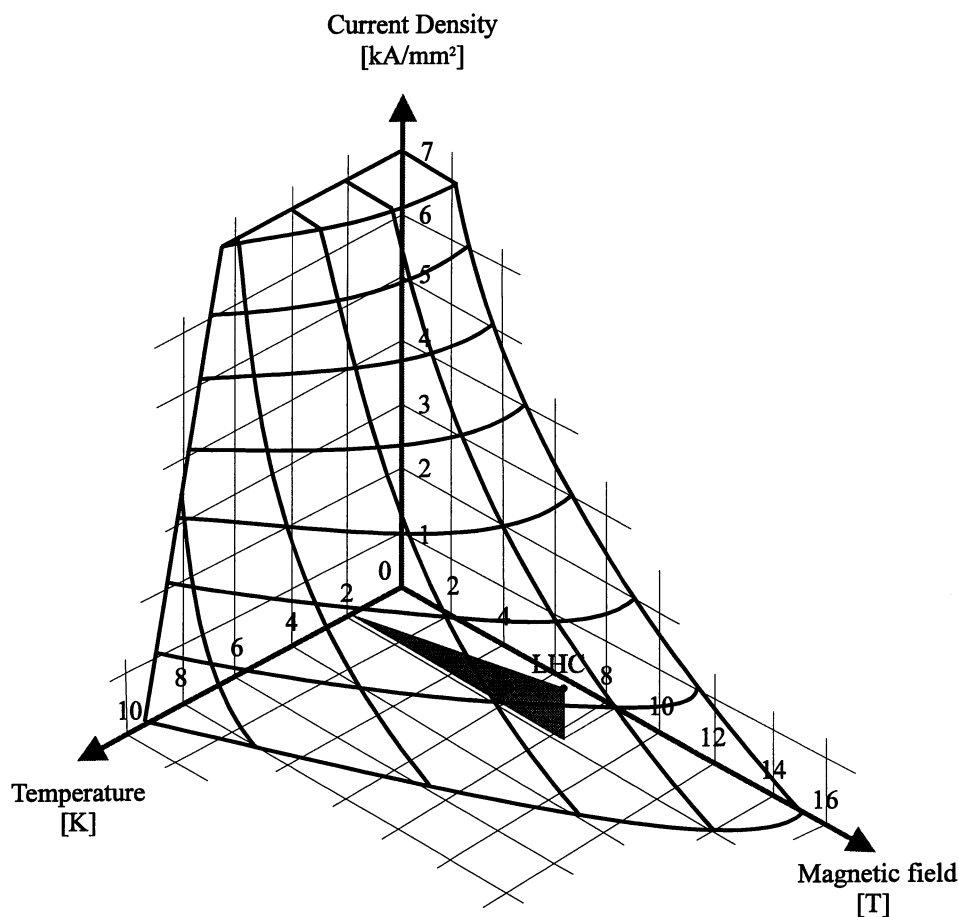


Figure I-1.5: Phase-transition surface of Niobium-Titanium

1.3.4 Protection against beam losses

During beam-beam collisions produced in the physics experiments, many elastic particles are emitted in the forward direction with the same momentum and a slight increase in the transverse angle. These particles are pushed outside of the stable region, creating a systematic halo which must be intercepted before it hits the cold inner bore of the magnet to prevent it from a quench. In order to clean a 7 TeV beam halo collimators are necessary. Beam dumping must be reliable since the onset of beam loss must be detected so that the beam can be safely extracted before it causes a quench. The dump itself is composed of graphite and aluminium blocks buried in an iron shield. The whole assembly will be installed in a waterproof cavern to prevent underground water contamination.

1.3.5 Vacuum

The LHC beam vacuum system represents a novel challenge. The magnet cold bore at 1.9 K must be protected from the power deposited by synchrotron radiation and image currents. A beam screen cooled to around 20 K by means of supercritical helium will be installed inside the cold bore. Synchrotron radiation will cause gas to be desorbed from the near surface layer, and later cryopumped again onto the same surface. The pumping capacity of the screen for hydrogen in this temperature range is not sufficient to maintain the low operating pressure. In order to avoid this, slots must be cut in the beam screen so that hydrogen can be cryopumped by the cold bore surface at much lower temperature.

1.3.6 The RF system

In order to ensure sufficiently short bunches in collision and avoid RF noise diffusion, a voltage of 16 MV per beam is needed. This is provided by strings of superconducting accelerator cavities, one on each circulating beam. To minimise the effects of transient beam loading, cavities with a high stored energy are preferred. Superconducting cavities with a wide beam tube aperture (30 cm) have been chosen for the LHC. Compared to conventional copper cavities they provide a gain of one order of magnitude against transient beam load effects.

CHAPTER 2

The LHC cryogenic system

The superconducting magnet windings will be immersed in a pressurised bath of superfluid helium at about 1 bar and a temperature of 1.9 K [6] over most of the 26.7 km circumference of the accelerator. This requires the development and the implementation of a cryogenic system unprecedented in size, refrigeration capacity and complexity [7].

2.1 General architecture

All the active cryogenic equipment [8] is grouped together at the four even points, so that the refrigeration power is transported over the complete length of a sector, 3.3 km. In order to limit hydrostatic and frictional pressure drops, the tube diameters have to be carefully dimensioned. The cryogenic pipes distributing cooling power are contained in a separate Cryogenic Distribution Line (CDL) running alongside the magnet cryostat with cryogenic interconnections at every half-cell (53.46 m).

The four-point feed scheme is shown in figure I-2.1. Two helium refrigerators (equivalent refrigeration power of 18 kW at 4.5 K each) are installed at each even point and serve the adjacent sectors. Partial redundancy is obtained by means of a Cryoplant Interconnection Box (CIB), allowing distribution of the cryogenic loads of each sector to either or both cryoplants [9].

Refrigeration at 1.8 K [10] is provided by two Cold Compressor Boxes (CCB), installed underground at the level of the machine tunnel and fed from the 4.5 K refrigerators through the CIB. The string of magnets is terminated by Tunnel Feed Boxes (TFB) on each end of a sector that is mainly used for electrical feed of the LHC. 1000 m³ and 1500 m³ storage vessel at 20 bars are used in the odd and even points respectively for recovery of gaseous helium after a generalised resistive transition of the magnets in the octant concerned.

2.2 Temperature levels and heat loads

The temperature levels in the LHC cryogenic system are the following:

- thermal shielding between 50 K and 75 K sheltering the cold mass from the heat inleaks from ambient,

- supercritical helium at 4.5 K for initial filling of the cryomagnets and lower temperature heat interception during operation. This circuit will be also used for cooling the beam screens between 4.5 K and 20 K,
- quasi-isothermal superfluid helium cooling the magnet cold mass at a maximum temperature of 1.9 K and transporting the applied heat loads across the length of a sector (3.3 km) to the cold compressor boxes at 1.8 K,
- normal helium cooling special superconducting magnets in insertion regions, superconducting acceleration cavities, and the lower sections of High Temperature Superconductor (HTS) current leads at a saturation temperature between 4.5 K and 4.7 K,
- gaseous helium cooling the resistive upper sections of HTS current leads, in forced flow between 20 K and ambient.

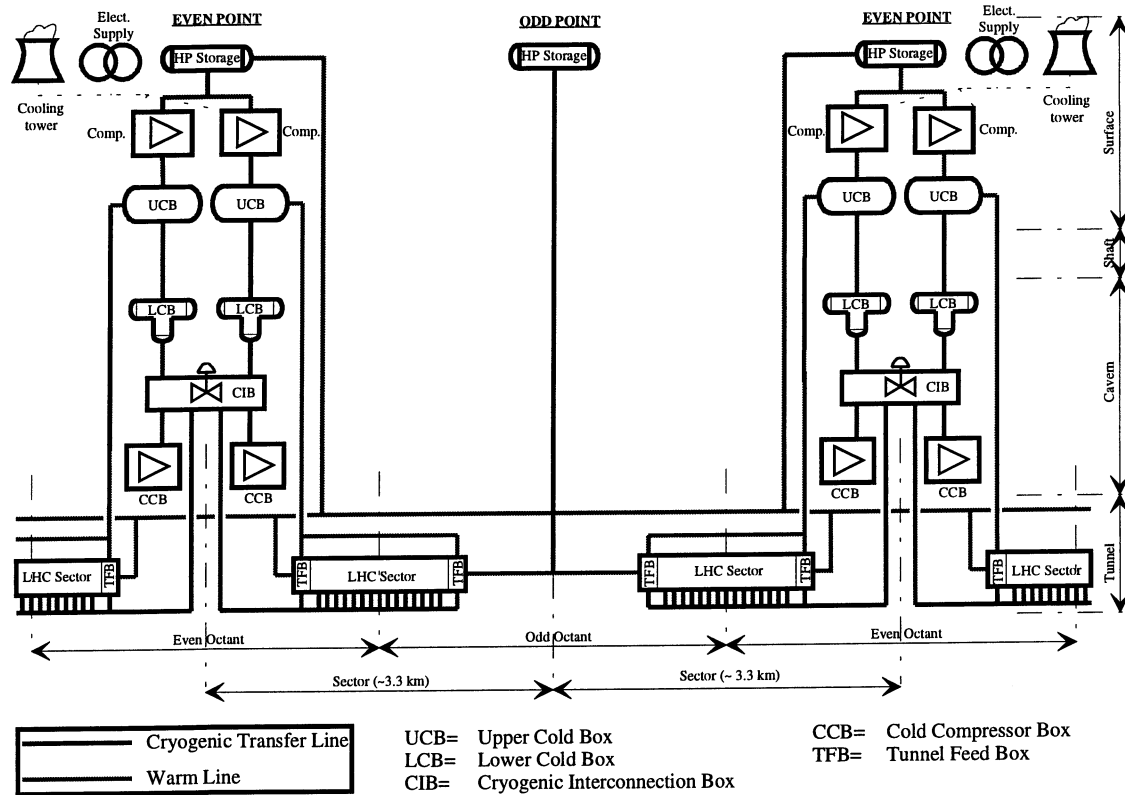


Figure I-2.1: General architecture of the LHC cryogenic scheme

The cryogenic components will be subject to three kinds of heat loads:

1. heat inleak from room temperature,
2. resistive heating in the non-superconducting sections of the magnets (essentially current feedthroughs and splices in the superconducting cables),
3. beam-induced heating due to circulation and collision of proton beams. Several processes determine this dynamic load strongly depending on the energy and intensity of the circulating beams:
 - synchrotron radiation from the bending magnets
 - resistive heating due to image currents induced in the conducting walls

- continuous loss of particles from the circulating beams, produced by nuclear inelastic beam-gas scattering
- continuous loss of particles escaping the collimation sections
- absorption of secondaries in the cold mass of the superconducting magnets located close to the high-luminosity experimental areas

Efficient cryostats must limit the heat loads, thus contributing to keep refrigeration power within budgeted values (table I-2.1) [11].

Table I-2.1: Distributed heat loads in LHC arcs [W/m]

	50-75 K	4.5-20 K	1.9 K
Heat inleak	6.38	0.13	0.27
Resistive heating	0.04	-	0.11
Beam induced (ultimate)(*)	-	1.35	0.05
Total	6.42	1.48	0.43

(*) 7 TeV, 2 x 0.848 A

2.3 Ring cooling system

The magnets operate in static baths of pressurised superfluid helium [12], through which heat is transported by conduction to a heat exchanger tube threading his way through the string and in which the heat is absorbed by gradual vaporisation of flowing saturated superfluid helium. The cryogenic flow-scheme of an LHC half-cell is shown in figure I-2.2.

Subcooled helium I, distributed through line A, is expanded to saturation through valve TCV1. It reaches the far end of the heat exchanger tube and gathers heat and vaporises as it flows back. The low saturation pressure is maintained by pumping the vapour through line B. Line C intercepts residual conduction at 4.5 K on magnet supports and supplies supercritical helium to the beam screens. Line D represents the return line of the circuit at 4.5-20 K. Lines E and F circulate high pressure helium at 50-75 K, which intercepts heat loads on magnet supports and thermal shield.

Cooldown and warmup is achieved by forced circulation of high-pressure gaseous helium, supplied at variable temperature by line C, tapped through valve CFV, and returned to the refrigerator through valve SRV and line D. In case of magnet resistive transition, the pressure rise is contained below the 20 bar design pressure by opening the SRV valves on the quench signal and discharging helium into line D.

2.4 Cryogenic plants

The LHC design makes the maximum possible use of the technical infrastructure of the LEP cryogenic system. LEP uses four cryogenic plants, each of 12 kW at 4.5 K capacity located at the four even points [13, 14].

On the basis of the heat load estimates for the LHC sectors, and allowing some spare capacity, the cryogenic plants should fulfil the refrigeration capacity listed in table I-2.2.

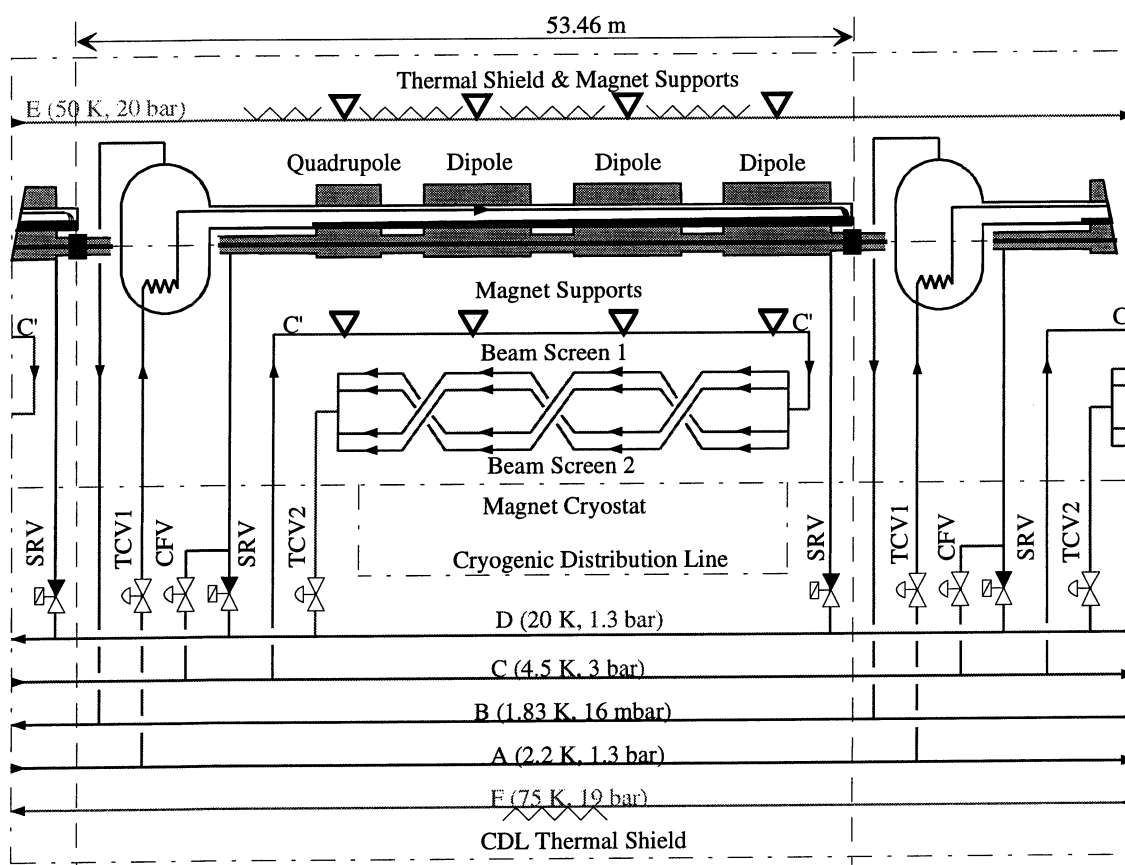


Figure I-2.2: Cryogenic flow-scheme of an LHC half-cell

Table I-2.2: Refrigeration capacity demands of LHC sector cryoplants

Sector	50-75 K [kW]	4.5-20 K [kW]	4.7 K [kW]	1.8 K [kW]	20-290 K [g/s]
High-load	31	4.3	0.80	2.80	35
Low-load	30	4.3	0.65	2.45	23

The sectors which house high luminosity insertions are subject to the largest 1.9 K heat loads, while sectors which feature the strings of superconducting acceleration cavities exhibit the largest 4.7 K heat loads. Moreover, depending on the operational mode of the LHC, the refrigeration plants must operate in wide ranges of variation in the cooling power requirements at 1.9 K (up to two-fold variation) and 4.5-20 K (up to five-fold variation). For the LHC the four existing cryogenic plants will be upgraded to 18 kW and supplemented by a further four 18 kW plants which will be located at the even points. In addition, eight CCBs, fed at 4.5 K from the cryoplants, will produce refrigeration at 1.8 K.

2.5 Helium inventory

An assessment of the helium inventory in the LHC [15] has led to a total amount of 93500 kg, mostly in the cold mass of the magnet system (54.5 %) and in the piping (41 %). Integrally storing this inventory in the conventional form would result in large investment costs and siting difficulties due to the high visibility of the 250 m³ reservoirs envisaged for this purpose. Two complementary lines of action are being followed: reduction of helium stored inside the magnet cold mass and partial storage in liquid form.

CHAPTER 3

The LHC prototype magnet cryostats

The cryostats must provide a stable mechanical support for the magnet cold mass and limit heat inleaks from room temperature to a level which matches the tight heat load budget [16, 17]. Cryostats must withstand thermal and mechanical transients, such as rapid cooldown and warmup and resistive transition. Moreover they must handle the resulting heat release during accidental operational modes including partial loss of vacuum insulation, degradation of the multilayer insulation (MLI) system efficiency and imperfect heat interception.

3.1 The prototype dipole cryostat

3.1.1 Introduction

The dipole magnets [18] are designed to be connected in series around the LHC machine. Each unit is connected electrically, hydraulically and thermally to identical elements up-and down-stream. The prototype dipole cryostats (table I-3.1) have a cold mass with an overall length of 10.05 m which is shorter than the final LHC dipole cryostat. Another difference between prototype and LHC cryostats is that all the cryogenic distribution piping is enclosed inside the vacuum vessel, in absence of a separate cryogenic line

3.1.2 Design and construction

The cold mass [19] consists of a twin aperture superconducting dipole magnet enclosed in a long cylindrical stainless steel shell. The ends are closed with covers with piping connections. There are two cold bore pipes, one helium heat exchanger running through the magnet, three pipes containing cables to be connected to the neighbouring units and the outlets for instrumentation feedthroughs. The helium vessel has a design pressure of 2 MPa and the desired overall leak-tightness is 10^{-10} Pa·m³/s.

The cold mass rests on two support posts. Each support post [20, 21] consists of a cylindrical column made of non-metallic low-thermal conductance materials and four metallic flanges, two of which act as heat intercepts. One support post is blocked to the vacuum vessel, the other one is free to move in the longitudinal direction. The top flange carries the cold mass, the second one is linked to 5 K pipe (line C), the third

flange is cooled by line E and the bottom flange serves to locate the cold mass, the cryogenic pipes and the shield in the vacuum vessel.

Table I-3.1: Main dimensions of prototype dipole cryostat

dipole magnet body overall length	10.052 m
thermal shield perimeter	2.8 m
radiative insulation perimeter	2.4 m
vacuum vessel outer diameter	0.98 m
cold mass diameter	0.58 m

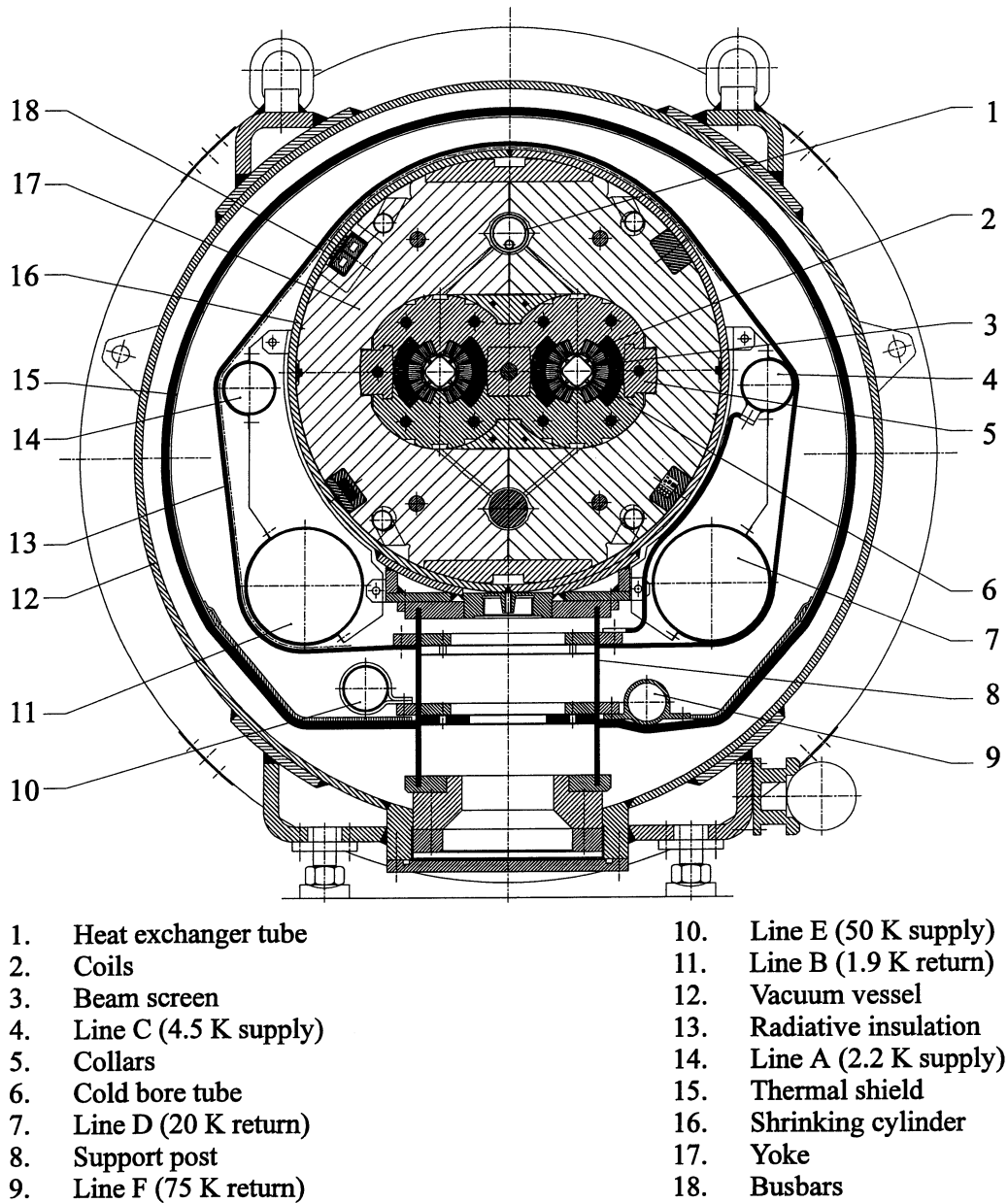


Figure I-3.1: Cross-section of the LHC prototype dipole cryostat

Six ***cryogenic pipes*** (table I-3.2) run externally along the length of the cold mass while sharing the same insulation system: lines A (supply) and B (return) at 1.9 K, lines C (supply) at 4.5 K and D (return) at 20 K, and lines E (supply) at 50-60 K and F (return) at 60-75 K. Lines A, B, C and D are directly supported by the stainless steel attachment plates welded onto the cold mass. Line C is also bridged to the support posts. Apart from line F all the cryogenic pipes are made of AISI 304L austenitic stainless steel. Line F forms an integral part of the thermal shield and is made of an extruded aluminium profile.

Table I-3.2: *Operational conditions for the cryogenic piping (in normal operation)*

Cryogenic pipes	DN [m]	Temperature [K]	Pressure [Pa·10⁵]
A	0.065	2.2	1
B	0.150	1.9	0.016
C	0.065	4.5	2.3-2.6
D	0.150	20	1
E	0.056	50-60	20
F	0.05	60-75	20

In order to maintain the heat inleak at 1.9 K within the budgeted value two levels of heat intercepts are needed: the radiative insulation at 4.5-20 K and the thermal shield at 50-75 K. The radiative insulation represents a thermal barrier between the interior part of the thermal shield and the low-temperature components, whereas the thermal shield serves to intercept the radiative heat coming from room temperature.

The ***radiative insulation*** is based on 10 layers of reflective aluminised polyester (Mylar®) film wrapped with fiberglass net spacer around a thin aluminium sheet enclosing the cold mass and the cryogenic pipes. The radiative insulation is insulated from the cold mass by means of non-metallic net spacers.

The ***thermal shield***, made of commercially pure aluminium alloy (AA1100), is composed of a 5 mm thick bottom tray and a 2.5 mm thick circular shell. The thermal shield is covered with 30 layers of MLI ensuring a minimum thickness of 10 mm.

External to the thermal shield there is the ***vacuum vessel***, which consists of a long cylindrical shell with end flanges. For reasons of costs and to screen the stray magnetic field, the cylinder of the vacuum is made of unalloyed steel of the type ISO FE 430, whereas all flanges are in stainless steel AISI 304L.

3.2 Prototype short straight section cryostat

3.2.1 Introduction

The Short Straight Section (SSS) [22] is composed of one twin-aperture quadrupole, a pair of tuning quadrupoles, MQTO, and a pair of correctors, MDSB (figure I-3.2). The short straight section cryostat also contains a barrier for sectorising the insulation

vacuum and a cryogenic service module (QSA). The design of the SSS cryostat (figure I-3.3) follows that of the prototype dipole cryostat.

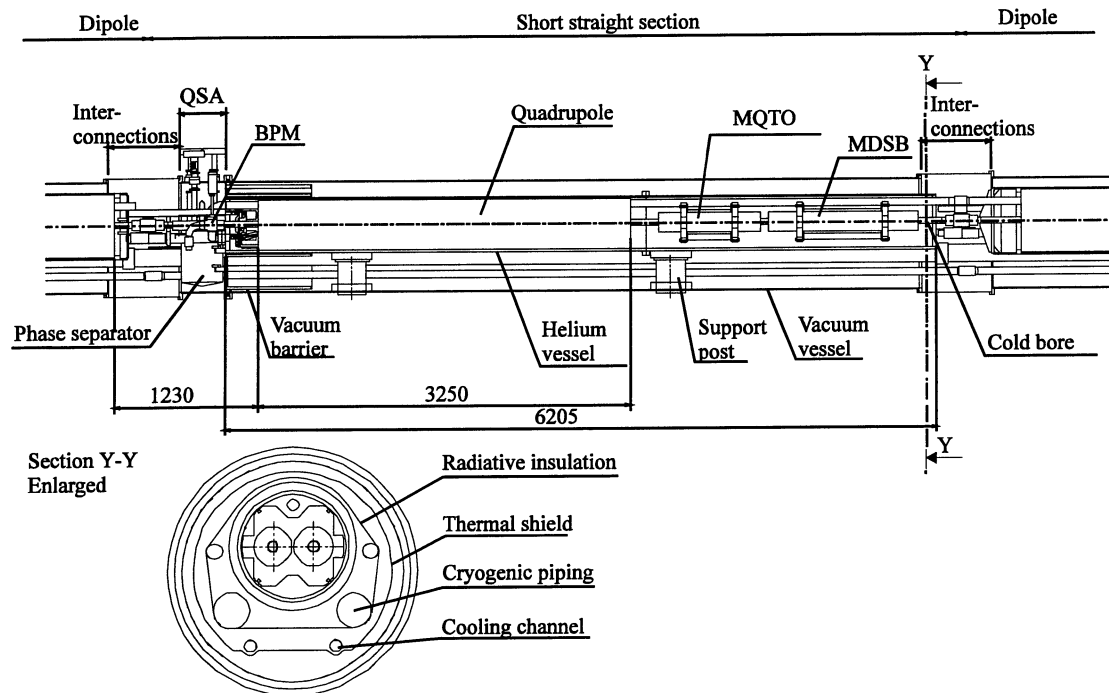


Figure I-3.2: Longitudinal section of the LHC prototype short straight section

3.2.2 Design and construction

The quadrupole and the corrector magnets, enclosed in its all-welded helium vessel, with heat exchanger and cold bore pipes, form the cold mass [23]. Support posts, radiative insulation and thermal shield, cryogenic pipes and vacuum vessel are identical to those of the prototype dipole cryostat. The only difference is the material used for the vacuum vessel. To reduce costs the vacuum vessel is entirely made of AISI 304L stainless steel. This was possible since no magnetic shielding is required, contrary to the dipole.

For measurement of the beam position and the diagnostics of its dynamic behaviour, transverse **Beam Position Monitors** (BPM) are mounted close to the quadrupole magnet on the outside of the cold mass. The BPM assembly consists of one H monitor and one V monitor. The cylindrical shaped BPMs, one for each beam, equipped with electrodes and feedthroughs are fixed in a bracket before being adjusted by a stainless steel support to the front plate of the helium vessel.

The **vacuum barrier** is mounted between the cold mass and the QSA with the purpose to limit the effects of helium leaks, facilitate leak detection and pump-down from atmospheric pressure. During the installation of the LHC, it will also enable independent leak testing of the half-cells. The vacuum barrier of the prototype short straight section consists of two double and corrugated stainless steel tubes, separated by an off-centered disc. Each corrugated tube is covered with MLI. All six cryogenic pipes are connected to the vacuum barrier by means of stainless steel sleeves. The outer flange will be at ambient temperature, the inner one at 1.8 K and the various transverse tubes between 1.9 K and 75 K. Thickness and length of the tubes are

optimised in order to minimise heat inleaks. In order to reduce costs an alternative vacuum barrier, made of non-metallic composite materials [24] and based on a similar thermo-mechanical design, has been developed and mounted on the LHC prototype magnet string.

The QSA, integrated into the SSS, is located between the interconnection region and the vacuum barrier. The QSA is the place where all cryogenics services for the adjacent half-cell are lumped, including current leads, instrumentation capillaries, control valves, phase separator and beam diagnostics.

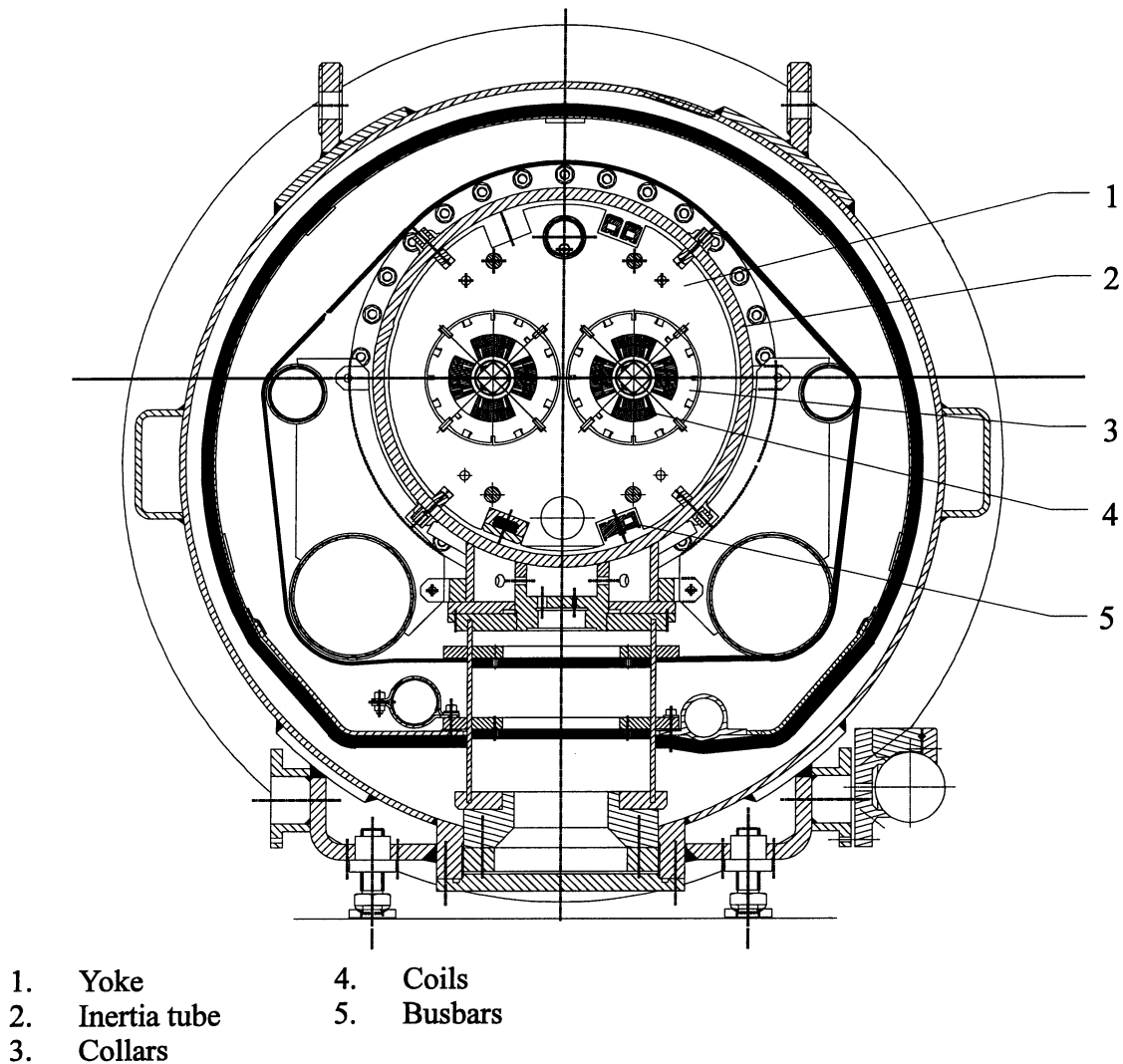


Figure I-3.3: *Cross-section of the LHC prototype short straight section cryostat, showing quadrupole*

PART 2

STEADY-STATE THERMAL PERFORMANCE OF THE LHC PROTOTYPE CRYOSTATS

CHAPTER 1

Modeling cryostat thermal performance

In this chapter an overview of heat transfer processes [25, 26] which occur in a cryostat is presented. The last part describes the mathematical model used to simulate the cryostat thermal performance.

1.1 Heat transfer processes

In the design of any cryogenic system an efficient thermal insulation from the environment must be achieved. The cryostat heat inleaks (solid conduction, conduction in residual gas, radiation, convection) have to be controlled and reduced by a proper design [27, 28].

1.1.1 Solid conduction

The fundamentals of heat conduction [29] were established over a century ago and are attributed to Fourier. When a temperature gradient exists in a body, there is a heat transfer from the high temperature region to the low temperature region. This heat is transferred by conduction and the heat transfer per unit area is proportional to the normal temperature gradient:

$$\frac{\dot{Q}}{A} \sim -\frac{\partial T}{\partial x} \quad (\text{II-1.1})$$

When the proportional constant is inserted:

$$\dot{Q} = -KA \frac{\partial T}{\partial x} \quad (\text{II-1.2})$$

where \dot{Q} is the heat-transfer rate expressed in watts and $\partial T/\partial x$ is the temperature gradient in the direction of the heat flow.

The proportional constant K [W/K·m] is the thermal conductivity of the material, and the minus sign indicates that temperature flows down-hill the temperature gradient. Equation II-1.2 is called Fourier's law of heat conduction.

For one-dimensional problems the steady-state heat-conduction equation, developed over a length l and applied between temperatures T_2 and T_1 ($T_2 > T_1$), can be written:

$$\dot{Q} = \frac{A}{l} \int_{T_1}^{T_2} K(T) dT \quad (\text{II-1.3})$$

Generally the thermal conductivity as function of temperature is not constant, so it is necessary to compute the integral. Conductivity integrals in the cryogenic temperature domain have been computed for most technical materials (table II-1.1).

Table II-1.1: Thermal conductivity integrals for selected materials ($T_1 = 4$ K)[30]

Temperature T_2	Copper ETP	Austenitic stainless steel	Aluminium 6063-T5	Glass	Teflon
[K]	[W/cm]	[W/cm]	[W/cm]	[mW/cm]	[mW/cm]
6	8	0.0063	0.85	2.11	1.13
8	19.1	0.0159	2.05	4.43	2.62
10	33.2	0.0293	3.60	6.81	4.4
20	140	0.163	16.5	20.0	16.4
30	278	0.424	36.5	36.8	32.3
40	406	0.824	62.0	58.6	50.8
50	508	1.35	89.5	84.6	71.6
60	587	1.98	117	115	93.6
70	651	2.70	143	151	116
76	686	3.17	158	175	130
80	707	3.49	167	194	139
90	756	4.36	190	240	163
100	802	5.28	211	292	187
120	891	7.26	253	408	237
140	976	9.39	293	542	287
160	1060	11.7	333	694	338
180	1140	14.1	373	858	390
200	1220	16.6	413	1030	442
250	1420	23.4	513	1500	572
300	1620	30.6	613	1990	702

The low value of thermal conductivity of non-metallic materials shows their interest in low heat inleak structural components as the cold mass support posts.

1.1.2 Conduction in residual gas

Conduction in residual gas depends on the mean free path of the gas molecules (L_p). If d is the distance between two surfaces at different temperatures, the following regimes of residual gas conduction are defined:

- $L_p < d$ *viscous regime*
- $L_p > d$ *molecular regime*
- $L_p \cong d$ *transition regime*

Residual gas conduction strongly depends on the vacuum insulation and can be made small by reduction of the residual pressure. At higher pressure $L_p < d$ and the viscous regime prevails: the heat transfer occurs by intermolecular interactions and thermal conductivity is independent of pressure. The molecules move from a high-temperature region to a lower-temperature and transport kinetic energy to the lower temperature part of the system giving up this energy through collisions with low energy molecules.

At lower pressure $L_p > d$ and conduction is governed by molecular regime. In this regime, the molecules the two surfaces several times before interacting with other molecules. In this case heat is exchanged by molecule-wall rather than intermolecular interactions. In this regime heat transfer is proportional to the residual pressure.

The mean free path L_p [cm] can be expressed as follows:

$$L_p = 11465.7 \frac{\eta}{P} \sqrt{\frac{T}{M}} \quad (\text{II-1.4})$$

where η is the gas viscosity [Pa·s] at the temperature T , M is the molecular weight [g/mol] and P is the pressure [Pa]. The value of L_p for helium is very high, so that, even for degraded vacuum (10^{-1} Pa), the heat transfer occurs in molecular regime. For a residual pressure of 10^{-1} Pa, the mean free path for helium at 4.2 K is about 0.12 cm.

The vacuum insulation of cryogenic vessels is efficient if pressure is lower than $5 \cdot 10^{-2}$ Pa and if conduction process is molecular regime.

In nominal operation, in the cryostat insulation space residual pressure is very low (10^{-4} Pa) so that heat transfer is represented by molecular-to-wall interactions. The molecular-to-wall interactions can be represented by an accommodation coefficient (table II-1.2) defined by:

$$\alpha = \frac{T_i - T_e}{T_i - T_w} \quad (\text{II-1.5})$$

where T_i is the effective temperature of the incident molecule, T_e that of the emitted or reflected molecule, and T_w the wall temperature. The maximum value for α is unity, associated with the molecule coming into complete thermal equilibrium with the wall.

Molecular conduction heat transfer between two parallel surfaces at temperatures T_1 and T_2 ($T_2 > T_1$), is given by Kennard's law:

$$Q_{mc} = \bar{A}_1 \alpha_0 \left(\frac{\gamma_c + 1}{\gamma_c - 1} \right) \left(\frac{R}{8\pi} \right)^{\frac{1}{2}} \frac{P}{(MT)^{\frac{1}{2}}} (T_2 - T_1) \quad (\text{II-1.6})$$

where $\gamma_c = C_p/C_v$ is the ratio of specific heats, R is the universal gas constant [J/mol K], \bar{A}_1 is the surface receiving the heat and α_0 is the accommodation coefficient.

Equation II-1.6 may be applied to concentric spheres, coaxial cylinders and parallel plates. For unequal values of α and \bar{A} , the quantity α_0 must be averaged over the two surfaces, that is,

$$\alpha_0 = \frac{\alpha_1 \alpha_2}{\alpha_2 + \frac{A_2}{A_1} (1 - \alpha_2) \alpha_1} \quad (\text{II-1.7})$$

Table II-1.2: Accommodation coefficient for different gases

T [K]	Helium	Hydrogen	Air
300	0.3	0.3	$\cong 0.8$
80	0.4	0.5	1
20	0.6	1	-
4	1	-	-

For many low-temperature applications, helium gas is the major contributor to gaseous conduction heat inleak, since most other gases condense or absorb on the cold surfaces.

1.1.3 Radiation

Thermal radiation is the electromagnetic radiation emitted by a body as a result of its temperature. An ideal thermal radiator, or *blackbody*, will emit energy at a rate proportional to the fourth power of the absolute temperature of the body and directly proportional to its surface area.

$$\dot{Q}_{emitted} = \sigma \bar{A} T^4 \quad (\text{II-1.8})$$

Equation II-1.8 is called the Stefan-Boltzmann's law of thermal radiation and σ ($5.667 \cdot 10^{-8} \text{ W/m}^2 \cdot \text{K}^4$) is called the Stefan-Boltzmann's constant. The emissive power associate with a blackbody is correlated to the peak wavelength λ_m of the thermal radiation by Wien's law:

$$\lambda_m T = 2898 \mu\text{m} \cdot \text{K} \quad (\text{II-1.9})$$

Equation II-1.8 governs only radiation emitted by a blackbody. A blackbody at room temperature emits about 460 W/m^2 by radiation. Practical surfaces do not radiate as much energy as the blackbody and are treated as “grey” body, characterised by an

emissivity ε ($0 < \varepsilon < 1$). To account for the “grey” nature of such surfaces we introduce another factor in equation II-1.8, called the *emissivity* factor E , which depends on the emissivities of the two surfaces, their related geometry (view factor) and the type of reflection (specular or diffuse).

In this case the radiated energy between two surfaces at temperature T_2 and T_1 ($T_2 > T_1$) can be written:

$$Q = \sigma E \bar{A}_1 (T_2^4 - T_1^4) \quad (\text{II-1.10})$$

In the case of diffuse reflection between long coaxial cylinders, E is given by:

$$E = \frac{\varepsilon_1 \varepsilon_2}{\varepsilon_2 + \frac{A_1}{A_2} (1 - \varepsilon_2) \varepsilon_1} \quad (\text{II-1.11})$$

where ε_1 and ε_2 are respectively the emissivities of the cold and warm surfaces.

Table II-1.3 shows the thermal emissivity of some technical materials frequently used in cryogenics.

In cryostats, radiation represents a dominant contribution once residual gas conduction is attenuated by adequate vacuum insulation.

For thermal insulation very low emissivities are required. Since radiation greatly depends on temperature it is possible to decrease the radiative heat inleak between two surfaces by a factor $(n+1)$ by inserting n shields of equal emissivity (floating shields). Another possibility consists of actively cooling a single shield at sufficiently low temperature.

Table II-1.3: Thermal emissivity of technical materials at cryogenic temperatures [31]

	From ambient to 77K	From 77 K to 4.2 K
St. St. as found + Al foil	0.056	0.011
St. St. silver plated	0.092	0.013
St. St. elect. polished	0.1	0.065
St. St. mech. polished	0.12	0.074
St. St. shot blast	0.24	0.14
St. St. as found	0.34	0.12
Cu mech. polished	0.06	0.023
Cu as found	0.12	0.062
Al elect. polished	0.075	0.036
Al mech. polished	0.1	0.058
Al. as found	0.12	0.07
Al+protective oxide layer	0.49	0.074

1.1.4 Convection

Convection is a process governing heat transfer between a solid surface and a liquid or a gas. There are two types of convection: natural or forced according to the way in which the liquid flow occurs.

To express the effect of convection we use Newton's law of cooling:

$$\dot{Q} = h\bar{A}(T_w - T_\infty) \quad (\text{II-1.12})$$

The heat transfer rate is related to the overall temperature difference between the wall and fluid and the surface area. The quantity h is called the *convection heat transfer coefficient*. Convection heat transfer depends on the viscosity, the thermal properties (thermal conductivity, specific heat, density) of the fluids and on flow conditions. Boiling and condensation phenomena are also grouped under the general subject of convection heat transfer.

There are numerous convection heat transfer correlations for internal and external flows. Several important factors must be considered when selecting a correlation to apply to a particular system. We must determine whether the fluid is in laminar or turbulent flow regime and whether the entry region has significant impact on either the hydrodynamics or temperature development. Once the conditions of flow are established, it is necessary to select among several possible correlations dependent on whether the range of parameters is appropriate for the particular empirical fit.

Apart from very simple cases of fully developed laminar flow with constant surface or constant heat flux boundary conditions, in all engineering correlations the average Nusselt number is a general function of Reynolds number and Prandtl number:

$$Nu = f(Re_D, Pr) \quad (\text{II-1.13})$$

The average Nusselt number is defined in terms of average heat transfer properties:

$$Nu = \frac{hD_h}{K} \quad (\text{II-1.14})$$

where K is the average fluid thermal conductivity.

For turbulent flow in circular pipe, the most common heat transfer expression for cryogenic fluids is the Dittus-Boelter correlation [32]:

$$Nu = 0.023 Re_D^{4/5} Pr^{2/5} \quad (\text{II-1.15})$$

In cryostats we find natural convection from external environment to the vessel and through the multilayer insulation system if the residual gas pressure of the insulation vacuum is higher than 10^3 Pa. Forced convection appears in helium flowing inside the cooling pipes.

1.1.5 Multilayer systems

Multilayer insulation (MLI) consists of reflective films alternate with low-density insulating spacers.

The effective thermal conductivity of MLI is a function of various parameters, such as film and spacer materials, number of layers and layer density, contact pressure, vacuum maintained and interstitial pressure [33-36]. Heat flux through MLI systems depends on a combination of solid conduction, conduction in residual gas and thermal radiation [37-39].

At low residual gas pressure (10^{-3} Pa) conduction in residual gas can be neglected and heat transfer is only given by radiation and solid conduction. Heat transfer through MLI also depends on density and total number of layers. Radiation heat transfer decreases with increasing number of radiation shields, whereas conduction heat transfer becomes larger as the packing density tends to increase. This means there is an optimum layer density for practical multilayer insulations. The existence of a minimum in the heat transfer through MLI as a function of layer density has been demonstrated experimentally (figure II-1.1).

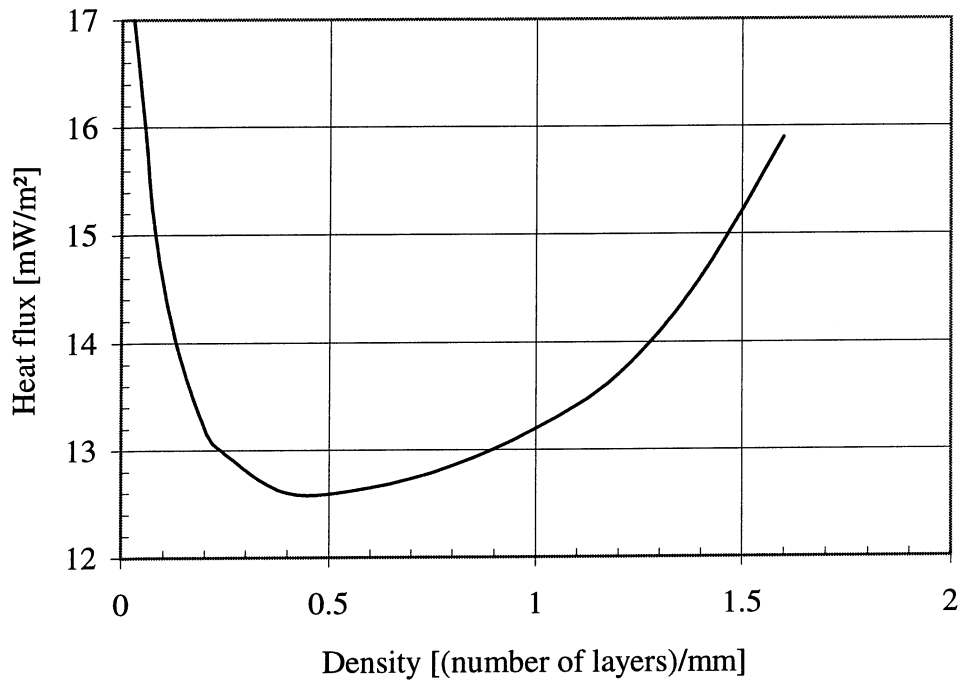


Figure II-1.1: Measured heat flux for varying layer densities of MLI between 77 K and 4.2 K [39]

The existence of a minimum near 0.5 layers/mm indicates the density where the solid-state conduction begins to play an important role.

For density higher than 0.5 layers/mm the heat flux increases with the number of layers. From these results the best values for the emissivity of aluminised Mylar® are 0.03 at 77 K and 0.011 at 4.2 K [39].

Heat flux through MLI can be expressed by the following relationship [41] which considers the conductive and the radiative effects:

$$\dot{q} = \frac{\alpha_S}{N_S} \frac{T_1 + T_2}{2} (T_2 - T_1) + \frac{\beta_S}{N_S} (T_2^4 - T_1^4) + \gamma_S P_S (T_2 - T_1) \quad (\text{II-1.16})$$

where \dot{q} is the heat flux in W/m^2 , N_S is the number of layers, T_2 and T_1 are the temperatures of respectively the warm and the cold surfaces, and α_S and β_S are two constants accounting for the average thermal conductivity and emissivity of the reflective insulation system. The third term represents the contribution of the conduction in residual gas and the coefficient γ_S can be calculated from equation II-1.6. In nominal operating condition (10^{-4} Pa), the two coefficients α_S and β_S can be evaluated by knowing the measured heat flux through MLI in two different cases:

- from 300 K to 80 K through 30 layers of MLI: 1.2 W/m^2 [42]
- from 80 K to 4.5 K through 10 layers of MLI: 0.060 W/m^2 [41]

At 10^{-4} Pa the values of α_S and β_S which represent the thermal performance of the LHC prototype cryostats are given:

$$\alpha_S = 1.401 \cdot 10^{-4} \text{ [W/m}^2 \cdot \text{K}^2]$$

$$\beta_S = 3.741 \cdot 10^{-6} \text{ [W/m}^2 \cdot \text{K}^4]$$

Figure II-1.2 shows the calculated heat flux through 30 layers of MLI as a function of the cold surface temperature when the warm surface temperature T_2 is kept at 300 K. Notice that thermal radiation is dominant and conduction through the spacers only represents a small fraction (about 20 %) of the total. Figure II-1.3 shows the calculated heat flux through 10 layers of MLI from the temperature T_2 to 4.5 K. In this case conduction heat transfer prevails for warm surface temperatures below 120 K. The contribution of conduction in residual gas starts becoming significant for residual pressure above $5 \cdot 10^{-3}$ Pa and increases proportionally to it.

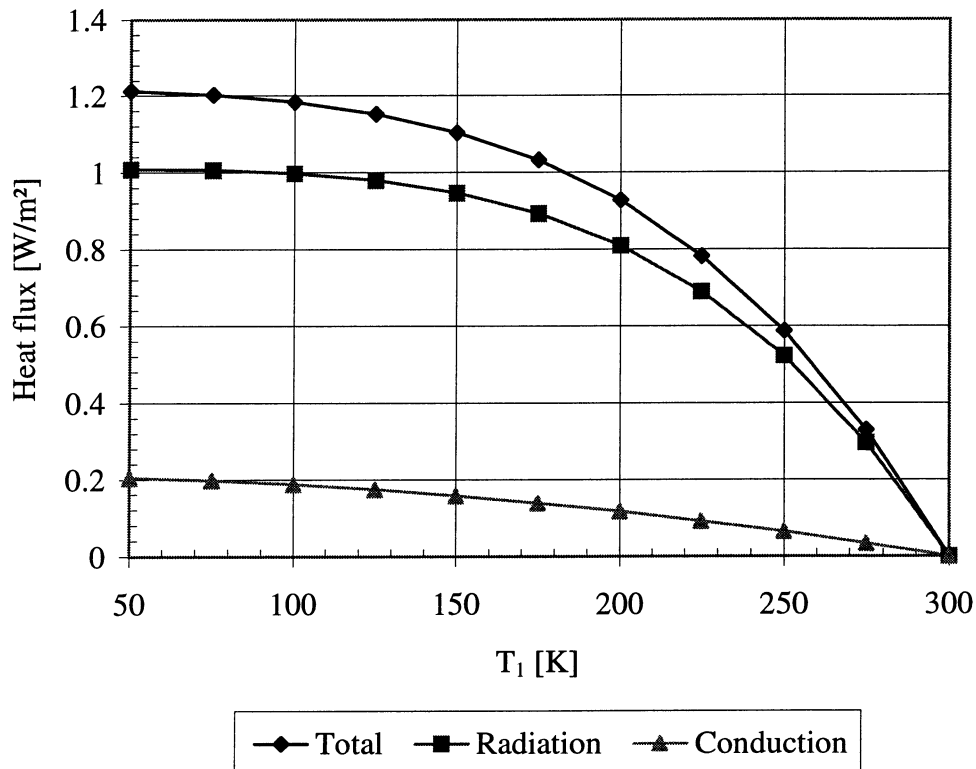


Figure II-1.2: Calculated heat flux through 30 layers of MLI from 300 K to T_1 at 10^{-4} Pa

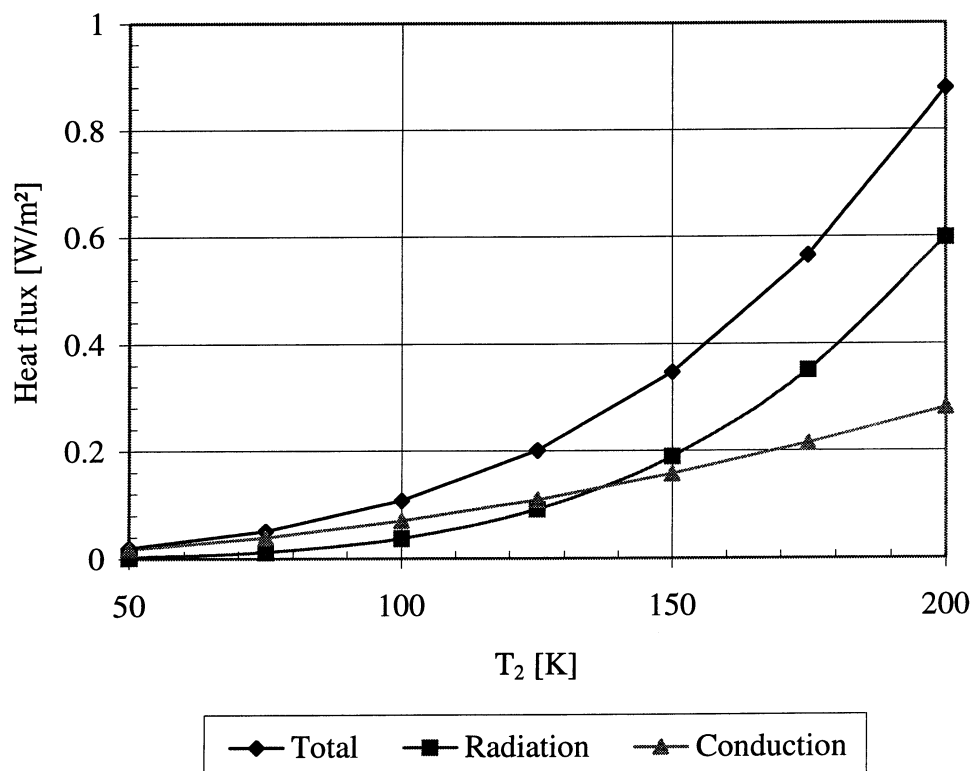


Figure II-1.3: *Calculated heat flux through 10 layers of MLI from T_2 to 4.5 K at 10^{-4} Pa*

Figure II-1.4 shows the heat flux from 80 K to 4.5 K through different types (table II-1.4) of insulation systems. We can notice that multilayer systems represent an advantage in case of degraded insulation vacuum (residual gas pressure higher than 10^{-3} Pa).

Table II-1.4: *Characteristics of some measured insulation systems [43]*

System	Film	Spacer
A	Single layer, double aluminised (2x250 Å) Mylar® film (25 µm)	None
B	Multilayer, double aluminised (2x250 Å) Mylar® film (25 µm)	Fiberglass grid (0.3 mm), 4x5 mm ² mesh
C	Single layer, double aluminised (2x400 Å) Mylar® film (6 µm)	Polyester net (0.3 mm), specific mass 5 g/m ²

Heat flux through 30 layers of MLI from 300 K to 80 K (figure II-1.5) is less sensitive to the residual gas pressures since its contribution becomes significant only for pressure higher than 10^{-1} Pa.

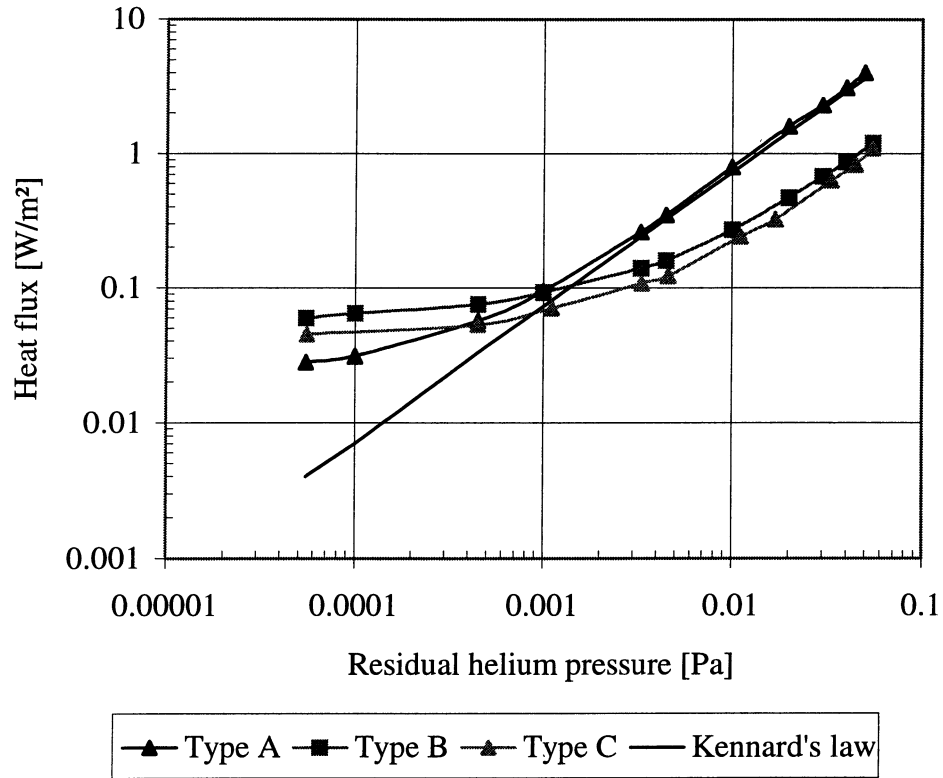


Figure II-1.4: Measured heat flux from 80 K to 4.5 K versus residual helium pressure [43]

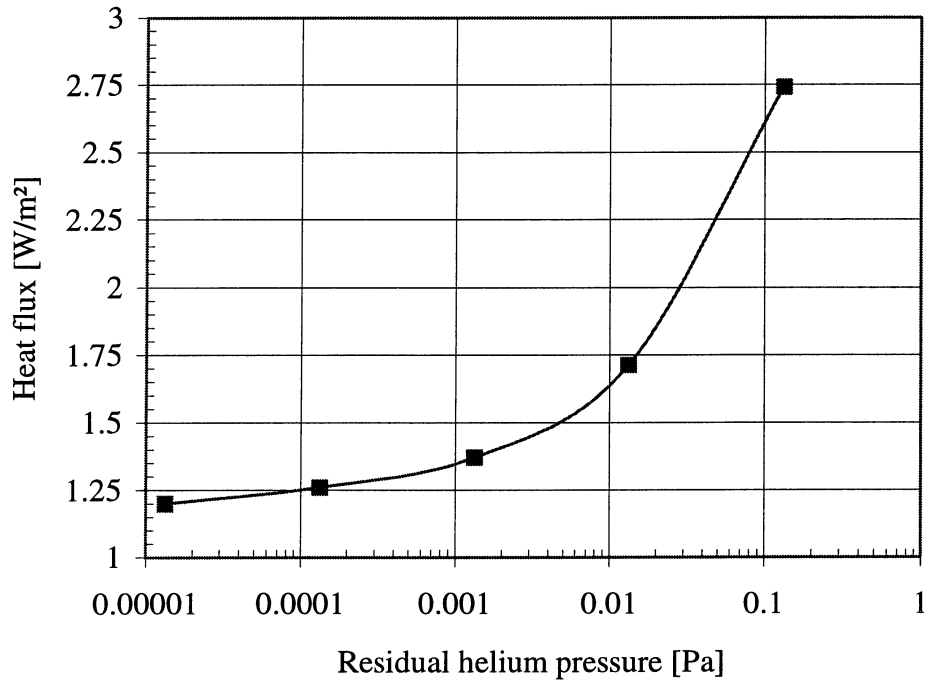


Figure II-1.5: Measured heat flux from 300 K to 80 K versus residual gas pressure [42]

1.1.6 Heat transfer in He II

The phase diagram of helium is shown in annex 3. There are two liquid phases, helium I and helium II separated by the “ λ -line”. Helium I is a conventional liquid; helium II is a superfluid. Liquid helium II can be obtained saturated or pressurised. Saturated HeII occurs when pressure is lowered below 5.0418 kPa along the saturation line while pressurised HeII is obtained by subcooling liquid He above saturation.

Superfluid helium heat transfer [44-46] is characterised by two distinct phenomena: heat transport between the solid surface and the liquid (or vice versa) and heat transport through the bulk liquid. The first process is governed by the Kapitza boundary conductance and is dependent on the material of the solid and its chemical and physical surface conditions. Figure II-1.6 shows the heat transfer between superfluid helium and a copper surface. To emphasise the high thermal conductivity of He II the heat transfer to boiling helium at 4.2 K is also presented. All the heat transfer characteristics refer to flat heated surfaces which are immersed in a large bath of liquid helium.

In superfluid helium, heat is transported by a conduction mechanism not yet completely understood. This mechanism is described in the two-fluid theory of superfluid helium, in which the bulk liquid is considered as a mixture of two interpenetrating fluids, one normal and the other superfluid. Energy is carried to the cold source by the normal component while the superfluid component returns in the opposite direction. At the hot surface the superfluid component receives energy which turns it into the normal state.

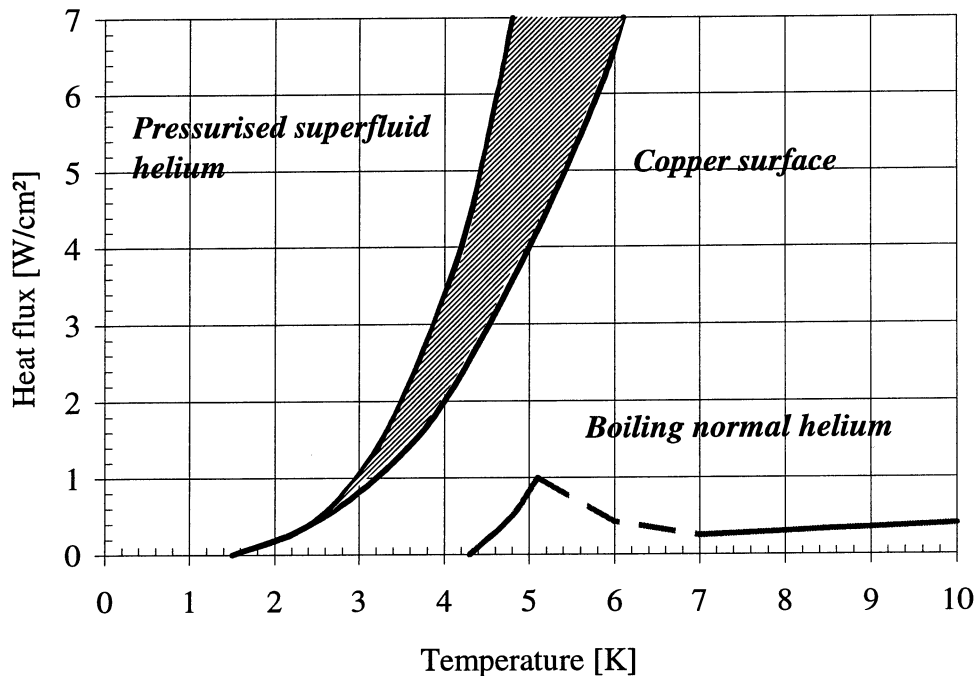


Figure II-1.6: Heat transfer from a copper surface to liquid helium I and II [47]

Consider the one-dimensional heat transfer in a channel of finite length l subjected to a constant heat flux and with a temperature difference across its length $T_2 - T_1$. Most practical applications refer to high heat fluxes (above 1 kW/m²) which permit to work

in the turbulent regime with full mutual friction between the two components. This regime, very powerful when compared with classical conduction, is known as the Gorter-Mellink regime and \dot{q} is found to vary approximately as the cubic root of the temperature gradient. In this case the heat transport in one dimension is written in the form:

$$\frac{dT}{dx} = f(T) \cdot \dot{q}^m \quad (\text{II-1.17})$$

where m is a numerical coefficient which theory indicates should be equal to 3 but which experimentally has been shown to vary from below 3 to nearly 4 as the temperature approaches the lambda temperature. The best experimental fit for m is found to be 3.4 [48]. The quantity $f^1(T)$ behaves like a thermal conductivity as it expresses the temperature gradient in the presence of heat flux. The conductivity function $f^1(T)$ (figure II-1.7) starts from zero at 0 K, passes through a maximum near 1.9 K and drops to zero again at lambda temperature. Notice that the peak heat flux decreases when pressure increases. Considering an empirical fit for the Gorter-Mellink parameter, it is possible to write an analytic expression for the heat conductivity function:

$$f^{-1}(T, P) = g(T_\lambda) \left[\theta^{5.7} (1 - \theta^{5.7}) \right]^3 \quad (\text{II-1.18})$$

where $g(T_\lambda) = \rho^2 s_\lambda^4 T_\lambda^3 / A_\lambda$, $\theta = T/T_\lambda$, $s_\lambda = 1.559 \text{ J/g}\cdot\text{K}$, and $A_\lambda \approx 115 \text{ cm}\cdot\text{s/g}$.

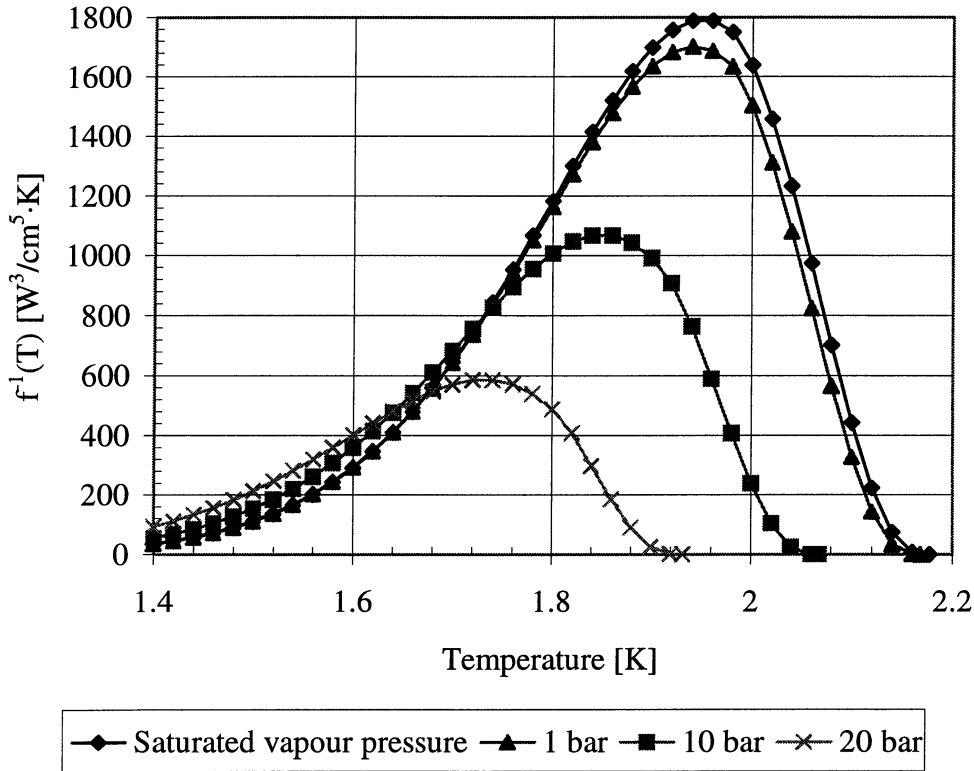


Figure II-1.7: Heat conductivity function for HeII in turbulent regime [49]

By integrating the Gorter-Mellink relation over the available temperature margin we can calculate the one-dimensional steady-state conduction in a channel:

$$\dot{q}^m l = \int_{T_1}^{T_2} \frac{dT}{f(T)} \quad (\text{II-1.19})$$

The integral is mostly a function of temperature and only weakly depends on other factors such as pressure. It is thus possible to write equation II-1.19 in the following form:

$$\dot{q}^m l = Z(T_2) - Z(T_1) \quad (\text{II-1.20})$$

$Z(T)$ as a function of temperature is shown in figure II-1.8. For each value of cold boundary temperature, the maximum heat flux which can be transported is attained when the warm temperature reaches the lambda temperature. This limitation implies that there may be technical applications where heat transport in superfluid helium is not large enough. One of the practical consequences of conduction in superfluid helium is the possibility of transporting heat over long distances: doubling the channel length would divide the available peak flux by only a factor 1.23.

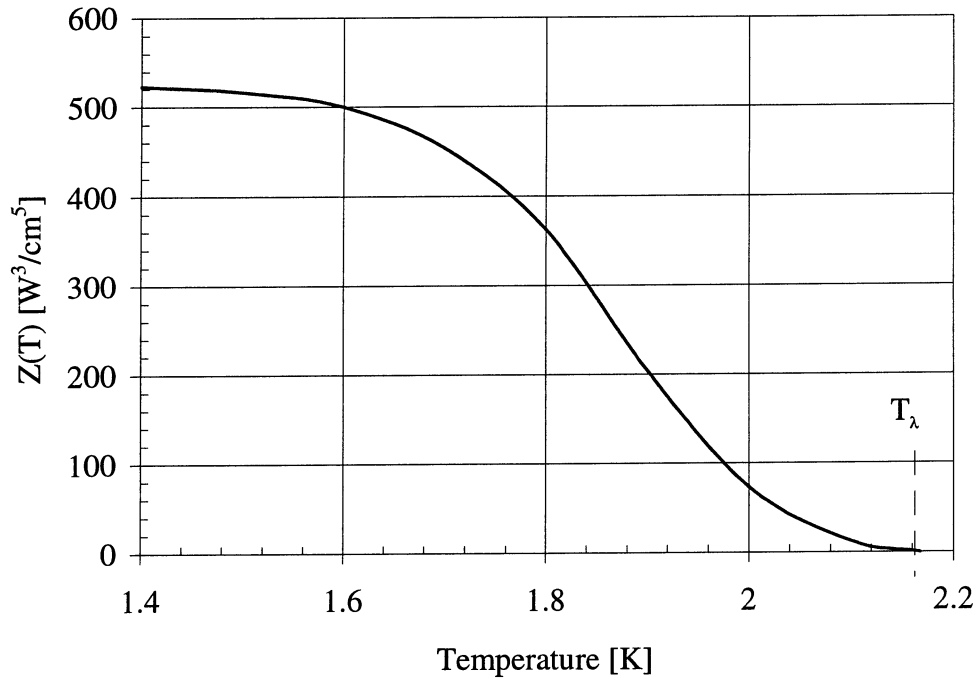


Figure II-1.8: *Thermal conductivity integral of pressurised superfluid helium ($m=3.4$, l in cm and \dot{q} in W/cm^2) [48]*

1.2 Thermal network model

The first part of the modeling consists in identifying the main components constituting the cryostat and the heat transfer processes between them in order to create a thermal network. The thermal network of the LHC prototype dipole and short straight section cryostats are shown in figures II-1.9 and II-1.10.

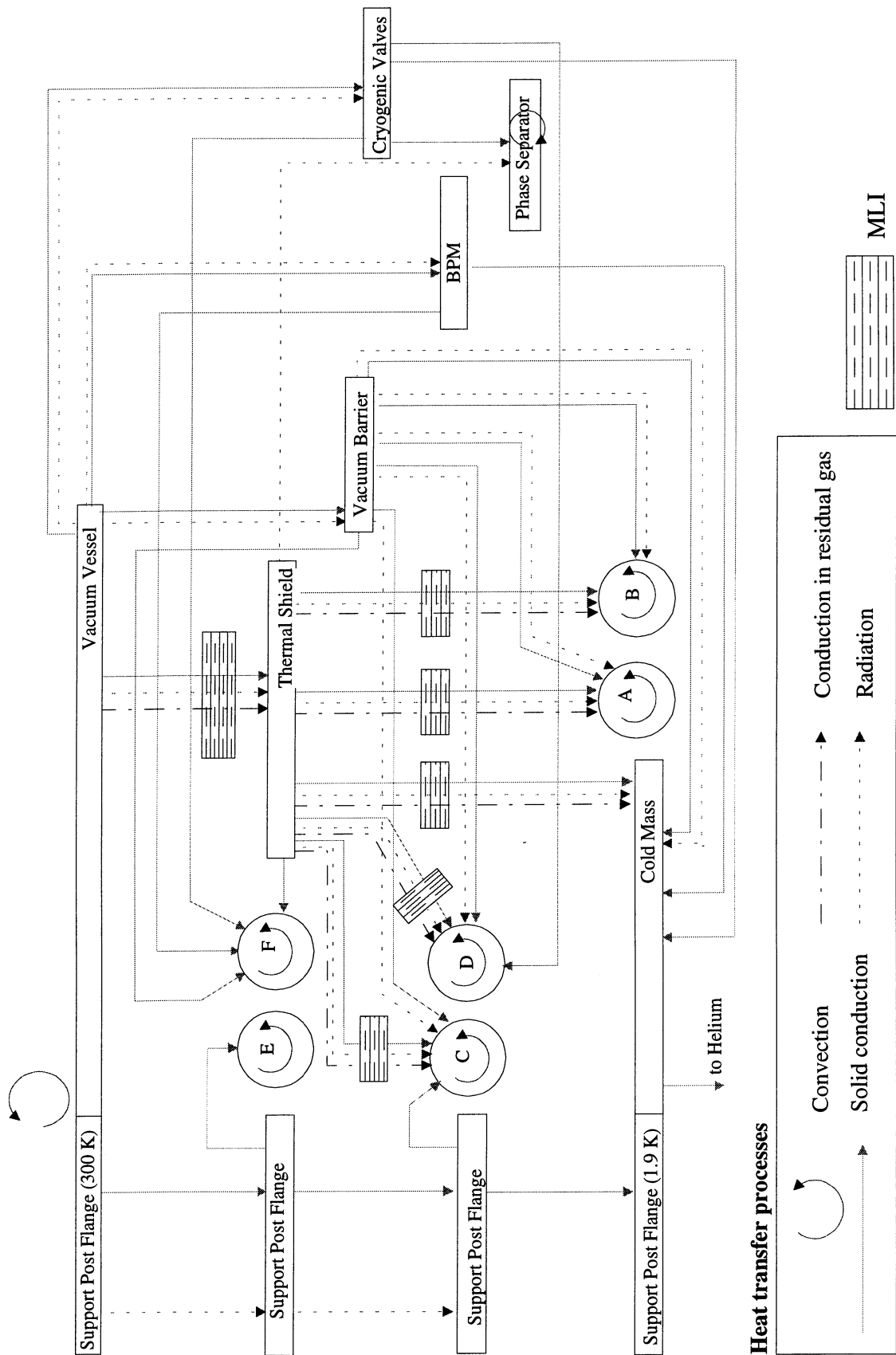


Figure II-1.10: Thermal network of the LHC prototype short straight section cryostat

The arrows represent the different heat transfer modes which may occur during cryostat operational conditions.

Solid conduction occurs between the support post flanges, through the MLI systems, from the thermal shield to the cooling line F, from the support posts to line C and to line E and from the cold mass to the superfluid helium inside it.

Conduction in residual gas occurs through the MLI systems and in the insulation vacuum for residual gas pressure higher than $5 \cdot 10^{-3}$ Pa.

Radiation is found between the support post flanges, from the vacuum vessel to the thermal shield through the MLI systems, from the thermal shield to the cryogenic lines and cold mass through the radiative insulation.

Free convection is due to heat transfer from external environment to the outer wall of the vacuum vessel, whereas forced convection occurs in the helium flowing in the cryogenic pipes.

Each component (e.g. vacuum vessel, thermal shield, support posts, cold mass and cryogenic lines) may be represented by a node in which the conservation of energy is applied.

In steady-state condition and without internal power generation, the heat balance equation at each node, is given by:

$$\dot{Q}_{in} = \dot{Q}_{out} \quad (\text{II-1.21})$$

where \dot{Q}_{in} is the heat reaching the component and \dot{Q}_{out} is the heat leaving it. Results from calculated heat inleaks [50] to the components were inserted in Excel [51] spreadsheet files. For each component, a table was created showing both heat exchange from higher temperatures and that to lower ones. From equation II-1.21 it is thus possible to evaluate the heat inleaks to the cryogenic sinks. This method results to be very practical since any change concerning both cryostat design and temperature levels can be easily integrated.

In order to compute equation II-1.21 a few assumptions, following from the cryostat design, have been taken into account.

The thermal shield temperature was supposed constant azimuthally since the transverse conduction gives a maximum thermal gradient of 6 K, which does not affect the heat inleaks from the vacuum vessel and to the lower temperature components. Typical values of thermal impedances for welded contacts are of the order of 0.1 K/W [52]. Considering line F at 70 K, the thermal shield results to be at 75 K with a heat flux from the vacuum vessel equal to 1.2 W/m^2 .

The radiative insulation is located in a region between the thermal shield at 50-75 K and the cold mass at 1.9 K and is in contact with components at 1.9 K and at 20 K. The azimuthal conduction along aluminised Mylar® between points at different temperature is negligible. The highest value, 0.025 W, is given by conduction from line D at 20 K to the support posts at 7 K.

The bottom and the top flanges of the support posts are considered respectively part of the vacuum vessel and the cold mass. For the sliding support post, we assume ideal thermal contact between the bottom flange and the vacuum vessel. The thermal contacts between the flanges and the cooling lines have been characterised by the following thermal impedances: 3.5 K/W at 4.5-20 K and 2 K/W at 50-75 K. These

values have been calculated by taking into account conduction along the thermalisation braids and the thermal impedance due to the bolted contact between the braids and the flanges. Knowing the heat inleaks to the support posts, it is possible to evaluate the temperatures of the two intermediate flanges: 7 K (line C at 4.5 K) and 65 K (line E at 50 K).

The cold bores and the connection tubes housing the electrical busbars have been included in the cold mass component. For the vacuum barrier, the BPMs and the cryogenic valves a heat interception at 50-75 K has been considered in order to lower the heat inleak at 1.9 K.

CHAPTER 2

Experimental tools and methods for assessing thermal performance of cryostats

In the LHC magnet cryostats, the heat inleaks represent a large fraction of the total heat loads: 100% at 50-75 K, 19% at 4.5-20 K and 53% at 1.9 K. Following calculation of heat inleaks, the thermal design has been experimentally validated on component prototypes.

Thermal performance assessment has been undertaken first on critical components (e.g. multilayer reflective insulation [37, 43], support posts [53, 54], cryogenic valves [55]) and then on complete cryomagnets. Full-scale prototype units have been designed, constructed and used to analyse their thermo-mechanical and cryogenic behaviour. Tests on a dedicated Cryostat Thermal Model (CTM) [56], on single magnets [57] and on a LHC prototype magnet string [58] permitted to validate the basic choices of the LHC cryostat design.

2.1 The Cryostat Thermal Model (CTM)

The CTM (figure II-2.1), has been designed built and tested in order to provide precise measurements of heat inleaks at 1.9 K, 4.5-20 K and 50-75 K without any contribution of interconnection regions and other parasitic equipment.

Precise calorimetric measurements cannot be performed during single magnet tests and string test as parasitic heat losses (supply and return end boxes, cryogenic valves, equipment for warm magnetic measurements in the apertures, large-current feedthroughs) largely exceed the cryostat heat inleaks to be measured.

The CTM simulates a real prototype cryomagnet (10 m long and 0.56 m in diameter) thermally and mechanically (figure II-2.2).

Heat inleaks at the three temperature levels have been measured and several (nominal and degraded) operational conditions have been tested in order to investigate the most critical components (superinsulation systems, thermal shield, radiative insulation, heat interceptions and support posts). The variation of temperature of cryostat components allowed a thorough investigation of the total heat leak sensitivity to the temperature of these components. Furthermore, the effect of changing the residual gas pressure and the direct consequences on the thermal budget were investigated.

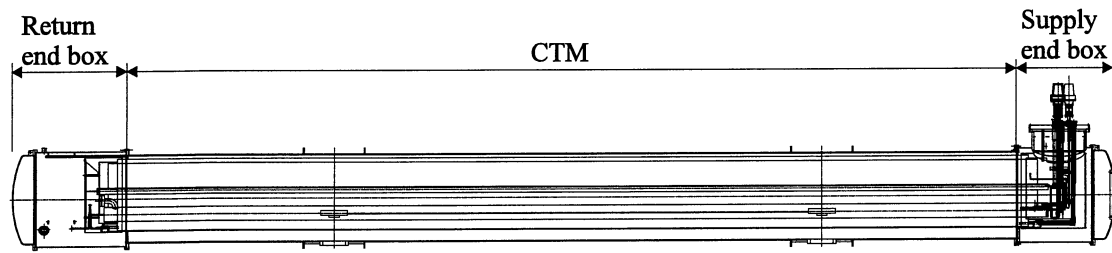
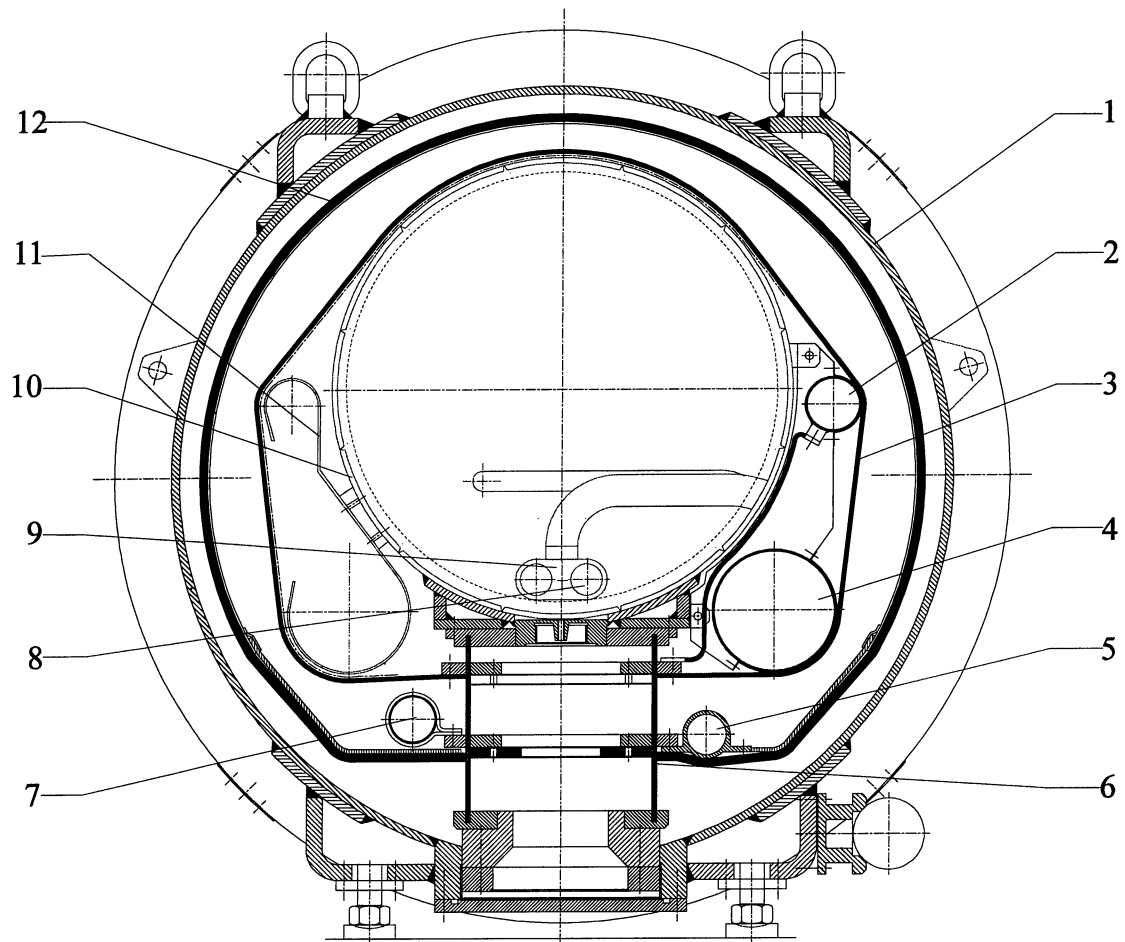


Figure II-2.1: Longitudinal view of the CTM with end boxes



- | | |
|-------------------------|--------------------------|
| 1. Vacuum vessel | 7. Line E |
| 2. Line C | 8. Heat exchanger tube |
| 3. Radiative insulation | 9. He collector |
| 4. Line D | 10. Dummy cold mass |
| 5. Line F | 11. Pseudo tubes A and B |
| 6. Support post | 12. Thermal shield |

Figure II-2.2: Cross-section of the CTM

2.1.1 Specifications

The CTM [59] consists of a standard prototype dipole cryostat with a dummy cold mass. The dummy cold mass contains only 500 kg of stainless steel and 70 l of He versus 18000 kg of stainless steel and 250 l of He for the real cold mass. Consequently cooldown and warmup times are minimised. Moreover, the dummy cold exhibits none of the large-section electrical connections found in a real cryomagnet.

The dummy cold mass (figure II-2.3) presents the same outer surface area and emissivity as a real cold mass. It is made of two concentric stainless steel cylinders 1.5 m long which are spot welded together at regular intervals to form a double walled structure promoting a uniform hydraulic cross-section of 5 cm². Seven such elements are axially welded together in series and stiffened with internal rings to form a hollow cylinder 0.56 m in external diameter and 10.252 m long offering a uniform temperature distribution under steady-state conditions. The pressure drop at 300 K and 2 g/s of the helium gas flow is 100 mbar. The maximum longitudinal thermal gradient during cooldown is fixed at 150 K/m and the design pressure at 4 bar. The outer skin of the double walled structure is thicker than the inner one thus giving a smoother surface with a maximum ripple of 1 mm. The self supporting cylindrical structure has a maximum deflection of less than 0.5 mm transverse and less than 2 mm longitudinal.

The helium collector, made of stainless steel, is placed inside the dummy cold mass and is hydraulically connected in series with it. It contains a copper heat exchanger and a stainless steel tube to simulate a cold bore. The tube representing the cold bore is open on both sides; the heat exchanger is opened on one end to be connected to the supply end box.

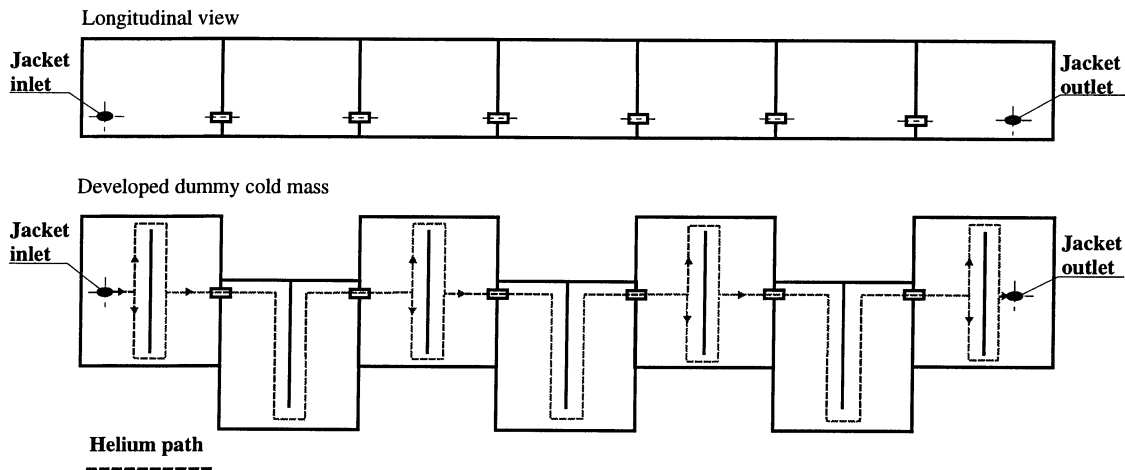


Figure II-2.3: *Simplified layout of the dummy cold mass*

The dummy cold mass is closed with aluminum covers fixed to the end flanges.

The 1.9 K lines A and B are simulated with preformed copper sheets fixed and thermally linked to the cold mass. The line D at 20 K is of identical diameter to that of the LHC prototype dipole cryostat, but double walled in order to minimise the helium inventory.

The thermal shield, radiative insulation, support posts, vacuum vessel, 4.5 K line C and the 50-75 K lines E and F are all identical to those of the LHC prototype dipole magnet cryostats.

The CTM is closed at one end by the supply end box and at the opposite end by the return end box. The two end boxes, housing all the cryogenic components for the helium supply at the three different temperature levels, have been designed to be easily dismountable to cope with any modification or intervention on the cryostat under test.

The specified thermal budget of CTM in steady-state condition is the following: 58 W at 50-75 K, 1.3 W at 4.5-20 K and 1.6 W at 1.9 K. The system must allow measurements at 4.5-20 K and 1.9 K in the range of 1 W and guarantee the required precision of 10%. This can only be attained if the error introduced by the parasitic heat losses (end boxes and instrumentation) and instrumentation reading is of the order of 0.1 W and therefore can be included in the measurement tolerance.

2.1.2 Cryogenics

The nominal steady-state temperature levels are the same as for the LHC cryogenic system: a thermal shield at 50-75 K intercepting the heat inleak from ambient, a 4.5-20 K level allowing initial filling and thermalising the radiative insulation and a dummy cold mass at 1.9 K cooled by quasi-isothermal saturated superfluid helium.

The process and instrumentation diagram of the CTM is shown in figure II-2.4.

Helium at 4.2 K and 1.25 bar from the phase separator is distributed to line C at 4.5 K, line E at 50 K, the supply end box screens and the cold mass for initial filling.

Cooldown of the cold mass occurs in two phases. In the first phase gaseous helium at 4.2 K from the helium collector reaches the cold mass, cooling it from 300 K to 4.2 K. During this phase valve V3 is open and valve V1 is closed. Valve V3 will be closed once the dummy cold mass is filled with liquid helium at 4.2 K. In the second phase liquid helium from the phase separator passes through the Joule-Thomson heat exchanger where it cools down to the lambda point. Subcooled liquid helium expands to saturation (1.6 kPa) in the Joule-Thomson valve V1 and is directed through a small bore tube to the blind end of the heat exchanger inside the helium collector. Returning, saturated helium at 1.9 K vaporises and cools the cold mass from 4.2 K to 1.9 K by conduction heat exchange. The low pressure on the 1.9 K helium bath is maintained by a pumping unit with a specified capacity of 1.4 g/s at 1.54 kPa.

In steady-state condition the helium inventory of the system is listed in table II-2.1.

Table II-2.1: Helium inventory in the CTM

Item	Volume [m ³]	Mass [kg]
Line C (4.5 K, 1.25 bar)	0.033	0.67
Line D (20 K, 1.25 bar)	0.024	0.07
Line E (50 K, 1.25 bar)	0.026	0.03
Line F (75 K, 1.25 bar)	0.020	0.02
Cold Mass (1.9 K, 1.25 bar)	0.070	10
Total [kg]		10.79

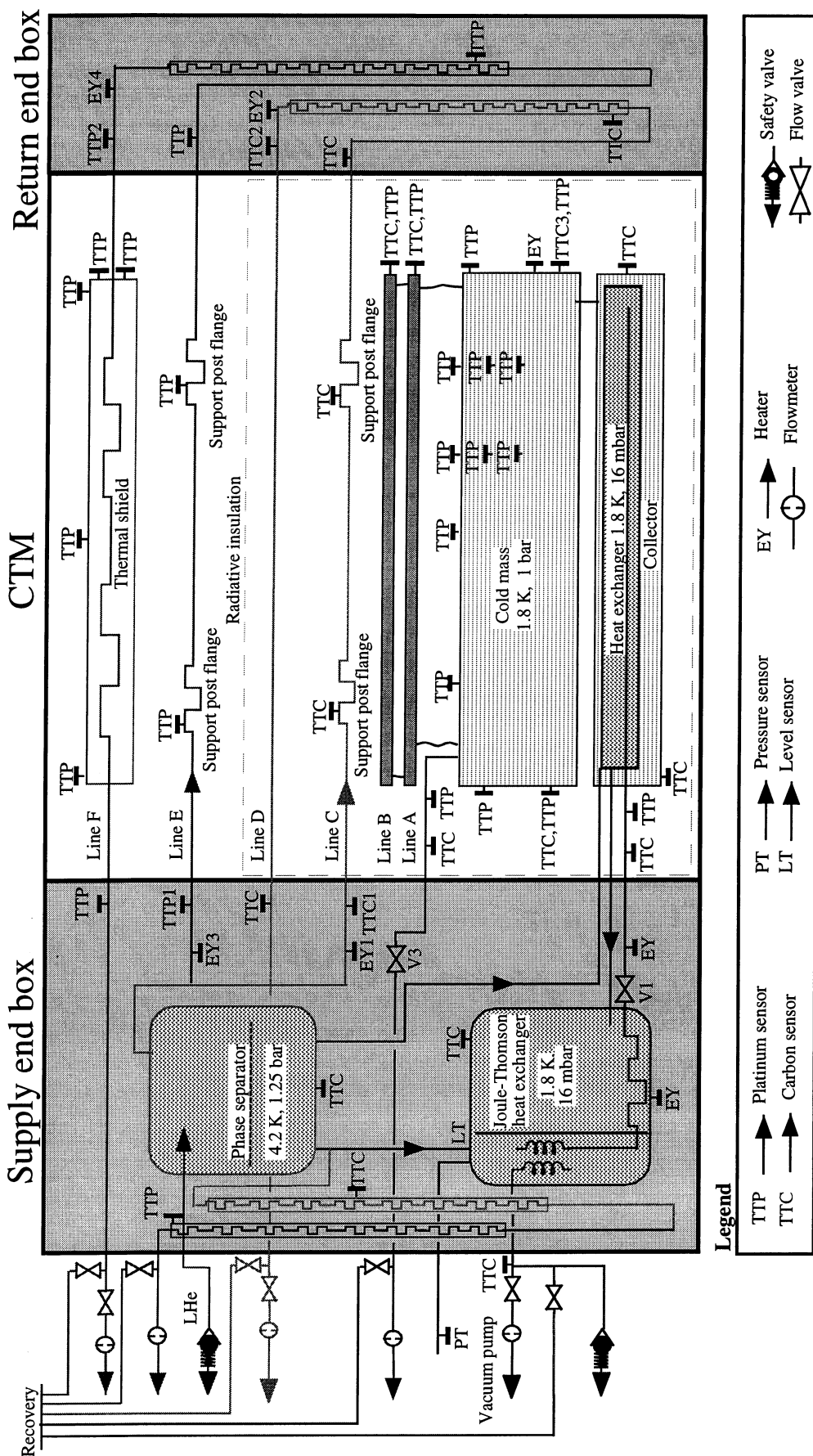


Figure II-2.4: Process and instrumentation diagram of the CTM

2.1.3 Supply and return end boxes

In the supply end box (figures II-2.5), the phase separator, made of stainless steel, is linked to the supply cryolines, the dummy cold and the Joule-Thomson heat exchanger at 1.8 K. The Joule-Thomson heat exchanger is made of stacked copper mesh plates.

Double walled stainless steel screens at 80 K and 4.5 K are connected in series and covered with 20 layers of type B superinsulation (see table II-1.4 in Part 2-Chapter 1). Heat inleak at 1.9 K from the valves V1 and V3 is lower than 0.1 W. In order to minimise conduction in superfluid helium the tubes connecting the phase separator with the Joule-Thomson heat exchanger, and the Joule-Thomson heat exchanger with the corrugated copper heat exchanger were dimensioned to keep heat inleak at 1.9 K lower than 0.05 W.

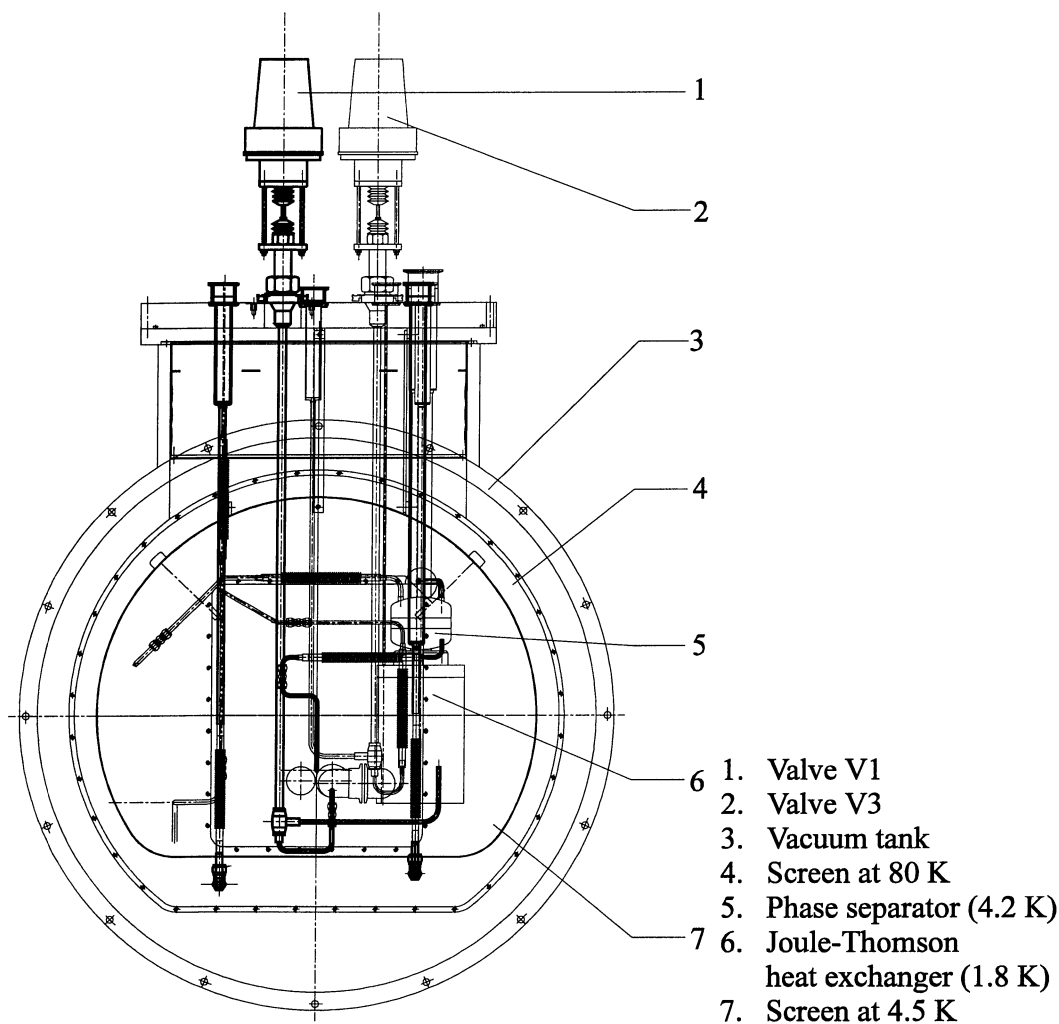


Figure II-2.5: Supply end box of the CTM

All the interconnection tubes from the supply (C and E) to the return cryogenic lines (D and F) are located in the return end box (figure II-2.6). The screens at 4.5 K and

80 K are connected in series respectively with the 4.5-20 K lines and the 50-75 K lines and each of them is covered with 20 layers of type B superinsulation.

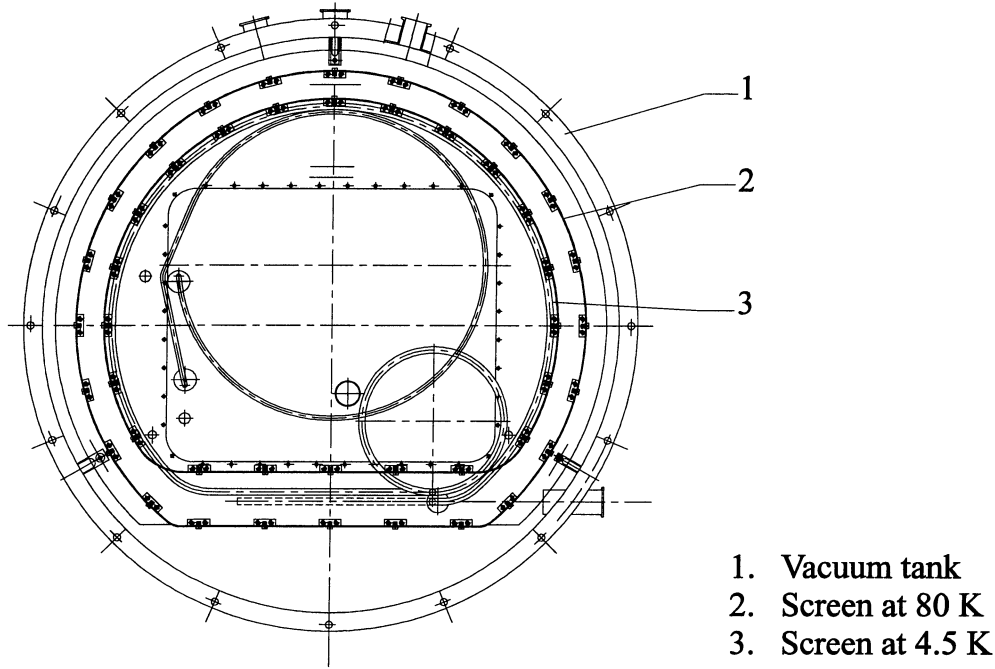


Figure II-2.6: Return end box of the CTM

2.1.4 Methods for measuring steady-state heat inleaks

In order to understand how the heat inleaks were measured, a brief recall of the first principle of thermodynamics is needed. In the following, we follow the formalism of reference 60. The first principle of thermodynamics expresses the conservation of energy in a system, as follows:

$$dU_t = \delta Q + \delta W \quad (\text{II-2.1})$$

where Q and W are respectively the heat and the work exchanged by the system. U_t is the total internal energy which is given by the sum of the internal energy (U) the kinetic energy (K) and the potential energy (Z):

$$dU_t = dU + dK + dZ \quad (\text{II-2.2})$$

Consider the open thermodynamic system shown in figure II-2.7. The introduction of an elementary mass of a fluid s into the system brings a contribution of total internal energy and transfers work to the system.

The mass dm_s contains a certain amount of total internal energy which can be expressed:

$$dU_{ts} = u_{ts} dm_s \quad (\text{II-2.3})$$

The fluid performs work to the system against the pressure P at the inlet section. This contribution is called *flow work* and is given:

$$\delta W_{fs} = v_s P_s dm_s \quad (\text{II-2.4})$$

The work exchanged by the system results to be the sum of the flow work (W_{fs}) and the mechanical work (W_m):

$$\delta W = \delta W_{fs} + \delta W_m \quad (\text{II-2.5})$$

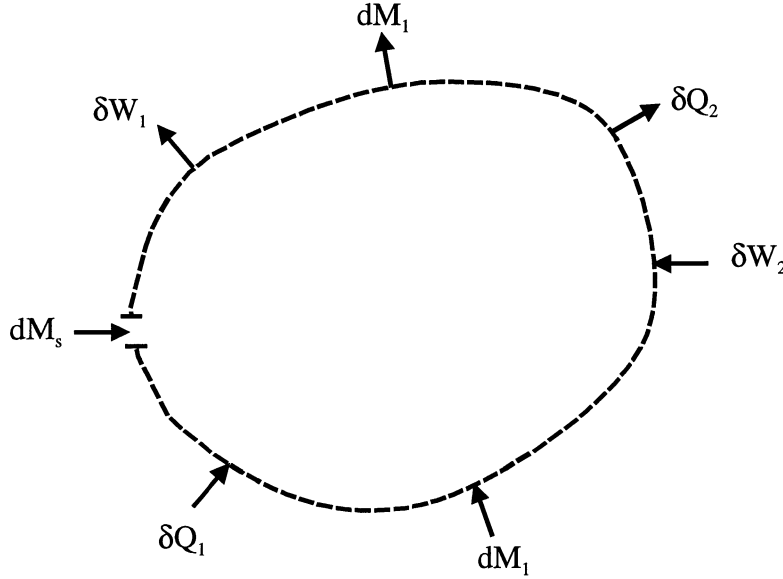


Figure II-2.7: Exchange of heat, work and mass in a thermodynamic system

The first principle of the thermodynamics is thus given by:

$$dU_t = \delta Q + \delta W_m + \delta W_{fs} + dU_{ts} \quad (\text{II-2.6})$$

and considering equations II-2.3 and II-2.4:

$$dU_t = \delta Q + \delta W_m + u_{ts} dm_s + v_s P_s dm_s \quad (\text{II-2.7})$$

We introduce a new function of state called *enthalpy* defined as:

$$h_t = u_t + vP \quad (\text{II-2.8})$$

From equations II-2.7 we obtain:

$$dU_t = \delta Q + \delta W_m + h_{ts} dm_s \quad (\text{II-2.9})$$

In the most general case different contributions of heat, work and masses are exchanged between the system and the external environment:

$$dU_t = \sum_i \delta Q_i + \sum_z \delta W_{mz} + \sum_s h_{ts} dm_s \quad (\text{II-2.10})$$

By integrating equation II-2.10, we obtain:

$$\Delta U_t = \sum_i Q_i + \sum_z W_{mz} + \sum_s \int h_{ts} dm_s \quad (\text{II-2.11})$$

Dividing equation II-2.10 by dt, we obtain the first principle of thermodynamics expressed in watts:

$$\frac{dU_t}{dt} = \sum_i \dot{Q}_i + \sum_z \dot{W}_{mz} + \sum_s h_{ts} \dot{m}_s \quad (\text{II-2.12})$$

Consider now a fluid flowing in a fixed-wall horizontal channel subjected to a pressure gradient in steady-state condition (figure II-2.8). There is no production of mechanical work, so that the term δW is only due to the flow-work. In presence of small variation of velocity, the kinetic energy can be neglected and the first principle of thermodynamics reduces:

$$\dot{Q} + \sum_s h_{ts} \dot{m} = 0 \quad (\text{II-2.13})$$

Applying equation II-2.13 between the sections 2 and 1, we obtain:

$$\dot{Q} = \dot{m}(h_2 - h_1) \quad (\text{II-2.14})$$

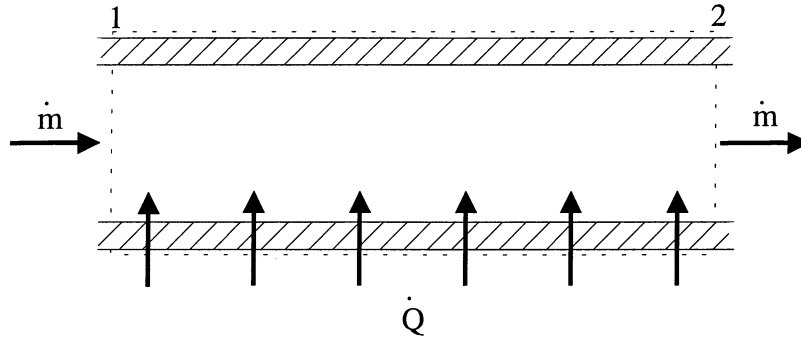


Figure II-2.8: Heat leak in a steady-state open system

4.5-20 K and 50-75 K levels

At 4.5-20 K and 50-75 K levels steady-state heat leaks are calculated from equation II-2.14 after measuring mass-flow rates and inlet-to-outlet temperature difference as follows:

$$\dot{Q} = \dot{m}(h(T_2) - h(T_1)) \quad (\text{II-2.15})$$

This method, applied to several values of the mass-flow, permits to evaluate the corresponding temperature difference and thus to confirm the measured heat leaks.

1.9 K level

Two measurement methods are used to evaluate the steady-state heat leak at 1.9 K: helium boil-off and temperature drift over time.

Helium boil-off

The heat inleak at 1.9 K are determined by knowing the mass flow rate of helium boil-off at 1.9 K (\dot{m}_v) and its temperature in the Joule-Thomson heat exchanger. The steady-state heat balance equation gives:

$$\dot{Q} = \dot{m}_v L \quad (\text{II-2.16})$$

where L is the latent heat of vaporisation at 1.9 K.

During the measurement the valve V1 is closed and the liquid level in the J-T heat exchanger decreases. In this condition, to obtain \dot{m}_v , the measured mass-flow rate \dot{m}_m should be divided by a factor taking into account that the level is decreasing. This factor can be neglected for saturated helium at 1.9 K. Consider the system represented in figure II-2.9.

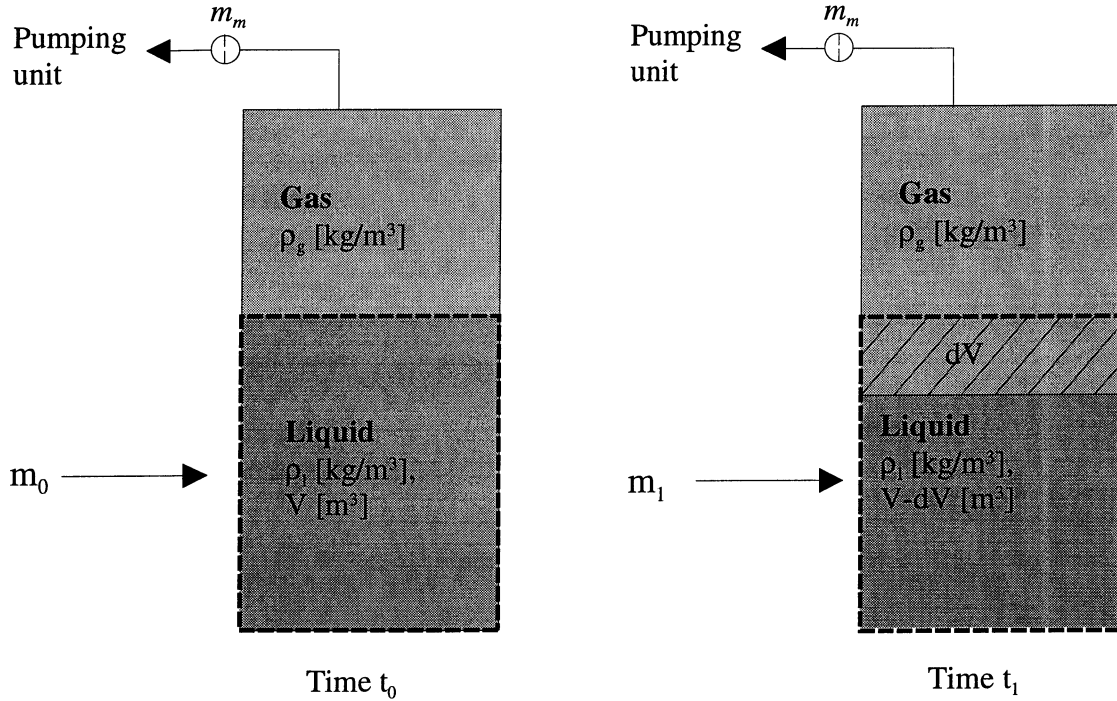


Figure II-2.9: Measurement of heat inleak at 1.9 K by helium boil-off

To compensate for the heat inleak at 1.9 K, the liquid mass vaporises and at the time t_1 the volume dV is occupied by the gas. At the times t_0 and t_1 the mass in the system volume can be expressed:

$$m_0 = \rho_l V \quad (\text{II-2.17})$$

$$m_1 = \rho_l (V - dV) + \rho_g dV \quad (\text{II-2.18})$$

The mass variation during the time dt ($t_1 - t_0$) is given:

$$\frac{m_1 - m_0}{t_1 - t_0} = \frac{dm}{dt} = (\rho_g - \rho_l) \frac{dV}{dt} = -(\rho_g - \rho_l) \frac{1}{\rho_l} \frac{dm_0}{dt} \quad (\text{II-2.19})$$

Introducing the mass-flow rates \dot{m}_v ($\dot{m}_v = \frac{dm_0}{dt}$) and \dot{m}_m ($\dot{m}_m = \frac{dm}{dt}$), we obtain:

$$\dot{m}_m = \dot{m}_v \left(\frac{\rho_l - \rho_g}{\rho_l} \right) \quad (\text{II-2.20})$$

For saturated helium at 1.9 K, ρ_l is 145.52 kg/m³ and ρ_g is 0.60896 kg/m³, so that:

$$\dot{m}_v = 1.004 \dot{m}_m \quad (\text{II-2.21})$$

Temperature drift over time

The heat leak at 1.9 K can also be measured by evaluating the temperature drift with time of the quasi isothermal helium II bath over the interval between 1.9 K and the lambda point. This requires only one temperature sensor.

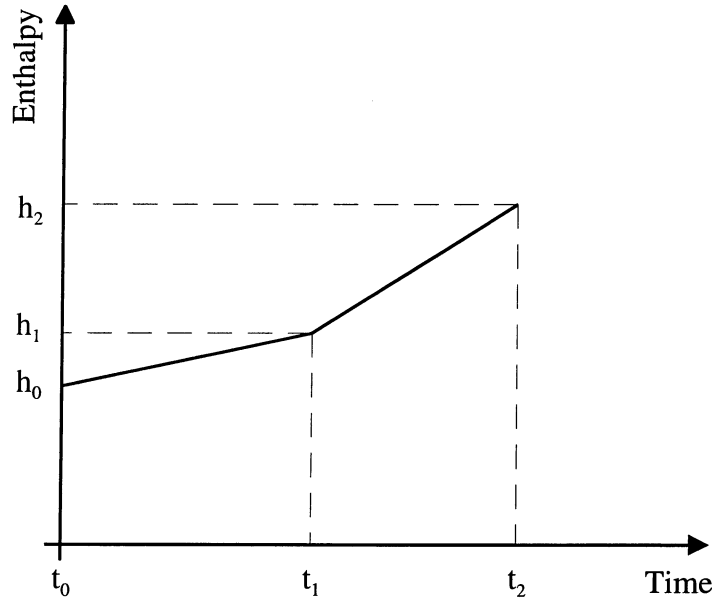


Figure II-2.10: Measurement of heat leak at 1.9 K by temperature drift

Starting from steady-state condition, at the time t_0 (figure II-2.10) one stops the pumping unit and as a consequence the temperature of the cold mass increases, while still remaining uniform due to the high conductivity of helium II. Applying the first principle of the thermodynamics to the cold mass we obtain the heat leak at 1.9 K as:

$$\dot{Q} = m_{He} \left. \frac{dh_{He}(T)}{dt} \right|_{t_0 \leq t < t_1} + m_{StSt} \left. \frac{dh_{StSt}(T)}{dt} \right|_{t_0 \leq t < t_1} \quad (\text{II-2.22})$$

where m_{He} and m_{StSt} are respectively the masses of the superfluid helium and the stainless steel. The contribution of the superfluid helium is predominant since that of the dummy cold mass is about 20 times lower. In equation II-2.22 an assumption has been made by considering constant the mass m_{He} . The cold mass is connected with the phase separator at 4.2 K. Knowing that for superfluid helium at 1.9 K an increase of temperature corresponds to an increase of density we can conclude that helium at 4.2 K reaches the cold mass to make up for contraction of the HeII. This introduces a measurement error, which can be estimated and compensated. It has been measured that the cold mass warms up from 1.86 K to 1.92 K in about 4 min. From the density difference (0.0382 kg/m^3) and knowing the total superfluid helium mass (10 kg) we can estimate the mass introduced into the cold mass (0.0025 kg). The supplementary heat inleak at 1.9 K has been calculated and is equal to 0.08 W (5 % of the total heat inleak at 1.9 K).

At the time t_l one may introduce a known additional power (Q_{el}) in the superfluid helium bath by means of an electrical heater. In this case the heat balance equation gives:

$$\dot{Q}_{el} + \dot{Q} = m_{He} \left. \frac{dh_{He}(T)}{dt} \right|_{t_1 \leq t < t_2} + m_{StSt} \left. \frac{dh_{StSt}(T)}{dt} \right|_{t_1 \leq t < t_2} \quad (\text{II-2.23})$$

Equations II-2.22 and II-2.23 form a system from which we can calculate the heat inleak at 1.9 K. We should remember that at 1.9 K the CTM cryogenic system does not allow to separate the heat inleak of the end boxes from that of the cryostat.

2.1.5 Instrumentation

Precise calorimetric measurements at very low temperatures are difficult to perform since parasitic heat inleaks coming from the cryostat, instrumentation wires and current introduce perturbations [61-65].

The cryostat thermal model is equipped with the following cryogenic instrumentation: temperature sensors, pressure and liquid level gauges and mass flowmeters.

Allen-Bradley carbon sensors (1/8 W) are used in the range 1.5-50 K while Pt100 platinum sensors cover the range 30-300 K. The thermal impedance between the thermometer and the component to be measured must be negligible. Thermal conduction through the wires and self-heating due to Joule effect must not affect the measurement. The current supply for carbon sensors is 10 μA and that for platinum sensors is 100 μA . Thermally resistive cryogenic wire is used and appropriate intermediate thermalisation implemented on all instrumentation.

Platinum sensor resistivity comprises a constant term due to defects (residual resistance) and a term varying with temperature. This variation is directly proportional to the temperature for temperatures above 100 K and becomes very small for temperature below 20 K. Sensibility of a platinum sensor (100 Ω at 273.15 K) varies from 0.04 Ω/K to 0.07 Ω/K between 20 and 300 K, whereas for temperatures below 20 K it decreases to 0.01 Ω/K . These thermometers do not need individual calibration. The law which fits best the temperature (T) variation over resistance (R) is the following [66]:

$$T = \frac{R + 7.67253}{0.3932} \quad 193.15 \leq T < 323.15 \quad (\text{II-2.24})$$

$$T = \frac{R + 10.7184}{0.409} \quad 123.15 \leq T < 193.15 \quad (\text{II-2.25})$$

$$T = \frac{R + 12.3686}{0.4224} \quad 73.15 \leq T < 123.15 \quad (\text{II-2.26})$$

$$T = \sqrt[1.90032]{\frac{R}{0.00524}} \quad 30 \leq T < 73.15 \quad (\text{II-2.27})$$

Carbon sensors are not reproducible and therefore each of them needs an individual calibration. The carbon sensors are calibrated with respect to two reference sensors (LAKESHORE carbon glass CGR-1-1000 and Alley-Bradley 50 Ω carbon sensor) and one gauge reading saturation pressure. According to the temperature range of interest, two types of functions have been used in the CTM:

$$T = \frac{B}{\log_{10} R + \frac{K}{\log_{10} R} - A} \quad (1.5 \text{ K} < T < 30 \text{ K}) \quad (\text{II-2.28})$$

$$T = 10 \exp \left(\sum_{i=0}^6 \frac{C_i}{(\log_{10} R)^i} \right) \quad (1.5 \text{ K} < T < 50 \text{ K}) \quad (\text{II-2.29})$$

where B , K , A , C_i are constant values obtained after calibration of the carbon sensor. The precision of the Allen-Bradley carbon sensor calibration is given in table II-2.2.

Table II-2.2: Precision of Allen-Bradley carbon sensor calibration

Temperature [K]	Precision [K]
1.5 - 4.2	0.010
4.2 - 6	0.020
6 - 10	0.050
10 - 20	0.100
20 - 80	0.500
80 - 300	1.000

Platinum and carbon sensors (figure II-2.3) installed on the cryogenic lines are duplicated and used to measure temperatures both in steady state and in transient

conditions. Platinum thermometers on the cold mass measure both transverse and longitudinal temperature distribution during cooldown and warmup. Platinum sensors on the thermal shield permit to measure its temperature profile both during transient modes and steady state operations. Each flange of the support posts has been equipped with two sensors, one inside and one outside the glass-fiber column.

Mass-flows are measured at the three temperature levels with thermal flowmeters (table II-2.3) working at 300 K.

Table II-2.3: CTM flowmeters

Circuit	Range [g/s]	Precision [% of full scale]	Reproducibility [% of full scale]
50-75 K	0.03-1.5	2	0.25
4.5-20 K	0.018-1	2	0.2
1.9 K	0.005-0.25	2	0.25

Heaters are made of thin resistive copper wire (25 Ω at 300 K) and wrapped around the inlet section of each line.

The range of measurements is limited by the maximum heater power (50 W for EY1, EY2 and EY4, and 150 W for EY3) and by the maximum and minimum flow-rates at the different temperature levels.

Measurements of heat inleak have been carried out with an error which takes into account both the reading and the calibration error

The reading error is due to the reading of voltage and mass-flow. The current I through the carbon sensor is 10 μA with an error of $\pm 0.05 \mu\text{A}$. At about 4.5 K, the voltage V is 9 mV and the voltmeter sensibility is 1 μV in the range 0-300 mV. The resistance R is obtained from:

$$R = \frac{V}{I} \quad (\text{II-2.30})$$

and the error:

$$\Delta R = \left| \frac{\partial R}{\partial V} \right| \Delta V + \left| \frac{\partial R}{\partial I} \right| \Delta I \quad (\text{II-2.31})$$

which gives numerically 9.1 Ω .

The carbon resistance temperature (equation II-2.28) is a function of the resistance, therefore:

$$\Delta T = \left| \frac{\partial T}{\partial R} \right| \Delta R \quad (\text{II-2.32})$$

which gives an error of $\pm 0.3 \%$. The calibration error for Allen Bradley carbon sensor (see table II-2.3) is $\pm 0.01 \text{ K}$ from 4.2 K to 6 K and $\pm 0.05 \text{ K}$ from 10 K to 20 K, so the total error in temperature measurement (calibration plus instrumentation) is $\pm 0.02 \text{ K}$ at

4.5 K and ± 0.06 K at 20 K. The error in the mass-flow reading is ± 0.01 g/s (see table II-2.4).

The heat inleak at 4.5-20 K is calculated by equation II-2.15 and the error is given:

$$\Delta \dot{Q} = \left| \frac{\partial \dot{Q}}{\partial \dot{m}} \right| \Delta \dot{m} + \left| \frac{\partial \dot{Q}}{\partial h} \frac{\partial h}{\partial T_2} \right| \Delta T_2 + \left| \frac{\partial \dot{Q}}{\partial h} \frac{\partial h}{\partial T_1} \right| \Delta T_1 \quad (\text{II-2.33})$$

From equation II-2.33 the total error in heat inleak at 4.5-20 K results to be $\pm 4.7\%$.

Similarly the errors in heat inleak measurements at 50-75 K and 1.9 K are found to be $\pm 5\%$ and $\pm 2.5\%$ respectively.

2.1.6 Control and data acquisition

The control and data acquisition system is based on the LabVIEW [67] application. The computer (figure II-2.11) used for this task is equipped with a GPIB interface (IEEE 488) [68] communicating with the multimeter and the scanner, an analog output card (NB-AO-6) [69] used to command the heater power supplies and a multifunction card (Lab-NB) [70] for reading out of flow-meters, valves, pressure and level gauges.

The multimeter can perform three measurements per second and is used in combination with the scanner which is made of 6 modules, each of them containing 20 on/off switches with one common contact per pair, such that it can be used as 10 change-over switches.

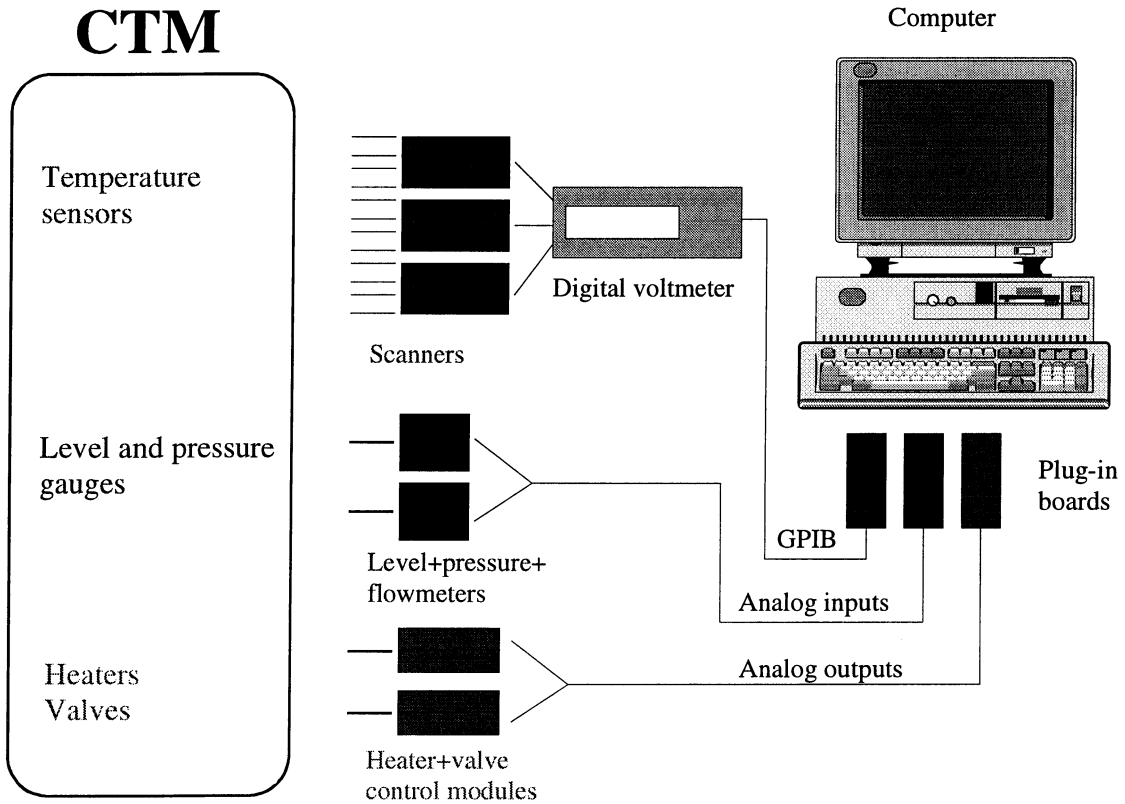


Figure II-2.11: Schematic layout of acquisition and control system

The program is mainly formed of five parts communicating with each other:

- the library with all the information concerning type of sensors and calibrations
- the acquisition process storing all the variables in a buffer ring
- the control process containing the controls loops for heaters and valves
- the data in on-line trend graphs
- the archiving of all data in spreadsheet files

Temperatures TTC1 and TTC2 on lines C and D and TTP1 and TTP2 on lines E and F as shown in figure II-2.3 are controlled either automatically or manually by varying heater power on EY1, EY2, EY3 and EY4. The temperature difference between the heat exchanger and TTC3 is maintained at less than 20 mK by controlling the flow of liquid helium through valve V1.

During all operational phases (cooldown, steady operation and warmup) data are saved on files as spreadsheets readable by most data analysis applications.

2.2 LHC Prototype Magnet String

The first version of the LHC Prototype Magnet String, aiming at validation of LHC systems, was assembled, commissioned and operated for the first time at the end of 1994 [71]. It makes use of one prototype short straight section and three 10 m long dipoles.

2.2.1 System layout

To reproduce the same condition as in the LEP tunnel, where LHC will be installed, the string was built on a concrete beam with a slope of 1.4 %. Due to delays in the delivery of 10 m-long prototypes, the first version of the String comprised only one quadrupole and two dipoles. The string was extended after the first run when the third dipole was installed [72, 73]. The correction elements, such as sextupoles, tuning quadrupoles and closed orbit correctors which belong to the short straight section, were replaced in the prototype short straight section by dummy steel masses of equivalent thermal capacity.

The string is closed at each end by the String Feed Box (SFB) and the String Return Box (SRB). The String Feed Box contains the main cryostat with current leads, a gas counterflow heat exchanger, a liquid/gas heat exchanger, a very low pressure liquid subcooler and all the valves necessary for supplying the cryogenic fluids to the different circuits. The SRB closes the cryogenic loops, the electrical circuit as well as the cryogenic vacuum. The SFB is connected to the short straight section where quench protection diodes for quadrupole and dipoles are also mounted. Between magnets there are the interconnection regions where 14 pipes are connected in such a way as to cope with 30 mm magnet contraction during cooldown and 20 bar pressure rise which may be produced during a quench magnet.

2.2.2 Cryogenics

The cooling scheme of the extended string is represented in figure II-2.12. It is implemented in three independent cooling loops: 1.9 K, 4.5-20 K and 90 K.

Liquid He I is taken from the main cryostat and is subcooled in a very low pressure heat exchanger. In the co-current two-phase flow version LHe at 2.2 K, 1 bar is distributed to line A and expands to saturation through a Joule-Thomson valve located

in the cryogenic service module and reaches the far end of the heat exchanger tube. The saturation pressure is maintained by pumping the vapour helium through line B by means of a low-pressure pumping unit with a specified capacity of 6 g/s at 1 kPa.

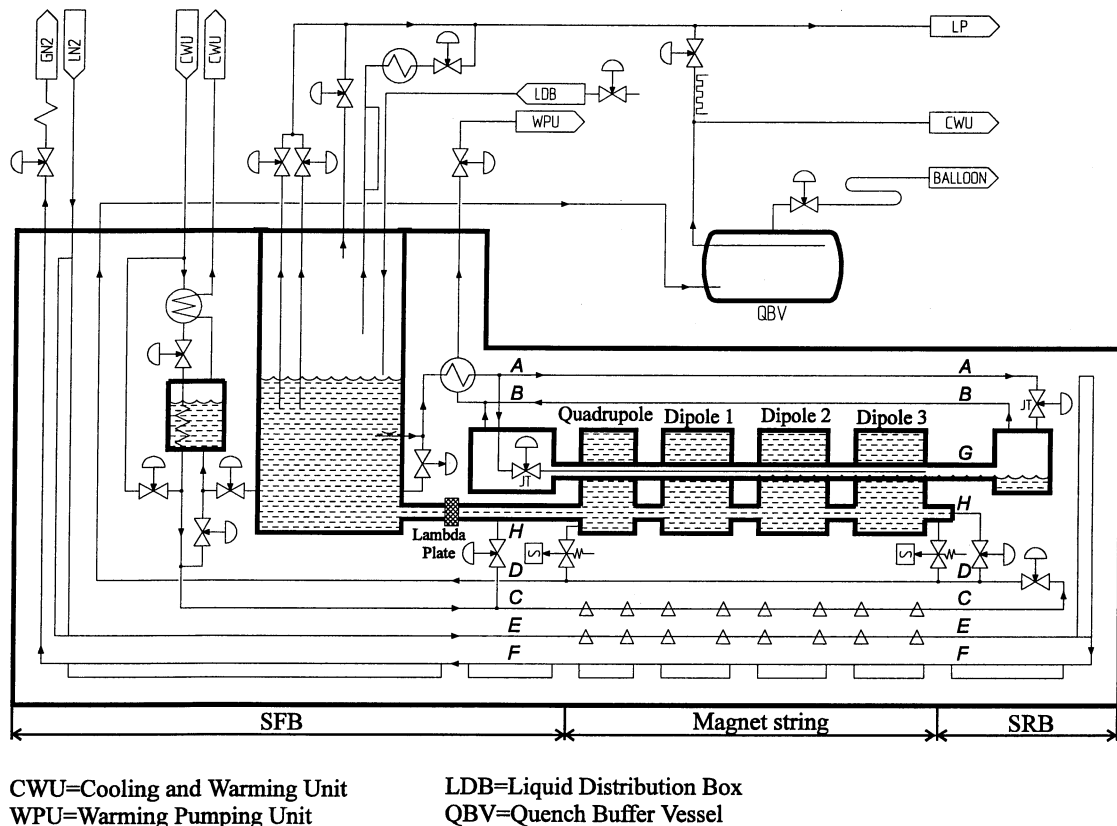


Figure II-2.12: Simplified process and instrumentation diagram of the LHC prototype magnet string

In the extended version the helium superfluid cooling loop was modified in order to test counter-current two phase flow. A Joule-Thomson valve was introduced at the higher end of the String together with a phase separator and a connection to the pumping line. In such a configuration pumping is shared between the two ends of the helium II heat exchanger tube, although the contribution of the higher end dominates due to the pressure drop in the heat exchanger tube.

Line C supplies supercritical helium to intercept residual conduction heat from the support posts and to perform the operation of cooldown, filling and warmup of the magnet cold mass. Line D is used to discharge helium in order to contain the pressure rise below 2 MPa after a magnet resistive transition (quench). In the first version three quench valves were implemented, one at the beginning of each magnet. Following the experience gained after the first run of measurements in the second version only two quench valves were installed, one at each end of the String.

Lines E and F are cooled by saturated nitrogen to intercept heat at 90 K from the magnet support posts (line E) and the thermal shield (line F).

The methods to measure the string heat inleaks are the same as those used in the CTM. The resistive dissipation in non-superconducting cable splices can be evaluated both by electrical (current and voltage) and calorimetric measurements.

2.2.3 Instrumentation, data acquisition and process control

The temperature sensors are of the same type as those for the CTM: Pt100 platinum sensors from 30 K to 300 K and Allen-Bradley carbon sensors from 1.6 K to 50 K. The carbon thermometers are recalibrated in situ since the magnet temperature needs to be regulated to within better than 0.05 K at a temperature around 1.9 K. The temperature reference is given by the pressure of saturated liquid helium flowing inside the distributed heat exchanger. Temperature sensors are placed on cryogenic lines, heat exchanger, cold mass, support posts, vacuum barriers, thermal shield and heat intercepts.

To measure liquid helium mass flow in the superfluid helium cooling circuit a Venturi flowmeter [74] at 4.5 K is used. It covers the range 0.6-8 g/s with an accuracy of $\pm 15\%$.

The magnet pressure is measured by means of piezoresistive cold sensors [Siemens KPY] used in the range from 0 to 3 MPa.

The control system [75, 76] of the String is mainly based on industrial Programmable Logic Controller (PLC) in which the number of I/O channels is of the order of 250 and the closed control loops are about 30. The supervision of the String PLCs makes use of a workstation running software packages (Factory Link [77]). For running the String and analysing the experimental data a data acquisition system was created. This system comprises the archiver monitoring continuously up to 600 channels and an externally triggered transient recorder sampling some of the previous channels at rates up to 1 kHz. All the data recorded by the acquisition system are periodically transferred to a database and then can be retrieved and analysed on an Excel sheet.

2.3 Single Magnet Test

The LHC magnets will be produced by European industry and delivered to CERN for reception testing before installation. Reception tests include procedures such as cooldown and warmup, powering to nominal current, magnetic measurements in the apertures, leaktightness and thermal check of the cryostat. The first cryogenic bench has started to operate for testing prototype magnets in the spring of 1994 [78, 79].

2.3.1 System layout

Cryogenic and electrical feed is done through a Magnet Feed Box (MFB) connected to one end of the magnet. On the opposite end the magnet is closed by the Magnet Return Box (MRB). In order to allow magnetic measurements to be performed, the magnet apertures are equipped with warm bore inserts. The simplified process and instrumentation diagram is shown in figure II-2.13.

In order to minimise the connections to the cryogenic pipework, the cryostat does not function in the test bench as it is designed to operate in the LHC. In particular, the helium II heat exchanger tube is not used and the heat load to the superfluid helium bath is transported by conduction along the magnet to a heat exchanger inside the MFB, with a nominal capacity of 55 W at 1.8 K. This heat exchanger is fed with liquid helium drawn from the bottom of the 4.5 K bath and later subcooled in a copper mesh heat exchanger before Joule-Thomson expansion to saturation at 1.35 kPa. The 4.5 K saturated helium bath, intercepting residual heat at the lower end of the vapour

cooled current leads, is thermally and hydraulically separated from the pressurised helium II enclosure by two “lambda plates”.

Line E and F are cooled by saturated nitrogen at a temperature around 80 K.

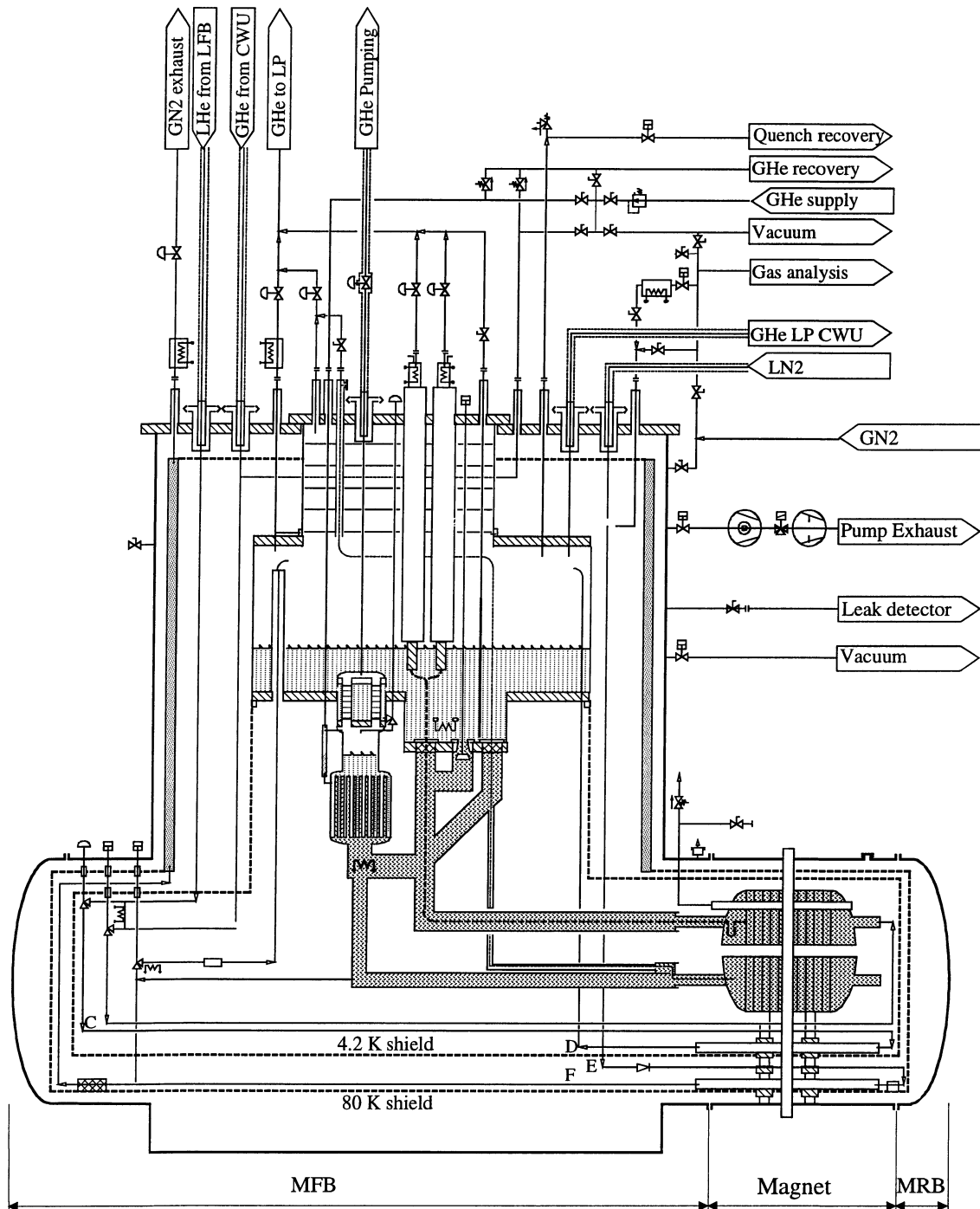


Figure II-2.13: *Simplified process and instrumentation diagram of the single magnet test bench*

2.3.2 Instrumentation and process control

The bench is instrumented with cold sensors for measuring temperatures (platinum and carbon resistors), pressures (Siemens KPY and Validyne sensors) and levels (superconducting wire gauges) in order to monitor and control the cryogenic processes. Transient phases of operation, such as cooldown and warm up, make use of signals from sensors mounted on the magnet cold mass and on the thermal shield.

All the main components of the cryogenic system are controlled by industrial PLC, supervised by a central supervision package (Factory Link).

CHAPTER 3

Calculated and measured thermal performance of the cryostats

Precise assessment of heat inleaks [80] has been carried out making use of the previously described tools.

Screen temperatures and residual gas pressure have been varied to investigate their influence on the cryostat heat inleaks.

The quality of heat interception of the thermal shield, support posts, vacuum barrier and cryogenic valves has been investigated.

Resistive dissipation [81] in the non-superconducting cable splices was measured both calorimetrically and electrically.

Measured heat loads have been compared with those calculated.

3.1 Heat load assessment

The heat inleaks depend on intermediate screen temperatures and residual gas pressure [82-85]. Thermal shield temperature is one of the most important parameter in the evaluation of the thermal budget since it influences directly the heat inleaks at the three temperature levels: 50-75 K, 4.5-20 K and 1.9 K. In particular, the heat inleak to the magnet cold mass is very sensitive to the screen temperatures. Line C intercepts heat from support posts affecting thus conduction heat to the magnet cold mass. Furthermore, heat inleaks at 1.9 K and 4.5-20 K strongly increase as the insulation vacuum degrades.

3.1.1 Heat loads under nominal steady-state conditions

Cryostat Thermal Model

In the first evaluation of heat inleaks, nominal LHC conditions were considered. After imposing mass-flows at 4.5-20 K and 50-75 K steady-state nominal condition (table II-3.1) were reached in about 20 hours and this time was mainly dictated by the thermal shield thermal capacity.

Table II-3.1: CTM parameters in nominal steady state condition

50-75 K level	Mass-flow [g/s]	0.5
	Line E inlet temperature [K]	50
	Line E outlet temperature [K]	56
	Line F inlet temperature [K]	65
	Line F outlet temperature [K]	75
4.5-20 K level	Mass-flow [g/s]	0.24
	Line C inlet temperature [K]	5.3
	Line C outlet temperature [K]	6.5
	Line D inlet temperature [K]	7.3
	Line D outlet temperature [K]	7.7
1.9 K level	Mass-flow [g/s]	0.8
	Cold mass temperature [K]	1.9

Under steady-state conditions the longitudinal temperature gradient of the thermal shield was less than 0.3 K/m. At 1.9 K the thermal gradient between the pressurised and the saturated helium was 100 mK and the longitudinal thermal gradient on the cold mass was below 50 mK under nominal operating conditions. After measuring the mass-flows and the inlet and outlet temperatures at each temperature level heat inleaks were calculated. Table II-3.2 lists the measured and the calculated heat inleaks of the cryostat in steady-state conditions at 10^{-3} Pa without the contribution of the end boxes, which amounts to 40 W at 50-75 K, 4.2 W at 4.5-20 K and 0.1 W at 1.9 K. Heat inleak measurements are in agreement with those calculated. In order to evaluate the heat inleak at 1.9 K due to the end boxes the first measurement of heat inleak was made on the two end boxes as one unit ("calibration test").

Table II-3.2: CTM heat inleaks under steady-state conditions

Heat inleak	50-75 K		4.5-20 K		1.9 K	
	Measured	Calculated	Measured	Calculated	Measured	Calculated
[W]	47.8±3	45.8	2.3±0.15	2.4	1.82±0.1	1.92
[W/m]	4.66±0.29	4.47	0.23±0.01	0.23	0.18±0.01	0.19

The heat inleak to the cold mass is the sum of thermal radiation from the thermal shield and conduction from the support posts. The heat inleak to the cold mass from the support posts has been maintained low by two heat intercepts at 10 K and at 88 K. Conduction from the support posts to the cold mass can be calculated and the radiative term can thus be evaluated.

Table II-3.3 shows the heat inleaks from the support posts. The heat inleak to line C is due to radiation heat from the thermal shield and conduction heat from the support posts. Radiation from the thermal shield has been considered half of that to line D in order to evaluate the measured heat inleak due to the support posts.

Table II-3.3: Heat inleaks to support posts

Heat inleak	Line E		Line C		Cold mass
	Measured	Calculated	Measured	Calculated	Calculated
[W]	15.8±1.2	14.2	1.8±0.13	2.08	0.21

The heat inleak from the support post to line E takes into account both radiation and conduction from the vacuum vessel at 300 K through the glass fiber-epoxy composite column.

The heat flux, from 300 K to 50-75 K through the MLI system only, was estimated to 32 W, corresponding to an average of **1.2 W/m²**. Radiation heat inleak from 50-75 K to 4.5-20 K confirmed the value of **90 mW/m²** already found during tests of multilayer reflective insulation [43].

LHC prototype magnet String

Heat inleaks in nominal steady state condition have been measured at the three temperature levels. Heat inleak contributions from auxiliary components (end boxes, quench valves) largely exceed those from the cryostat and render their measurements difficult. This justifies a posteriori the interest of the CTM for proper validation of cryostat design.

The main differences between LHC design and String test (table II-3.4) refer to the cooling fluid of the circuit E-F, the thermal shield temperature and the heat intercept temperatures.

Table II-3.4: Main differences between LHC design and LHC prototype magnet String

Item	LHC design	String test
Cooling Fluid	GHe	LN ₂
Line E-F	50-75 K	90-100 K
Support Post Heat Intercept 1	65 K	115 K
Support Post Heat Intercept 1	7 K	11 K
Vacuum Barrier Intercept	80 K	125 K
Cryogenic Valves Heat Intercept	80 K	100 K

Adding a third dipole increased the length of the LHC prototype magnet String from 33.7 m to 45.6 m.

Calculated and measured heat inleaks from Run 1 (1 quadrupole, 2 dipoles and auxiliaries) and Run 2 (1 quadrupole, 3 dipoles and auxiliaries) are presented in table II-3.5. The calculated values have been obtained by using the temperature conditions as quoted in table II-3.4.

Table II-3.5: Heat inleaks of the LHC prototype magnet string under steady-state conditions [W]

RUN	90-100 K		4.5-10 K		1.9 K	
	Measured	Calculated	Measured	Calculated	Measured	Calculated
1	250±20	179.40	15±1.1	13.11	20±0.2	16.91
2	358±27	238.74	20.6±1.5	16.69	27.2±2.7	21.21

Measured global heat loads have been performed with a reasonable precision and are quite in agreement with those calculated. The calculated heat leak at 1.9 K neglects helium II leakage across quench valves. The measured heat leak from the thermal shield to the cold mass is larger (0.3 W/m) than what expected (0.2 W/m) because of the higher thermal shield temperature. The increase of the average heat inleaks at 90 K during Run 2 is mainly due to the composite vacuum barrier installed in the String return box before Run 2. At 1.9 K the presence of only two quench valves compensates for the further heat leak introduced by the second vacuum barrier in the SRB.

Single-magnet test

The heat load measurements during single magnet tests have been carried out at zero magnet excitation under steady-state conditions with the equipment for “warm” magnetic measurements in the apertures maintained at 1.9 K. Even in this case, component heat loads are difficult or impossible to measure. The measured heat inleaks presented in table II-3.6 include end boxes, current leads and bore anticryostats which represent a large contribution to the total heat inleaks. The calculated heat inleaks only refers to the cryostat.

Table II-3.6: Heat loads of the single-magnet test under steady-state conditions [W]

80 K		4.5-10 K		1.9 K	
Measured	Calculated	Measured	Calculated	Measured	Calculated
150±20	87.9	40±5	5.3	9.4±1.5	6.4

Heat load at 4.5-20 K due to current leads is about 30 W representing thus 75 % of the total heat losses. A precise calculation of heat inleaks is difficult and base load measurement of MFB and MRB would be needed in a “calibration test” without the magnet in place.

3.1.2 Influence of cryogenic line temperatures

The influence of thermal shield and circuit C-D temperatures on the cryostat thermal performance has been investigated in the CTM. Several tests have been performed during which only one parameter at a time has been changed (table II-3.7).

Table II-3.7: Range of cryoline temperatures investigated in the CTM

Thermal shield [K] Line C [K]	50	65	75	90	105	120	135	150
4.5	×	×	×	×	×	×	×	×
10			×					
15			×					
25			×					
35			×					

× Nominal condition

The CTM cryogenic system allows temperature of the line E to be varied, while keeping constant temperature of line C. Maintaining the residual gas pressure at nominal value (10^{-3} Pa) the temperature of the thermal shield has been varied from 50 K to 150 K in steps of 10-15 K and the temperature of line C from 4.5 K to 35 K in steps of 5-10 K. Off-design measurements were particularly difficult to control since the mass-flows were low and as a consequence longer time was required to reach steady-state stability.

Figures II-3.1 and II-3.2 show the measured and the calculated steady-state heat inleaks at 1.9 K as a function of respectively line F and line C temperatures.

The increase on the heat leak at 1.9 K with the temperature of line C mirrors the variation of the glass fiber-epoxy composite thermal conductivity between 4.5 K and 20 K. The thermal shield temperature largely affects the heat leak to the cold mass since radiation heat represents the predominant contribution on the total heat leak. Heat transfer through the MLI system has been calculated from equation II-1.16 (part 2- chapter 1), where the parameters α and β have been obtained by knowing the heat inleaks from 300 K to 75 K (1.2 W/m^2) and from 75 K to 4.5 K (0.09 W/m^2). This relationship fits well experimental data for thermal shield temperatures around 75 K, but its slope is steeper than that of the experimental curve.

Heat leak at 4.5-20 K depends on line E and line C temperatures by conduction through the support posts and line F temperature by radiation from the thermal shield (figures II-3.3, II-3.4, II-3.5 and II-3.6). Heat leak at 4.5-20 K due to heat flux through MLI represents a small contribution only for thermal shield temperatures below 80 K.

Radiation from the vacuum vessel (line F) and conduction from the support posts constitute the main contributions to the heat leak to 50-75 K. Heat leak to 50-75 K (figures II-3.7 and II-3.8) increases as the thermal shield temperature decreases. On the other hand a lower thermal shield temperature has the advantage to lower the heat inleaks at 4.5-20 K and 1.9 K.

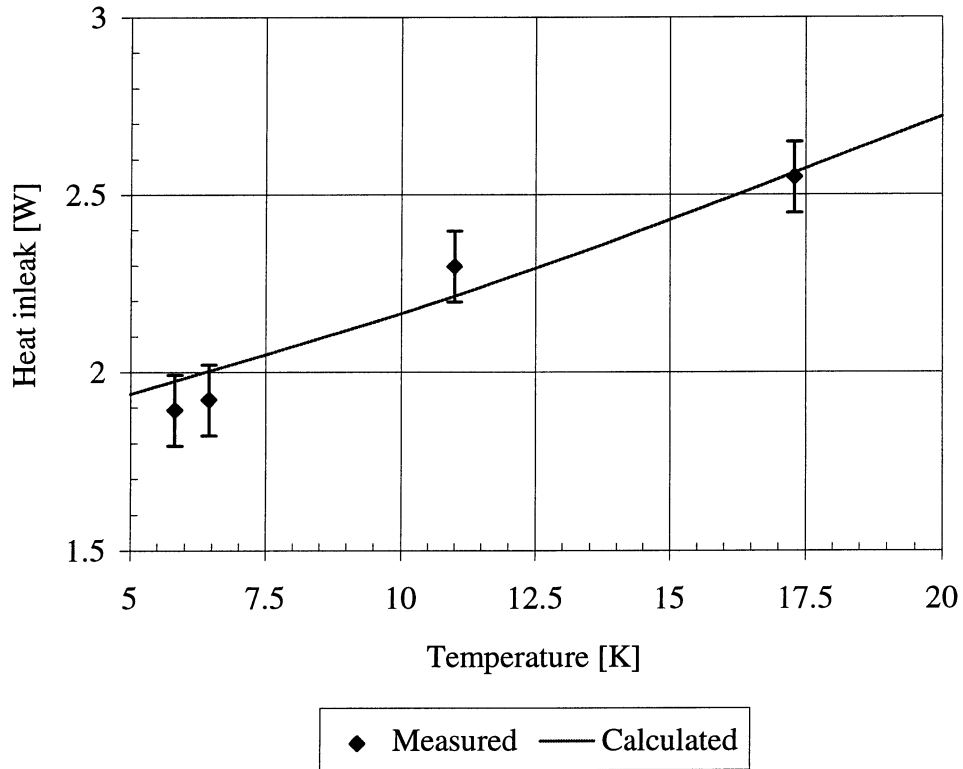


Figure II-3.1: Heat leak at 1.9 K versus line C temperature (residual gas pressure= 10^{-3} Pa, Lines E-F=50-75 K)

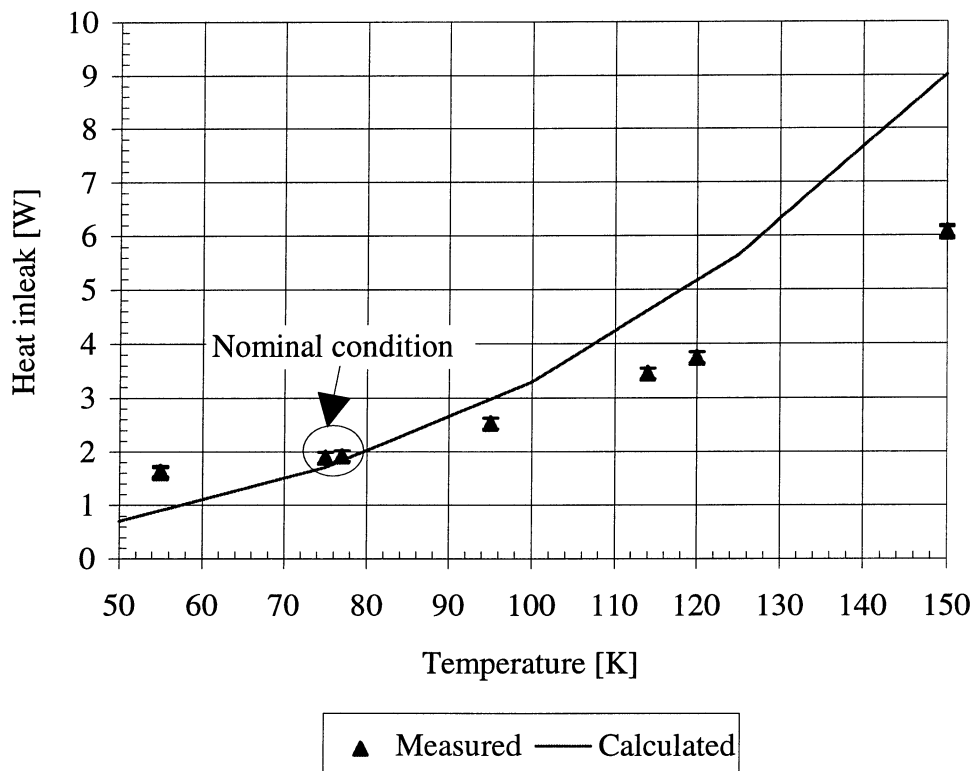


Figure II-3.2: Heat leak at 1.9 K versus thermal shield temperature (residual gas pressure= 10^{-3} Pa, Lines C-D=4.5-20 K)

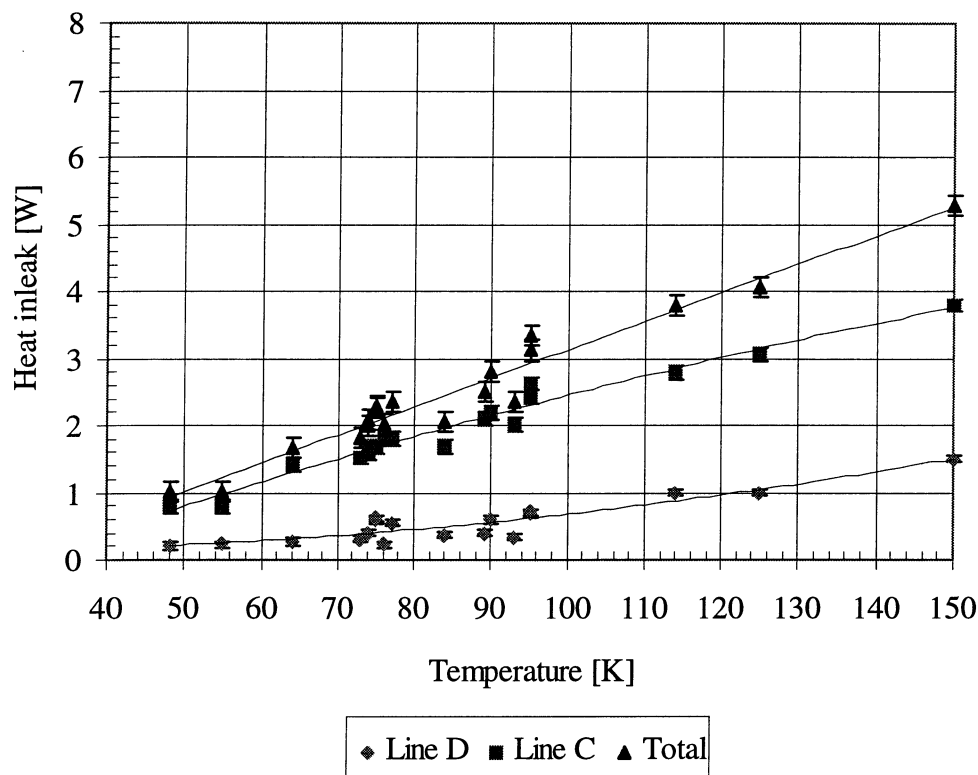


Figure II-3.3: Measured heat inleak at 4.5-20 K versus thermal shield temperature (residual gas pressure= 10^{-3} Pa)

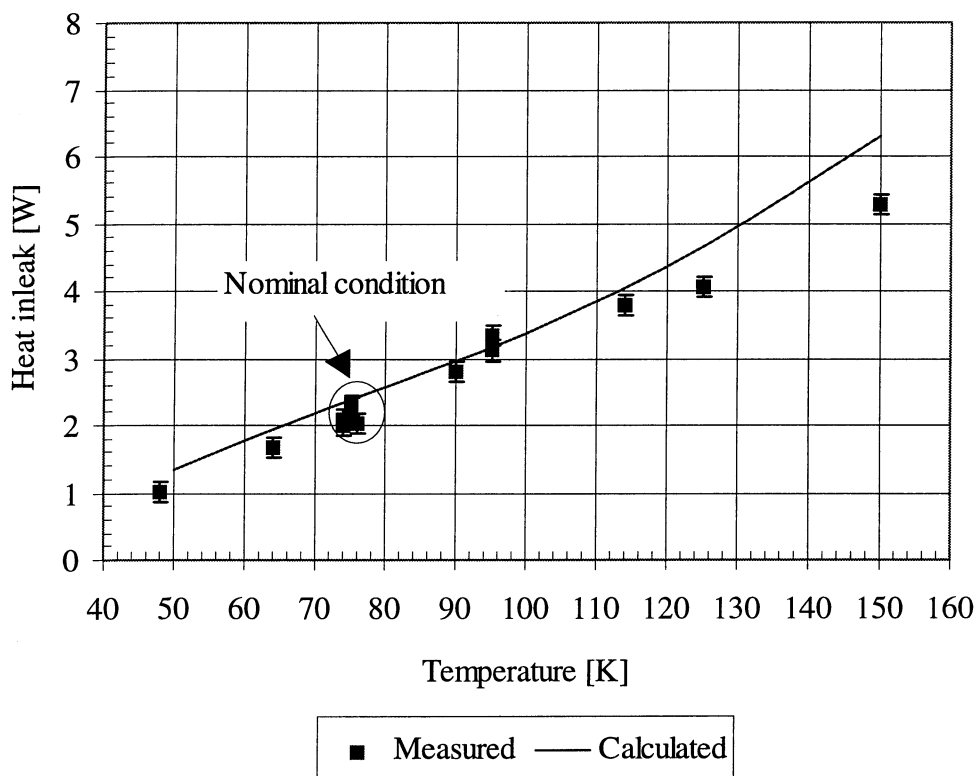


Figure II-3.4: Heat inleak at 4.5-20 K versus thermal shield temperature (residual gas pressure= 10^{-3} Pa)

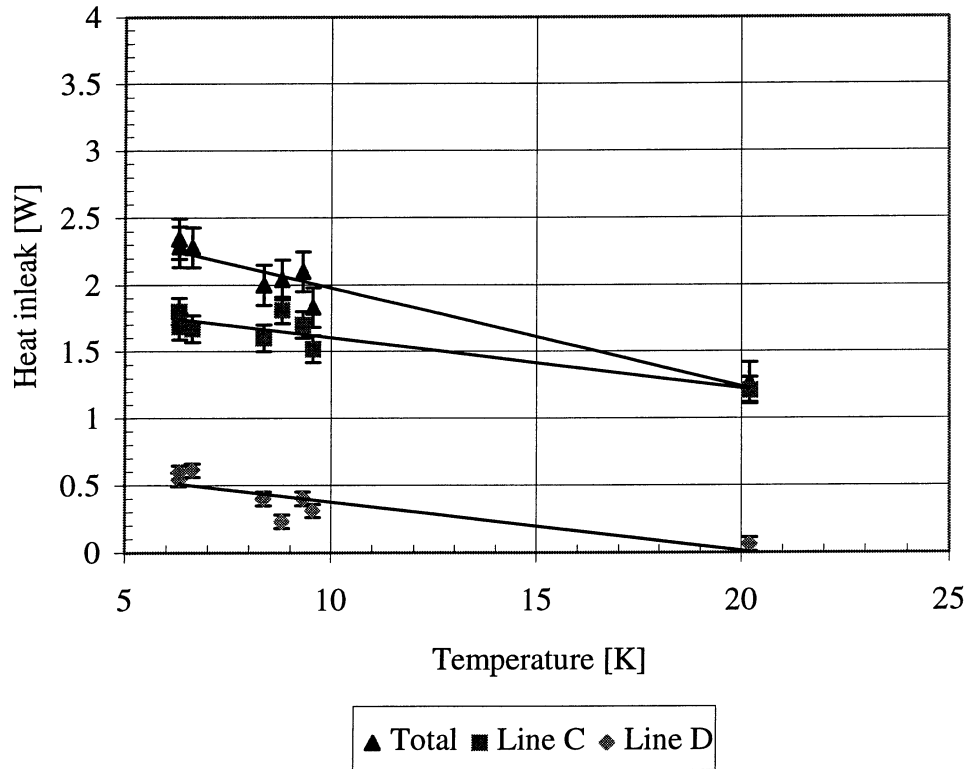


Figure II-3.5: Measured heat leak at 4.5-20 K versus line C temperature (residual gas pressure= 10^{-3} Pa, Lines E-F = 50-75 K)

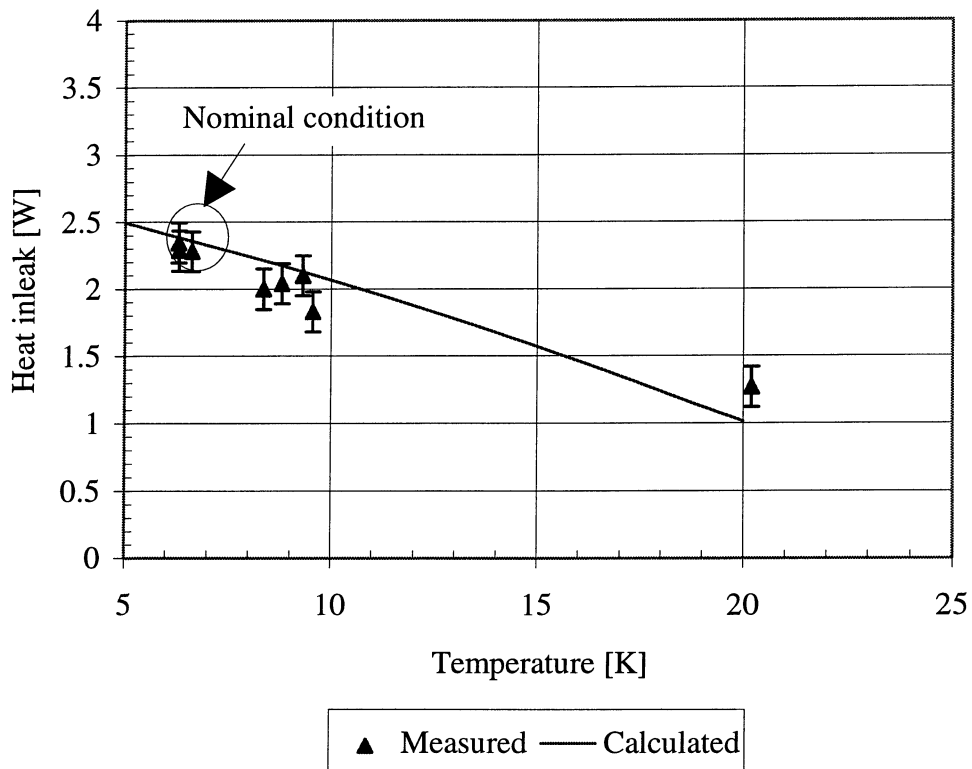


Figure II-3.6: Heat leak at 4.5-20 K versus line C temperature (residual gas pressure= 10^{-3} Pa, Lines E-F = 50-75 K)

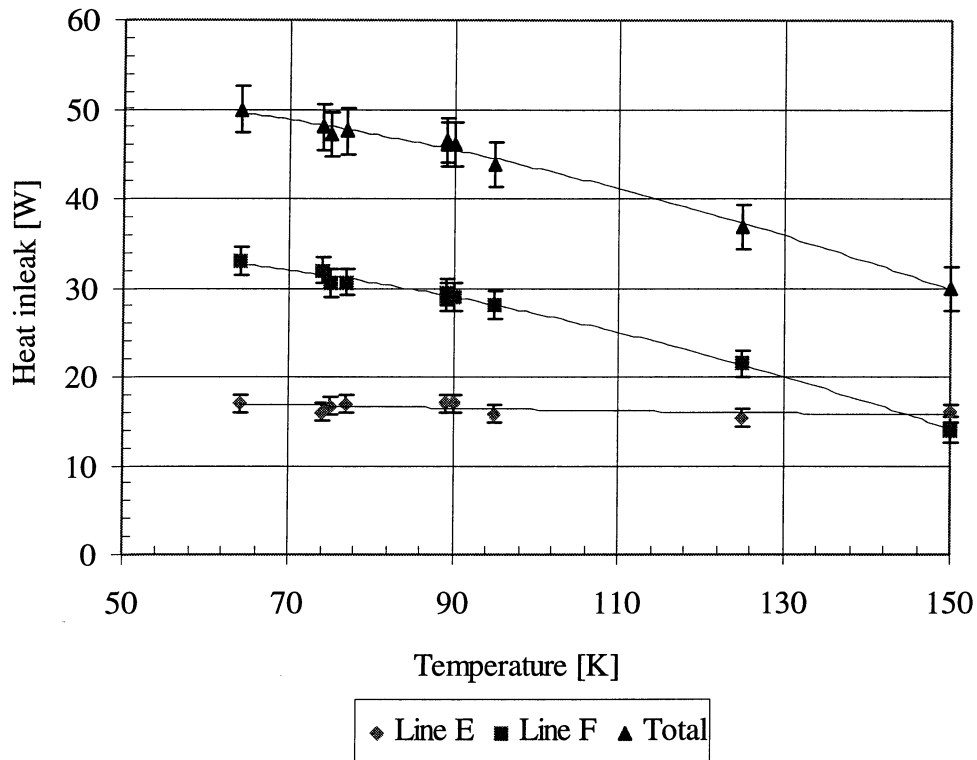


Figure II-3.7: Measured heat leak at 50-75 K versus thermal shield temperature (residual gas pressure= 10^{-3} Pa, Lines C-D = 4.5-20 K)

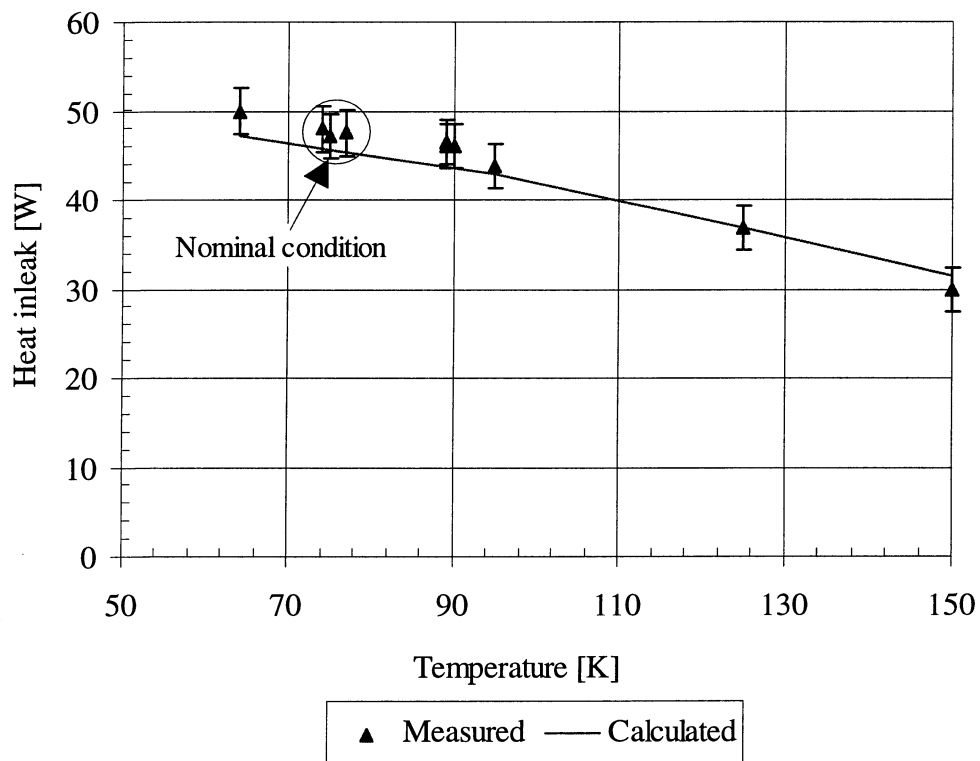


Figure II-3.8: Heat leak at 50-75 K versus thermal shield temperature (residual gas pressure= 10^{-3} Pa, Lines C-D = 4.5-20 K)

The comparison between calculated and measured heat inleaks show that experimental data are in good agreement with expectations. The mathematical model used to calculate the cryostat heat inleaks, now validated against experimental data, constitutes an useful tool to simulate any nominal and accidental operating conditions. For all the different tests reported in this chapter the temperatures and pressures of the single components are listed in Annex 2.

Heat flux from the vacuum vessel to the thermal shield and from the thermal shield to the cold mass through respectively 30 and 10 layers of type-B MLI as a function of thermal shield temperatures is listed in table II-3.8. The heat flux from the thermal shield to the cold mass through MLI has been evaluated by subtracting the calculated heat by conduction through the support post from the measured heat inleak at 1.9 K.

Table II-3.8: Measured heat flux through multilayer reflective insulation systems (type B).

Thermal shield [K]	300 K to thermal shield [W/m ²]	Thermal shield to 1.9 K [W/m ²]
50	1.28	0.08
75	1.19	0.09
100	1.06	0.14
125	0.92	0.20
150	0.76	0.32

The relationships, expressed in W/m², which better fits the experimental values are the following:

300 K to thermal shield ($N_S=30$)

$$\dot{q}_{ts} = \frac{0.154}{N_S}(300 - T_{ts}) + \frac{1.304 \cdot 10^{-10}}{N_S}(300^4 - T_{ts}^4) \quad (\text{II-3.1})$$

Thermal shield to 1.9 K ($N_S=10$)

$$\dot{q}_{cm} = \frac{0.011}{N_S}(T_{ts} - 1.9) + \frac{2.732 \cdot 10^{-9}}{N_S}(T_{ts}^4 - 1.9^4) \quad (\text{II-3.2})$$

The heat fluxes calculated by equations II.3.1 and II-3.2 have been compared to measured values and results are shown in figures II-3.9 and II-3.10.

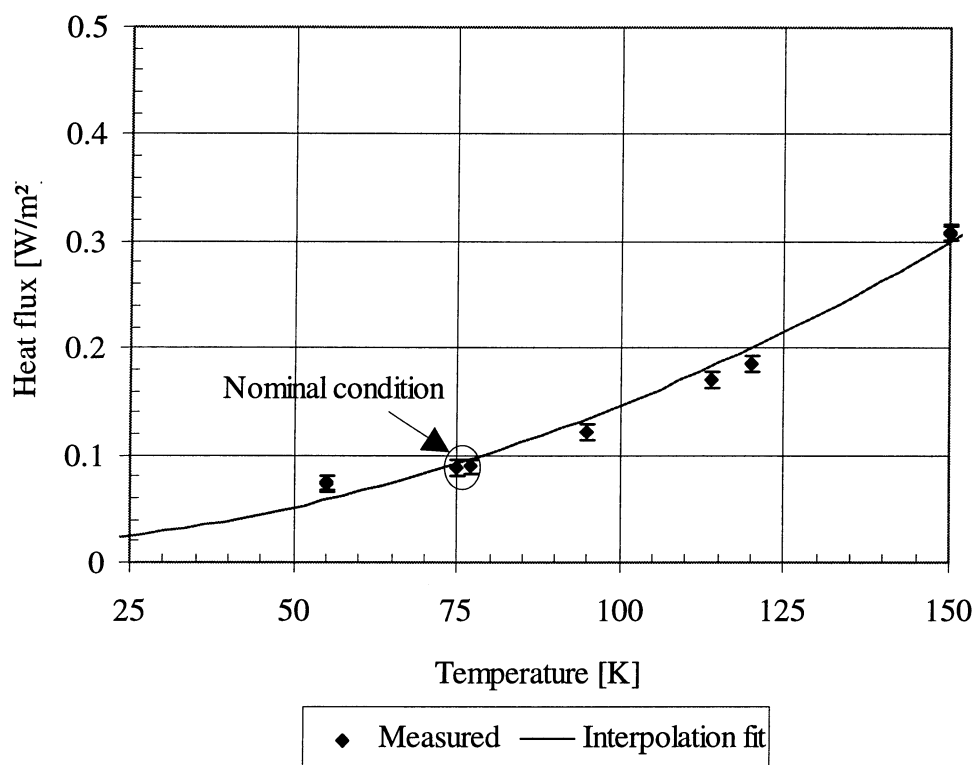


Figure II-3.9: Heat flux from the thermal shield to 1.9 K through 10 layers of type-B MLI (residual gas pressure= 10^{-3} Pa)

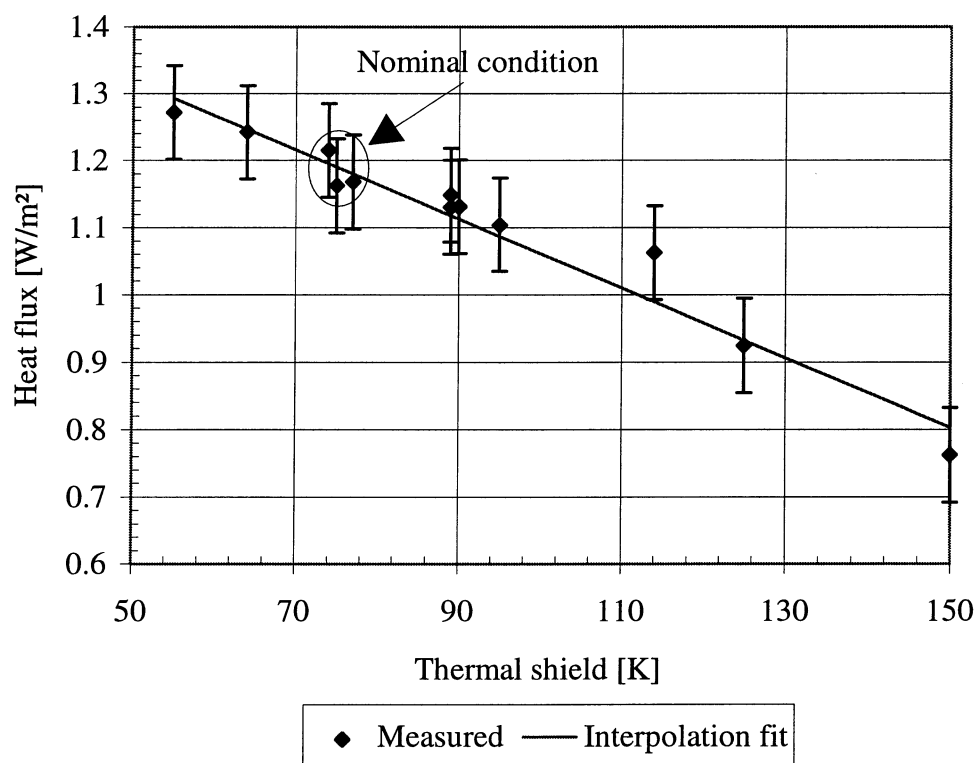


Figure II-3.10: Heat flux from 300 K to the thermal shield through 30 layers of type-B MLI (residual gas pressure= 10^{-3} Pa)

3.1.3 Influence of insulation vacuum

In the cryostat thermal model, under nominal steady-state temperatures, the insulation vacuum was degraded in steps from $4 \cdot 10^{-4}$ Pa to 10^{-1} Pa by introducing dry helium gas into the insulation space. From $4 \cdot 10^{-4}$ Pa to $2 \cdot 10^{-2}$ Pa the cold mass temperature could be maintained below the lambda point (T_λ). According to the hydraulic section of the dummy cold mass (5 cm^2), the peak conduction in superfluid helium from 1.8 K to the lambda point is about 10 W. Above $2 \cdot 10^{-2}$ Pa the heat inleak at 1.9 K is larger than 10 W and the cold mass temperature cannot be kept below T_λ and therefore rises. From $2 \cdot 10^{-2}$ Pa to 10^{-1} Pa the cold mass temperature was maintained between 4.5 and 10 K but the heat inleak from the thermal shield to the cold mass does not change significantly if the cold mass varies from 1.9 K to 10 K.

Following a degradation of the vacuum insulation the 1.9 K level (figure II-3.11) is the most affected since in nominal steady-state conditions the heat transfer through the radiative insulation represents 80 % of the total heat inleak.

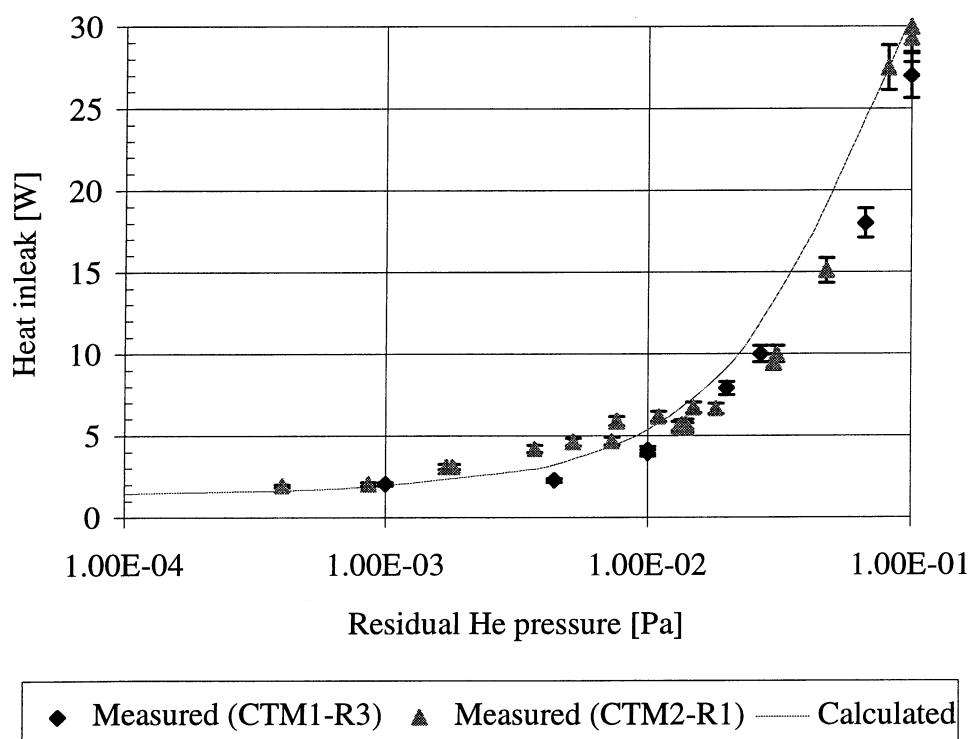


Figure II-3.11: Heat inleak at 1.9 K versus residual helium pressure (Lines C-D=4.5-20 K, Lines E-F=50-75 K)

Calculated heat inleak at 1.9 K versus residual helium pressure is in agreement with that measured. Calculations are based on heat flux through MLI measured in a dedicated vertical cryostat [43]. This means that thermal performance of type-B MLI does not depend on the cryostat position and the effect of gravity appears negligible.

Multilayer reflective systems present a great advantage for residual gas pressure higher than $2 \cdot 10^{-3}$ Pa. At 10^{-2} Pa heat flux through 10 layers of type-B MLI from 80 K to 4.5 K is about 0.25 W/m^2 while conduction in helium gas is 0.8 W/m^2 .

Heat inleaks at 4.5-20 K and 50-75 K are less sensitive to the residual gas pressure. At 10^{-2} Pa heat leak at 4.5-20 K is 2.5 W and at 50-75 K is 55 W.

Degradation of the insulation vacuum has been performed also in the LHC prototype string where residual gas pressure was increased from 10^{-4} Pa to $4 \cdot 10^{-2}$ Pa by introducing dry helium gas. The test was stopped at $4 \cdot 10^{-2}$ Pa as, above this value, heat leak at 1.9 K exceeds the available refrigeration capacity. Table II-3.9 compares measured to calculated heat leak at 1.9 K for different values of residual helium pressures. At 10^{-4} Pa, the measured heat leak at 1.9 K is higher than the value presented in table II-3.5 because of the increased leakage across the cryogenic valves. For degraded insulation vacuum the calculated heat inleaks are lower than those measured and the difference confirms the results obtained at nominal insulation vacuum.

Table II-3.9: Heat leak at 1.9 K under degraded insulation vacuum (LHC prototype String test)

Insulation vacuum [Pa]	Measured [W]	Calculated [W]
10^{-4}	37.2	21.21
$5 \cdot 10^{-3}$	49.0	37.1
10^{-2}	62.7	48.3

3.1.4 Resistive dissipation in non-superconducting cable splices

Splices in superconducting cables are needed either to subdivide coils into regions of different current density in order to match the local field (current grading) in a magnet, or to join magnets after installation. Common solder (40% lead, 60% tin) is a superconductor with a critical field of only 0.3 T. The solder becomes resistive in most magnet situations (the electrical resistivity is about $3 \cdot 10^{-9} \Omega \cdot m$ from 1.9 K to 10 K, greater than that of copper which is $1.7 \cdot 10^{-9} \Omega \cdot m$) [86, 87].

Figure II-3.12 shows the electrical scheme of the LHC prototype magnet string during Run 2. The quadrupole magnet and the three prototype dipole magnets (A1, A2, A3) are connected in series.

At the cold side of the main current leads the superconducting cables are clamped whereas all other splices are soldered. Most of them are located in regions of high magnetic flux density.

Resistive dissipation in non-superconducting cables may be evaluated both by electrical and calorimetric methods.

The current ramping procedure over time is shown in figure II-3.13. The contact resistance can be deduced from current and voltage measurements. Voltage is measured with an accuracy of 100 nV.

Due to the high conductivity of the connections it is impossible to measure a single contact resistance. The average value per splice is evaluated by measuring the voltage drop over a certain number of splices.

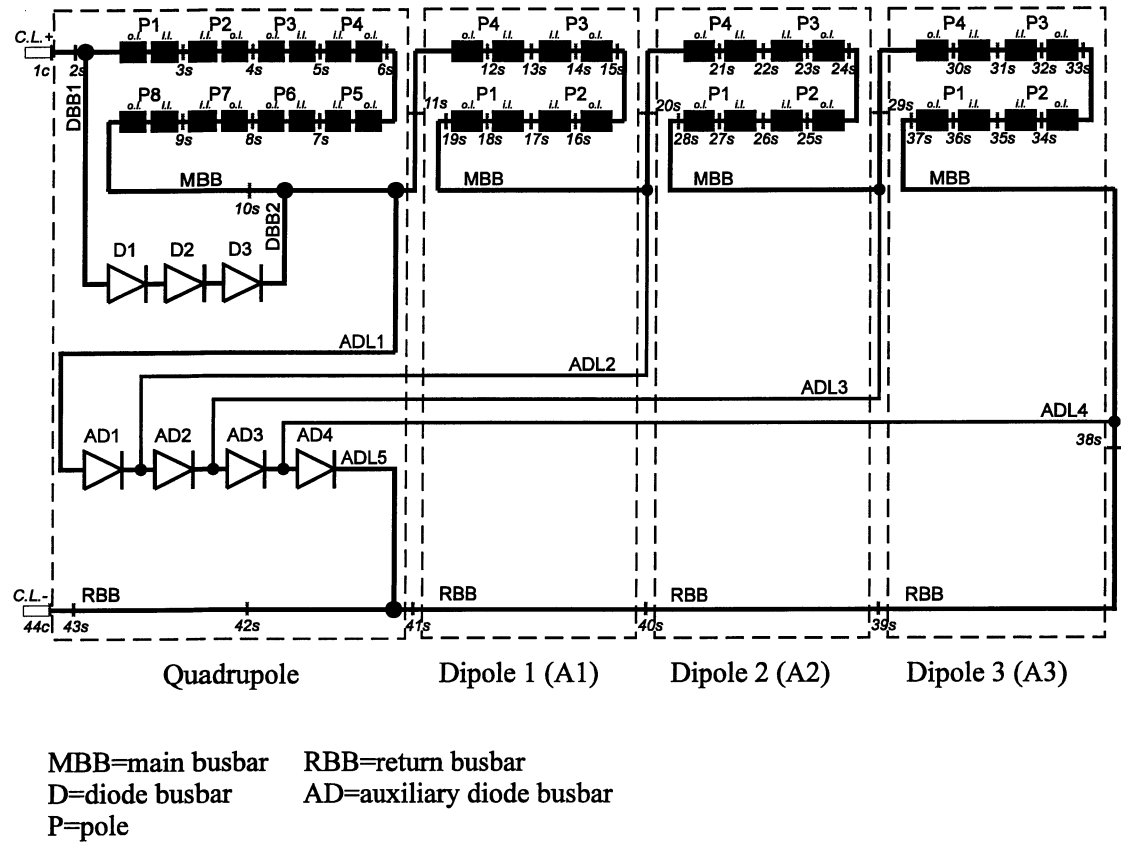


Figure II-3.12: Electrical scheme of LHC prototype magnet string in RUN 2

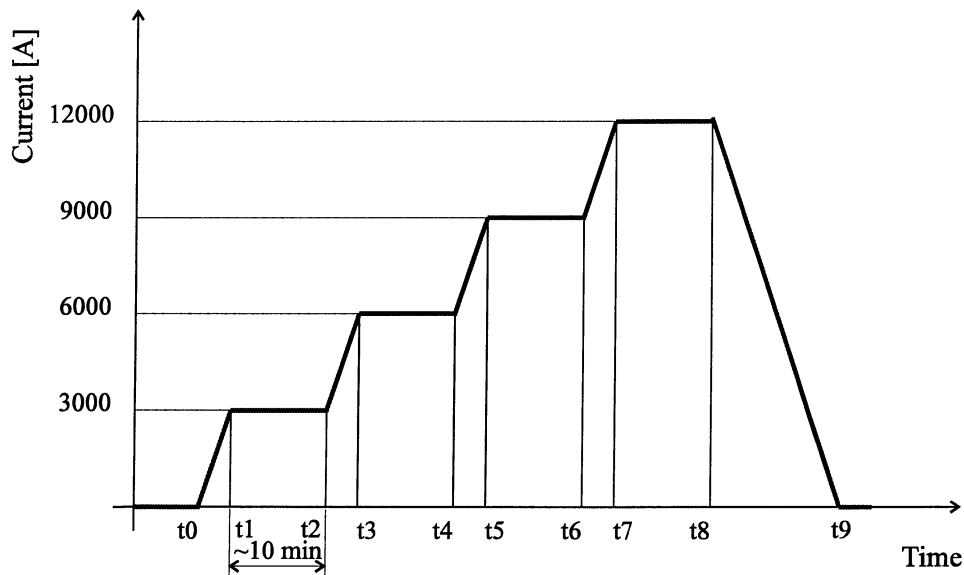


Figure II-3.13: Magnet current ramping procedure for contact resistance measurement

The voltage changes linearly with the string current. The contact resistance for different current values is constant since in the splice regions the cooling effect is

stronger than the heat generation due to high current density. Results of contact resistance measurements are shown in table II-3.10.

The resistive heating is also deduced by calorimetric measurement of the heat loads at 1.9 K with and without current. The calorimetric measurement permits to evaluate only the integral of the heat loads due to contact resistance in the whole magnet string, whereas the electrical measurement gives the average contact resistance in each magnet (see figure II-3.12).

Table II-3.10: Summary of contact resistance measurements

	Number of splices	Calorimetric measurement		Electrical measurement	
		Resistive heating [W]	Average Resistance/splice [nΩ]	Resistive heating [W]	Average Resistance/splice [nΩ]
Run 1 (1 quadrupole +2 dipoles)	34	8.7±1.5	1.7	9.4±1.3	1.8±0.3
Run 2A (1 quadrupole +3 dipoles)	44	9.1±1.5	1.3	=	=
Run 2B (1 quadrupole +3 dipoles)	44	10.3±1.5	1.5	9.1±1.3	1.3±0.2

The measurements on contact resistance of superconducting cable performed on the LHC prototype magnet string, both by calorimetric and electrical methods, are in agreement and have shown a higher average value of resistance per splice (i.e. 1.5 nΩ calorimetrically and 1.3 nΩ electrically) than expected. The average value which appears in reference 4 is 0.85 nΩ and it has been obtained considering 18 internal splices (1.2 nΩ each) and 26 external splices (0.6 nΩ each). Adding a further magnet to the LHC prototype magnet string, that is increasing the number of soldered joints, has not changed essentially the average resistance per splice.

3.2 Experimental investigation of heat interceptions

Cryostat heat inleaks are kept within the budgeted values by performant heat interception. In the LHC prototype cryostats, thermal shield, cryogenic valves, support posts and vacuum barrier are cooled by cryogenic lines and through bolted and brazed contacts.

The single magnet test and the LHC prototype magnet string have been equipped with temperature sensors in order to measure thermal gradients across heat interceptions and evaluate the quality of thermal contacts under vacuum. Impedance of thermal contacts should ideally be very low and easily reproducible. This analysis permitted to understand which type of contacts represents a reliable solution for the future LHC cryostats.

3.2.1 Prototype magnet support posts

The thermal budget envisaged for the support system is of the order 10 W at 50-75 K, 1 W at 4.5-20 K and 0.1 W at 1.9 K. In the support posts two heat intercept plates in aluminium alloy (AA-6082) are glued and shrink-fitted to the glass fiber-epoxy composite column to allow thermalisation at 4.5-20 K (line C) and at 50-75 K (line E) [20].

Figures II-3.14 and II-3.15 show the heat interception layout. The heat intercept (table II-3.11) is constituted by copper braids (Cu ETP) brazed on a copper sleeve which is brazed on the cryogenic lines (C and E). On the opposite side the copper braids are brazed between two copper plates which are then bolted on the support post flange. In the quadrupole cryostat in the short straight section the copper braids at 4.5-20 K have been replaced by copper strips (Cu ETP) in order to increase the cross-section and to reduce the thermal gradient across them.

Table II-3.11: Main dimensions of support post heat interceptions

Temperature	Braids (Cu ETP)			Plates (Cu ETP)		
	Number	Cross-section [mm ²]	Length [mm]	Number	Cross-section [mm ²]	Length [mm]
4.5-20 K	8	30x3.5	320	2	20x3.5	140
50-75 K	4	30x3.5	115	1	20x3.5	140

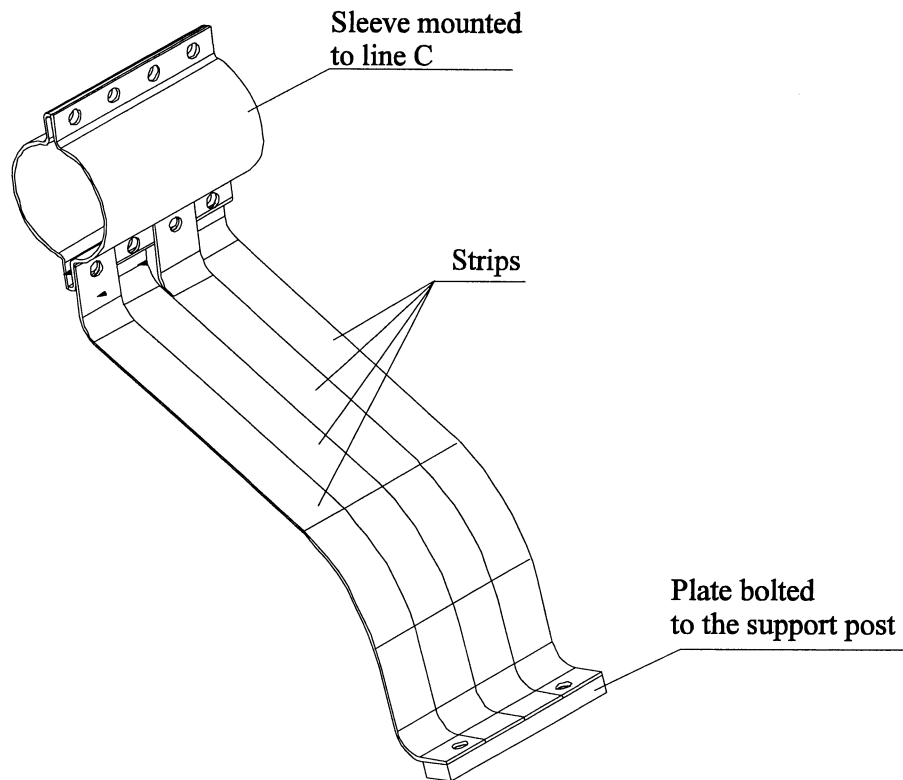


Figure II-3.14: Heat interception between the magnet support post and line C

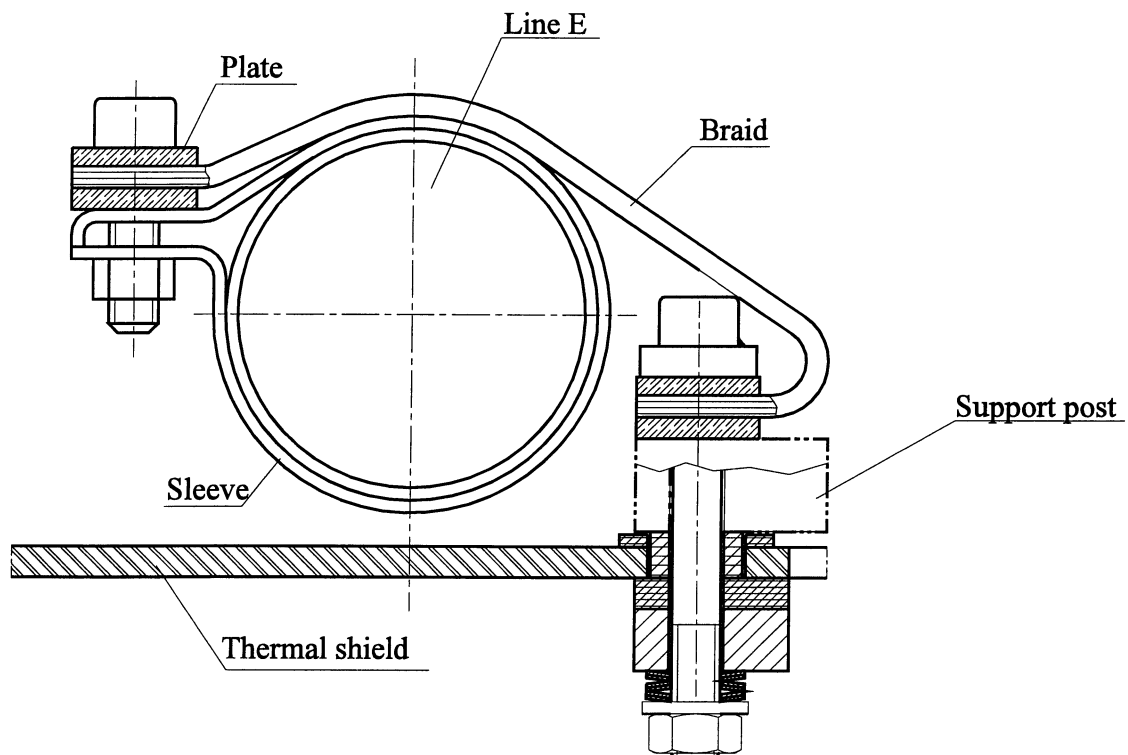


Figure II-3.15: Heat interception between the magnet support post and line E

The quality of thermal contacts and the braid dimensions determine the thermal gradient between the support flange and the cooling line as a function of the heat flux (figure II-3.16) reaching the support post flange.

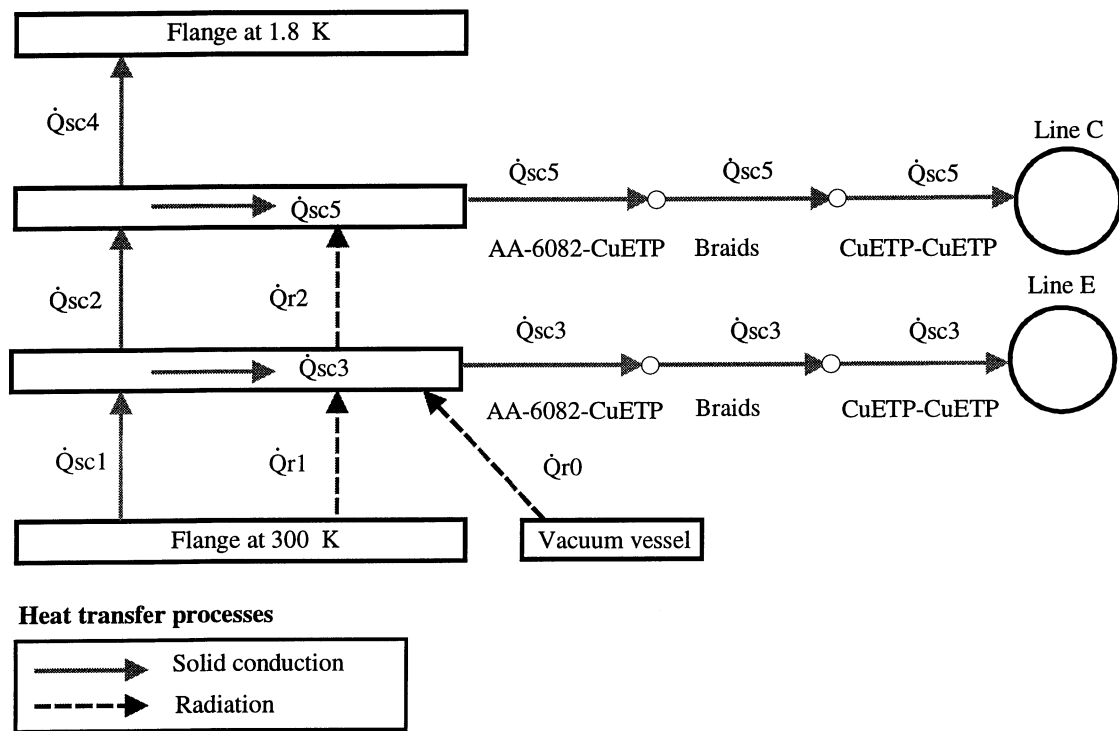
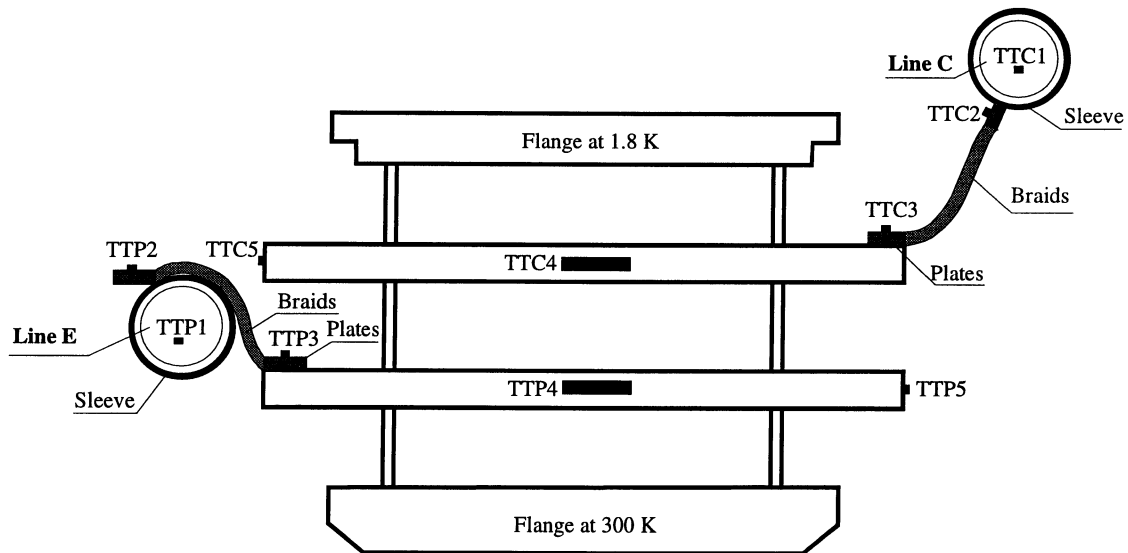


Figure II-3.16: Thermal network of support post

The total thermal gradient between the support post flange and the cryogenic line is given by the following contributions:

- thermal contacts between the line and the braids (line and collar plus collar and braids)
- conduction along the strips
- thermal contacts between braids and flanges (braids and plates plus plates and flanges)

Thermometer sensors (figure II-3.17) placed at each extremity of the braids permitted to evaluate the thermal gradients of interest. Furthermore, the thermal gradient in the aluminum flange has been investigated by installing two temperature sensors on each flange. Due to calibration and instrument errors we expect to measure temperatures with an estimated precision of 0.5 K.



Thermometers



Heat intercept between Line C and support post (carbon sensor= )	Heat intercept between Line E and support post (platinum sensor= )
TTC1=Line C temperature	TTP1=Line E temperature
TTC2=Braid temperature at tube side extremity	TTP2=Braid temperature at tube side extremity
TTC3=Braid temperature at flange side extremity	TTP3=Braid temperature at flange side extremity
TTC4=Flange temperature	TTP4=Flange temperature
TTC5=Flange temperature	TTP5=Flange temperature

Figure II-3.17: Instrumentation scheme of support post

Table II-3.12 lists the measurement results from two prototype dipole magnet cryostats: A3 and N2. Measurements have been performed with a precision of $\pm 15\%$. The difference in the thermal performance of the bolted contacts shows that this type of contacts is not easily reproducible.

Table II-3.12: Measurements on instrumented prototype cryostat

Heat interception		Cryostat identification	
		A3	N2
4.5-20 K	Temperature [K]	TTC1	4.5
		TTC2	6.1
		TTC3	7.5
		TTC4	16.3
		TTC5	=
	Thermal gradient [K]	Tube-braids	1.6
		Braids	1.3
		Braids-flange	8.8
		Total	11.8
	Thermal impedance [K/W]	Tube-braids	1.6
		Braids-flange	8.9
50-75 K	Temperature [K]	TTP1	75.0
		TTP2	86.9
		TTP3	101.9
		TTP4	114.8
		TTP5	=
	Thermal gradient [K]	Tube-braids	11.9
		Braids	15.0
		Braids-flange	12.9
		Total	39.8
	Thermal impedance [K/W]	Tube-braids	0.9
		Braids-flange	1.0

The steady-state heat balance equation applied to each support post flange yields:

$$\dot{Q}_{sc5} = \dot{Q}_{sc2} + \dot{Q}_{r2} - \dot{Q}_{sc4} \quad (\text{II-3.3})$$

$$\dot{Q}_{sc3} = \dot{Q}_{sc1} + \dot{Q}_{r1} + \dot{Q}_{r0} - \dot{Q}_{sc2} - \dot{Q}_{r2} \quad (\text{II-3.4})$$

Heat by conduction to line C (\dot{Q}_{sc5}) and line E (\dot{Q}_{sc3}) can be calculated by knowing either the flange temperatures (from equations II-3.3 and II-3.4) or the temperatures across the braids. Table II-3.13 shows that the calculated thermal budget exceeds the budgeted values. The measured temperature of the flange linked to line E is probably

higher than the real value and this may explain the difference in heat leaks obtained by applying the two methods

Table II-3.13: Calculated heat leaks of prototype magnet support system (2 posts)

Cryostat identification	A3		N2	
Temperature [K]	Heat balance [W]	Braids [W]	Heat balance [W]	Braids [W]
1.9 K	0.72	=	0.34	=
4.5-20 K	3.01	2.21	3.26	2.30
50-75 K	16.8	20.5	17.1	20.2

The heat leaks to 4.5-20 K and 1.9 K strongly depend on the temperatures of the support post flanges (figures II-3.18 and II-3.19). If the temperature of the flange linked to line C increases from 5 K to 10 K the heat leak to the cold mass is a factor 4 higher. In the heat leak to the 50-75 K level (figure II-3.20) radiation from the vacuum vessel to each support post account for about 2.5 W and can be lowered to a negligible value by wrapping a reflective aluminium foil around the glass fiber-epoxy composite column [88].

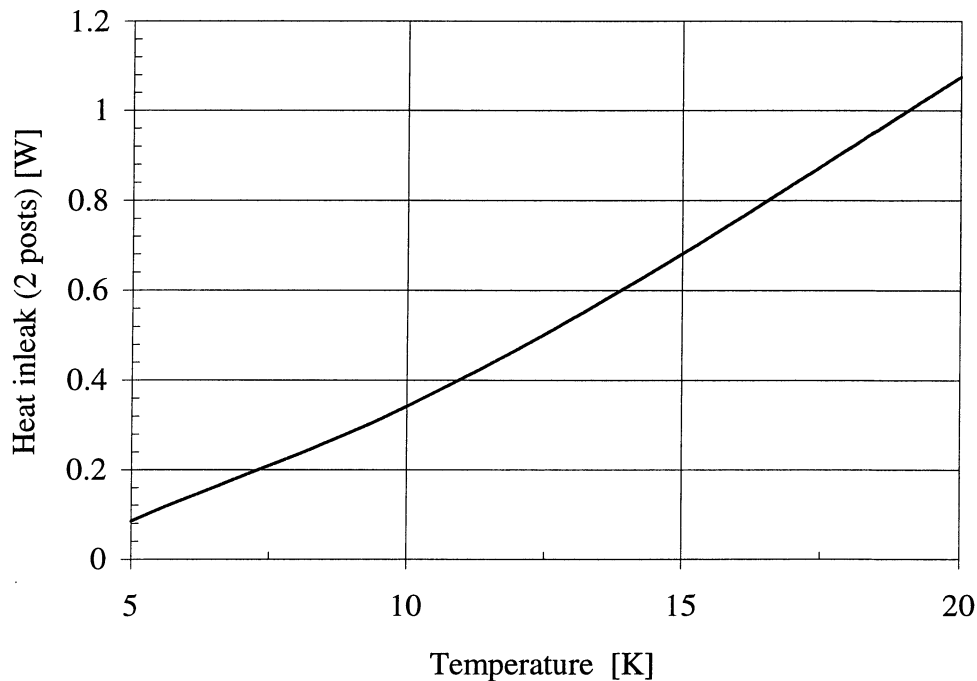


Figure II-3.18: Calculated heat leak at 1.9 K versus the temperature of the flange cooled by line C

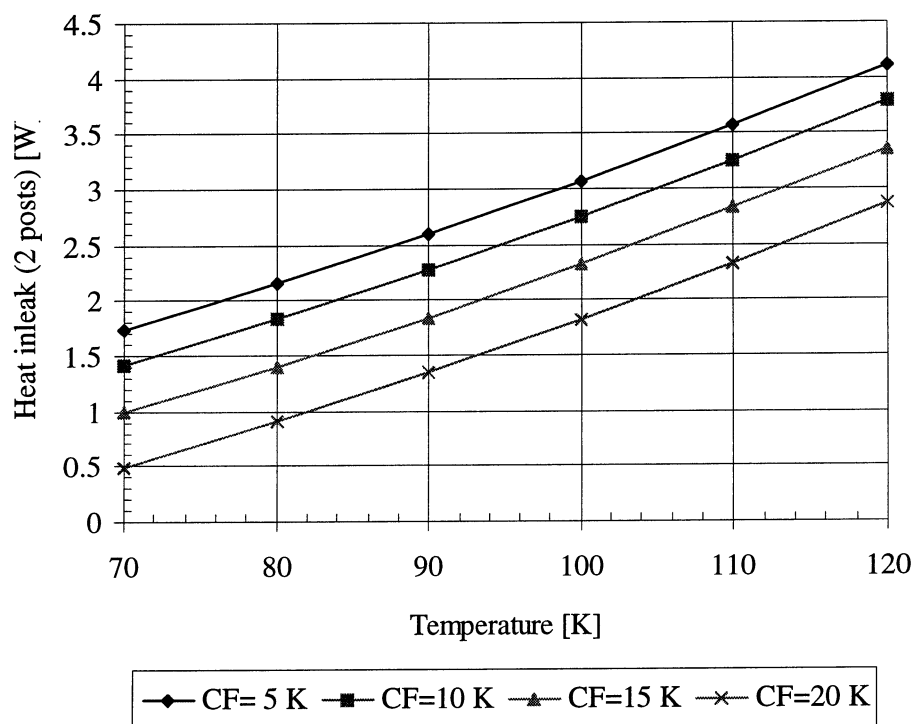


Figure II-3.19: Calculated heat inleak at 4.5-20 K versus the temperature of the flange cooled by line E (CF=temperature of the flange cooled by line C)

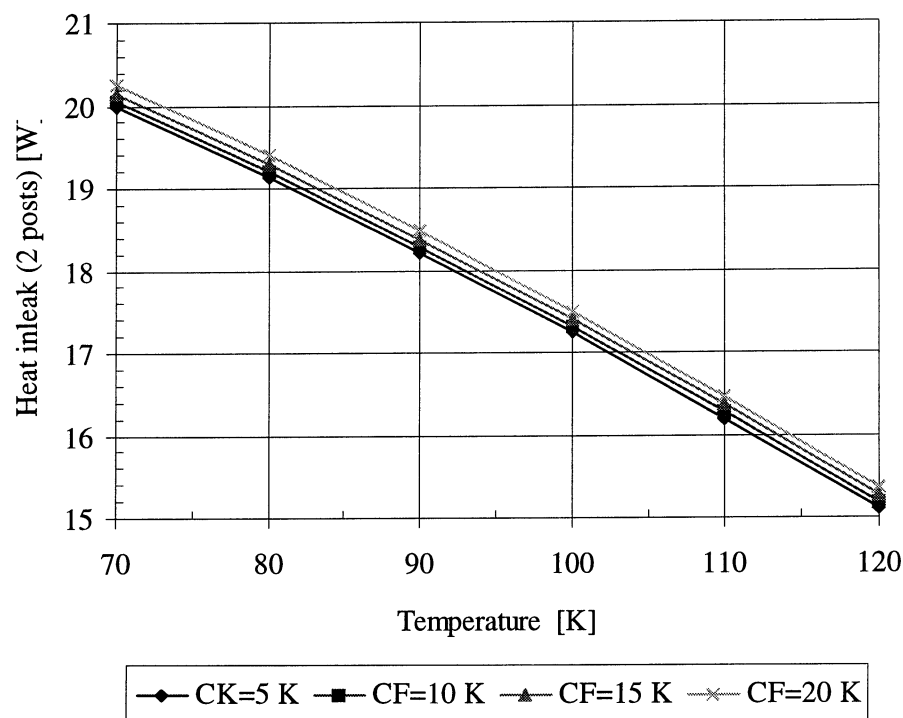


Figure II-3.20: Calculated heat inleak at 50-75 K versus the temperature of the flange cooled by line E (CF=temperature of the flange cooled by line C)

From the measurements on the prototype dipole N2 the thermal gradients through the intermediate flanges result to be 1.6 K at 4.5-20 K and 4.4 K at 50-75 K. Imposing heat inleaks of 1.5 W per post at 4.5-20 K and 10 W at 50-75 K, the estimated temperature difference across the flanges were 1.05 K at 4.5-20 K and 4.6 K at 50-75 K confirming thus the measured data.

A summary of the measurements performed in several prototype magnet cryostats is shown in table II-3.14.

Table II-3.14: Summary of measurements on prototype cryostats

Heat interception		Cooling line [K]	Flange [K]	Temperature difference [K]
4.5-20 K	A1	4.5	23*	18.5*
	A2	4.5	18*	13.5*
	N1	4.5	10	5.5
	A3	4.5	16	11.5
	N2	4.5	9.4	4.9
	CTM	7	13	6
	String quadrupole	6	12	6
50-75 K	A1	85	130*	45*
	A2	85	125*	40*
	N1	75	98	23
	A3	75	115	40
	N2	75	110	35
	CTM	50	82	32
	String quadrupole	85	102	17

* instrumentation wires non properly thermalised

The temperature differences at 50-75 K and 4.5-20 K across the copper braids can be lowered by increasing their cross-sections. The thermal impedance between line C and the support posts, even in the best case (5-6 K), does not guarantee heat inleak to the 1.9 K within the budgeted value.

The large spread in the results presented in table II-3.14 is mainly due to the non-reliability of bolted contacts. They depend of many parameters (e.g., force applied, pressure, material, surface roughness, temperature) which are hardly controllable and as a consequence they do not represent an adequate solution for the future LHC cryostats.

3.2.2 Prototype magnet thermal shield

The thermal shield (AA-1100) is cooled by line F made of an extruded aluminum profile and forming an integral part of the bottom tray. The circular upper shell is divided into four longitudinal sections and the bottom tray into 2 longitudinal parts. The upper parts are clipped to the bottom tray and are then tack-welded to provide a continuous thermal path azimuthally. Thermometer sensors (figure II-3.21) located on different sections of the thermal shield permitted to investigate the azimuthal and the

longitudinal temperature profiles and the thermal impedance between the cooling pipe and the thermal shield.

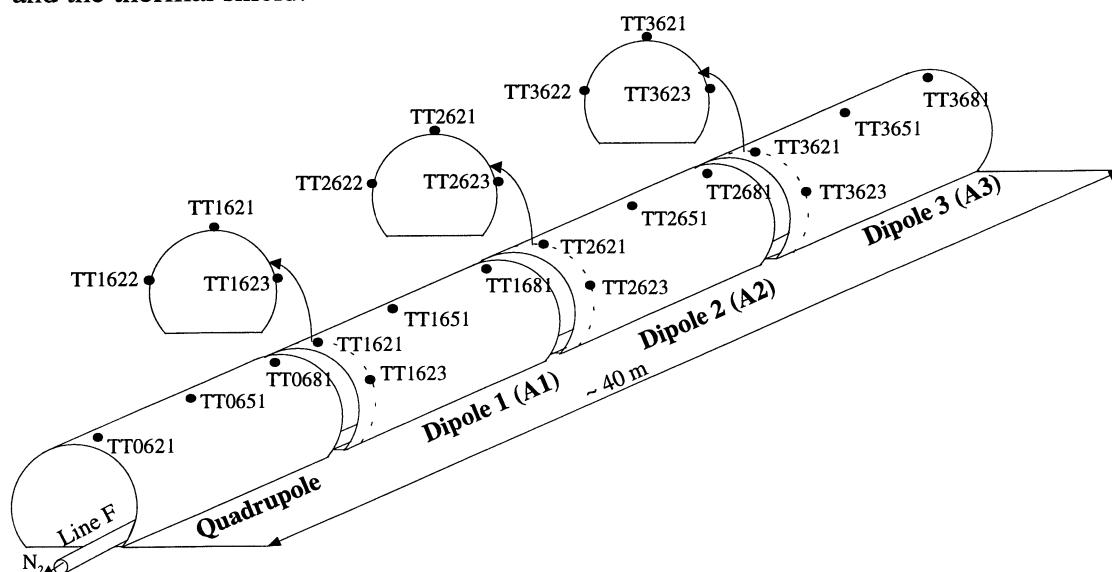


Figure II-3.21: Instrumentation scheme of the thermal shield of the LHC prototype magnet String (Run 2)

Table II-3.15: Measured temperatures on the thermal shield

SRB	Line F inlet	88.5 K
A3	TT3681	91.1 K
	TT3651	89.9 K
	TT3621	92.4 K
	TT3622	91.7 K
	TT3623	91.1 K
A2	TT2681	92.6 K
	TT2651	91.7 K
	TT2621	94.3 K
	TT2622	93.5 K
	TT2623	92.1 K
A1	TT1681	92.1 K
	TT1651	91.2 K
	TT1621	93.3 K
	TT1622	92.6 K
	TT1623	91.8 K
String quadrupole	TT0681	90.7 K
	TT0651	89.3 K
	TT0621	90.8 K
SFB	Line F outlet	92.0 K

Measurements from the LHC prototype string (table II-3.15) show that the longitudinal (over 40 m) and the azimuthal temperature differences are lower than 3 K. The thermal contact between the shield and line F performs well since the maximum temperature difference between the shield and line F is only 5 K which gives a thermal impedance of $4 \text{ K}\cdot\text{m}^2/\text{W}$ for a measured heat flux to the thermal shield of $1.2 \text{ W}/\text{m}^2$. Measurements from the CTM and single magnet tests confirmed the above results.

3.2.3 Prototype magnet vacuum barrier

In the extended version of the string test two vacuum barriers were installed: one made of stainless steel, located in the short straight section and the other one, in non-metallic composite material, placed in the SRB. In order to reduce heat leak at 1.9 K, conduction and radiation are intercepted by line E at 50-75 K. In the stainless steel vacuum barrier the heat sink is made of a copper ring ($A=120 \text{ mm}^2$; $l=3 \text{ m}$) brazed on the outer edge of the off-centered disk (see Part 1 - Chapter 3), while in the composite vacuum barrier copper braids ($A=129 \text{ mm}^2$; $l=3.05 \text{ m}$) replace the copper ring. Thermometer sensors (figure II-3.22) have been mounted on both vacuum barriers in order to evaluate the thermal contact to line E and the maximum temperature difference in the disk linked to the cooling pipe.

The measured temperatures (table II-3.16) were higher than those expected. The average temperature difference between the vacuum barrier and line E is about 32 K and the maximum average temperature difference in the heat intercept is 19 K. The estimated heat flux to line E is about 5 W and the thermal impedance between the vacuum barrier and line E results to be $1.6 \text{ K}/\text{W}$. The thermal contact needs improvement and the maximum temperature difference may be lowered by increasing the copper cross-section. Considering a heat interception at 120 K, the calculated heat leak at 1.9 K is 1.5 W which is a factor 2.5 higher than the budgeted value.

Table II-3.16: Measured temperature on the vacuum barrier heat intercepts

	Line E	85.5 K
Stainless steel vacuum barrier	Heat intercept: line E side	117.4 K
	Heat intercept: line E opposite side	138.5 K
	Line E	88.5 K
Composite vacuum barrier	Heat intercept: line E side	120.2 K
	Heat intercept: line E opposite side	137.8 K

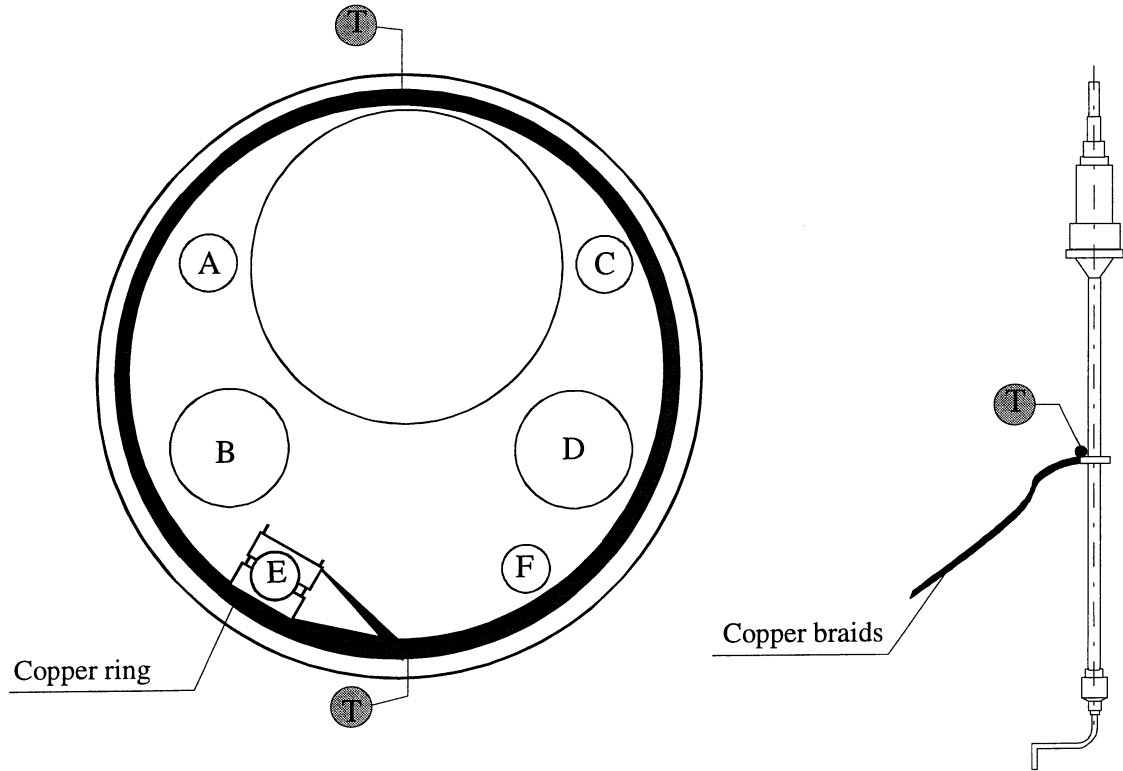
3.2.2 Prototype cryogenic valves

The cryogenic valves situated in the cryogenic service module of the short straight section are thermalized to line E. The valve body is linked to the cooling line by means of brazed copper braids ($0.002 \times 0.2 \times 0.27$).

The quality of the thermal contact is evaluated by measuring the temperature of the valve body at the thermalisation section. The measured temperature difference, about 20 K, takes into account the thermal contact between line E and the braids, conduction along the braids and the thermal contact between the braids and the valve.

Table II-3.17: Measured temperatures on the valve heat intercepts

Line E	85.5 K
Valve TCV2	106.2 K
Valve CFV	103.7 K
Valve TCV1	102.6 K



a) Vacuum Barrier (stainless steel version)

b) Cryogenic valve

Figure II-3.22: Temperature sensors on vacuum barrier and cryogenic valves

CHAPTER 4

Potential of an actively cooled screen at 4.5-20 K

The residual heat inleak from the thermal shield at 75 K to the cold mass represents the largest contribution to the thermal budget of the cryostats at 1.9 K [4]. The insulation system at 4.5-20 K of the prototype magnet cryostats is constituted of multilayer reflective insulation (“floating” system). The thermal performance of multilayer reflective insulation systems at low boundary temperature have already been investigated on representative samples and geometries, and measurements confirmed that multilayer insulation system [37] represent a great advantage over single reflective surfaces in case of degraded insulation vacuum [43, 89].

In order to lower the heat inleak at 1.9 K, the possibility of inserting an actively cooled screen, as an alternative solution to the “floating” insulation system, has been envisaged. The actively cooled screen, made of aluminum, can be cooled at 4.5-20 K by line C’. It is not self-supported (“soft” screen) and leans on the cold mass through net-type insulating spacers [90, 91].

In this chapter the potential of different configurations of an actively cooled “soft” screen at 4.5-20 K is presented and the results are compared to the “floating” solution

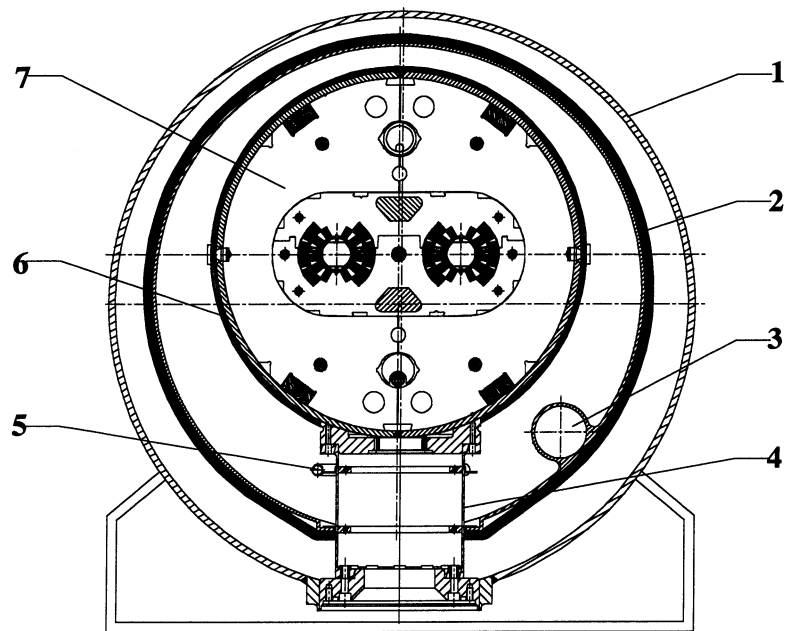
A program to qualify the thermal contact between screen and cooling line has been undertaken and a dedicated cryostat has been developed. Different samples have been tested at 4.5-20 K and 50-75 K and the measurements of thermal impedance are presented.

4.1 Actively cooled screen at 4.5-20 K

In the prototype magnet cryostat [see figure I-3.1, page 16] the residual heat inleak from the thermal shield is shared between the cold mass and the cryogenic lines A, B, C and D. Due to the large surface area, the cold mass receives about 70% of the above heat inleak which represents 40 % of the total heat inleak at 1.9 K.

In the LHC cryostats (figure II-4.1), 95% of the heat from the thermal shield reaches the cold mass (figure II-4.2) and consequently its contribution to the total heat inleak increases to 60%.

Depending on the thermal contact to the cooling pipe and the thermal insulation to the cold mass an actively soft screen at 4.5-20 K may perform better than a floating insulation system.



- | | |
|-------------------------|--------------------------|
| 1. Vacuum vessel | 5. Line C (4.5 K supply) |
| 2. Thermal shield | 6. Radiative insulation |
| 3. Line E (50 K supply) | 7. Cold mass |
| 4. Support post | |

Figure II-4.1: LHC dipole cryostat, reference design

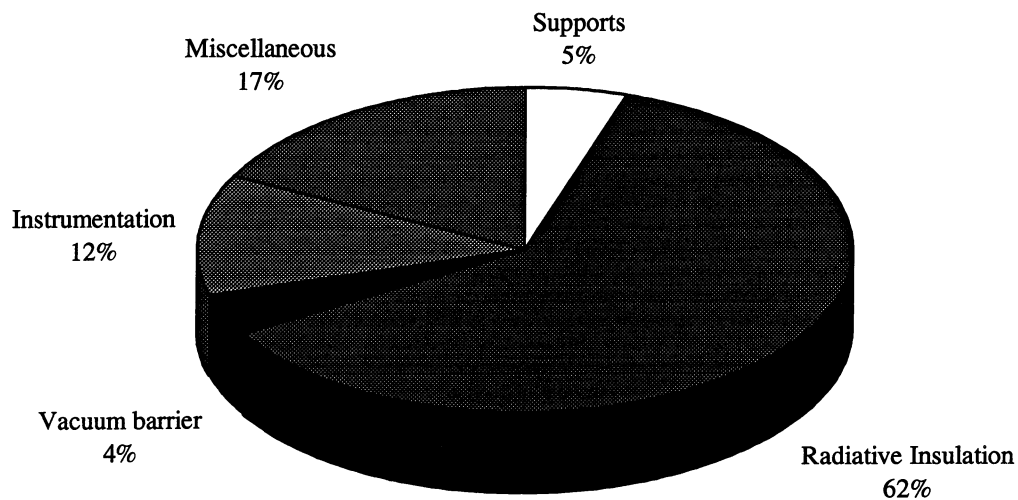
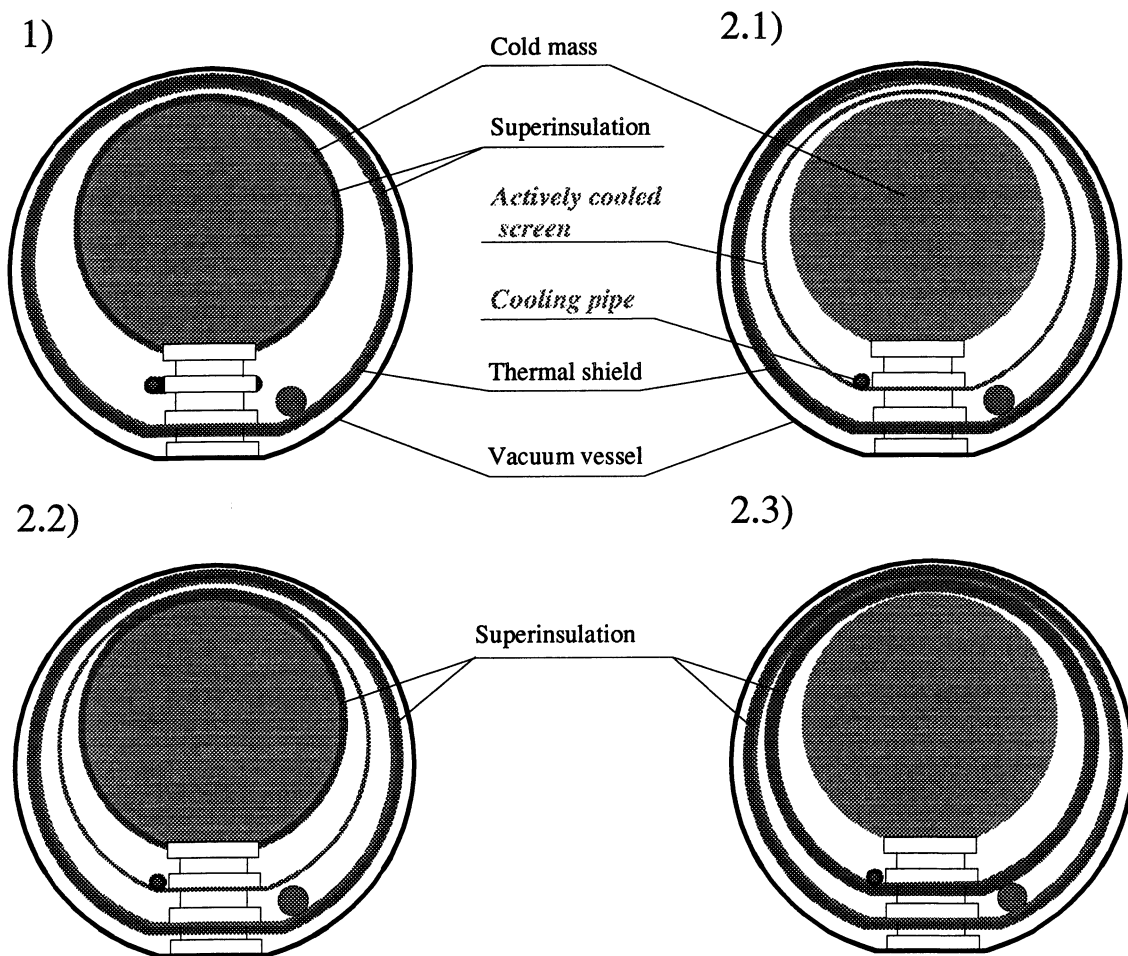


Figure II-4.2: Heat inleak at 1.9 K [4]

4.1.1 Thermal design

The principle schemes for floating and thermalized multilayer systems are shown in figure II-4.3. According to the position of the multilayer insulation different configurations of thermalised system are envisaged (2.1, 2.2, 2.3). In cases 2.1 and 2.3 the cold mass is covered with 1 aluminum foil in order to lower its emissivity. From 77 K to 4.2 K the emissivity of stainless steel (as found) is about 0.12, while that of one aluminum reflective foil is around 0.01. This means that by wrapping one aluminum foil around the cold mass radiation heat from 77 K to 4.2 K can be reduced by a factor 10.



Case 1: Reference design

Case 2.1: MLI on the thermal shield

Case 2.2: MLI on the thermal shield and cold mass

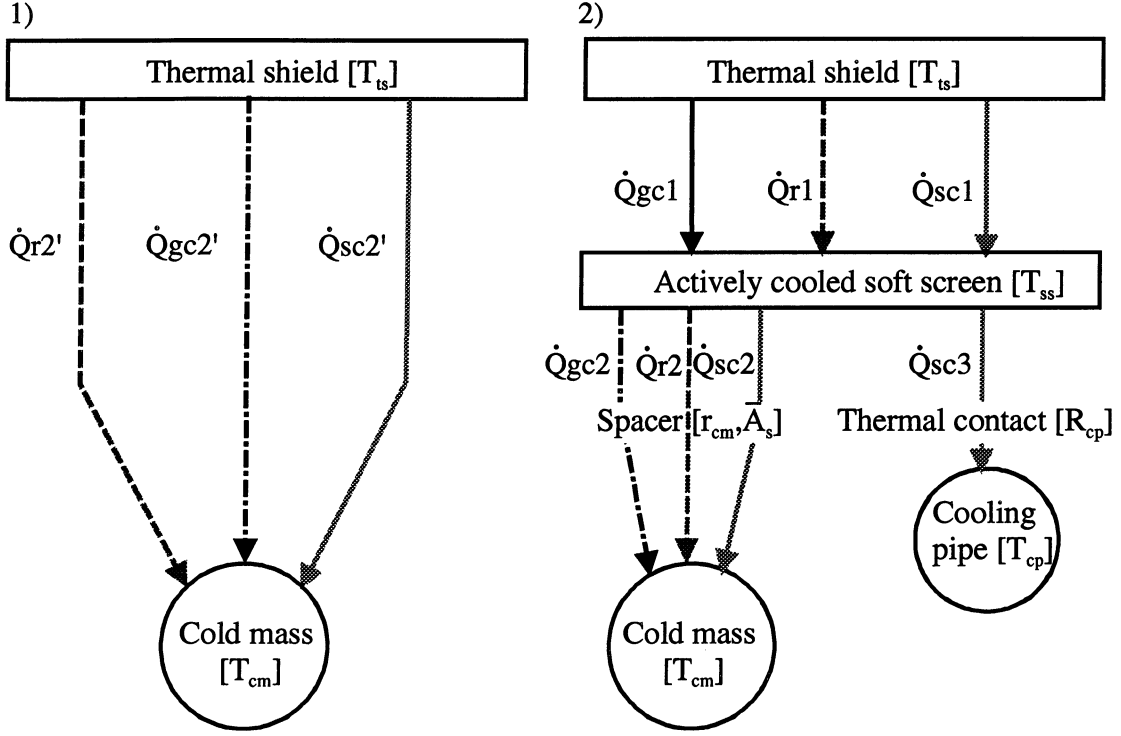
Case 2.3: MLI on the thermal shield and actively cooled screen

Figure II-4.3: Principle schemes for “floating” (1) and “thermalised” (2) multilayer systems

The thermal network of the “floating” and thermalised superinsulation systems is represented in figure II-4.4.

In the “floating” version the distributed heat leak to the cold mass (\dot{Q}'_{cm}) is represented by the heat flux through multilayer insulation which is the combination of solid conduction ($\dot{Q}_{sc2'}$), residual gas conduction ($\dot{Q}_{gs2'}$) and radiation ($\dot{Q}_{r2'}$).

$$\dot{Q}'_{cm} = \dot{Q}_{gc2'} + \dot{Q}_{r2'} + \dot{Q}_{sc2'} \quad (\text{II-4.1})$$



Heat transfer processes

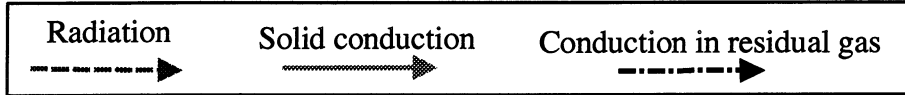


Figure II-4.4: Thermal network of “floating” and thermalised multilayer systems

In the thermalized case the actively cooled soft screen receives heat (\dot{Q}_{ss}) from the thermal shield by solid conduction (\dot{Q}_{sc1}), residual gas conduction (\dot{Q}_{gs1}) and radiation (\dot{Q}_{r1}). From the soft screen heat flows to the thermalisation pipe (at 5 K) by solid conduction (\dot{Q}_{cp}) and to the cold mass (\dot{Q}_{cm}) by solid conduction through the spacers (\dot{Q}_{sc2}), residual gas conduction (\dot{Q}_{gc2}) and radiation (\dot{Q}_{r2}).

$$\dot{Q}_{ss} = \dot{Q}_{gc1} + \dot{Q}_{r1} + \dot{Q}_{sc1} \quad (\text{II-4.2})$$

$$\dot{Q}_{cp} = \dot{Q}_{sc3} \quad (\text{II-4.3})$$

$$\dot{Q}_{cm} = \dot{Q}_{gc2} + \dot{Q}_{r2} + \dot{Q}_{sc2} \quad (\text{II-4.4})$$

Solid conduction, residual gas conduction and radiation are expressed respectively by Fourier's law, Kennard's law and Boltzmann's law.

The steady-state heat balance equation applied to the actively cooled soft screen yields:

$$\dot{Q}_{ss} = \dot{Q}_{cm} + \dot{Q}_{cp} \quad (\text{II-4.5})$$

Heat inleak at 1.9 K depends on the soft screen temperature and on the thermal impedance between the soft screen and the cold mass:

$$\dot{Q}_{cm} = \frac{T_{ss} - T_{cm}}{R_{cm}} \quad \text{with} \quad R_{cm} = \frac{r_{cm}}{A_s} \quad (\text{II-4.6})$$

$$\dot{Q}_{cp} = \frac{T_{ss} - T_{cp}}{R_{cp}} \quad (\text{II-4.7})$$

Low residual heat flux to the cold mass can be attained if the thermal contact between the screen and the cooling pipe performs well (R_{cp} small) and if the cold mass is well insulated from the screen (r_{cm} large)

4.1.2 Potential of a thermalised multilayer insulation system

Applying the mathematical model presented above to a 15-m long LHC dipole cryostat, we can find the range of values of R_{cp} and r_{cm} for which a thermalised system performs better than "floating" multilayer insulation. Considering cases 2.1 and 2.2 and assuming an emissivity of the soft screen of 0.05 in the 5 to 30 K range we can firstly define the variation of the thermal impedance (R_{ss}) between the thermal shield and the soft screen as a function of the soft screen temperature.

$$R_{ss} = \frac{T_{ts} - T_{ss}}{\dot{Q}_{ss}} \quad (\text{II-4.8})$$

Figure II-4.5 shows the thermal impedance R_{ss} does not change significantly if the soft screen temperature increases from 5 K to 30 K. At 10^{-4} Pa the heat inleak from the thermal shield to the soft screen is about 2.8 W and is not very sensitive to the lower temperature.

By knowing R_{ss} we can calculate the break-even lines by comparison with 10 layers of type B MLI, which presently equip the LHC prototype cryomagnets and constitute the reference solution. The surface covered by the spacers has been considered equivalent to 25% of the total cold mass area.

Figure II-4.6 shows that the thermalized version has lower heat inleak at 1.9 K if the design point of the two thermal impedances, R_{cp} and r_{cm} , is placed in the region above the break-even lines.

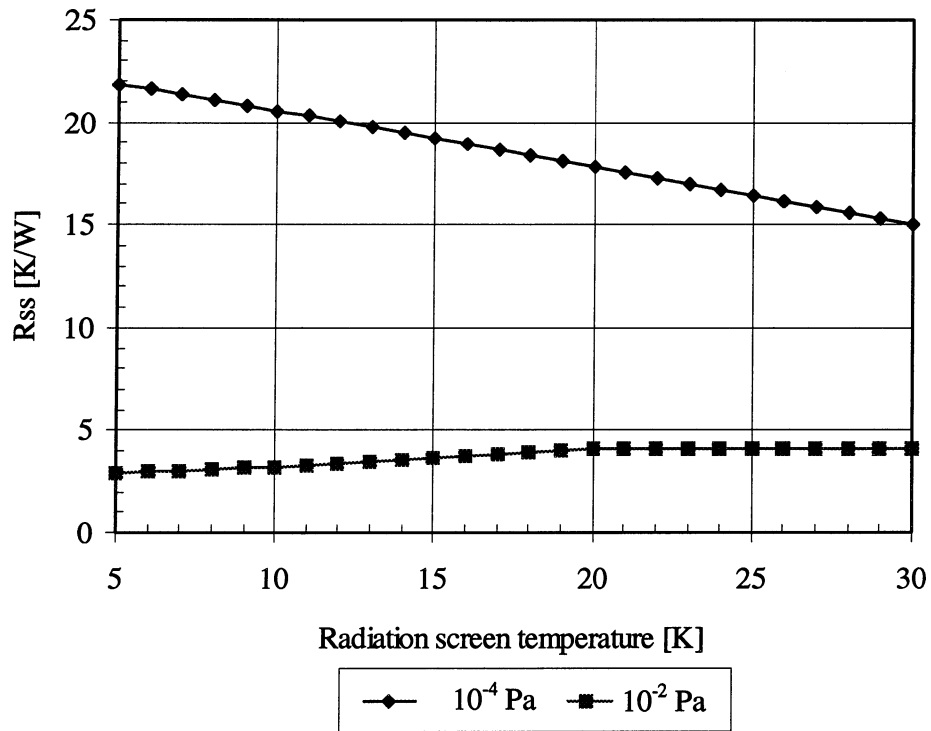


Figure II-4.5: Thermal impedance between the thermal shield and the soft screen

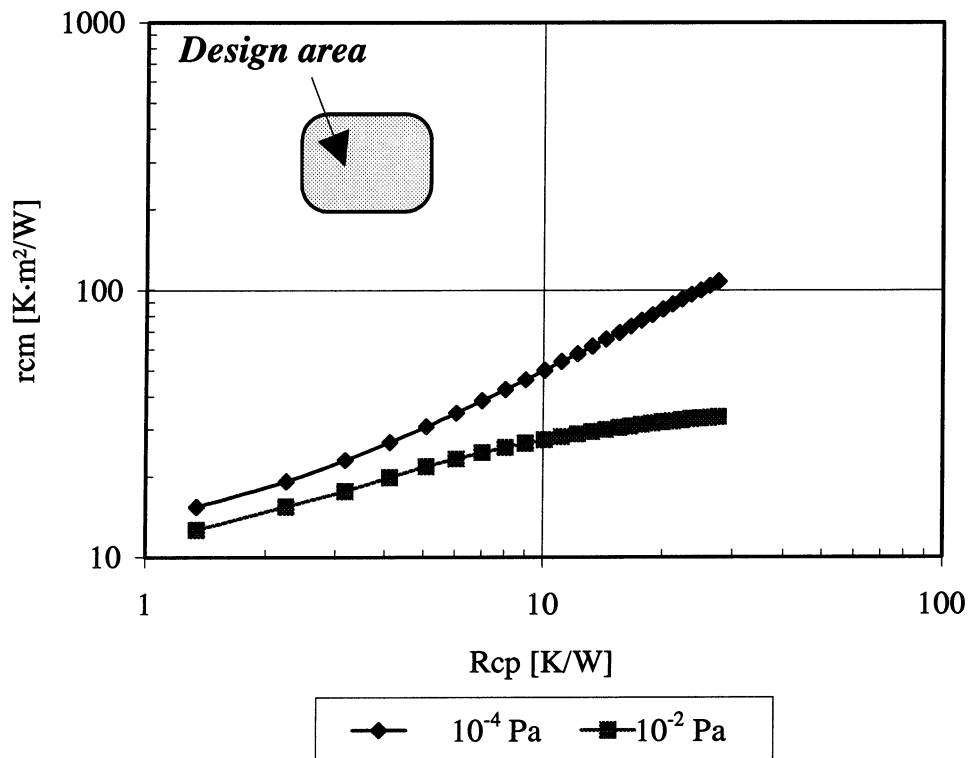


Figure II-4.6: Break-even lines for thermalized versus "floating" systems, in terms of R_{cp} and r_{cm}

4.1.3 Thermal contact to cooling pipe and net-type insulating spacers

A dedicated experiment has been performed to measure the impedance of thermal contacts which is representative for the heat intercepts to be implemented in large numbers in LHC cryostats.

The thermal contact between a stainless steel tube and an aluminium sleeve shrink-fitted on it has been tested at different temperatures and performs as follows: 1.2 ± 0.1 K/W at 4.5 K and 0.5 ± 0.05 K/W at 20 K. Measurements and results obtained from different samples are presented in detail in the next chapter.

A specific experiment (figure II-4.7) has been developed to measure, by means of a heatmeter, the heat flux between two circular aluminium plates separated by spacers. The cold plate temperature is at 2 K and that of the warm plate, which simulates the soft screen, can be varied from 10 K to 30 K.

The insulating spacers considered in this study consist of a set of piled-up nets of non-metallic, low-thermal conductivity materials which provide support at low residual heat flux. Different types of nets are alternatively inserted to avoid large contact area due to accidental superposition.

At liquid helium temperature and under good insulation vacuum, the most significant heat transfer process through the spacers occurs by conduction. A mathematical model [92, 93] has been developed in order to estimate the heat flux from calculated thermal impedances and solid conduction.

In the test set-up, the variation of the compressive pressure between the two plates is attained by adding weight on the top of the warm plate. In this fashion, the compressive pressure can be increased from 40 Pa to 331 Pa. The spacers are made of a combination of two types of glass fiber nets (N1 and N2) from industry. N1 has a 10x10 net grid with a thread thickness of 1 mm. N2 has a 6x6 net grid with a thread thickness of 0.5 mm.

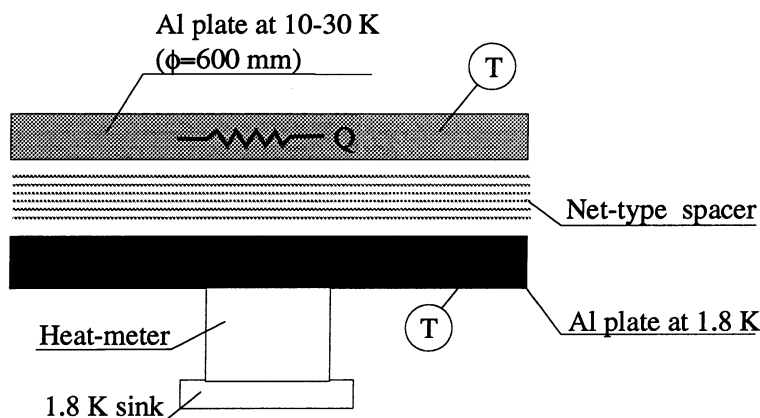


Figure II-4.7: *Experimental measurements of thermal impedance of net-type insulating spacers under variable applied pressure [94, 95]*

For 1 mm thick aluminum alloy shield of diameter equal to 570 mm, leaning 40° on the cold mass, the pressure on the spacer is $P=238$ Pa. Considering three net-type spacers and a warm temperature of 15 K, the measured thermal impedance at 10^{-4} Pa is $482 \text{ K}\cdot\text{m}^2/\text{W}$.

4.1.4 Comparison of thermal performance

Considering a thermal contact resistance of 4 K/W which corresponds to a thermal contact over 30% of length of 15-m soft screen at about 12 K, and an insulator spacer thermal impedance of 482 K·m²/W at 10⁻⁴ Pa we can calculate the variation of heat inleak at 1.9 K as a function of residual gas pressure for the three different cases of interest. The change of thermal resistance R_{cm} and soft screen temperature (figure II-4.8) with insulation vacuum have been evaluated.

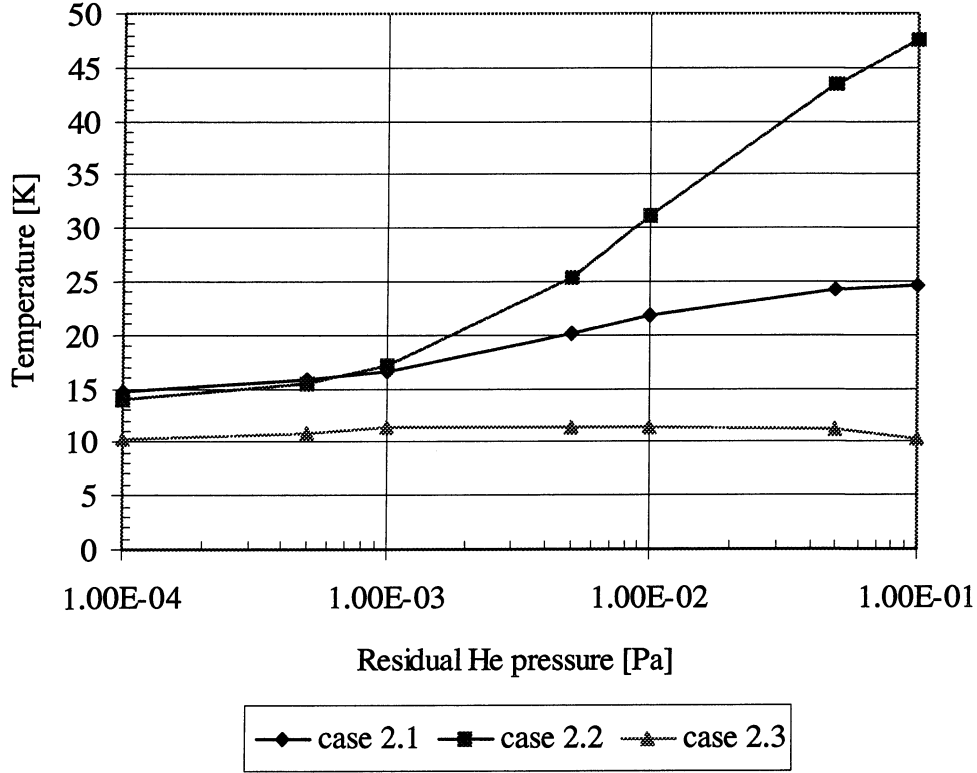


Figure II-4.8: Temperature of the screen at 4.5-20 K versus residual helium pressure ($R_{cp}=4$ K/W; $r_{cm}=482$ K·m²/W at 10⁻⁴ Pa)

The multilayer insulation wrapped over the screen at 4.5-20 K (case 2.3) reduces the heat inleak at 4.5-20 K decreasing thus the soft screen temperature. In this configuration the soft screen temperature decreases with increasing residual gas pressure since the heat inleak to line C decreases (in other words, the heat inleak to the cold mass increases more rapidly with pressure than the heat inleak to the soft screen).

In case 2.2 the screen temperature is very sensitive to the quality of the insulation vacuum, as the superinsulation preserves low heat inleak at 1.9 K. In this case in order to satisfy the heat balance equation the soft screen temperature must increase. As the residual pressure grows from 10⁻⁴ Pa to 10⁻¹ Pa the soft screen temperature increases from 14 K to 48 K.

By knowing the soft screen temperature for different values of insulation vacuum we can calculate the heat inleak at 1.9 K and compare it to the performance of the reference solution (figure II-4.9).

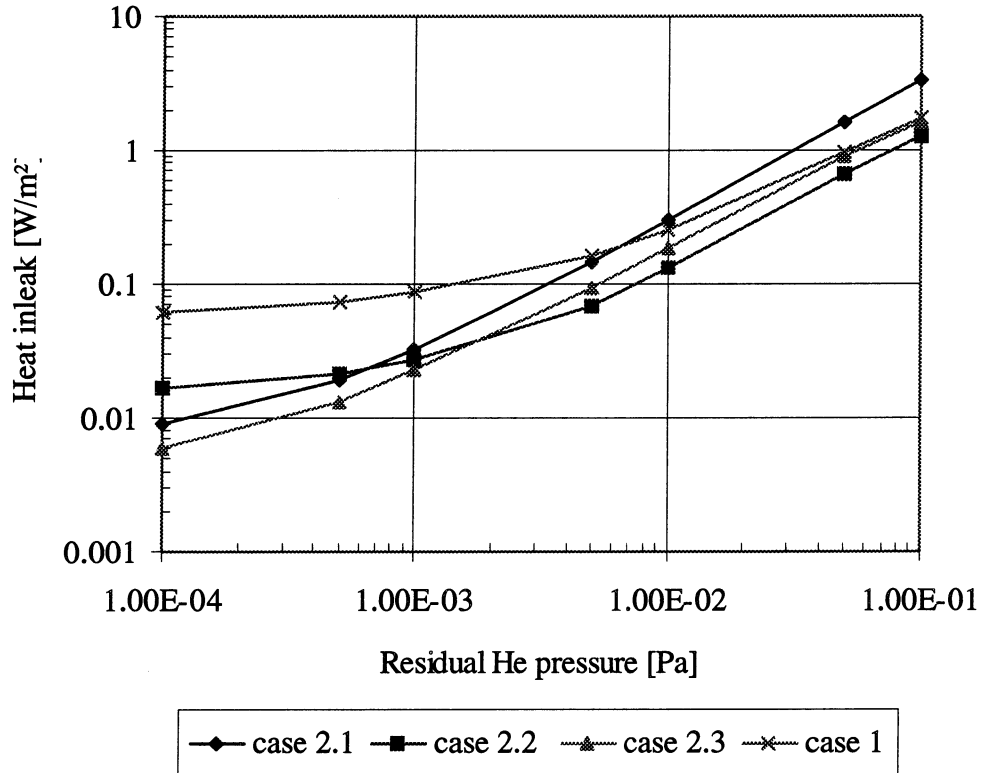


Figure II-4.9: Comparison of heat inleak at 1.9 K between “floating” and thermalized systems ($R_{cp}=4$ K/W; $r_{cm}=482$ K·m²/W at 10^{-4} Pa)

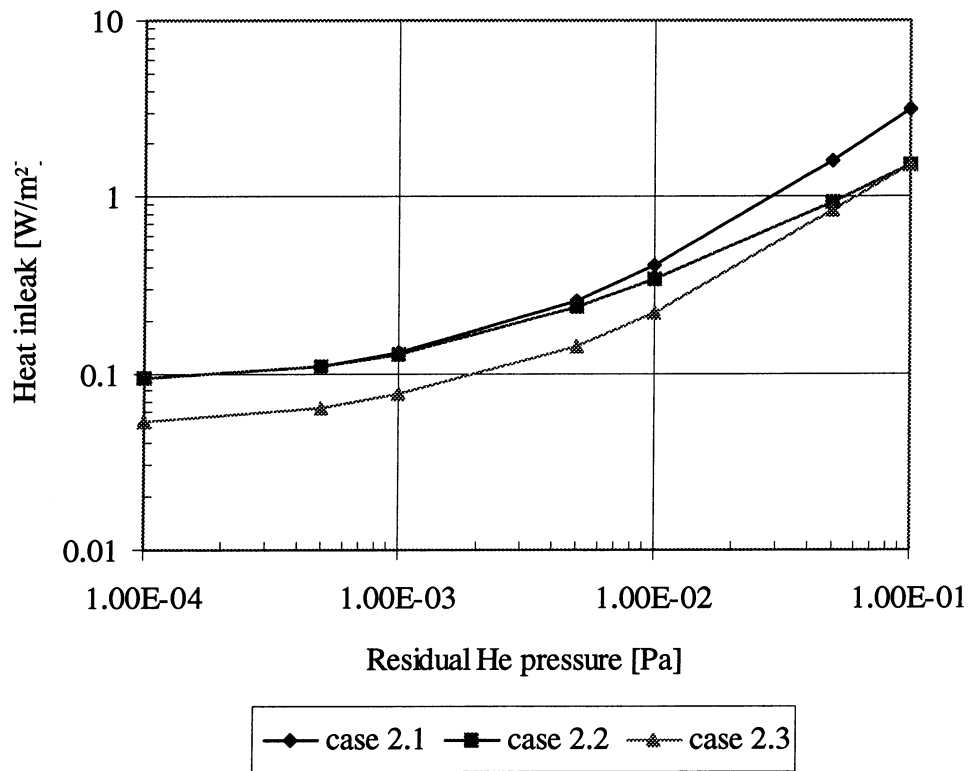


Figure II-4.10: Heat inleak at 4.5-20 K versus residual helium pressure ($R_{cp}=4$ K/W; $r_{cm}=482$ K·m²/W at 10^{-4} Pa)

Under nominal steady-state conditions the thermalized system has always lower residual heat flux at 1.9 K. Case 2.2 corresponding to the cold mass wound with 10 layers of multilayer reflective insulation, shows the lowest heat leak at 1.9 K since the temperature difference through the spacer is smaller than in the other cases. If the cold mass is only wrapped with one aluminum foil (case 2.1) the heat flux to 1.9 K is higher than that of the reference solution for residual gas pressure above $5 \cdot 10^{-3}$ Pa.

The thermalized system increases the heat leak at 4.5-20 K (figure II-4.10) in comparison with the “floating” system, specially in the case 2.2 due the higher soft screen temperature. The evolution of the heat leak at 4.5-20 K mirrors that of the soft screen temperature behaviour. Results of heat leaks at 1.9 K and 4.5-20 K for cases 1 and 2 and for a 15-m long LHC dipole cryostat are summarised in table II-4.1.

Table II-4. 1: Heat leaks under steady-state conditions (15-m dipole)

Residual He	Cold mass				Screen at 4.5-20 K		
Pressure	Case 2.1	Case 2.2	Case 2.3	Case 1	Case 2.1	Case 2.2	Case 2.3
[Pa]	[W]	[W]	[W]	[W]	[W]	[W]	[W]
10^{-4}	0.24	0.44	0.16	1.66	2.82	2.83	1.62
10^{-3}	0.86	0.74	0.61	2.37	3.91	3.88	2.31
10^{-2}	8.10	3.51	4.96	6.88	12.42	10.19	6.70
10^{-1}	88.38	34.45	44.06	46.63	93.45	45.23	45.54

At 10^{-4} Pa the residual heat flux to the cold mass as low as 15 mW/m^2 can be in principle achieved, thus resulting in a 4-fold reduction with respect to the reference solution. The total heat load at 4.5-20 K is mainly due to the dynamic heat load and as a consequence the corresponding increase of heat leak at 4.5-20 K with respect to the reference solution appears negligible.

A particular case of this study may be represented by a self-supporting screen at 4.5-20 K which is not in contact with the cold mass. In such a case the conducting thermal impedance between the soft screen and the cold mass (spacers) can be considered infinite and the only heat transfer processes involved are radiation and conduction in residual gas. We can calculate the heat leak at 1.9 K assuming the same thermal impedance to line C as above (4 K/W for 15-m long LHC dipole cryostat). Considering cases 2.1 and 2.3, figure II-4.11 shows the heat flux to 1.9 K at 10^{-4} Pa could be reduced to 4 mW/m^2 . The heat leak to 4.5-20 K is about 2.8 W in case 2.1, 2.4 W in case 2.2 and 1.6 W in case 2.3.

At present an actively cooled screen has been mounted in two LHC prototype dipole cryostats. The screen is linked to line C by means of thermalisation braids and wrapped with 10 layers of type-C superinsulation (case 2.3). The thermal insulation between the screen and the cold mass is made by fiber glass plates.

The measured steady-state screen temperature was about 16 K at line C inlet section and 30 K on the opposite extremity. Line C was at about 4.5 K and the longitudinal screen temperature increase may be attributed both to bad heat intercept performance and higher heat leaks.

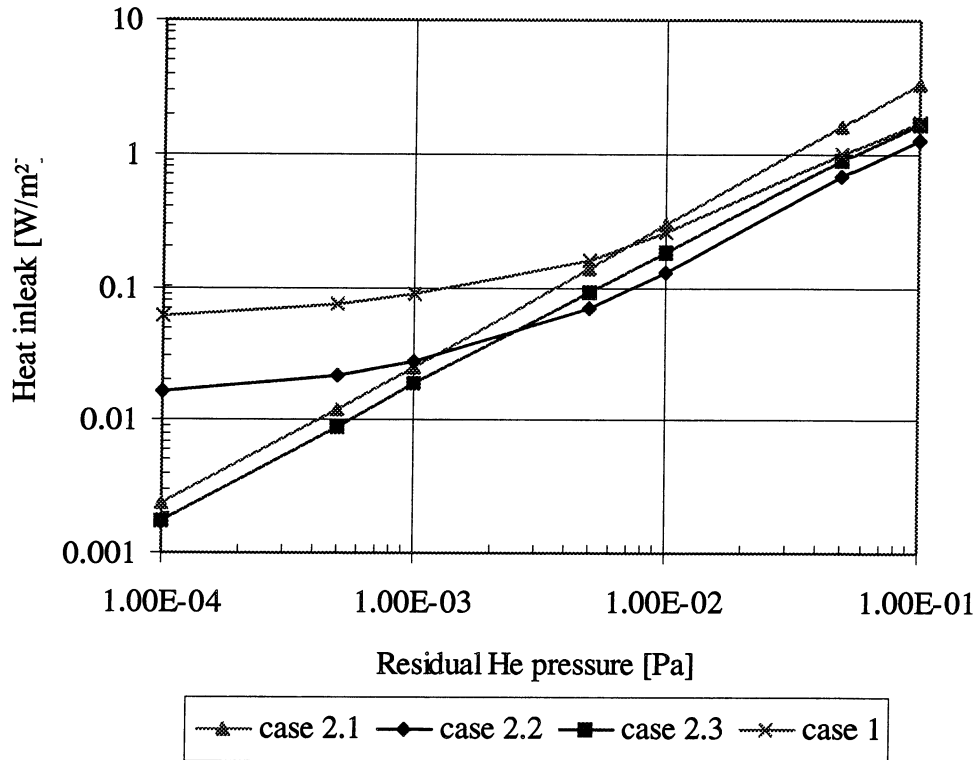


Figure II-4.11: Heat inleak at 1.9 K with “hard” screen at 4.5-20 K ($R_{cp}=4$ K/W; $r_{cm}=0$ at 10^{-4} Pa)

4.2 Improvement of thermal contacts

In this chapter a simple, reliable and cheap technical solution for heat intercepts at 4.5-20 K and 50-75 K is proposed. Samples with different materials and diameters have been tested in order to investigate the consequences on the thermal impedance. The dependence of thermal impedance on temperature and residual gas pressure has also been investigated.

4.2.1 Test set-up

The heat intercept is formed of a conducting sleeve (figure II-4.12) which is shrink-fitted onto a stainless steel tube. A filler cylinder is inserted inside the stainless-steel element in order to cool the sample uniformly and obtain the same flow velocity and thus the same heat transfer coefficient as in the LHC cryogenic lines.

The sleeve is connected to an isothermally heated block by means of either strips or braids to simulate cryostat heat inleaks.

A copper screen at 50-75 K covered with 20 layers of superinsulation intercepts radiation heat coming from ambient thus reducing the heat inleak to the sample to a negligible value.

Helium at 4.2 K and 1 bar is tapped from the phase separator to cool the screen and the test sample. The inlet temperature of the sample can be varied from 4.5 K to 150 K by increasing the electrical input on the heater \dot{Q} .

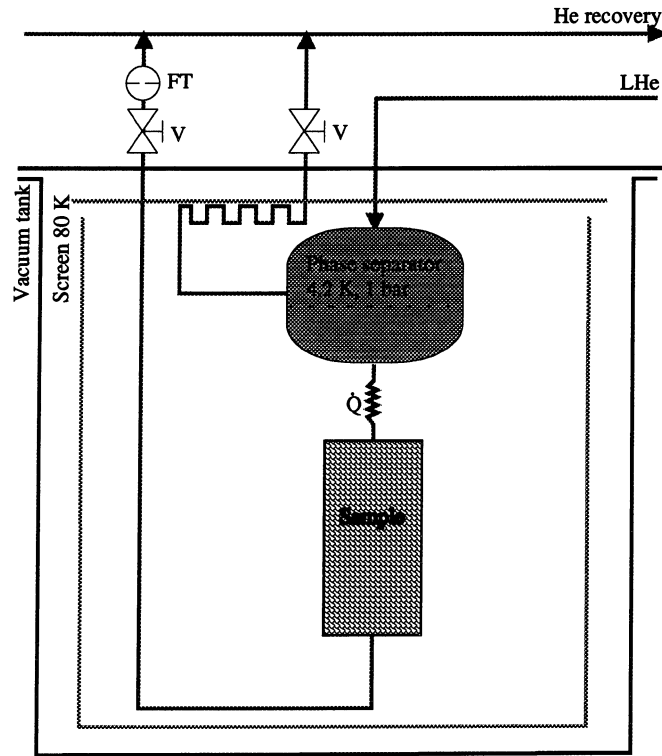


Figure II-4.12: Test set-up for measuring thermal impedance of thermal contacts

The characteristics and main dimensions of the different samples are summarised in table II-4.2. Materials, geometry and operational temperature define the differences between the samples.

Table II-4.2: Test program of the cryostat to measure the impedance of thermal contacts

Sample	Operational temperature	Stainless steel tube	Conducting sleeve		Connection between heater block and conducting sleeve		
	[K]	Diameter [mm]	Material	Diameter [mm]	Material	Type	Size [mm ³]
1	50-75	65/69	Al	69/80	Al	Strip	5x(30x3x200)
2	4.5-20	65/69	Al	69/80	Al	Strip	5x(30x3x200)
3	4.5-20	65/69	Cu	69/80	Cu	Strip	4x(30x3x210)
4	50-75	65/69	Cu	69/80	Cu	Strip	4x(30x3x210)
5	50-75	65/69	Al	69/80	Al	Braid	5x(30x6x200)
6	4.5-20	15/18	Al	18/29	Al	Strip	1x(200x1x5)

4.2.2 Instrumentation

Temperature sensors (figure II-4.13) placed at four different locations on the sample permit to measure the thermal impedance due to the contact between the stainless steel tube and the conducting sleeve. The thermal contact resistance due to the welding of the strips (or braids) on the sleeve and the thermal gradient across the strips are also measured.

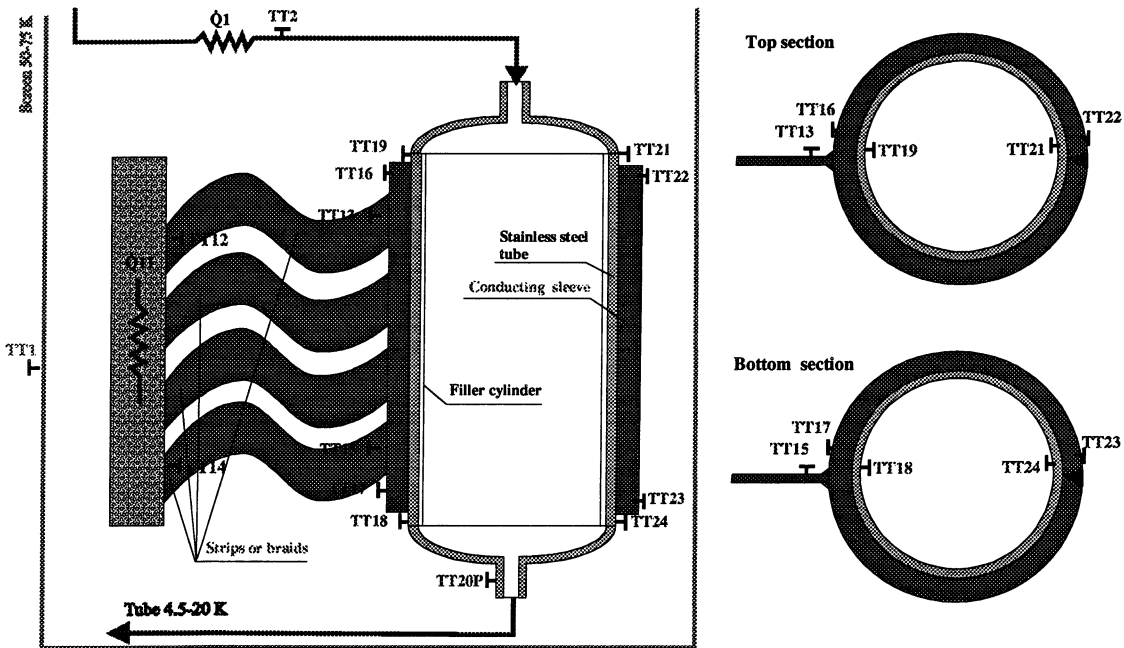


Figure II-4.13: *Experimental measurement of thermal impedance of thermal contacts*

For each sample, several tests have been performed by changing the helium temperature TT2 and the heating source \dot{Q}_{11} . Maintaining constant temperature TT2, the heat input \dot{Q}_{11} was varied from 0.5 W to 15 W. Following a change in setting of a parameter, steady-state conditions could be reached in less than 30 minutes as the heat capacity of the sample is small.

4.2.3 Results

For each sample the measurements of thermal impedance, under different operational conditions, are presented. The thermal impedance between the conducting strips (or braids) and the stainless steel tube has been evaluated from temperature measurements with a precision of $\pm 10\%$. In steady-state condition the insulation vacuum was maintained at 10^{-6} mbar.

Sample 1

All the tests showed that the thermal contact between the stainless tube and the conducting sleeve is higher on the helium inlet extremity (TT16-TT19) than on the opposite extremity (TT17-TT18). This may be attributed to longitudinal conduction in the sample. The thermal impedance slightly depends on helium temperature, as shown

in figure II-4.14. The temperature difference between the aluminum sleeve and the stainless steel tube showed, as expected, a linear dependence on electrical power \dot{Q}_{11} (figure II-4.15). The temperature difference (figure II-4.16) between the aluminum strips and the aluminum sleeve is comparable to that between the aluminum sleeve and the stainless steel tube. The temperature difference across the aluminum strips is a factor 8-9 higher than that between the strips and the sleeve.

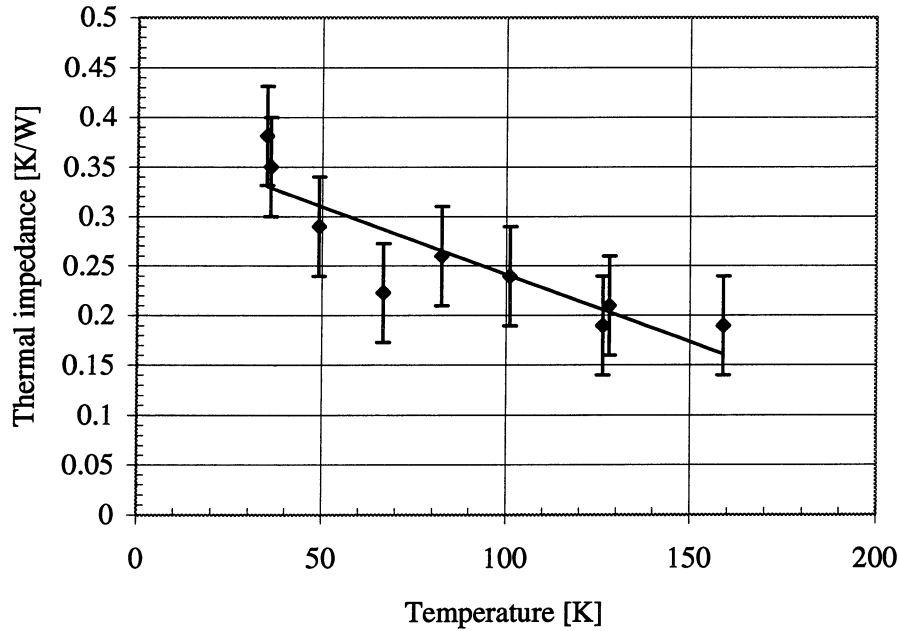


Figure II-4.14: Thermal impedance of the shrink-fitted contact versus helium temperature (sample 1)

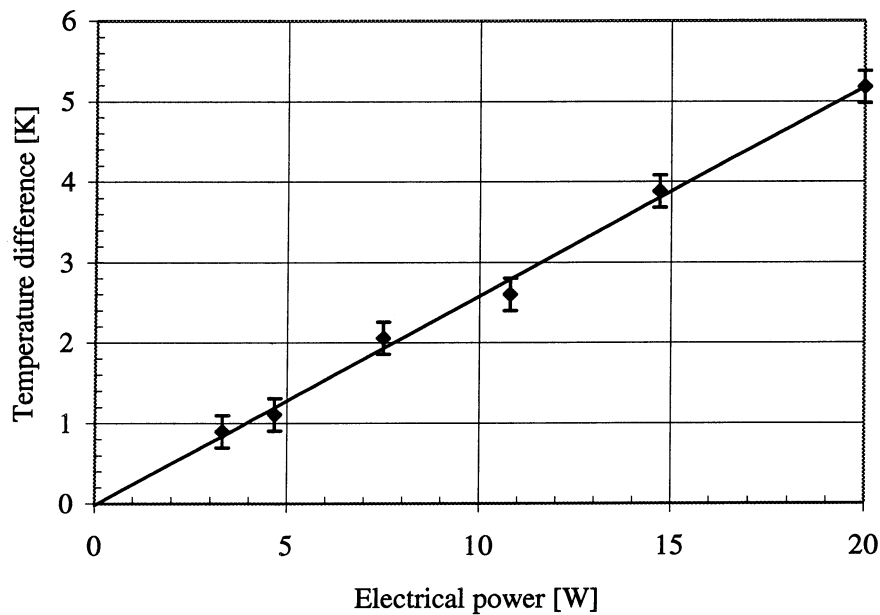


Figure II-4.15: Temperature difference across the shrink-fitted contact versus heating power (sample 1)

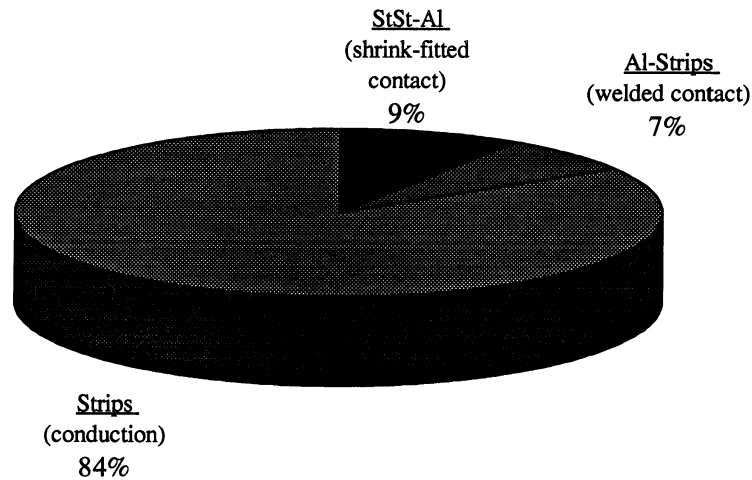


Figure II-4.16: Breakdown of thermal impedance (sample 1)

Sample 2

The thermal contact between the aluminum sleeve and the stainless steel tube measured on helium inlet side has the highest thermal impedance. Since the conduction heat coming from the strips is not equally distributed to the aluminum sleeve, the temperature differences (TT22-TT21) and (TT23-TT24) are lower than those on the strip side. The helium temperature was varied from 4.5 K to 20 K and the results of the thermal impedance between the sleeve and the tube are shown in figure II-4.17.

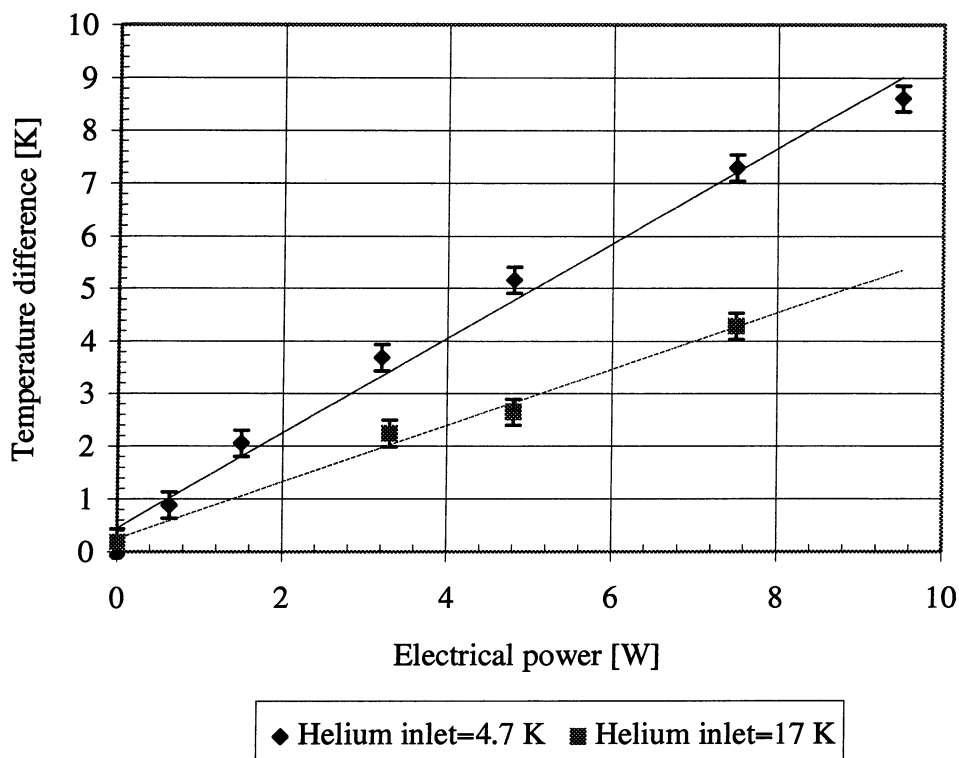


Figure II-4.17: Temperature difference across the shrink-fitted contact versus electrical power (sample 2)

The thermal impedance between the strips and the sleeve is a factor 2.5 higher than that between the sleeve and the tube. Conduction heat calculated from the temperature difference across the strips confirm the value of heating power \dot{Q}_{11} and the resulting thermal impedance is a factor 5.5 higher than that between the sleeve and the tube.

Sample 3

The helium temperature was maintained at 8 K and the thermal impedance between the copper sleeve and the stainless steel tube resulted to be 5.5 ± 0.5 K/W. The heat intercept does not perform as well as that made of aluminum probably because of the lower thermal contraction of the copper.

The insulation vacuum was degraded from 10^{-4} Pa to $5 \cdot 10^{-3}$ Pa and the quality of thermal contact did not vary. Measurements for residual helium pressure higher than $5 \cdot 10^{-3}$ Pa were not carried out as the heat inleak at 1.9 K would have affected the test results.

The thermal impedance along the copper strips is 1.5 ± 0.12 K/W, as well as that between the strips and the sleeve.

Sample 4

The thermal impedance between the copper sleeve and the stainless steel tube was found to be 2 ± 0.2 K/W with the helium temperature at 50 K. The thermal impedances across the welding is about 1.9 ± 0.2 K/W, as well as that due to conduction along the strips.

Sample 5

The measured thermal impedance of the contact between the aluminum sleeve and the stainless steel tube is 0.4 ± 0.05 K/W at 75 K. The welded contact performs better than in sample 1 as its thermal impedance is only 0.5 ± 0.05 K/W. The thermal impedance due to conduction along the strips is 2 ± 0.02 K/W. Since this value is lower than that found in sample 1, we can conclude that the copper cross section is higher than 50% of the cross-section of the braid.

Insulation vacuum was degraded from 10^{-4} Pa to 10^{-2} Pa and the values of thermal impedances did not vary significantly.

Sample 6

To simulate a possible heat intercept configuration between the soft screen and the cooling line, the sample has been connected to the heated block by a thin aluminum sheet (1 mm thick) welded onto the conducting sleeve. The inlet helium temperature was maintained at about 8 K. The time to reach steady-state conditions was shorter than in the previous samples because of the lower heat capacity.

The thermal impedance between the conducting sleeve and the stainless steel tube, measured in four locations, is about 1 ± 0.1 K/W and is not dependent on the measurement position. This is due to the smaller diameter which guarantees a more uniform heat distribution. The welded contact gives a thermal impedance of 1.3 ± 0.15 K/W.

4.2.4 Summary of tests

The heat intercept presented in this chapter, formed by a conducting sleeve shrink-fitted onto a stainless steel tube, represents an efficient and reliable solution for the LHC cryostats. The samples with the conducting sleeve made of aluminum give a lower thermal impedance both at 50-75 K and 4.5-20 K. The thermal impedance increases by a factor 2 when temperature decreases from 20 K to 4.5K. The thermal impedance due to the welded contact is higher than that of the shrink-fitted contact. Insulation vacuum and geometry do not affect strongly the quality of the heat intercept. Samples with smaller diameters guarantee a more uniform thermal contact between the conducting sleeve and the stainless steel tube.

PART 3

TRANSIENT THERMAL PERFORMANCE OF THE LHC PROTOTYPE CRYOSTATS

CHAPTER 1

Forced-flow cooldown and warmup

Standard operating modes of LHC cryogenics, such as magnet forced-flow cooldown and warmup, have been experimentally investigated in the LHC prototype magnet string [96]. These thermal transient modes [97-99] have been studied to assess thermal gradients in magnets during cooldown and warmup and thus verify design calculations. A one-dimensional non linear mathematical model has been developed in order to estimate the parameter characterising the global magnet-to-helium heat transfer. Simulated behaviour has been compared to measured results. The now validated mathematical model can be used to simulate the magnet behaviour during fast cooldown and warmup.

1.1 Short description of the cold mass

LHC prototype dipole

The two sets of coils are supported by collars (201x381 outer dimension) and iron yoke (580 mm outer diameter), surrounded and compressed by a shrinking cylinder (figure III-1.1) [100]. The inner diameter of the coil is 50 mm and the outer diameter is 120.2 mm. The axis of the two sets of coils are separated by 180 mm. The shrinking cylinder is at the same time the outer shell of the helium tank, while its inner wall forms the beam vacuum chamber. The cold mass is closed at the ends by covers, which leave passages for the beam vacuum chambers, the heat exchanger tube and the pipes containing the electrical connections.

LHC prototype quadrupole

The lattice quadrupoles, like the dipoles, have a two-in-one geometry with a beam axis spacing of 180 mm. A common yoke (444 mm outer diameter) is shared by the two quadrupole coils as for the dipoles. The coil inner diameter is 56 mm and the outer one is 110.6 mm. The collars are made of stainless steel and their outer diameter is 164 mm.

The mass M (table III-1.1) and the specific heat of the cold mass C_{pM} (figure III-1.2) have been calculated from magnet design data. Materials properties were obtained from reference 30.

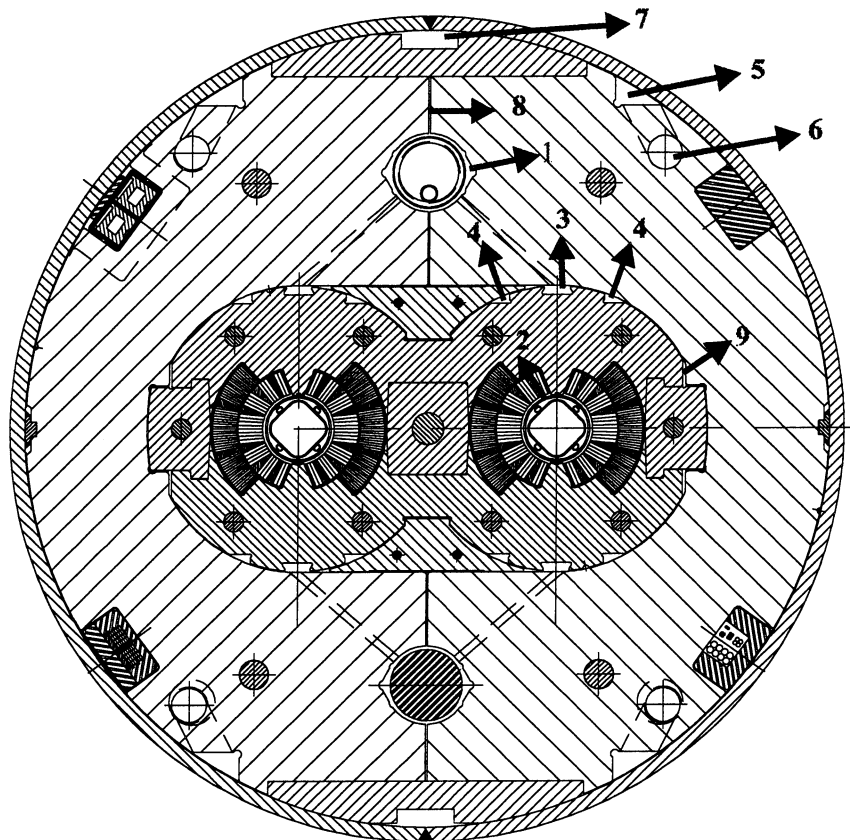


Figure III-1.1: *Transverse cross-section of the LHC prototype dipole magnet*

Table III-1.1: *Mass of the LHC prototype main lattice magnets*

	Main Prototype Dipole		Main Prototype Quadrupole	
	Material	Mass [kg/m]	Material	Mass [kg/m]
Coils	Copper	111.7	Copper	96.5
Collars	Aluminum	124.6	Stainless steel	221.8
Yoke	Iron	1451.0	Iron	768.3
Shrinking cylinder + Pipework	Stainless steel	144.1	Stainless steel	179.2
Total		1831.4		1265.8

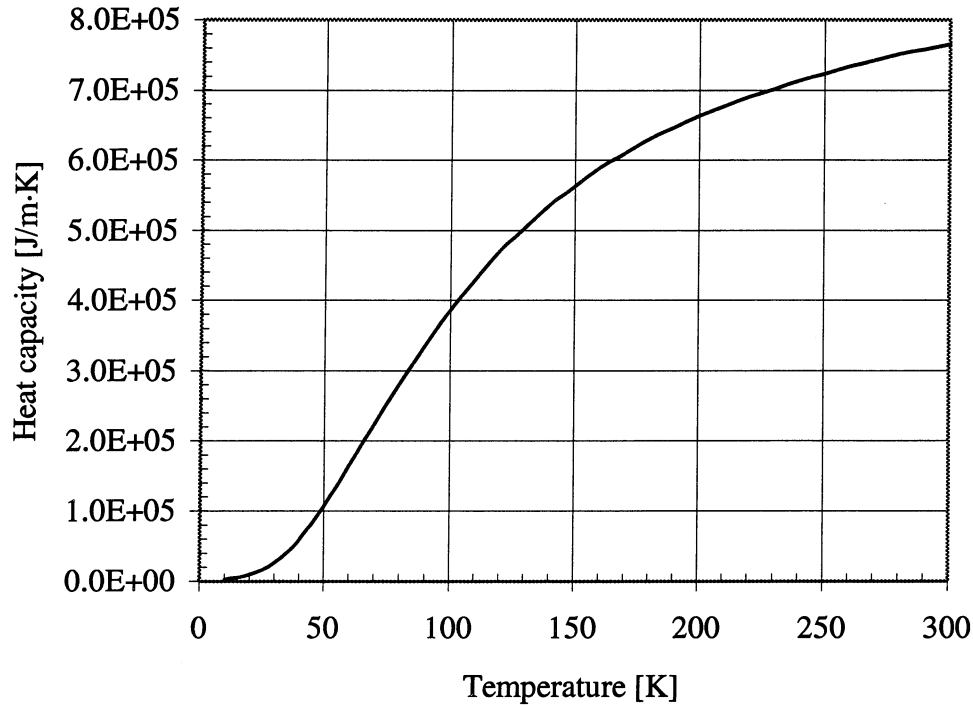


Figure III-1.2: Heat capacity of the cold mass of the LHC prototype magnet string (1 quadrupole and 3 dipoles)

1.2 Mathematical model

Cooldown from room temperature to 80 K and warmup from 80 K to 300 K are achieved by flowing gaseous helium respectively at decreasing and increasing temperatures. The inlet helium temperature is controlled by the overall string gradient in order to limit thermal stresses in the magnets.

The evolution of the temperatures of the cold mass and helium can be calculated from the energy conservation. Consider the elementary volume shown in figure III-1.3.

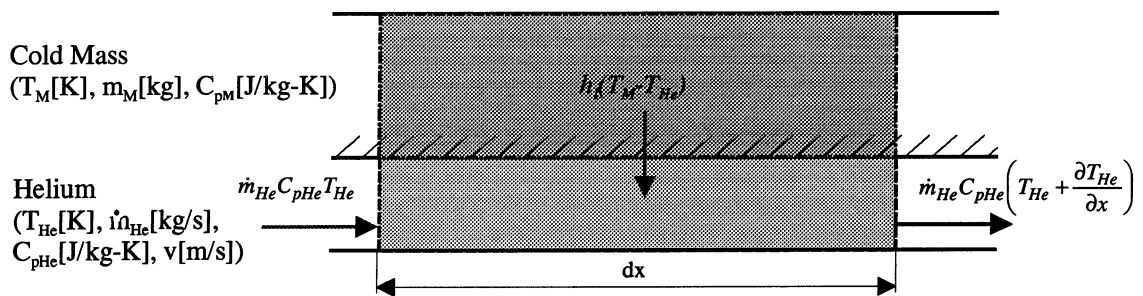


Figure III-1.3: Scheme of the mathematical model for forced-flow cooldown and warmup

The cold mass laminated structure allows longitudinal heat conduction to be neglected. As a consequence only convective heat exchange contributes to the heat transfer between cold mass and helium. The equations representing the heat exchange between helium and cold mass are the following:

$$m_M C_{pM} \frac{\partial T_M}{\partial t} = -h_l (T_M - T_{He}) \quad (\text{III-1.1})$$

$$\dot{m}_{He} C_{pHe} \left(\frac{\partial T_{He}}{\partial x} + \frac{1}{v} \frac{\partial T_{He}}{\partial t} \right) = h_l (T_M - T_{He}) \quad (\text{III-1.2})$$

The one-dimensional non linear model constituted by equations III-1.1 and III-1.2 can be solved explicitly using the finite difference method [101]. The cold mass can be divided in sections, for each of them we can write:

$$m_M C_{pM} \cdot \frac{T_M^{(x,t+1)} - T_M^{(x,t)}}{\Delta t} = -h_l (T_M^{(x,t)} - T_{He}^{(x,t)}) \quad (\text{III-1.3})$$

$$\dot{m}_{He} C_{pHe} \left(\frac{T_{He}^{(x+1,t)} - T_{He}^{(x,t)}}{\Delta x} + \frac{1}{v} \frac{T_{He}^{(x,t+1)} - T_{He}^{(x,t)}}{\Delta t} \right) = h_l (T_M^{(x,t)} - T_{He}^{(x,t)}) \quad (\text{III-1.4})$$

The boundary conditions are the following:

- at any location, $T_M(t=0) = \text{constant}$
- at any time, $T_{He}(x=0) = \text{constant}$

At each node, we can thus calculate the cold mass temperature (T_M) and the helium temperature (T_{He}) as a function of time (t).

The heat transfer coefficient h_l between helium and magnet has been calculated from design data. Helium flows through several channels connected in parallel and for each of them the heat transfer coefficient h_l has been estimated from the Nusselt number (Nu). For channels (1, 2, 4, 7, 8 and 9) in which the Reynolds number is taken lower than 2000, fully developed laminar flow was assumed. In this condition Nu is taken as constant and equal to 3.7 [25]. For the other channels, Nu has been evaluated by using the Dittus-Boelter correlation [32] which is valid for fully developed turbulent flow:

$$Nu = 0.023 Re^{0.8} Pr^n \quad (\text{III-1.5})$$

where n is 0.4 for heating and 0.3 for cooling

Table III-1.2 shows results for the different channels in the case of cooldown. D_h is the hydraulic diameter, \dot{m}_{He} is the mass-flow, \bar{A} / l is the wetted perimeter and v is the helium velocity.

The channels which contribute to heat exchange are mostly those seeing turbulent flow (channels 3, 5, 6). Neglecting heat exchange in the channels which see laminar flow, the overall coefficient h_l results to be 220 W/K.m at 300 K. The heat transfer coefficient depends on temperature and decreases to 175 W/K.m once the cold mass is

at 50 K (figure III-1.4). These calculated values are in good agreement with observations during magnet cooldown and warmup.

The helium specific heat C_{pHe} has been considered constant in the range of temperatures of interest and its value, 5200 J/kg·K, has been evaluated from property tables [49].

Table III-1.2: Helium-to-magnet heat transfer coefficient (forced-flow cooldown)

Channel	D_h	\dot{m}_{He}	\bar{A} / l	\dot{v}	h_l	$h_l \bar{A} / l$
	[m]	[kg/s]	[m ² /m]	[m/s]	[W/m ² ·K]	[W/m·K]
1 (Hx tubes)	5.00E-03	6.74E-04	6.60E-01	5.09	43.10	28.44
2 (Bore tubes)	4.00E-03	2.76E-04	6.03E-01	2.85	28.35	17.10
3 (Collar)	9.23E-03	2.44E-03	2.08E-01	31.66	164.45	34.19
4 (Collar)	4.84E-03	8.45E-04	3.22E-01	13.52	94.74	30.50
5 (Yoke)	1.48E-02	8.78E-03	3.75E-01	39.47	178.50	66.87
6 (Yoke)	2.50E-02	3.64E-02	3.14E-01	115.64	379.81	119.32
7 (Yoke)	5.40E-03	5.69E-04	2.58E-01	10.19	73.91	19.05
8 (Yoke)	1.00E-03	1.08E-06	4.24E-01	0.06	1.78	0.75
9 (Collar/Yoke)	1.00E-03	2.16E-06	4.24E-01	0.13	3.10	1.31

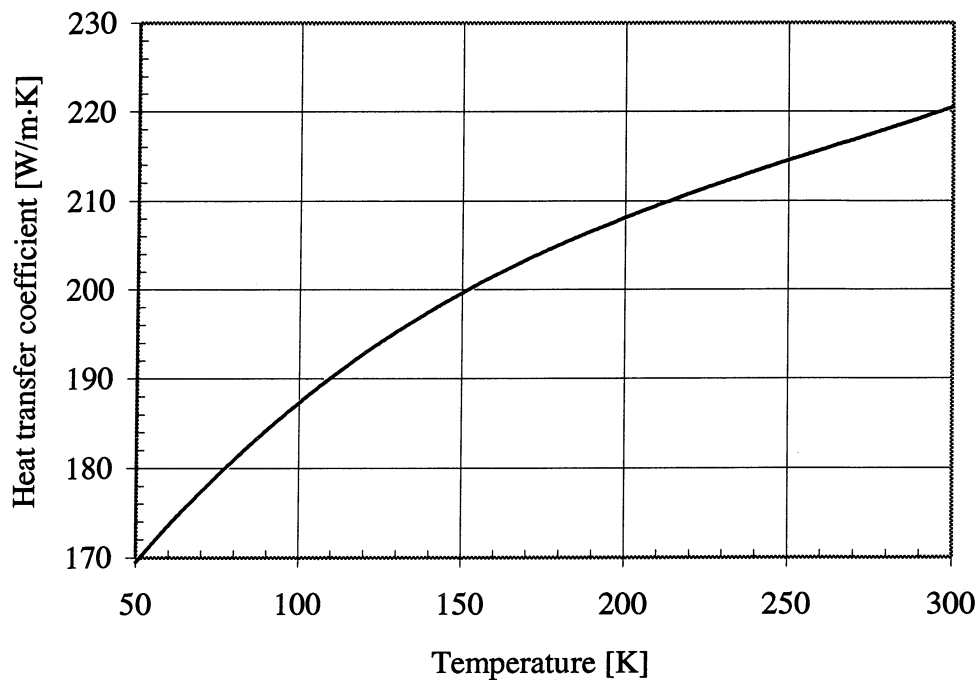


Figure III-1.4: Calculated heat transfer coefficient between magnet and helium

1.3 Results

Table III-1.3 lists the value of the cold mass m_M , the helium mass-flow \dot{m} and the maximum temperature difference (ΔT_{max}) between helium and magnet during the different measurement runs.

The time needed for cooldown and warmup strongly depends on the imposed maximum driving temperature difference between helium and cold mass as well as on the mass-flow.

For the first three runs, string cooldown started once the insulation vacuum was around 10^{-2} Pa whereas during Run 2B residual gas pressure was maintained at about 1 Pa. Residual gas pressure of 1 Pa did not affect the cooldown time, as the added heat inleak is negligible in comparison with the high heat capacity of the cold mass.

During the first two runs the string was warmed up by helium forced flow, while in Run 2 natural and accelerated warmup, with or without pumping of the insulation vacuum, were experimented. In Run 2B the insulation vacuum during warmup was maintained at $5 \cdot 10^{-3}$ Pa.

Table III-1.3: Main parameters of the string forced-flow cooldown and warmup

	m_M [kg]	Cooldown			Warmup		
		\dot{m}_{He} [g/s]	ΔT_{max} [K]	Time [h]	\dot{m}_{He} [g/s]	ΔT_{max} [K]	Time [h]
Run 0	$45 \cdot 10^3$	50	50	85	50	50	100
Run 1	$45 \cdot 10^3$	50	60	70	80	60	55
Run 2A	$65 \cdot 10^3$	60	60	85	natural and accelerated warmup		
Run 2B	$65 \cdot 10^3$	80	60	70	natural warmup		

For all the measurement runs, calculated results have been compared with those measured. The forced flow cooldown (Run 2A) and warmup (Run 1) of the LHC prototype string are shown in figures III-1.5 and III-1.6.

During Run 1 the helium inlet section corresponds to the quadrupole (Q) inlet, the middle section to the first dipole (D1) inlet and the outlet section to the second dipole (D2) outlet. During Run 2 the middle helium section corresponds to the first dipole outlet and the outlet section to the third dipole (D3) outlet.

Since good agreement has been found between measured and simulated results, the mathematical program has been used to simulate fast cooldown and warmup. During fast cooldown (figure III-1.7), the helium entered the cold mass at 80 K from the beginning and in the fast warmup (figure III-1.8) it was at 300 K from the beginning. In both cases the time needed to cooldown or to warmup is reduced by a factor 4 respect to the case of an imposed temperature difference of 75 K between helium and magnet. On the other hand, the maximum temperature difference in the magnets results to be 180 K for cooldown and 130 K for warmup.

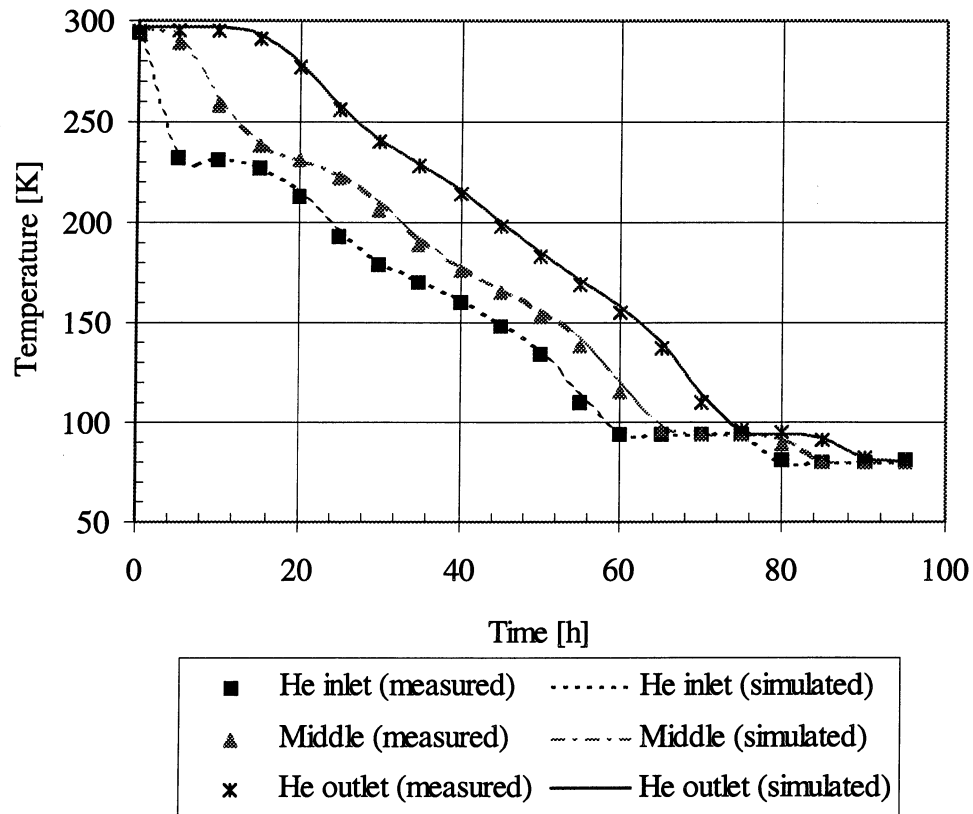


Figure III-1.5: Forced-flow cooldown of LHC prototype magnet String (Run 2A)

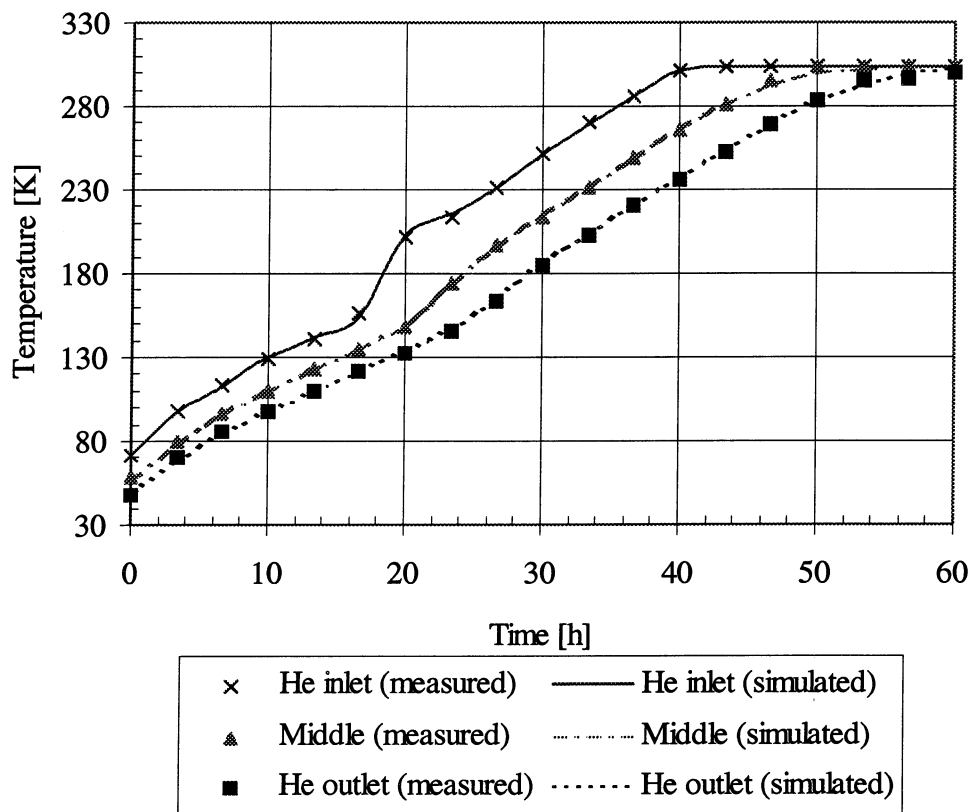
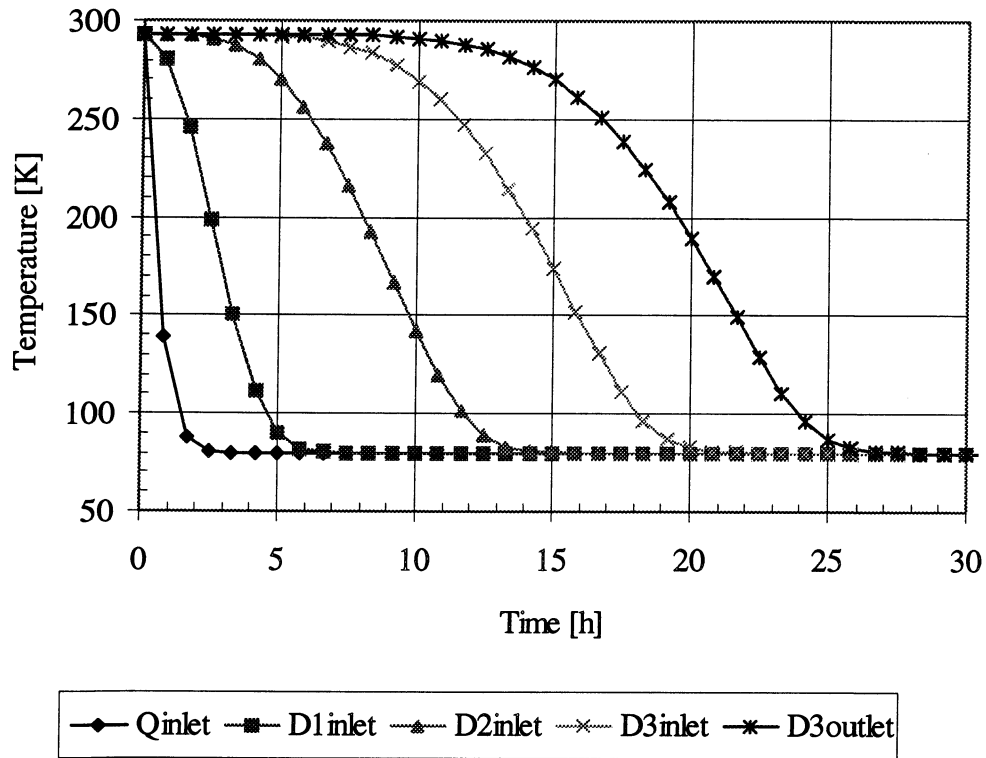
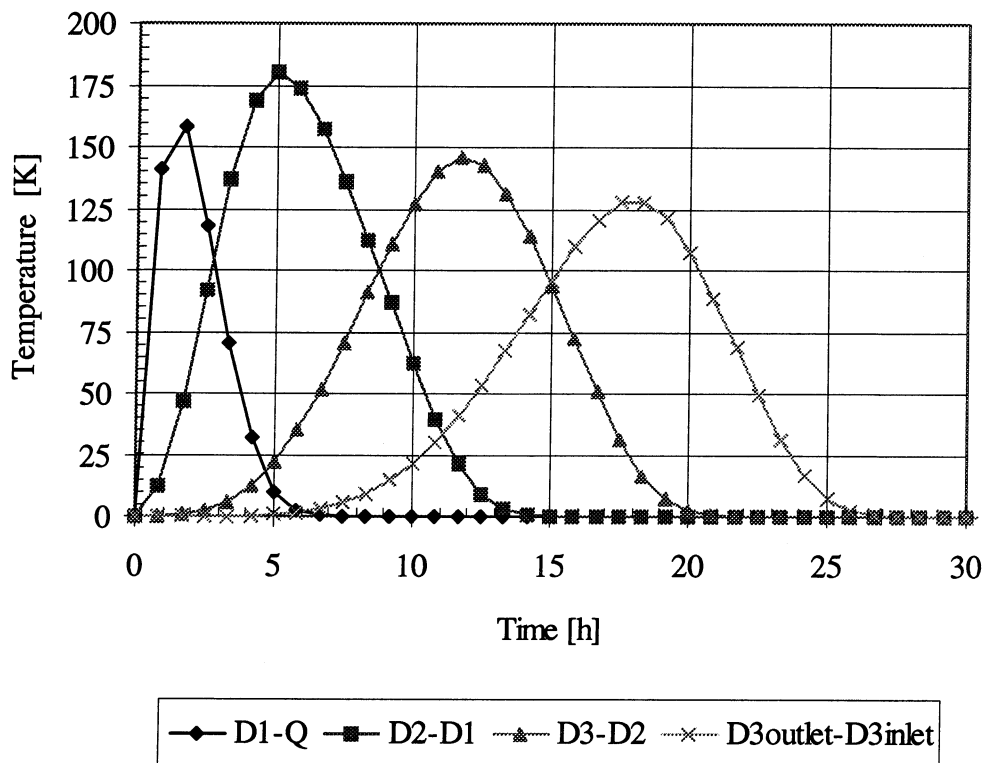


Figure III-1.6: Forced-flow warmup of LHC prototype magnet string (Run 1)

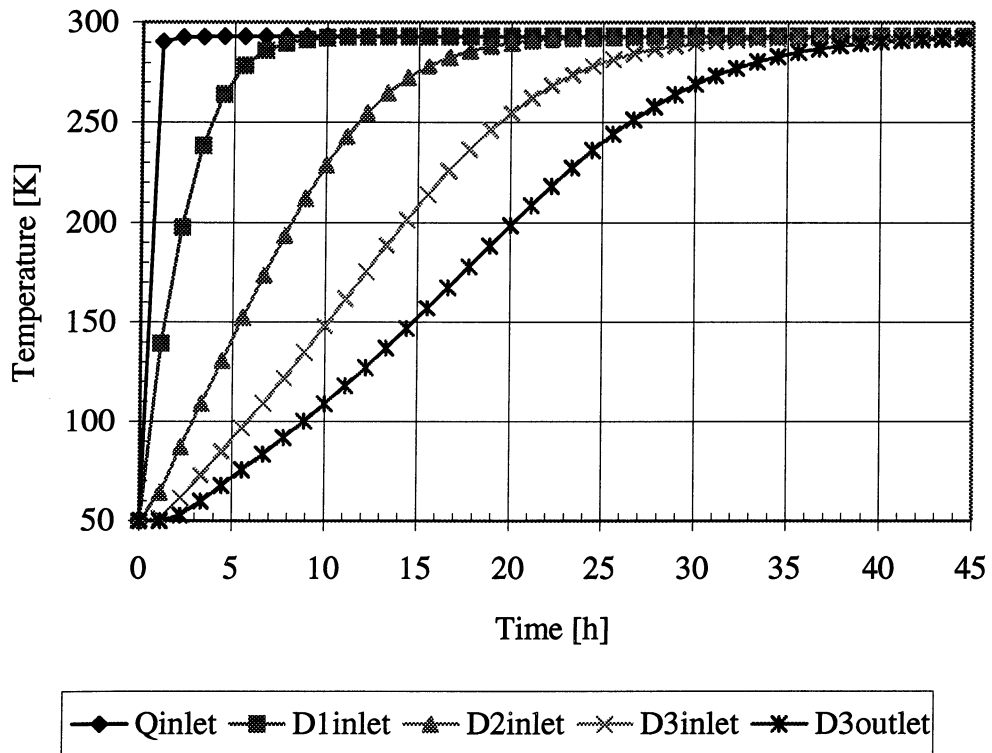


a) Cold mass temperature

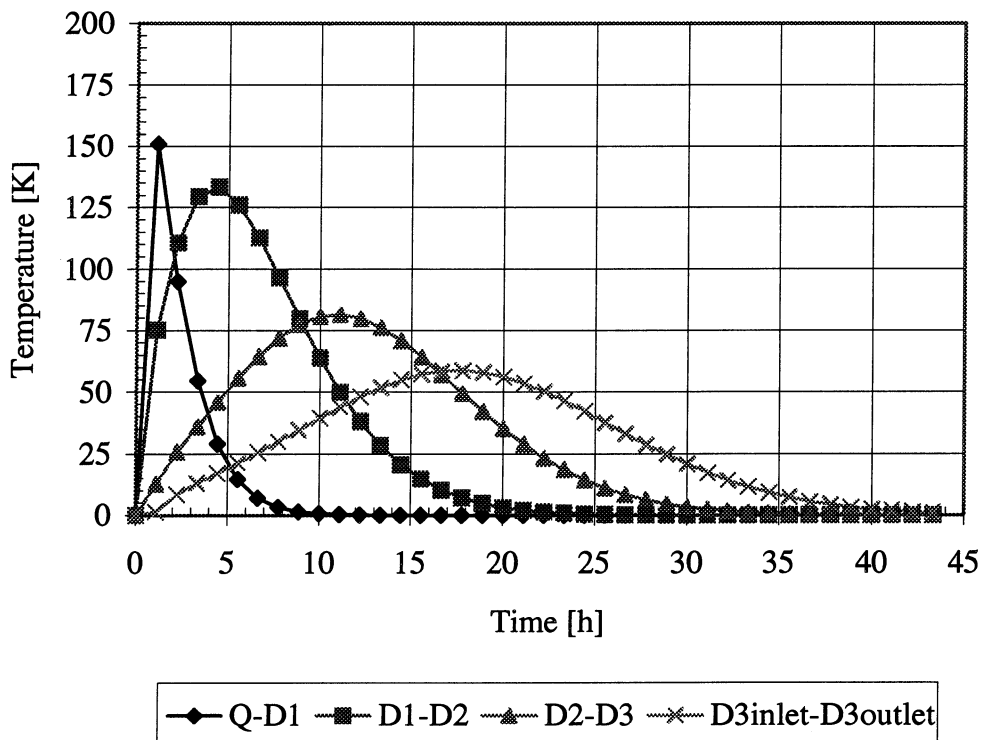


b) Temperature difference across magnet

Figure III-1.7: Simulation of the fast forced-flow cooldown of LHC prototype magnet string (Run 2; He mass-flow=65 g/s)



a) Cold mass temperature



b) Temperature difference across magnet

Figure III-1. 8: Simulation of the fast forced-flow warmup of LHC prototype magnet string (Run 2; He mass-flow=65 g/s)

CHAPTER 2

Natural warmup and accidental loss of insulation vacuum

Warmup with no helium supply in the cryogenic lines (natural warmup) and accidental loss of insulation vacuum (accelerated warmup) was performed in the LHC prototype string [102].

Since interventions on the LHC machine may concern only a few of magnets, it is of interest to know the time required for warming up, pumping down and cooling down and to understand how the rest of the machine will behave in case of natural warmup, with or without active pumping of the insulation vacuum.

An accidental loss of insulation vacuum may occur because of an air leak from the ambient surroundings, or an internal helium leak from a cryogenic circuit [103]. The vacuum vessel for the LHC dipole cryostat is made of ISO 430 carbon steel and in case of loss of insulation vacuum it will progressively cool down, but must not reach the embrittlement temperature of the material.

In this chapter the evolution of residual vacuum pressure and temperatures in natural warmup, as well as in the case of catastrophic loss of insulation are presented.

One-dimensional non linear mathematical models are found to fit experimental data reasonably well, and consequently can be used to simulate other off-design modes.

2.1 Mathematical model

The thermal networks used for the one-dimensional radial model simulating heat transfer during natural and accelerated warmup are shown in figures III-2.1 and III-2.2.

Heat by radiation ($\dot{Q}_{r_{vv}}$) and convection ($\dot{Q}_{cv_{vv}}$) flows from ambient to the vacuum vessel.

$$\dot{Q}_{r_{vv}} = \sigma \bar{A}_{vv} (T_{amb}^4 - T_{vv}^4) \quad (\text{III-2.1})$$

$$\dot{Q}_{cv_{vv}} = h_C \bar{A}_{vv} (T_{amb} - T_{vv}) \quad (\text{III-2.2})$$

h_c is the natural convection heat transfer coefficient:

$$h_c = 1.3 \left(\frac{T_{amb}}{D_{vv}} \right)^{0.25} \quad (\text{III-2.3})$$

The total heat reaching the vacuum vessel can be written as follows:

$$\boxed{\dot{Q}_{vv} = \dot{Q}_{r_{vv}} + \dot{Q}_{cv_{vv}}} \quad (\text{III-2.4})$$

From the vacuum vessel to the outer layer of superinsulation, heat is exchanged by radiation ($\dot{Q}_{r_{s1}}$) and convection ($\dot{Q}_{cv_{s1}}$):

$$\dot{Q}_{r_{s1}} = \sigma \bar{A}_{s1} E_1 (T_{vv}^4 - T_{s1}^4) \quad (\text{III-2.5})$$

$$\dot{Q}_{cv_{ts}} = \frac{2\pi l K \left(\frac{T_{vv} + T_{ts}}{2} \right) f_c}{\ln \left(\frac{D_{vv}}{D_{ts} + 2e_{s1}} \right)} (T_{vv} - T_{s1}) \quad (\text{III-2.6})$$

where T_{s1} is the temperature of the outer layer of MLI, E_1 is the emissivity factor and e_{s1} is the thickness of MLI. f_c is the convection factor [25] which depends on the Prandtl (Pr) and Grashof (Gr) numbers which are function of the isobaric thermal expansion, the density and the viscosity.

$$f_c = a(Pr Gr)^b \quad (\text{III-2.7})$$

where: $a=0.53$ and $b=0.25$ if $(Gr \cdot Pr)=10^4-10^9$ [25]
 $a=0.13$ and $b=0.33$ if $(Gr \cdot Pr)=10^9-10^{12}$ [25]

Heat transfer through the 30 layers of MLI covering the thermal shield ($\dot{Q}_{s_{ts}}$) is given by solid conduction ($\dot{Q}_{sc_{ts}}$), conduction in residual gas ($\dot{Q}_{gc_{ts}}$) and radiation ($\dot{Q}_{r_{ts}}$).

$$\dot{Q}_{sc_{ts}} = \bar{A}_{s1} \left[\frac{\alpha_s}{N_{s1}} \frac{T_{vv} + T_{ts}}{2} (T_{vv} - T_{ts}) \right] \quad (\text{III-2.8})$$

$$\dot{Q}_{r_{ts}} = \bar{A}_{s1} \left[\frac{\beta_s}{N_{s1}} (T_{vv}^4 - T_{ts}^4) \right] \quad (\text{III-2.9})$$

Since conduction in residual gas depends on the insulation vacuum, the heat transfer is governed by molecular regime during natural warmup ($P < 1$ Pa) and by viscous regime during accelerated warmup.

$$\dot{Q}gc_{ts} = \bar{A}_{S1}\gamma_{S1}P(T_{vv} - T_{ts}) \quad \text{molecular regime} \quad (\text{III-2.10})$$

$$\dot{Q}gc_{ts} = \frac{2\pi lK \left(\frac{T_{vv} + T_{ts}}{2} \right)}{\ln \left(\frac{D_{ts} + 2e_{S1}}{D_{ts}} \right)} (T_{vv} - T_{ts}) \quad \text{viscous regime} \quad (\text{III-2.11})$$

Finally, the heat transfer from the vacuum vessel (\dot{Q}_{ts}) to the thermal shield is given by:

$$\boxed{\dot{Q}_{ts} = \dot{Q}r_{S1} + \dot{Q}cv_{ts} = \dot{Q}s_{ts}} \quad (\text{III-2.12})$$

From the thermal shield heat by radiation ($\dot{Q}r_{S2}$) and convection ($\dot{Q}cv_{S2}$) reaches the outer layer of MLI wrapped on the cold mass:

$$\dot{Q}r_{S2} = \sigma \bar{A}_{S2} E_2 (T_{ts}^4 - T_{S2}^4) \quad (\text{III-2.13})$$

$$\dot{Q}cv_{S2} = \frac{2\pi lK \left(\frac{T_{ts} + T_{cm}}{2} \right) f_c}{\ln \left(\frac{D_{ts}}{D_{cm} + 2e_{S2}} \right)} (T_{ts} - T_{cm}) \quad (\text{III-2.14})$$

Heat transfer to the cold mass through the MLI system ($\dot{Q}s_{cm}$) is given by

$$\dot{Q}s_{cm} = \bar{A}_{S2} \left[\frac{\alpha_S}{N_{S2}} \frac{T_{ts} + T_{cm}}{2} (T_{ts} - T_{cm}) \right] \quad (\text{III-2.15})$$

$$\dot{Q}r_{cm} = \bar{A}_{S2} \left[\frac{\beta_S}{N_{S2}} (T_{ts}^4 - T_{cm}^4) \right] \quad (\text{III-2.16})$$

$$\dot{Q}gc_{cm} = \bar{A}_{S2}\gamma_{S2}P(T_{ts} - T_{cm}) \quad \text{molecular regime} \quad (\text{III-2.17})$$

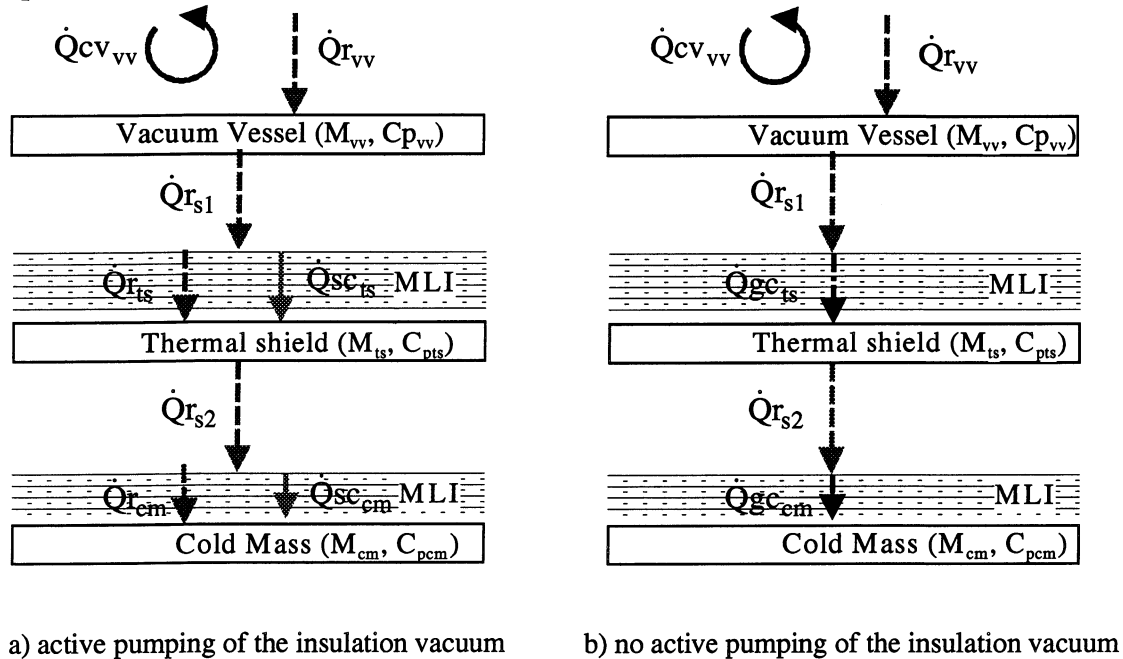
$$\dot{Q}gc_{cm} = \frac{2\pi lK \left(\frac{T_{ts} + T_{cm}}{2} \right)}{\ln \left(\frac{D_{cm} + 2e_{S2}}{D_{cm}} \right)} (T_{ts} - T_{cm}) \quad \text{viscous regime} \quad (\text{III-2.18})$$

The heat transfer from the thermal shield to the cold mass yields:

$$\boxed{\dot{Q}_{cm} = \dot{Q}r_{S2} + \dot{Q}cv_{cm} = \dot{Q}s_{cm}} \quad (\text{III-2.19})$$

In the case of natural warmup, convection in the residual gas is negligible, while it becomes relevant during accelerated warmup. Conduction in residual gas can be

neglected in the case of natural warmup with active pumping of the insulation vacuum. Solid conduction through the insulator spacers and radiation between the layers of MLI are negligible for residual gas pressure higher than 10^{-2} Pa as conduction in residual gas is predominant. Radiation is negligible in the case of accelerated warmup. Convection cannot occur in the MLI system due the restricted space between spacers.



Heat transfer processes

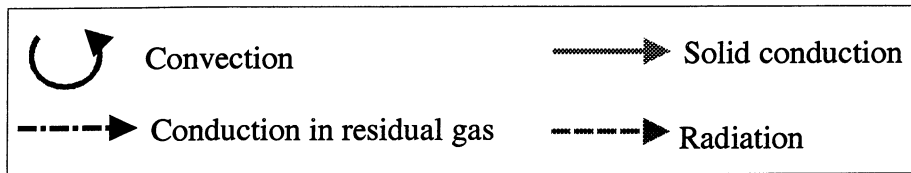


Figure III-2.1: Thermal network of natural warmup

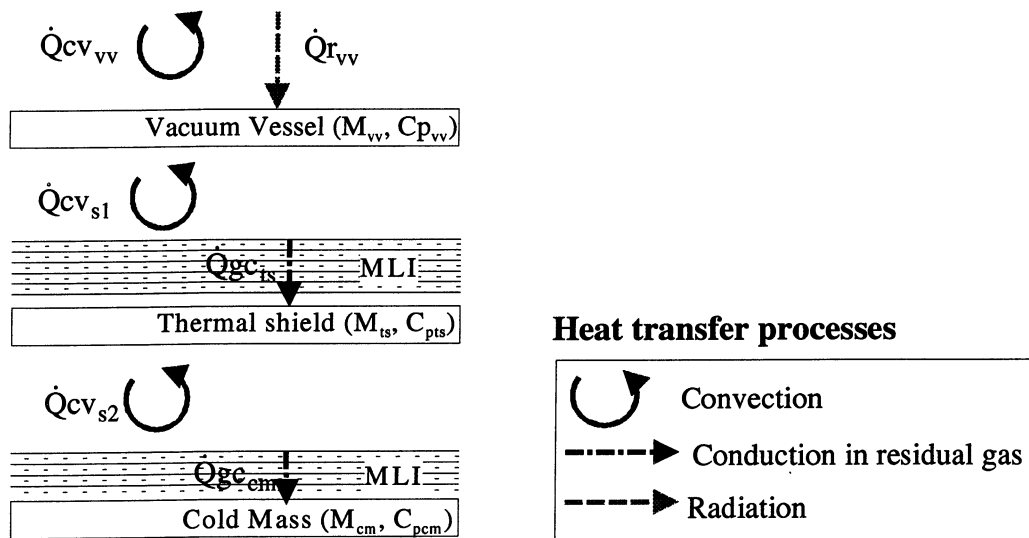


Figure III-2.2: Thermal network of accelerated warmup

Applying the energy conservation to the vacuum vessel, thermal shield and cold mass, we obtain a system of three differential equations, from which we can calculate T_{vv} , T_{ts} and T_{cm} :

$$M_{vv} \cdot C_{p_{vv}}(T_{vv}) \cdot \frac{dT_{vv}}{dt} = \dot{Q}_{vv}(T_{vv}) - \dot{Q}_{ts}(T_{vv}, T_{ts}) \quad (\text{III-2.20})$$

$$M_{ts} C_{p_{ts}}(T_{ts}) \cdot \frac{dT_{ts}}{dt} = \dot{Q}_{ts}(T_{vv}, T_{ts}) - \dot{Q}_{cm}(T_{ts}, T_{cm}) \quad (\text{III-2.21})$$

$$M_{cm} C_{p_{cm}}(T_{cm}) \cdot \frac{dT_{cm}}{dt} = \dot{Q}_{cm}(T_{ts}, T_{cm}) \quad (\text{III-2.22})$$

Masses and main dimensions used as inputs in the mathematical model are summarised in table III-2.1.

Table III-2.1: Masses and main dimensions of the string test

	Vacuum vessel	Thermal	Cold mass
Material	Iron	Aluminium	Iron/StSt/Al/Cu
Outer diameter [m]	0.980	0.884	0.580
Inner diameter [m]	0.960	0.877	=
Lateral surface [m ² /m]	3.079	2.777	1.822
Mass [kg/m]	238.3	27.6	1601.7
Superinsulation thickness [m]	=	0.015	0.005

2.2 Test procedure and results

Natural warmup without active pumping of the insulation vacuum was performed during the Run 2A and started after a quench when the cold mass temperature was around 30 K and the thermal shield at 90 K. After about 20 hours of natural warmup residual gas pressure in the insulation vacuum degraded rapidly to 1 Pa (figure III-2.3). The final gas composition at 50 K was mainly composed of hydrogen (10%) and carbon monoxide (25%) from the superinsulation outgassing, as well as of nitrogen (40%) and oxygen (10%) from a known air leak. The gas species at this pressure is not relevant since the thermal impedance given by radiation is at least a factor 5 higher than that due to conduction in the residual gas. The test was stopped after 6 days when the cold mass was at 90 K and the thermal shield at 180 K. In order to simulate an accidental loss of insulation vacuum, warmup was then accelerated by injecting N₂ in the insulation space of the cryostat. Atmospheric pressure inside the cryostat was reached after 30 minutes. After another 30 minutes, condensation followed by frost was observed in distinct cold spots on the external surface of the cryostat beneath the lower end of each dipole. They could be attributed to the longitudinal heat transfer by natural convection. The lowest temperature reached was 230 K locally. In order to prevent embrittlement of the carbon steel wall of the vacuum vessel the insulation

vacuum was re-pumped down to $5 \cdot 10^4$ Pa. The string temperatures were allowed to evolve at this pressure for 2 weeks until they reached 300 K.

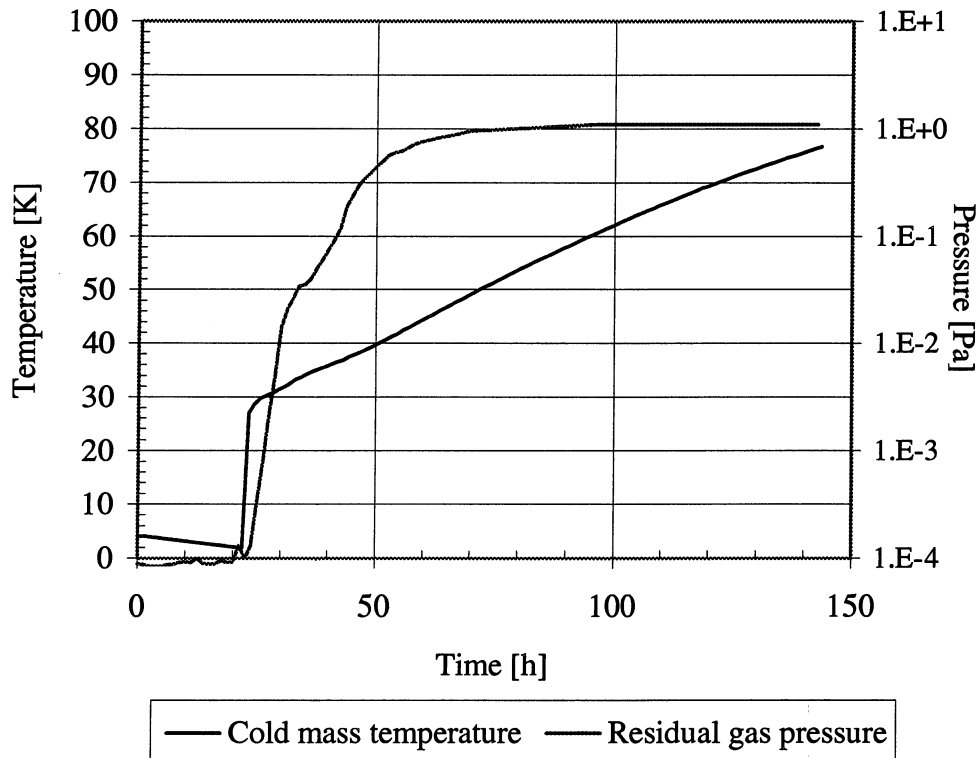


Figure III-2.3: *Evolution of the residual gas pressure respect to the cold mass temperature measured during natural warmup without active pumping of the insulation vacuum (Run 2A)*

Figure III-2.4 shows the evolution of the string average temperatures during natural (1 Pa) and accelerated warmup ($5 \cdot 10^4$ Pa), and compares experimental and calculated results. The thermal impedance due to conduction in the residual gas is determinant and this underlines the important role of superinsulation in case of an accidental loss of insulation vacuum.

From the measured temperatures, it is possible to calculate the evolution of the heat flux with time. Considering the accelerated warmup (figure III-2.5), the maximum calculated heat flux from the thermal shield to the cold mass was 300 W/m, reached after a few hours. For comparison, in nominal steady-state conditions the heat inleak at 1.9 K is about 0.4 W/m and during a magnetic resistive transition may reach 100 kW/m.

During Run 2B the natural warmup was performed with active pumping of the insulation vacuum. The residual gas pressure was stabilised at about 10^{-3} Pa when the cold mass was 30 K and the thermal shield 125 K. The string was left to warmup for 6 days and the test was stopped once the cold mass attained 50 K and the thermal shield 190 K. Figure III-2.6 shows the evolution of the string temperatures over time and compares experimental and simulated values.

To compare the performances of the two types of natural warmup, figure III-2.7 shows the simulated behaviour of the cold mass obtained by imposing in the two cases the same starting conditions: cold mass at 30 K and thermal shield at 90 K. After about 3 weeks the cold mass reaches 65 K if residual gas pressure is 10^{-3} Pa and 125

K in the case of no active pumping on the insulation vacuum (1 Pa). The time needed to recool the magnet string (about 40 m) to 4.2 K is about 1 day if the cold mass temperature is 125 K at the beginning and 5 h if it is at 65 K. This means a factor 4 reduction between the two cases.

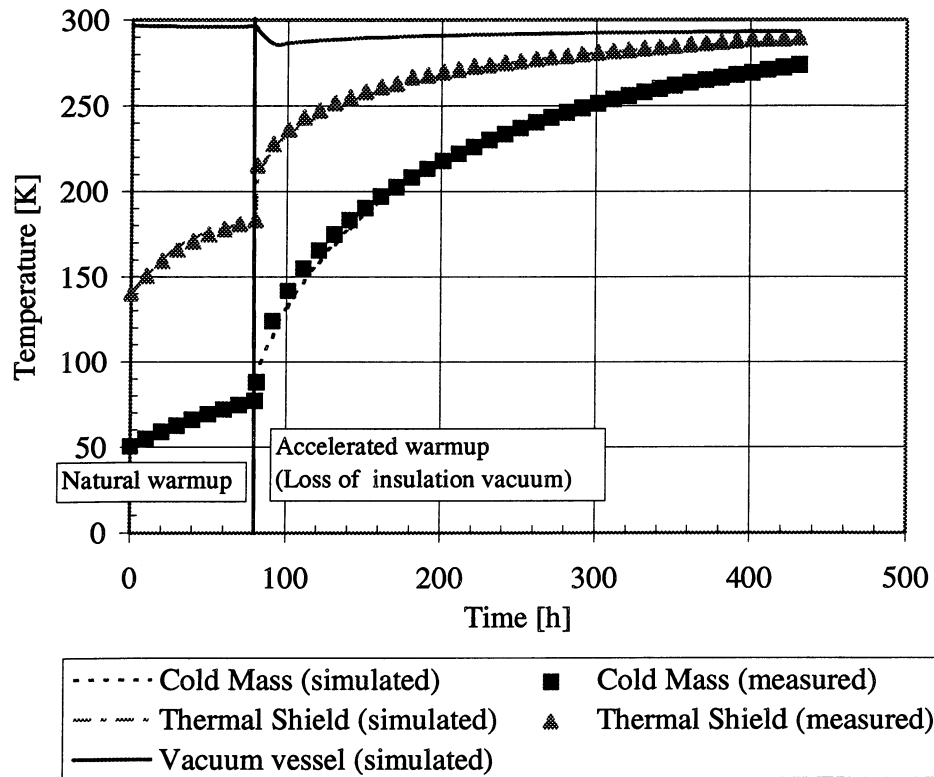


Figure III-2.4: LHC prototype magnet string temperatures during natural and accelerated warmup (Run 2A)

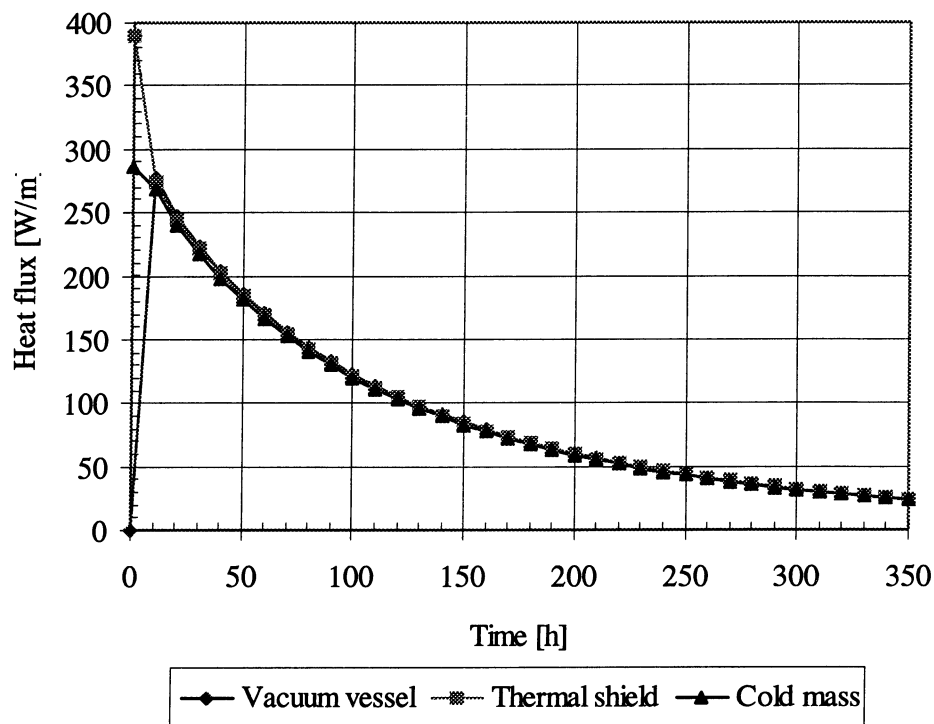


Figure III-2.5: Heat flux evolution over time during accelerated warmup (Run 2A)

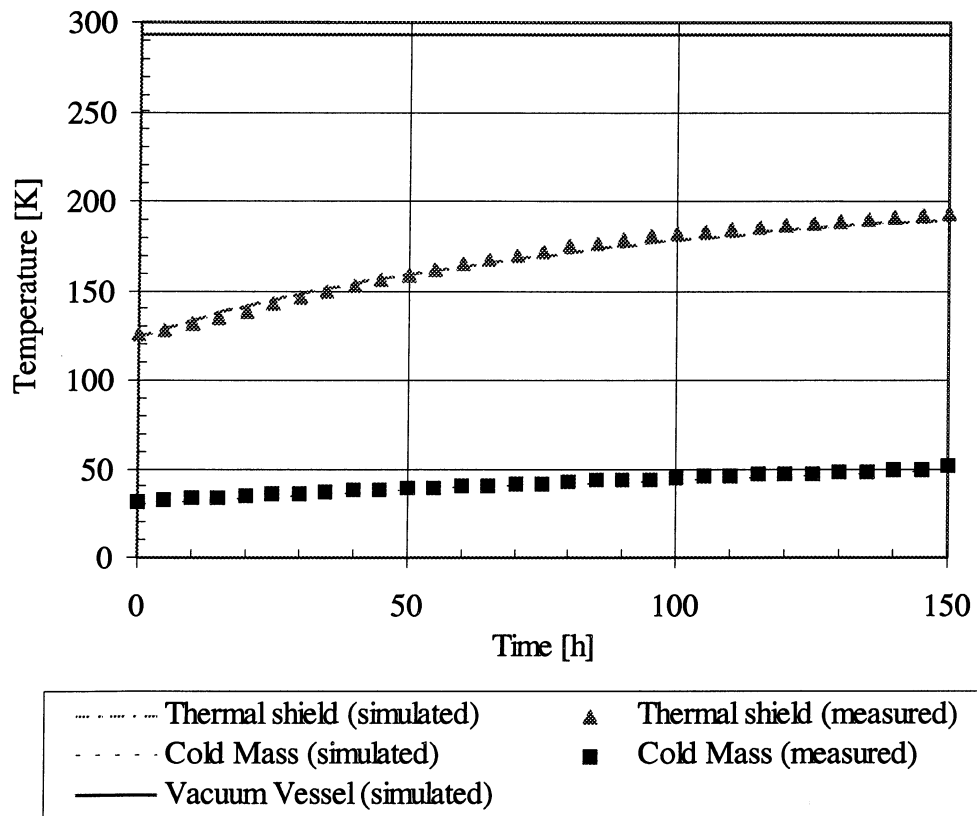


Figure III-2.6: LHC prototype magnet String temperatures during natural warmup with pumping on the insulation vacuum (Run 2B)

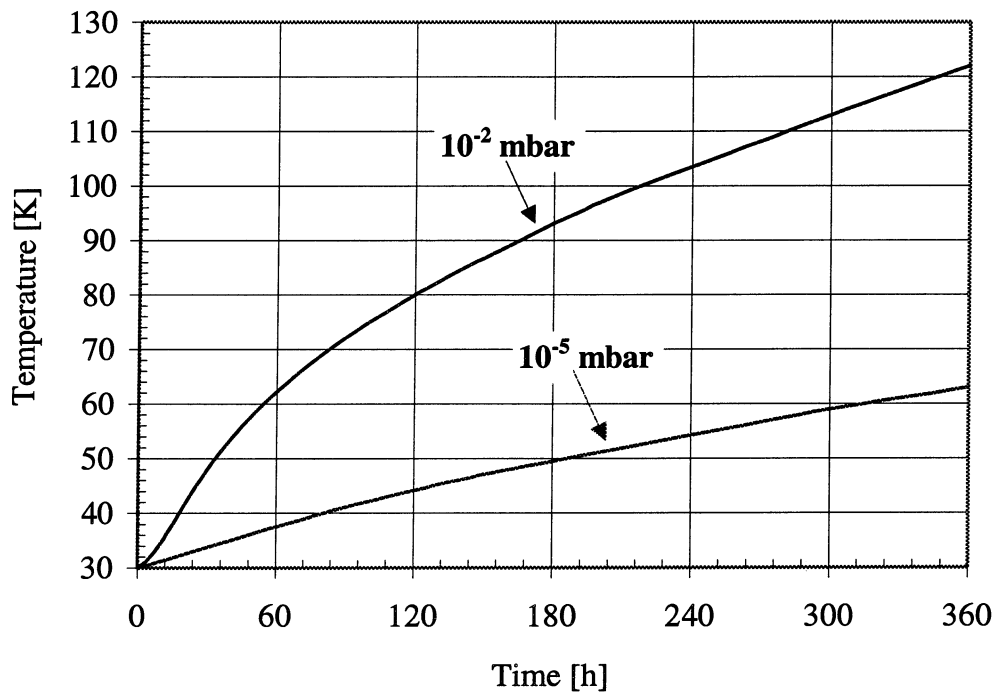


Figure III-2.7: Simulation of the cold mass temperature during natural warmup

CONCLUSION

An efficient thermal design of the LHC cryostats is of primary importance in order to maintain the heat inleaks within the imposed thermal budget of the cryogenic system.

Cryostats have to be constructed to withstand steady-state and transient modes. For steady-state operating conditions a lumped parameter mathematical model has been created to simulate the thermal performance of 10-m long cryostats. For transients one-dimensional linear models have been developed and solved by the finite difference method.

Full-scale prototypes amply permitted to investigate the thermal performances of cryostats and validate thus the mathematical models. In nominal steady operation the heat inleaks of the LHC prototype dipole cryostats are 5 W/m at 50-75 K, 0.23 W/m at 4.5-20 K and 0.19 W/m at 1.9 K. Performing these measurements with a precision of 10% in a 10-m long cryostat requires specific methods and a very fine instrumentation. For this purpose, the Cryostat Thermal Model (CTM) was designed to measure very precise heat inleaks and to analyse the heat interceptions at intermediate temperatures. The system flexibility and simplicity allowed different operating conditions to be investigated and analysed. The nominal steady heat inleaks have been measured and experimental results have confirmed those calculated. The measured heat flux to 50-75 K through the MLI system only was 1.2 W/m² and from 50-75 K to 1.9 K was 0.09 W/m² confirming results previously obtained. Tests have been performed by varying the screen temperatures and the residual gas pressure of the insulation space. Heat inleak at 1.9 K was found to be very sensitive to the residual gas pressure, increasing by a factor 1.5 if the insulation vacuum degrades from 10⁻⁴ Pa to 10⁻³ Pa and by a factor 3 if it degrades up to 10⁻² Pa. Calculated heat inleaks are in good accordance to those measured over a large range of parameter variation, and the mathematical model, now validated, can be used to simulate several other operating conditions.

Low heat inleaks at the lowest temperature level can be attained by efficient heat interception at intermediate temperatures. In the prototype cryostats the quality of thermal contacts has been analysed. It was found that bolted contacts are not reliable and cannot achieve low-enough thermal impedance. Welded, brazed and shrink-fitted thermal contacts perform well and represent a valid solution for heat interception in the LHC cryostats.

Heat inleak at 1.9 K is mainly due to the distributed heat flux from the thermal shield through the MLI system. It is therefore of interest to try and reduce this source

of heat inleak. A possibility is to replace the “floating” insulation system with an actively cooled screen at 4.5-20 K. For the LHC cryostats a self supporting screen at 4.5-20 K could not be envisaged due to lack of space. Consequently, a “soft” screen at 4.5-20 K cooled by the supply line C’ and leaning onto the cold mass via net-type insulating spacers was considered. In such a configuration the performance of the actively cooled screen is function of two parameters: a good thermal contact between the screen and the cooling pipe and an efficient insulation between the screen and the cold mass. Considering thermal impedances achieved in practise, the potential of improvement of such an actively-cooled “soft” screen for the LHC cryostats is a reduction of the heat inleak to 1.9 K (0.015 W/m^2) of a factor 4 with respect to the floating system version (0.060 W/m^2).

Transient operating modes play an important role in the cryostat thermal performance. They have been performed in a full scale LHC prototype magnet String and results confirmed the LHC basic design choices.

It has been shown that it is possible to cooldown the $65 \cdot 10^3 \text{ kg}$ of the LHC String cold mass in less than 4 days with 60 g/s of gaseous helium and a maximum longitudinal thermal gradient in the magnet of 60 K. In case of fast cooldown and warmup this time can be strongly reduced, but at the cost of higher temperature gradients along the magnets. The mathematical model developed for studying forced cooldown and warmup have been checked and validated against experimental data and now can be used to predict the behaviour of the LHC machine cryostats under nominal and accidental conditions.

Other transient modes which were tested are the natural warmup and the accidental loss of insulation vacuum. Natural warmup with or without pumping of the insulation vacuum has been tested on the 40 m long string test. The mathematical models used for simulating natural warmup give results in good accordance with measured data. The simulations of natural warmup show that if good vacuum is maintained during 3 weeks warmup, the recooling time can be reduced by a factor 4 with respect to the case with no pumping of the insulation vacuum.

Accidental loss of vacuum insulation is not considered catastrophic and the minimum temperature of 230 K attained on the vacuum vessel is still within the limit accepted for embrittlement carbon steel. The maximum heat power received by the cold mass is about 300 W/m and is small in comparison with that dissipated after a magnetic resistive transition.

References

Introduction to the LHC project

- [1] The LHC Study Group, DESIGN STUDY OF THE LARGE HADRON COLLIDER (LHC) A multiparticle collider in the LEP tunnel, CERN Report 91-03 (1991)
- [2] The LHC Study Group, The Large Hadron Collider Accelerator Project, CERN Report AC/93-03 (LHC) (1993)
- [3] L.R. Evans, The Large Hadron Collider, presented at PAC'95, Dallas (1995), Note AC-95-002, CERN (1995)
- [4] The LHC Study Group, The Large Hadron Collider, Conceptual Design, CERN Report AC/95-05 (LHC) (1996)
- [5] L.R. Evans, The Large Hadron Collider Project, paper presented at ICEC16/ICMC, Kitakyushu (1996)

The LHC cryogenic system

- [6] Ph. Lebrun, Superfluid Helium Cryogenics for the Large Hadron Collider Project at CERN, Cryogenics 34, ICEC Supplement (1994) pp 1-8,
- [7] Ph. Lebrun, Cryogenic systems for accelerators, presented at US-CERN-Japan Topical Course on Accelerator Physics and Technology "Frontiers of Accelerator Technology", Hawaii (1995)
- [8] V. Benda, A. Bézaguet, J. Casas-Cubillos, S. Claudet, W. Erdt, Ph. Lebrun, G. Riddone, V. Sergo, L. Serio, L. Taviani, B. Vullierme, R. van Weelderen, U. Wagner, Conceptual design of the cryogenic system for the Large Hadron Collider (LHC), presented at EPAC-96, Sitges, Barcelona (1996)

- [9] Ph. Lebrun, Helium Cryogenic Systems for the LEP2 and LHC projects at CERN, presented at NIFS Symposium, Toki (1996), Note LHC/96-05 (ACR), CERN (1996)
- [10] Ph. Lebrun, L. Tavian, G. Claudet, Development of large-capacity refrigeration at 1.8 K for the Large Hadron Collider at CERN, presented at Kryogenika'96, Praha, (1996)
- [11] Ph. Lebrun, G. Riddone, L. Tavian, U. Wagner, Demands in refrigeration capacity for the Large Hadron Collider, paper presented at ICEC16/ICMC, Kitakyushu, (1996)
- [12] A. Bézaguet, J. Casas-Cubillos, Ph. Lebrun, M. Marquet, L. Tavian, R. van Weelderen, The superfluid helium model cryoloop for the CERN Large Hadron Collider (LHC), Adv. Cryo. Eng. 39A, pp. 649-656 (1994)
- [13] L. Tavian, Utilisation des réfrigérateurs LEP200 pour LHC: conditions de fonctionnement et interfaces, Note LHC 164, CERN (1991)
- [14] S. Claudet, W.K. Erdt, P.K. Frandsen, Ph. Gayet, N.O. Solheim, Ch. Titcomb, G. Winkler, Four 12 kW/4.5 K Cryoplants at CERN, Cryogenics 34, ICEC supplement, pp 99-102 (1994)
- [15] L. Tavian, Stockage hélium et interconnexion des différents points du système cryogénique du LHC, Note LHC 198, CERN (1992)

The LHC prototype cryostats

- [16] T. H. Nicol, Design development for the 50 mm superconducting collider dipole cryostat, Supercollider 3, pp 1029-1036 (1991)
- [17] M. Clausen, H. Herzog, G. Horlitz, U. Knopf, R. Lange, H. Lierl, Cryogenic test and operation of the superconducting magnet system in the HERA proton storage ring, Adv. Cryo. Eng. 37A, pp 653-660 (1992),
- [18] J.C. Brunet, J. Kerby, Ph. Lebrun, P. Rohmig, B. Szeless, L.R. Williams, Design of LHC prototype dipole cryostats, Cryogenics 32, ICEC supplement, pp 191-194 (1992)
- [19] Technical specification manufacture and assembly of helium cryostats for the LHC prototype dipole magnets, Note IT-1878/LHC/AT Bis, CERN (1991)
- [20] Specification technique pour la fabrication de pieds supports en matériau composite pour les aimants dipôles et quadropoles prototypes du LHC, Note MT-DO/91, CERN (1991)

-
- [21] M. Mathieu, Systeme de supportage du LHC, Note MT-ESM/94-03, CERN (1994)
- [22] W. Cameron, B. Jenny, G.Riddone, P.Rohmig, R.van Weelderen, "Design and construction of a prototype superfluid helium cryostat for the short straight sections for the CERN Large Hadron collider", Adv. Cryo. Eng. 39A, pp 663-670 (1994)
- [23] W. Cameron, B. Jenny, P. Mésange, R. Moiroux, T. Renaglia, P. Rohmig, P. Seraphin, Ph. Trilhe, P. Viret, Ch. Vuitton, LHC short straight section prototype n 1: conception and assembly analysis, Note MT-ESH/95-04, CERN (1995)
- [24] B. Jenny, P. Rohmig, J.-M. Uriarte, A composite vacuum barrier for the LHC short straight section, Adv. Cryo. Eng. 41A, pp 793-798 (1996)

Modeling of cryostat thermal performance

- [25] J.P. Holman, Heat transfer 7th ed., McGraw-Hill Book Company, London (1992)
- [26] D.Q. Kern, Process heat transfer, McGraw-Hill Book Company, New York (1992)
- [27] Ph. Lebrun, Cryogenic systems, CAS (CERN accelerator school) Superconductivity in particle accelerators, Haus Rissen, Hamburg, Fed. Rep. Germany, 30 May-3 June 1988, pp 41-86 (1989)
- [28] K.D. Timmerhaus, Conductive heat transfer, in Heat Transfer at low temperatures, W. Frost (Ed.) Chapter2, Plenum Press, New York (1975)
- [29] H.S. Carslaw, J.C. Jaeger, Conduction of heat in solids, Oxford University Press, Oxford (1959)
- [30] V.J. Jonhson (Ed.), A compendium of the properties of materials at low temperatures, WADD Technical Report (1960)
- [31] W. Obert et al., Emissivity Measurements of Metallic Surfaces used in Cryogenic Applications, Adv. Cryo. Eng. 27, p.293 (1982)
- [32] F.W. Dittus, L.M.K. Boelter, University of California, Berkeley, Publ. Eng. 2, p 443 (1930)
- [33] J. D. Gonczy, W. N. Borosky, R. C. Nieman, Multilayer insulation (MLI) in the superconducting super collider - A practical engineering approach to

- physical parameters governing MLI thermal performance, Supercollider 1, Plenum Press, New York, pp 483-491 (1989)
- [34] W.N. Boroski, T.H. Nicol, C.J. Schoo, Design of the multilayer insulation system for the superconducting supercollider 50 mm dipole cryostat, Supercollider 3, Plenum Press, New York, pp 849-860 (1991)
- [35] S.D. Augustynowicz, J.A. Demko, V. I. Datskov, Analysis of multilayer insulation between 80 K and 300 K, Adv. Cryo. Eng. 39, pp 1675-1682 (1994)
- [36] E. F. Daly, R.K. Pletzer, Analysis of ER String test thermally instrumented interconnect 80-K MLI blanket, Supercollider 5, pp 323-326, Plenum Press, New York (1994)
- [37] V. Benda, Ph. Lebrun, L. Mazzone, V. Sergo, B. Vullierme, Qualification of thermal insulation systems between 80 K and 4.2 K, Proc. Kryogenika '94 Usti nad labem, pp 107-110 (1994)
- [38] S. Jacob, S. Kasthuriengan, R. Karunanithi, Investigations into the thermal performance of multilayer insulation (300-77 K). Part 1: Calorimetric studies, Cryogenics 32, pp 1137-1146 (1992)
- [39] S. Jacob, S. Kasthuriengan, R. Karunanithi, Investigations into the thermal performance of multilayer insulation (300-77 K). Part 2: Thermal analysis, Cryogenics 32, pp 1147-1153 (1992)
- [40] E. M. Leung, R.W. Fast, H.L. Hart, J.R. Jeim, Techniques for Reducing Radiation Heat Transfer Between 77 K and 4.2 K, Adv. Cryo. Eng. 25, p.489 (1980)
- [41] T.C.Nast, D.J. Frank, I.E. Spradley, Investigations of multilayer insulation at low boundary temperatures, ICEC-11, Berlin west, pp 561-564 (1986)
- [42] R.R. Conte, Éléments de cryogénie, Masson (1970)
- [43] Ph. Lebrun, L. Mazzone, V. Sergo, B. Vullierme, Investigation and qualification of thermal insulation systems between 80 K and 4.2 K, Cryogenics 32, ICMC Supplement, pp 44-47 (1992)
- [44] S. W. Van Sciver, Helium cryogenics, Plenum Press, New York (1986)
- [45] W.F. Vinen, Superfluidity, CAS (CERN accelerator school) Superconductivity in particle accelerators, Haus Rissen, Hamburg, Fed. Rep. Germany, 17-24 May 1995, pp. 309-319 (1996)

-
- [46] Ph. Lebrun, Operating at 1.8 K: the technology of superfluid helium, CAS (CERN accelerator school) Superconductivity in particle accelerators, Haus Rissen, Hamburg, Fed. Rep. Germany, 17-24 May 1995, pp. 321-334 (1996)
- [47] P. Seyfert, G. Claudet, Superfluidity, CAS (CERN accelerator school) Superconductivity in particle accelerators, Haus Rissen, Hamburg, Fed. Rep. Germany, 30 May-3 June 1988, pp.239-251 (1989)
- [48] G. Bon Mardion, G. Claudet, P. Seyfert, Practical data on steady state heat transport in superfluid helium at atmospheric pressure, Cryogenics **19**, pp 45-47 (1979)
- [49] Hepak, Version 3.3, Cryodata Inc., Niwot, Colorado (1994)
- [50] G. Riddone, Bilancio Termico della Semicella Prototipo dell' Acceleratore di Particelle LHC, Tesi di Laurea in Ingegneria Nucleare, Politecnico di Torino, Italy (1993)
- [51] Excel, Windows version 5.0, Microsoft Corporation (1995)
- [52] K. Coeck, Contacts thermiques à basses températures, Master Degree, Industriële Hogeschool Leuven, Belgium (1995)

Experimental tools and methods for assessing thermal performance of cryostats

- [53] H. Danielsson, Ph. Lebrun, J.M. Rieubland, Precision heat inleak measurements on cryogenic components at 80 K, 4.2 K and 1.8 K, Cryogenics **32**, ICEC Supplement, pp.215-218 (1992)
- [54] M. Blin, H. Danielsson, B. Evans, M. Mathieu, Design, construction and performance of magnet support posts for the Large Hadron Collider, Adv. Cryo. Eng. **39 A**, pp. 671-677 (1994)
- [55] H. Danielsson, G. Ferlin, B. Jenninger, C. Luguët, S.E. Milner, J.-M. Rieubland, Cryogenic performance of a superfluid helium relief valve for the LHC superconducting magnets, Adv. Cryo. Eng. **41A**, pp 805-810 (1996)
- [56] L. Dufay , G.Ferlin, Ph. Lebrun, G. Riddone, J.-M.Rieubland, A. Rijllart, B. Szeless, L. Williams, A full-scale thermal model of a prototype dipole cryomagnet for the CERN LHC project, Cryogenics **34**, ICEC supplement, pp 693-696 (1994).
- [57] L. Rossi, V. Sergo, B. Szeless, L. Taviani, B. Vullierme, R. van Weelderen and L. Williams, Thermal behaviour and cryogenic performance of the first

-
- CERN/INFN prototype dipole cryomagnet for the CERN LHC project, Cryogenics 34, ICEC supplement, pp 697-700 (1994)
- [58] A. Bézaguet, J. Casas-Cubillos, B. Flemsaeter, B. Gaillard-Grenadier, Th. Goiffon, H. Guinaudeau, Ph. Lebrun, M. Marquet, L. Serio, A. Suraci, L. Taviani and R. van Weelden, The superfluid helium cryogenic system for the LHC test string: design, construction and first operation, Adv. Cryo. Eng. 41A, pp 777-784 (1996)
- [59] Specification for the construction of the dummy cold mass, Note AT-MA/93-71, CERN (1993)
- [60] L. Borel, Thermodynamique et énergétique, Presse Polytechnique Romandes, Lausanne (1984)
- [61] CUEFA, COURS DE CRYOGENIE, Thermométrie a basse température, Universités de Grenoble, Formation CERN (1995)
- [62] T.A. Kibel, M.A. Kozyczak, S.W. Schwenterly, W.M. Bell, Effects of mounting methods on temperature sensor accuracy below 10 K, Supercollider 4, pp 619-625, Plenum Press, New York (1992)
- [63] H.D. Ramsbottom, S. Ali, D.P. Hampshire, Response of a new ceramic-oxynitride (Cernox) resistance in temperature sensor in high magnetic field, Cryogenics 36, pp 61-63 (1996)
- [64] D.A. Dimitrov, A.L. Zahariev, J.K. Georgiev, G.A. Kolev, J.N. Petrinski, Tz. Ivanov, Thin film platinum resistance thermometers: calibration and mathematical description of T(R) function, Cryogenics 34, pp 487-489 (1994)
- [65] J. Ylöstalo, P. Berglund, T.O. Niinikoski, R. Voutilainen, Cryogenic temperature measurement for large applications, Cryogenics 36, pp 1033-1038 (1996)
- [66] Norm DIN 43 760 (class B)
- [67] LabVIEW2.2, User manual, National Instruments Corporation, Austin, USA (1992)
- [68] LabVIEW2.2 GPIB, User manual, National Instruments Corporation, Austin, USA (1992)
- [69] DAQ NB-AO-6, User manual, National Instruments Corporation, Austin, USA (1993)

-
- [70] DAQ Lab-NB, User manual, National Instruments Corporation, Austin, USA (1993)
- [71] P. Faugeras, Assembly and Commissioning of the LHC test String, presented at PAC'95, Dallas (1995)
- [72] A. Bézaguet, J. Casas-Cubillos, H. Guinaudeau, B. Hilbert, Ph. Lebrun, L. Serio, A. Suraci, R. van Weeldereen, Cryogenic operation and testing of the extended LHC prototype magnet string, paper presented at ICEC16/ICMC, Kitakyushu (1996)
- [73] A. Bézaguet et al., The LHC test string: first operational experience, presented at EPAC-96, Sitges, Barcelona (1996)
- [74] A. Rivetti, G. Martini and G. Birello, Metrological performances of Venturi flowmeters in normal, supercritical and superfluid helium, Adv. Cryo. Eng. 39B, pp 1051-1058 (1994)
- [75] Specification for a Data Acquisition System for the LHC Test String, Note AT-94-02, CERN (1994)
- [76] D. Brahy, J. Casas-Cubillos, M. Grippeling, D. Lavielle, G. Leo, L. Madaro., A. Rijllart, R. Saban, M. Skiadelli, The control and data acquisition of the LHC test String, presented at the International Conference on Accelerator and Large Experimental Physics Control Systems, Chicago (1995).
- [77] USData®, Factory link® fundamentals, Version 4.4 (1995)
- [78] V. Benda, G. Duraffour, A. Guiard-Marigny, Ph. Lebrun, F. Momal, R. Saban, V. Sergo, L. Taviani and B. Vullierme, Cryogenic infrastructure for superfluid helium testing of LHC prototype superconducting magnets, Adv. Cryo. Eng. 39A, pp 641-648 (1994)
- [79] V. Benda, M. Granier, Ph. Lebrun, G. Novellini, V. Sergo, L. Taviani and B. Vullierme, Cryogenic benches for superfluid helium testing of full-scale prototype superconducting magnets for the CERN LHC project, Cryogenics 34, ICEC supplement (1994)

Calculated and measured thermal performance of cryostats

- [80] V. Benda, L. Dufay, PG. Ferlin, Ph. Lebrun, G. Riddone, J.-M. Rieubland, B. Szeless, L. Taviani, L. Williams, Measurement and analysis of thermal performance of LHC prototype cryostats, Adv. Cryo. Eng. 41A, pp 785-792 (1996)

-
- [81] G. Krainz, G. Riddone and L. Serio, Contact Resistance of Superconducting Cable Splices on the LHC Prototype Magnet String, LHC project report 61, CERN (1996)
- [82] J.T. DeLalio, D.P. Brown, J.H. Sondericker, Heat leak testing of a superconducting RHIC dipole magnet at Brookhaven National Laboratory, Adv. Cryo. Eng. 39A, pp 325-334 (1994)
- [83] A.I. Ageyev, M.V. Levin, S.N. Logachev, A.N. Shamichev, S.I. Zinchenko, Static heat leak measurements for UNK superconducting dipoles, Adv. Cryo. Eng. 37A, pp 573-576 (1991)
- [84] W.N. Boroski, T.H. Nicol, M.K. Rushman, C.J. Schoo, SSC 50mm dipole magnet magnet cryostat thermal measurement results, Supercollider 5, Plenum Press, New York, pp 847-848 (1994)
- [85] G.E. Hardy, S.C. Peck, J.D. DiRe, Thermal analysis of the production dipole magnets for the superconducting super collider, Supercollider 2, Plenum Press, New York (1990)
- [86] Wilson, M.N., Superconducting Magnets, Clarendon, Oxford (1983)
- [87] W. Burgett, L. Cromer, D. Haenni, M. Hentges, T.Jaffery, P. Kraushaar, M. Levin, A. McInturff, G. MulHolland, D. Richter, W. Robinson, D. Voy, J. Weisend II, J. Zatopek, Power tests of a string of magnets comprising a full cell of the superconducting super collider, SSC Note (1994)
- [88] B. Jenninger, Influence of reflecting surfaces on the LHC Support Posts. LHC Project Note 65 (1996)

Potential of an actively cooled screen at 4.5-20 K

- [89] S.L. Bapat, K.G. Narayankhedkar and T.P. Lukose, Experimental investigation of multilayer insulation, Cryogenics 30, pp 710-719 (1990)
- [90] G.Ferlin, B. Jenninger, Ph.Lebrun, G.Peon, G. Riddone, B. Szeless, Comparison of floating and thermalized multilayer insulation systems at low boundary temperature, paper presented at ICEC16/ICMC, Kitakyushu (1996)
- [91] A.F. Zeller, J.C. DeKamp, E.M.W. Leung, R.W Fast, Long term results from the elimination of MLI between 4 and 77 K, Adv. Cryo, Eng 39, pp 1691-1697 (1994)

-
- [92] M. Taneda, T. Ohtani, M. Okuda, J. Tsukuda, Systematic analysis of characteristics for different types of multilayer insulation, Adv. Cryo. Eng. 33, pp 305-311 (1988)
- [93] S.L. Bapat, K.G. Narayankhedkar and T.P. Lukose, Performance prediction of multilayer insulation, Cryogenics 30, pp 700-710 (1990)
- [94] B. Jenninger, G. Peon, B. Szeless, Characterisation of net-type thermal insulators at 1.8 K low boundary temperature, presented at ICMC'96, CERN (1996)
- [95] G. Peon, Thermo mechanical study optimisation of vapour shielded cryostats, Design of components of the half-cell LHC superfluid helium cryostat, Doctoral thesis (in preparation), University of Zaragoza, Spain (1997)

Forced-flow cooldown and warmup

- [96] P.Cruikshank, N.Kos, Ph. Lebrun, G.Riddone, L.Tavian, Investigation of thermal and vacuum transients on the LHC prototype magnet String, paper presented at ICEC16/ICMC, Kitakyushu (1996)
- [97] R.H. Carcagno, W.E. Schiesser, A. Yücel, Cooldown and warmup computer simulations for the SSC ring, Adv. Cryo. Eng. 37A, pp. 699-708 (1992)
- [98] G. Horlitz, H. Lierl, Computer calculations on steady-state operation and different modes of cooldown and warmup of the HERA superconducting proton ring, Adv. Cryo. Eng. 31, pp 723-731 (1986)
- [99] G.Peon, G.Riddone, L.R.Williams, Analytical model to calculate the transient thermo-mechanical behaviour of long thin structures cooled from a pipe: application to the LHC thermal shield, paper presented at ICEC16/ICMC, Kitakyushu (1996)
- [100] R. Perin, The superconducting magnet system for the LHC, LHC note 136, Note AT-MA/90-19, CERN (1990)
- [101] S.V. Patankar, Numerical Heat Transfer and fluid flow, Taylor and Francis, USA (1980)

Natural warmup and accidental loss of insulation vacuum

- [102] Ph. Lebrun, B. Szeless, L. Tavian, L.R. Williams, Experimental investigation of accidental loss of insulation vacuum in an LHC prototype dipole cryostat, Adv. Cryo. Eng. 41A, pp 799-804 (1996)

- [103] D.E. Franks, R.K. Pletzer, The effect of vacuum gas pressures and species on internal heat leak in the SSC magnet design, Supercollider 4, Plenum Press, pp 267-274 (1992)

Annexes

- [104] W.H. McAdams, Heat transmission, Mc-Graw Book Company, New York (1954)
- [105] F. Kreith, W.Z. Black, Basic heat transfer, Harper and Row, Publishers, New York
- [106] R.P. Reed, A.F. Clark, Materials at low temperatures, American Society of Metals, (1983)
- [107] D.A. Wigley, Mechanical properties of materials at low temperatures, Plenum Press, New York (1971)
- [108] T. Horiuchi, T. Ooi, Cryogenic properties of composite materials, Cryogenics 35, pp 677-679 (1995)
- [109] G.K. White, Metals and Alloys: Expansion and Contraction, Adv. Cryo. Eng. 30, pp 407-410 (1984)
- [110] Handbook on materials for superconducting machinery, Metals and ceramics information center, Batelle, Columbus, Note MCIC-HB-04 (1977)
- [111] Fenech, Rohsenow, Prediction of thermal conductance of metallic surfaces in contact, J. of Heat Transfer 85, pp15-24 (1963)
- [112] Hsieh, Touloukian, Correlation and prediction of thermal conductance for nominally flat surfaces, Thermal conductivity, New York, pp 477-494 (1969)
- [113] Thomas, Probert, Correlation for thermal contact conductance in vacuo, J. of Heat Transfer 94, pp 276-281 (1972)
- [114] Fletcher, Gyroog, Prediction of thermal contact conductance between similar metal surfaces, Progress in aeronautics and astronautics 24, pp 273-288 (1971)
- [115] Astrabadi, O' Callaghan, Probert and Jones, thermal contact conductance correlation for stacks of thin layers in high vacuums, J. of Heat Transfer 99, pp 139-142 (1977)
- [116] Miller, Fletcher, Thermal contact conductance correlation for porous materials, Progress in aeronautics and astronautics 39, pp 81-92 (1975)

- [117] L.J. Salerno, P. Kittel, W.F. Brooks, A.L. Spivak and W.G. Marks Jr, Thermal conductance of pressed brass contacts at liquid helium temperatures, Cryogenics 26, pp 217-221 (1986)
- [118] L.J. Salerno, P. Kittel and A.L. Spivak, , Thermal conductance of augmented pressed metallic contacts at liquid helium temperatures, Cryogenics 33, pp 1104-1109 (1993)
- [119] P. Kittel, A.L. Spivak, L.J. Salerno, Thermal conductance of gold plated metallic contacts at liquid helium temperatures, Adv. Cryo. Eng. 37A, pp 241-248 (1992)
- [120] J. Yu, A.L. Yee, R.E. Schwall, Thermal conductance of Cu/Cu and Cu/Si interfaces from 85 k to 300 K, Cryogenics 32, pp 610-615 (1992)
- [121] L.J. Salerno, P. Kittel and A.L. Spivak, Thermal conductance of pressed metallic contacts augmented with indium foil or Apiezon grease at liquid helium temperatures, Cryogenics 34, pp 649-654 (1994)
- [122] M.J. Nilles, S.W. Van Sciver, Effects of oxidation and roughness on Cu contact resistance from 4 K to 290 K, Adv. Cryo. Eng. 34, pp 443-450 (1988)

ANNEX 1

Detailed heat inleaks

A1.1 Heat inleaks of the LHC prototype magnet string

Table A1.1: Calculated heat inleaks in short straight section cryostat in steady-state conditions

Heat inleak	90 K [W]	4.5-10 K [W]	1.9 K [W]
Cold mass (6.915 m)			
Support posts	10.80	2.90	0.80
Thermal shield	19.57		
Radiative insulation		0.27	1.19
Vacuum barrier	9.16	0.19	0.80
Valves	2.15	0.15	0.49
Instrumentation feedthrough	0.41		0.03
<i>Sub-total</i>	42.09	3.51	3.31
Interconnection (0.44 m)			
Instrumentation feedthrough	0.43		0.24
Safety valve	0.35		0.48
Thermal shield	1.40		
Radiative insulation		0.03	0.08
Beam vacuum feedthrough	0.91		0.01
<i>Sub-Total</i>	3.09	0.03	0.81
Total	45.18	3.54	4.12

Table A1.2: *Calculated heat inleaks in dipole cryostat in steady-state conditions*

Heat inleak	90 K	4.5-10 K	1.9 K
	[W]	[W]	[W]
Cold mass (10.252 m)			
Support posts	10.80	2.90	0.80
Thermal shield	32.60		
Radiative insulation		0.40	2.02
<i>Sub-total</i>	43.40	3.30	2.82
Interconnection (0.44 m)			
Instrumentation feedthrough	0.43		0.24
Safety valve	0.35		0.48
Thermal shield	1.40		
Radiative insulation		0.03	0.08
<i>Sub-Total</i>	2.18	0.03	0.80
Total	45.58	3.37	3.62

Table A1.3: *Calculated heat inleaks in the LHC prototype magnet string in steady-state conditions*

Heat inleak	90 K	4.5-10 K	1.9 K
	[W]	[W]	[W]
String Feed Box	24.31	1.73	3.46
Short Straight Section	45.18	3.54	4.12
Dipole 1	45.23	3.37	3.14
Dipole 2	45.23	3.37	3.14
Dipole 3	45.58	3.37	3.62
String Return Box	33.21	1.31	3.73
Total	238.74	16.69	21.21

A1.2 Heat inleaks of the Cryostat Thermal Model

The following tables show the calculated steady-state heat inleaks from measured data under different operating conditions. The nominal steady-state nominal conditions are 1.9 K, 5-10 K and 50-75 K at 10^{-4} Pa. The tables are presented according to the parameters varied from the nominal conditions: temperature in the circuit E-F, temperature in the circuit C-D and residual He pressure in the insulation vacuum.

Table A1.4: *Measured steady-state heat inleaks for different temperatures of the circuit E-F (precision= $\pm 5\%$)*

Temperature level		Test TS1	Test TS2	Test TS3
1.9 K	Cold mass [K]	1.86	1.88	1.72
	Mass-flow [g/s]	0.08	0.11	0.27
	Heat inleak [W]	1.82	2.53	6.1
	Heat inleak [W/m]	0.18	0.25	0.61
4.5-20 K	Line C_inlet [W]	5.3	5.6	7.0
	Line C_outlet [W]	6.5	7.9	9.8
	Line D_inlet [W]	7.3	9.2	12.6
	Line D_outlet [W]	7.7	9.8	13.8
	Support post [W]	11	13	15
	Mass-flow [g/s]	0.24	0.2	0.15
	Heat inleak [W]	2.35	3.44	5.29
	Heat inleak [W/m]	0.23	0.33	0.53
50-75 K	Line E_inlet [K]	46	50	80
	Line E_outlet [K]	53	63	101
	Line F_inlet [K]	65	84	133
	Line F_outlet [K]	76	102	148
	Support post [K]	88	105	126
	Thermal shield [K]	77	100	150
	Mass-flow [g/s]	0.5	0.3	0.15
	Heat inleak [W]	47.8	44.7	30.0
	Heat inleak [W/m]	4.8	4.4	3.0

In the tests TS the temperature of the circuit E-F was varied keeping constant the other parameters. Tests LC were performed changing the temperature of the circuit C-D

Table A1.5: *Measured steady-state heat inleaks for different temperatures of the circuit C-D (precision= $\pm 5\%$)*

	Temperature level	Test LC1	Test LC2
1.9 K	Cold mass [K]	1.8	1.84
	Mass-flow [g/s]	0.08	0.11
	Heat inleak [W]	1.85	2.58
	Heat inleak [W/m]	0.18	0.26
4.5-20 K	Line C_inlet [W]	5.0	15.4
	Line C_outlet [W]	7.0	19.2
	Line D_inlet [W]	11.7	25.0
	Line D_outlet [W]	12.3	26.0
	Support post [W]	11	18
	Mass-flow [g/s]	0.12	0.06
	Heat inleak [W]	2.1	1.27
	Heat inleak [W/m]	0.21	0.13
50-75 K	Line E_inlet [K]	40	46
	Line E_outlet [K]	46	52
	Line F_inlet [K]	58	62
	Line F_outlet [K]	70	73
	Support post [K]	77	86
	Thermal shield [K]	74	75
	Mass-flow [g/s]	0.5	0.5
	Heat inleak [W]	48.0	43.2
	Heat inleak [W/m]	4.8	4.3

In the following table only the 1.9 K level is shown since the degradation of insulation vacuum does not affect significantly the steady-state heat inleaks at 4.5-20 K and 50-75 K.

Table A1.6: *Measured steady-state heat inleaks at 1.9 K under varying residual He pressure (precision= $\pm 5\%$)*

	Vacuum	Heat inleak	
	[Pa]	[W]	[W/m]
Test VD1	$5 \cdot 10^{-4}$	1.9	0.19
Test VD2	10^{-3}	2.1	0.21
Test VD3	$4.4 \cdot 10^{-3}$	3.4	0.34
Test VD4	10^{-2}	5.4	0.54
Test VD5	$5 \cdot 10^{-2}$	15.1	1.50
Test VD6	10^{-1}	29.9	2.97

To confirm that the new end boxes of CTM2, all made of stainless steel, did not increase the cryostat heat inleaks, steady state heat losses under nominal conditions were performed and results compared with those obtained with the previous CTM version (table A1.7).

Table A1.7: *Comparison between CTM1 and CTM2 heat inleak measurements in nominal steady-state condition*

	Temperature level		
	50-75 K	4.5-20 K	1.9 K
	[W]	[W]	[W]
CTM1 (residual He pressure = 10^{-3} Pa)	47.8 ± 3	2.35 ± 0.15	1.82 ± 0.15
CTM2 (residual He pressure = $4 \cdot 10^{-4}$ Pa)	47.4 ± 3	2.21 ± 0.15	1.90 ± 0.15

ANNEX 2

Material properties at low temperatures

Knowledge of material properties at low temperatures [104-107] is fundamental in the design and construction of performant cryostats. Investigations of new materials constitute an active field of research. This chapter presents a survey of the thermal, mechanical and electrical properties which are important in cryogenics. Elastic properties are not mentioned as they do not change significantly at low temperature.

A2.1 Specific heat

In cryogenics, specific heat is involved in numerous calculations including the dynamics of cooling, thermal energy stored and transient heat transfer.

For solids, two simple theories describe the behaviour of metals and insulators over the entire range of temperature of interest. The first theory describes the specific heat of phonons which exist in a solid. For most solids, except metals at very low temperature, the phonon contribution to the heat capacity dominates (Debye law). For metals at low temperatures (T around 1 K), the heat capacity is mainly governed the conduction electrons (Fermi gas model).

The specific heat of material increases with temperature and approaches to zero near the absolute zero (figure A2.1).

A2.2 Electrical resistivity

Near room temperature, the electrical resistivity of most pure metals decreases with temperature as the result of electron-phonon scattering representing the temperature-dependent contribution to the resistivity ($\rho(T)$). At vanishingly low temperature, the resistivity approaches a constant value ρ_0 that depends on metal purity and lattice imperfections. The total resistivity is given by Matthiessen's law:

$$\rho = \rho(T) + \rho_0 \quad (\text{A2.1})$$

The effect of impurities is to shift the curve uniformly upward. The residual resistivity ratio [$RRR = \rho(273 \text{ K}) / \rho(4.2 \text{ K})$] is used often as a measure of the purity of the metal. At very low temperature ρ_0 is much greater than $\rho(T)$ so that temperature variations do not affect significantly the value of resistivity. At high temperature the

opposite behaviour occurs and resistivity is independent of purity. The electrical resistivity of selected materials is shown in figure A2.2.

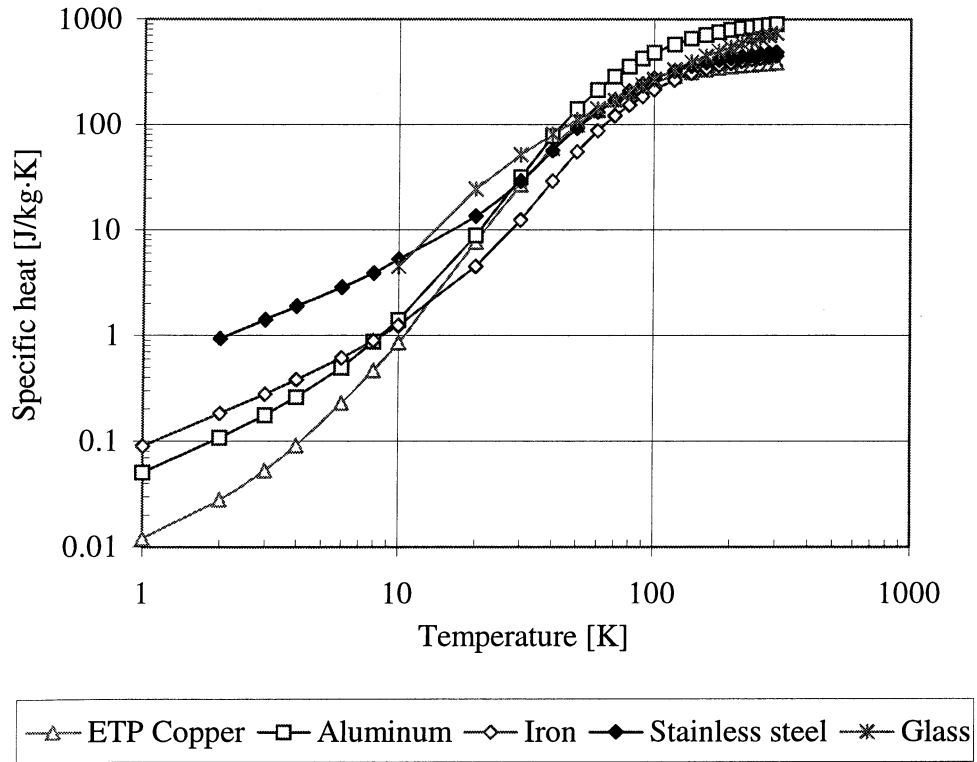


Figure A2.1: Specific heat of selected materials at low temperature [30]

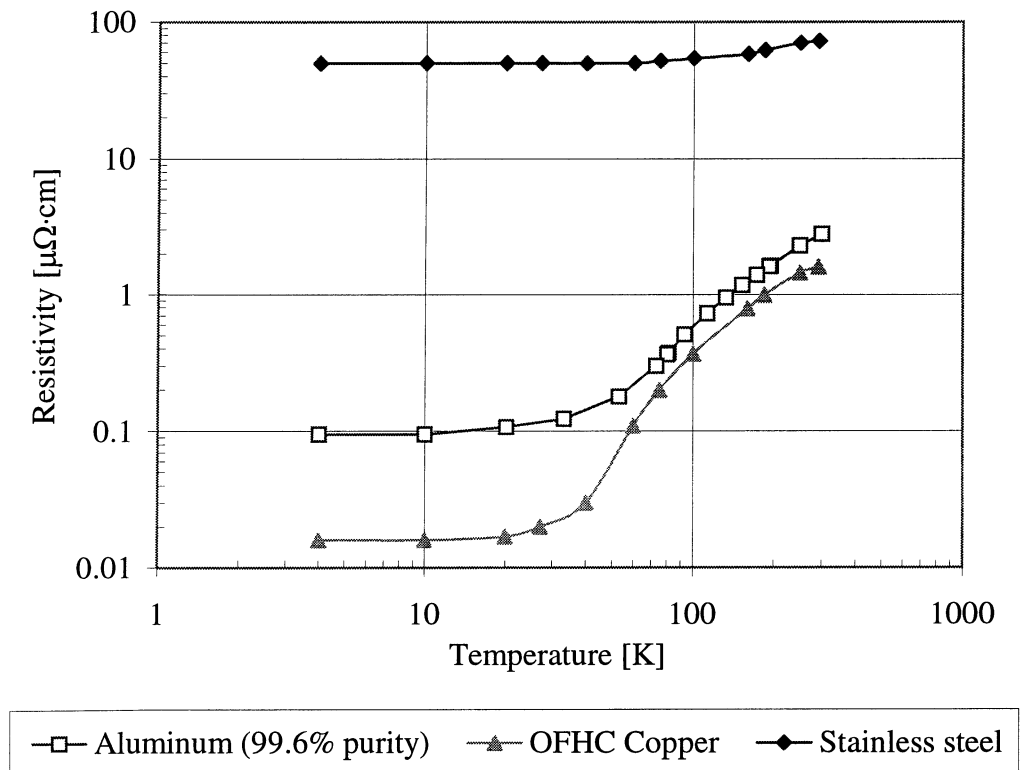


Figure A2.2: Electrical resistivity of selected materials at low temperature [30]

A2.3 Thermal conductivity

The thermal conductivity k is a property that determines the temperature gradient across a substance in the presence of a heat flow. Experimental measurements made to determine the thermal conductivity of materials showed it depends on many parameters, such as the chemical composition, the phase (solid, liquid, gaseous), the crystalline structure, the temperature and the pressure.

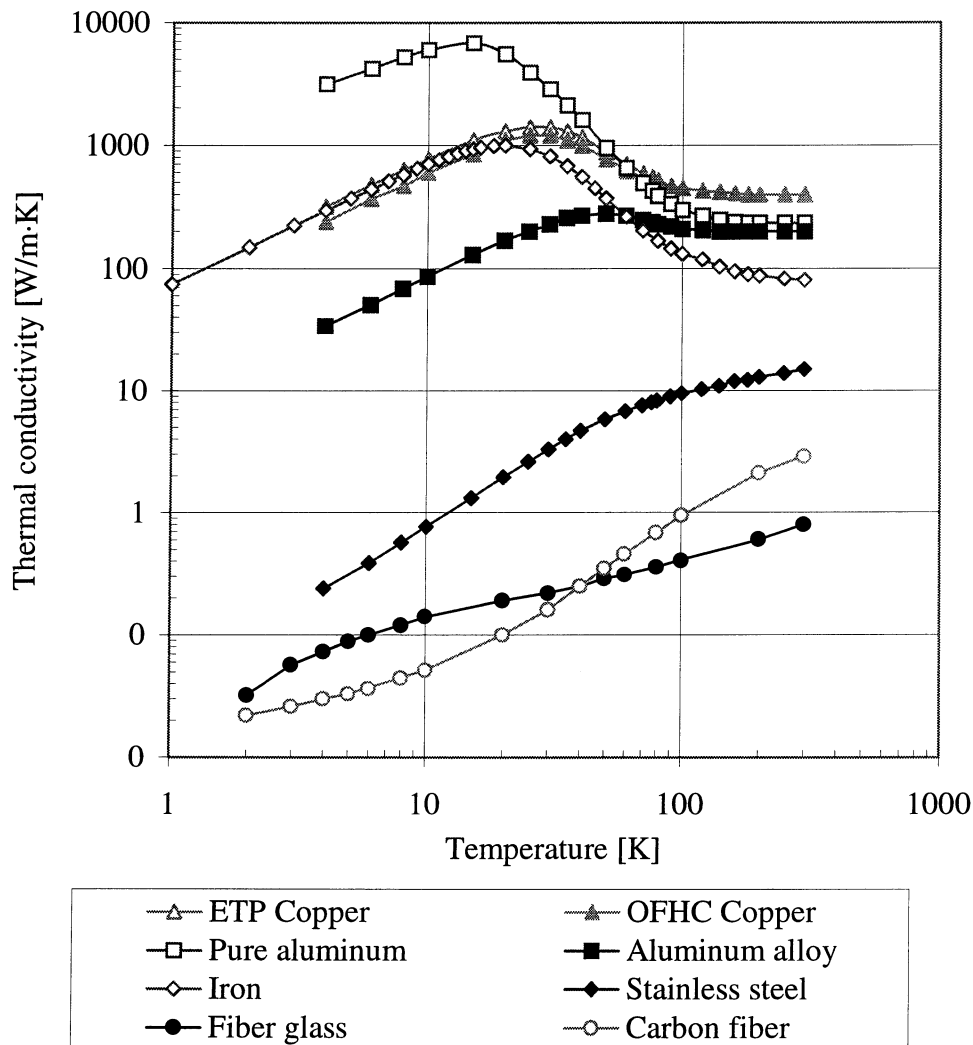


Figure A2.3: Thermal conductivity of selected materials at low temperature [30]

In solids, heat is conducted by two processes: lattice vibration and transport by free electrons.

For pure metals, the first mechanism is very small and conduction is dominated by electron motion. The electrons transport both electric charge and thermal energy from a high-temperature region to a low-temperature region. The pure metals have in general the thermal conductivity decreasing with temperature, but the presence of impurities may completely change this tendency. Normally it is possible to represent the thermal conductivity of a metal with the following relationship:

$$K = K_0(1 + cT) \quad (\text{A2.2})$$

where K_0 is the thermal conductivity of reference and c a constant.

In insulators, the principal mechanism of heat conduction is lattice vibrations. The thermal conductivity on temperature increases almost linearly with temperature. The thermal conductivity of several technical materials as a function of temperature is shown in figure A2.3.

In liquids, the thermal conductivity depends on temperature and is not very sensitive to pressure. Most liquids show a thermal conductivity decreasing with temperature.

In gases, in case of classical conduction the thermal conductivity is independent of pressure and increases with pressure and decreases with molecular weight (figure A2.4).

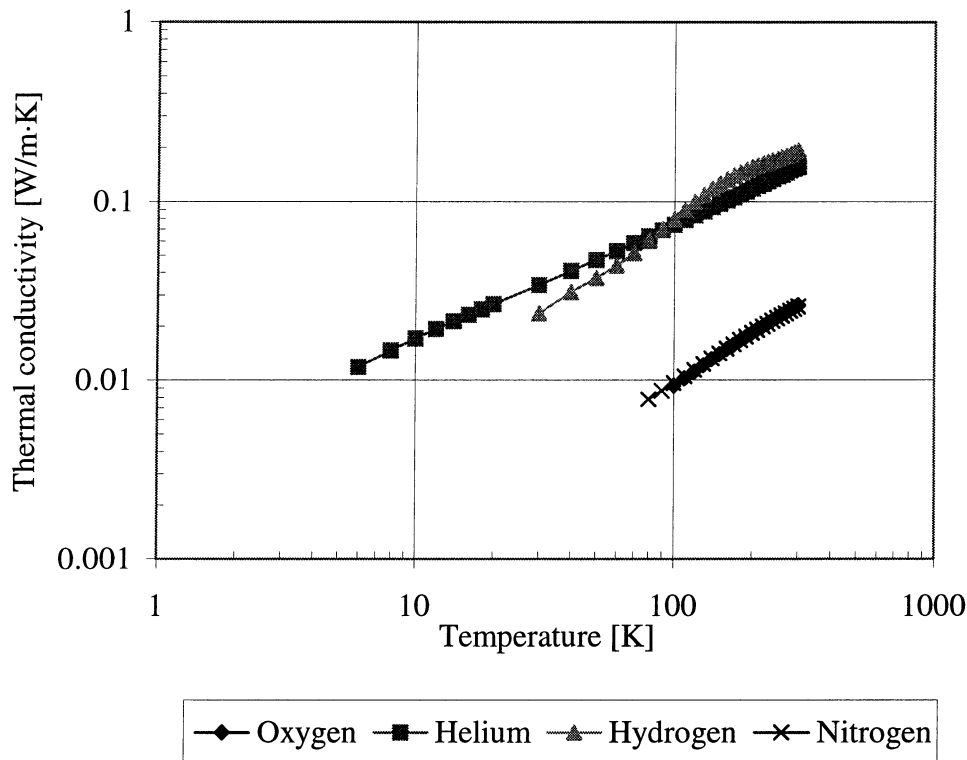


Figure A2.4: Thermal conductivity of selected gases at low temperature [49]

A2.4 Thermal contraction

All materials change their physical dimensions when they are cooled to low temperatures [108, 109]. Most of the contraction occurs between ambient and liquid nitrogen temperatures. When designing a cryostat, it is very important to understand the thermal contraction behaviour of technical materials. The thermal expansivity or contraction is given by a thermodynamic definition. For liquids and gases the factor to consider is the volume expansivity given by:

$$\beta_T = \frac{1}{V} \left(\frac{\partial V}{\partial T} \right)_P \quad (\text{A2.3})$$

where β_T is generally a function of temperature.

For solids, the changes in individual dimensions may be different because of anisotropic effects and the linear thermal expansion coefficient is given by:

$$\alpha_T = \frac{1}{l} \left(\frac{\partial l}{\partial T} \right)_p \quad (\text{A2.4})$$

For isotropic materials:

$$\alpha_T = \frac{1}{3} \beta_T \quad (\text{A2.5})$$

For most common solids near room temperature, the linear expansion coefficient is almost constant. At low temperatures, the expansion coefficient α_T decreases and approaches absolute zero with zero slope.

Because of the non-linear nature of the expansion of materials, it is often more useful to have the integrated thermal contraction for the purpose of design. Figure A2.5 shows the integrated thermal contraction of several materials at low temperatures. It is important to note that metals typically have integrated contractions in the range of 0.5% or less. Polymers such as nylon and teflon contract three times as much as metals. Some amorphous materials, particularly glasses, have nearly zero or sometimes negative thermal contraction.

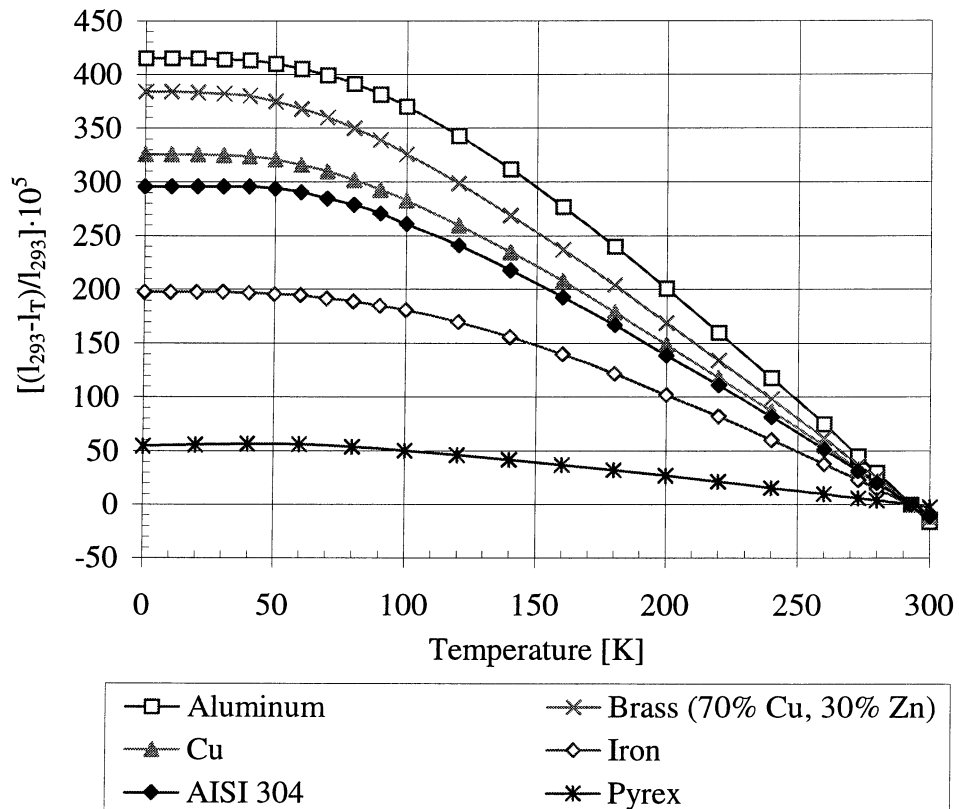


Figure A2.5: Thermal contraction of selected materials at low temperature

A2.4 Mechanical properties

It is important to know which structural materials remain ductile at low temperature. The low-temperature embrittlement represents one of the limits in the choice of the material. In particular, the structural materials should operate above the ductile-to-embrittlement transition temperature. Ductility is desirable, so that eventual stresses beyond design values can be redistributed to safe levels. Brittle materials are not protected against excessive stress as an overstress often produces the failure of the material. The plastic deformation in crystalline materials depends on the mobility of dislocations within the crystal which also depends on temperature. The face-centered cubic metals, such as copper and its alloys, nickel and its alloys, aluminum and its alloys, and austenitic stainless steel show a ductile behaviour at low temperature if they are ductile at room temperature. In contrast, body-centered cubic metals, such as iron, carbon and low-alloy steel have a brittle behaviour at low temperatures. Most plastics become brittle at low temperatures.

Structural materials used in cryogenics should also be characterised by sufficient yield and ultimate tensile strengths.

Figures A2.6 and A2.7 show the yield and the ultimate tensile strengths for several materials of interest in cryogenic applications.

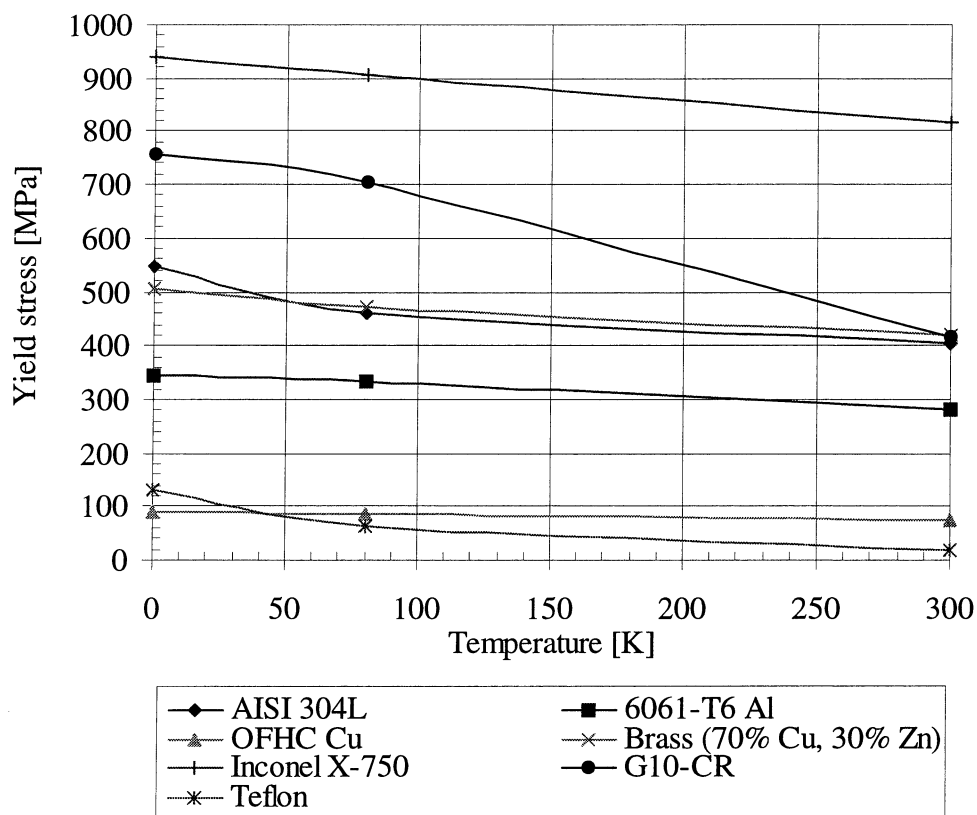


Figure A2.6: Yield stress of selected materials at low temperature [110]

For most common solids, the yield and the ultimate tensile strengths are greater at low temperatures than at ordinary temperatures. The increase in strength is seen to result from the reduced thermal excitation within the lattice, which inhibits the

mobility of dislocations. For metals, the strength at 4 K may be two to five times that at ambient temperature. For body-centered cubic steels, the yield strength increases so rapidly with decreasing temperature that below a certain temperature these materials fracture before they reach their yield strengths. For plastics, the strength at 76 K may be one and a half to eight times greater than the room-temperature value. Glasses show less change in strength at low temperature.

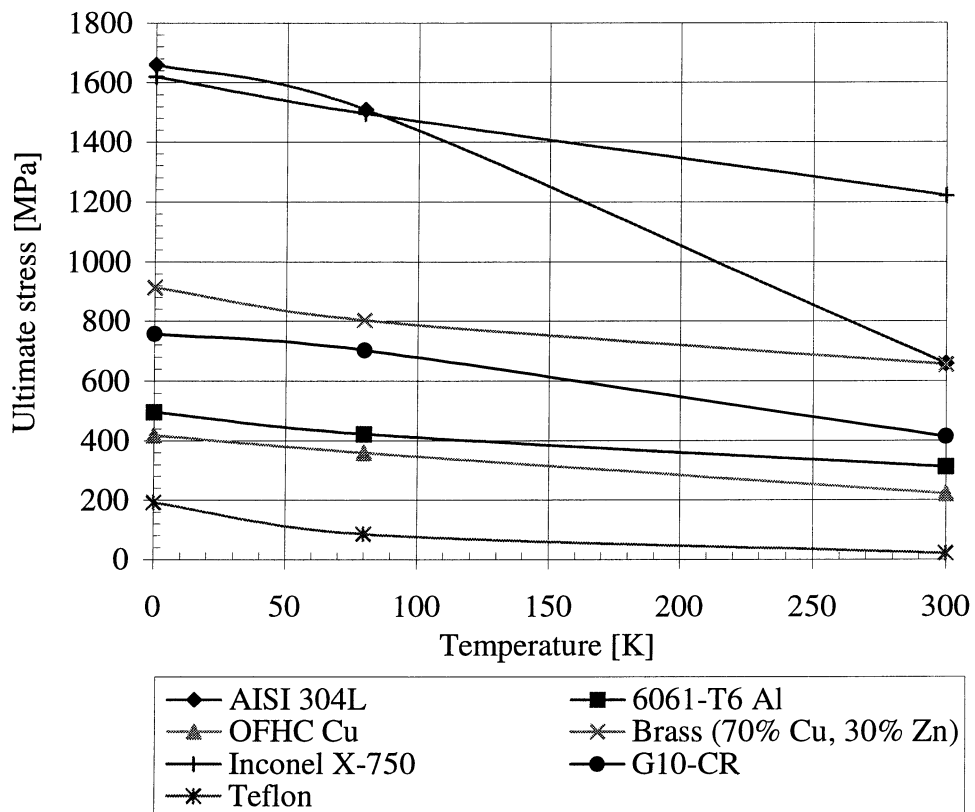


Figure A2.7: *Ultimate stress of selected materials at low temperature [110]*

ANNEX 3

Helium properties

The helium properties [49] mostly involved in thermal calculations are shown in figures A3.3, A3.4, A3.5, A3.6. The phase and the T-S diagrams are presented in figures A3.1 and A3.2. Some important constants of helium are listed in table A3.1.

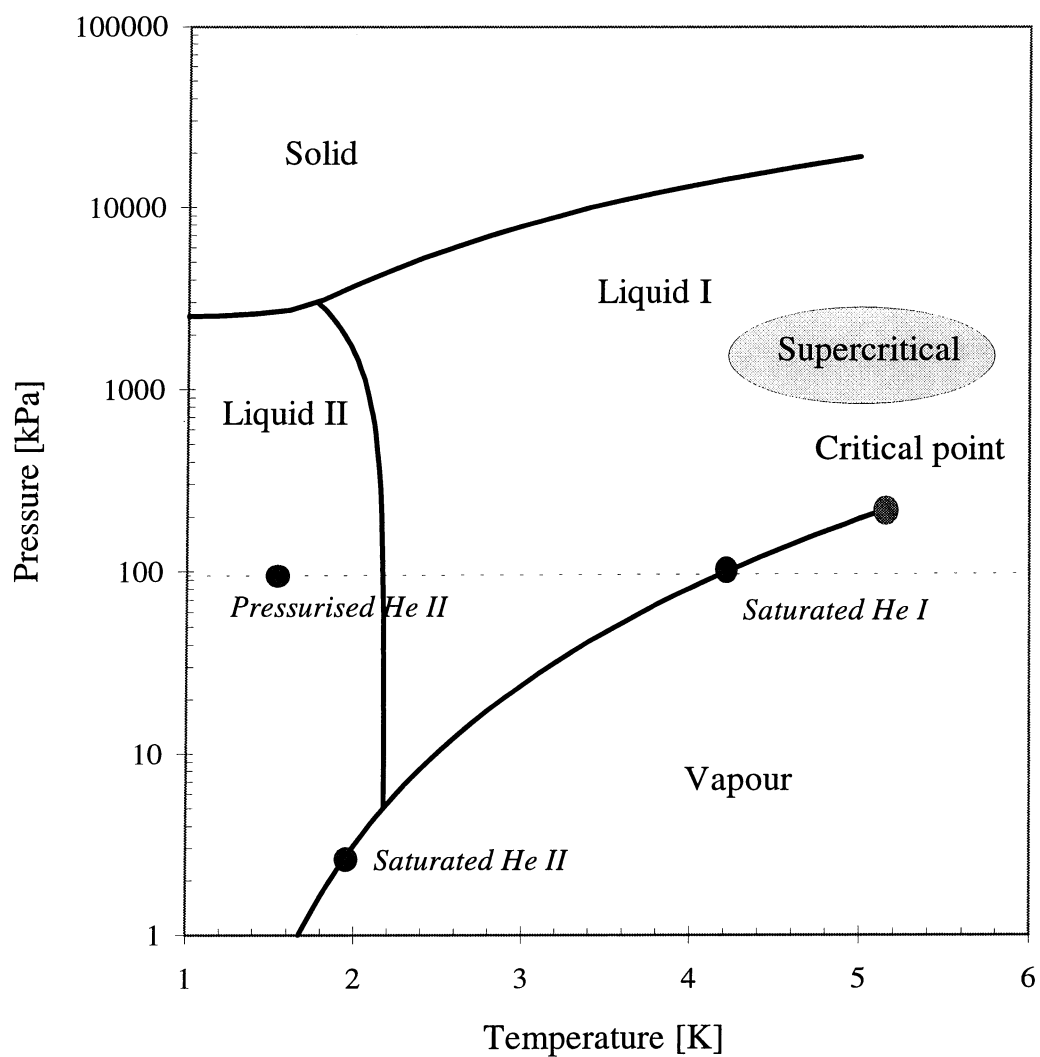


Figure A3.1: Phase diagram of helium

Figure A3.2: Temperature-entropy diagram for helium (NBS)

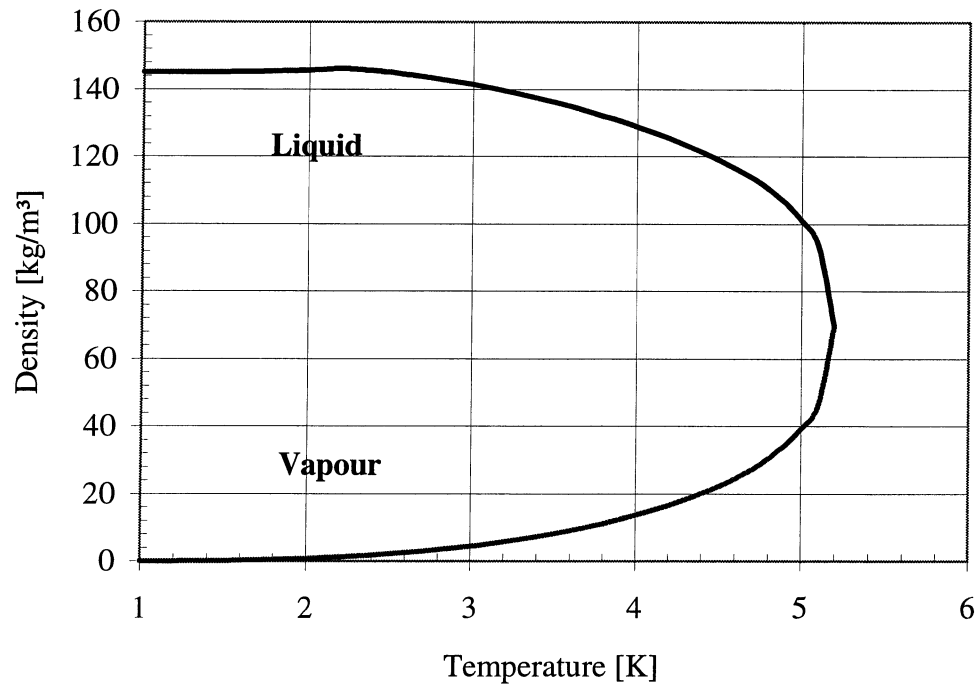


Figure A3.3: *Density of helium at saturation*

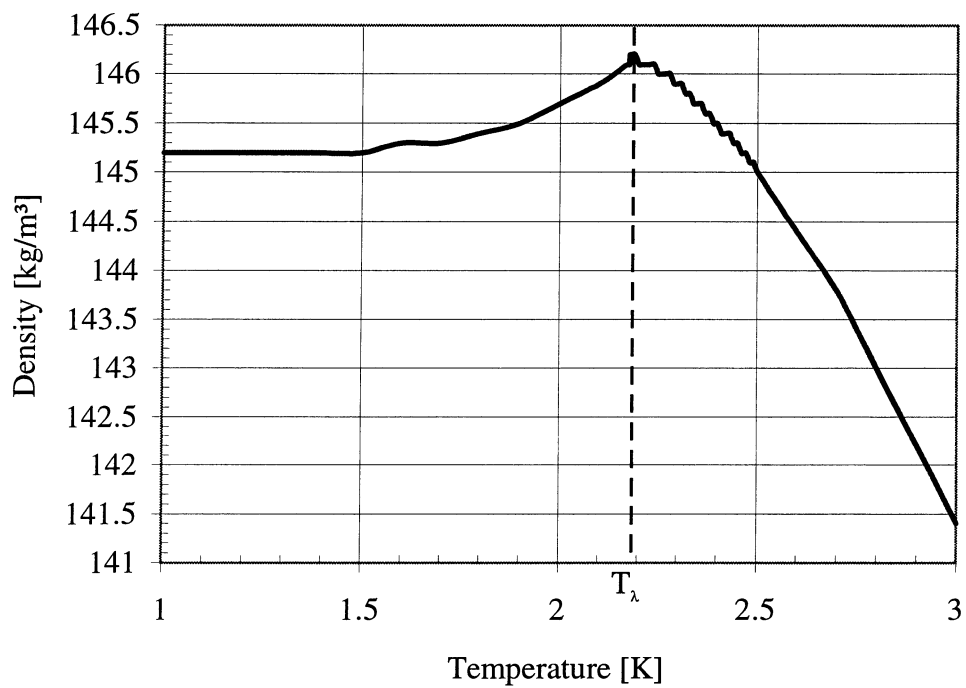


Figure A3.4: *Density of liquid helium at saturation*

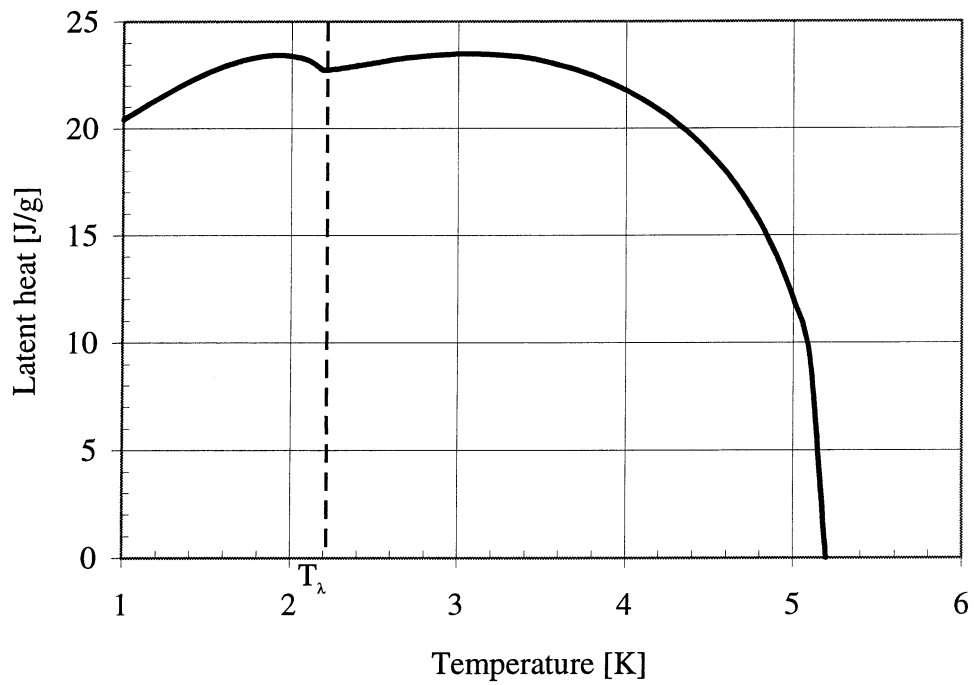


Figure A3.5: Latent heat of vaporisation of helium

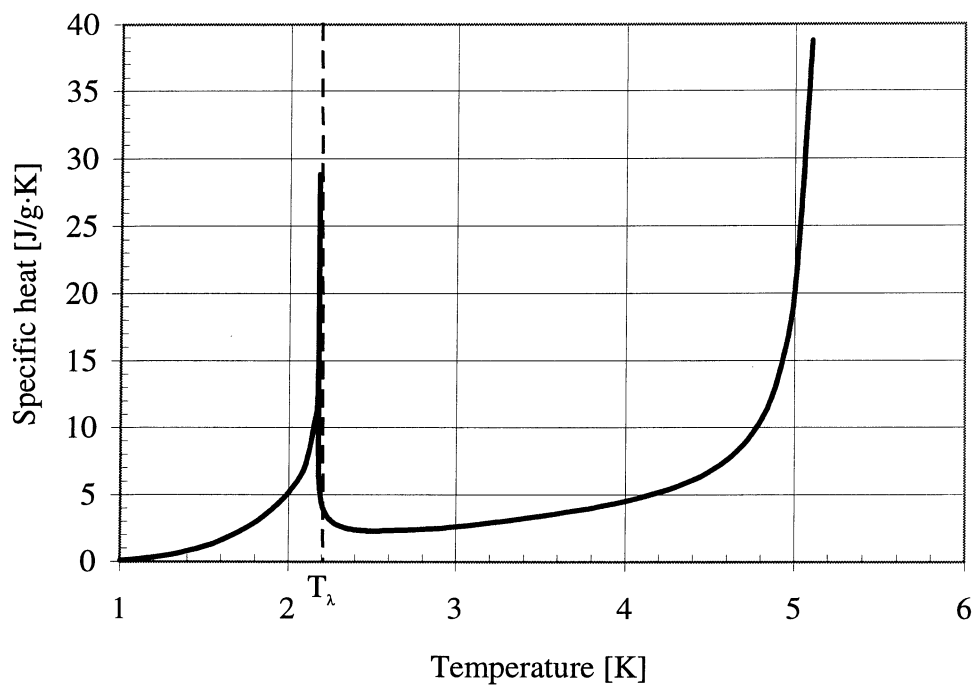


Figure A3.6: Specific heat of liquid helium at saturation

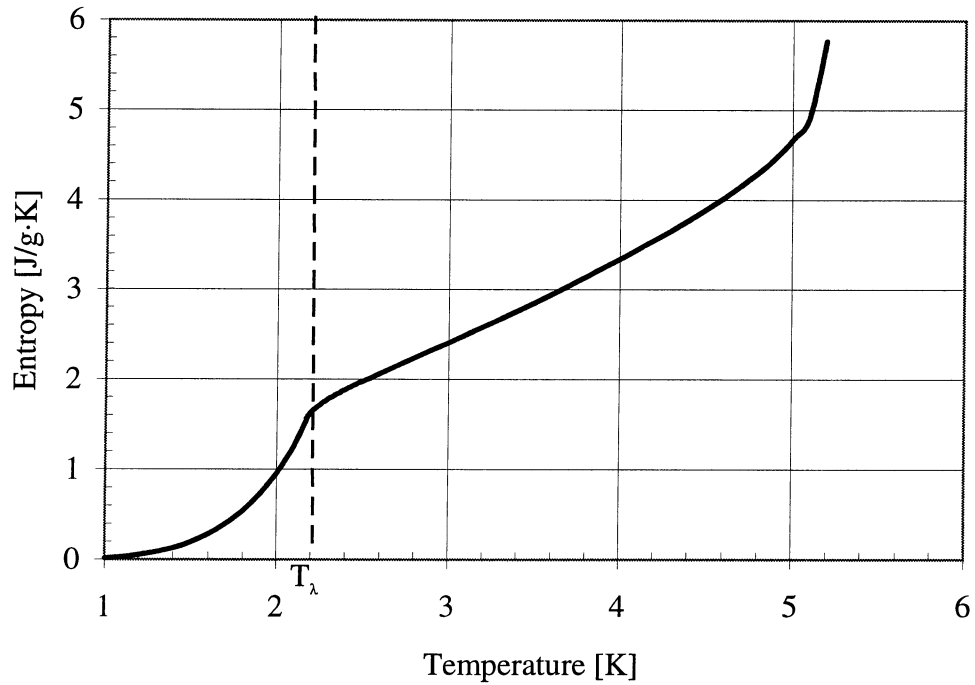


Figure A3.7: Entropy of liquid helium at saturation

Table A3.1: Helium characteristics

Gas constant	2077.23476 J/kg·K
Molar weight	4.0026 g/mole
Pressure in standard state	0.101325 Pa
Critical pressure	227.4623 Pa
Critical temperature	5.1953 K
Critical density	69.6412 kg/m ³
Saturated condition on lambda line	
Temperature	2.1768 K
Pressure	5.0418 kPa
Density of liquid helium	146.15 kg/m ³
Density of gaseous helium	1.1924 kg/m ³
Melting condition on lambda line	
Temperature	1.7673 K
Pressure	3013.4 kPa
Density	179.83 kg/m ³

ANNEX 4

Thermal contacts

When different surfaces are placed in contact, a thermal impedance is always present at the interface of the solids. The interface impedance is developed because the two materials do not fit tightly together. The subject of interface impedance is a complex one, and no single theory or set of empirical data accurately describes it for surfaces of engineering importance.

A4.1 Model for solid-to-solid contacts

Imagine two solid bars brought into contact as indicated in figure A4.1. The sides of the two bars are insulated, so that heat flows only in the axial direction. The materials may have different thermal conductivity, but if the sides are insulated the heat flux must be the same through both materials under steady-state conditions.

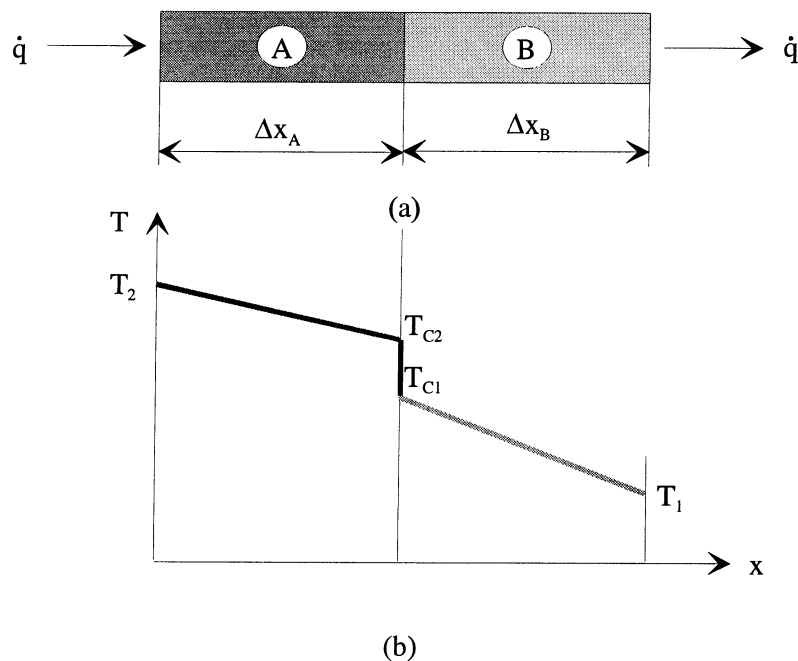


Figure A4.1: *Physical situation (a) and temperature profile (b) of the thermal contact*

Performing an energy balance on the two materials, we obtain:

$$\dot{q} = K_A A \frac{T_2 - T_{C2}}{\Delta x_A} = \frac{T_{C2} - T_{C1}}{\frac{1}{h_C A}} = K_B A \frac{T_{C1} - T_1}{\Delta x_B} \quad (\text{A4.1})$$

or

$$\dot{q} = \frac{T_2 - T_1}{\frac{\Delta x_A}{K_A A} + \frac{1}{h_C A} + \frac{\Delta x_B}{K_B A}} \quad (\text{A4.2})$$

where the quantity $1/h_C A$ is the thermal impedance and h_C is the contact coefficient. This factor can be extremely important in many heat-transfer situations involving mechanical joining of two materials.

The parameters which mostly influence the thermal impedance are:

- surface roughness,
- pressure holding the two surfaces in contact,
- oxidation,
- interface fluid,
- temperature level.

Examination of an enlarged view of the contact between the two surfaces (figure A4.2), shows that no particular surface is perfectly smooth and the surface roughness plays a central role in determining the thermal impedance. The solids touch only at peaks in the surface and the valleys in the mating surfaces are occupied by a fluid, a liquid or a vacuum.

There are two principal contributions to the heat transfer at joint:

1. The solid-to-solid conduction at the spots of contact
2. The conduction through entrapped gases in the void spaces created by the contact

The second factor represents the major resistance to heat flow, because the thermal conductivity of the gas is quite small in comparison with that of solids.

Designating the contact area by A_C and the void area by A_V , we can write the heat flow across the joint

$$\dot{q} = \frac{T_A - T_B}{\frac{e_g}{2K_A A_C} + \frac{e_g}{2K_B A_C}} + K_s A_V \frac{T_A - T_B}{e_g} = \frac{T_A - T_B}{\frac{1}{h_C A}} \quad (\text{A4.3})$$

where e_g is the thickness of the void space and K_s is the thermal conductivity of the fluid filling the void space. The total cross-sectional area of the bars is A . Solving for h_C , we obtain:

$$h_C = \frac{1}{e_g} \left(\frac{A_C}{A} \frac{2K_A K_B}{K_A + K_B} + \frac{A_V}{A} K_s \right) \quad (\text{A4.4})$$

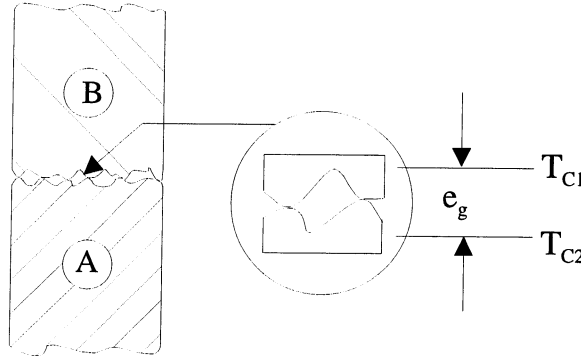


Figure A4.2: *Joint-roughness model for modeling thermal contact impedance*

In most cases, air is the fluid filling the void space and K_S is small compared with K_A and K_B . If the contact area is small, the major thermal impedance results from the void space. The main problem with this simple theory is that it is very difficult to determine effective values of A_C , A_V and e_g for surfaces in contact.

From equation A4.4 we notice that the thermal impedance should increase when the thermal conductivity of the entrapped gas decreases. The thermal impedance should decrease for an increase in the joint pressure since this results in a deformation of the high spots of the contact surfaces, creating thus a greater contact area between the solids.

Radiation heat transfer across the joint can also be important when high temperatures are encountered.

A4.2 Empirical correlations

There is no satisfactory theory which will predict the thermal impedance or the thermal conductance for all types of engineering materials. Experimental studies yield empirical correlations. The thermal conductance C is expressed in $\text{W/m}^2\text{K}$. For the other parameters which appear in the following relationships, refer to the section “List of symbols”.

- **Fenech and Rohsenow’s correlation: metallic surfaces in contact** [111]

$$C = \frac{4.26\lambda\sqrt{n}}{(1 - \lambda_C^2) \left(\frac{4.26\lambda\sqrt{n} \frac{\Delta_A}{\lambda} + 1}{K_A} + \frac{4.26\lambda\sqrt{n} \frac{\Delta_B}{\lambda} + 1}{K_B} \right)} \quad (\text{A4.5})$$

where λ_C is the contact factor, defined as follows:

$$\lambda_C = \sqrt{\frac{\sigma}{3R_e}} \quad (\text{contact surface/apparent surface}) \quad (\text{A4.6})$$

- **Hsieh and Touloukian's correlation**: flat surfaces [112]

$$C = \frac{4K}{472.424\pi\Delta} \lambda \quad (\text{A4.7})$$

- **Thomas and Probert's correlation**: same materials [113]

$$C_{inox} = \frac{8.0975K\Delta}{A_a} \left(\frac{F}{\Delta^2 R_r} \right)^{0.743} \quad (\text{A4.8})$$

$$C_{Aluminum} = \frac{1.6613K\Delta}{A_a} \left(\frac{F}{\Delta^2 R_r} \right)^{0.72} \quad (\text{A4.9})$$

- **Fletcher and Gyorog's correlation**: similar metal surfaces [114]

$$C = \frac{K}{r_c} \exp \left(170\alpha_T T_m \frac{r_c}{\Delta} \frac{P}{E} \right) \left(5.22 \cdot 10^{-6} \frac{\Delta}{r_c} + 0.036\alpha_T T_m \frac{P}{E} \right)^{0.6} \quad (\text{A4.10})$$

- **Astrabadi, O' Callaghan, Probert and Jones's correlation**: stacks of thin layers in high vacuum [115]

$$C = 3.025 \frac{K}{e} \left(\frac{P}{R_r} \right)^{0.58} \quad (\text{A4.11})$$

- **Miller and Fletcher's correlation**: porous metals [116]

$$C = 2.335 \frac{K}{e} \left(\frac{P}{R_r} (1 - \varepsilon) \right)^{0.72} \quad (\text{A4.12})$$

where ε is the porosity coefficient given by:

$$\varepsilon = 1 - \frac{\rho_{powder}}{\rho_{matrice}} \quad (\text{A4.13})$$

A4.3 Methods to improve thermal contact

Thermal conductance increases with applied force [117, 118] in all materials as well as with plating [119] of the contact surfaces by adequate material. Experimental

data show that the conductances of the aluminum, brass and copper contacts increase by approximately a factor 2 by gold plating the contact surfaces.

In many instances a further improvement of thermal performance is attained by inserting solid thermal interposers or vacuum grease between the contact surfaces [120]. Since for two surfaces pressed together the heat flow occurs at a few contacts points, materials such as indium or Apiezon, will increase the actual contact area, thereby decreasing the resistance due to constriction of the heat flow and improving the conductance of all the materials. The Apiezon grease becomes rigid at cryogenic temperatures. If good contact is not made at room temperature the resultant thick, non-deforming layer of Apiezon separates from the contact surfaces at helium temperatures, and the thermal impedance across the contact actually increases. To be effective, a large force must be applied at room temperature. For indium, a lower applied force is needed because of its softness. Experiments [121] showed that the addition of indium foil or Apiezon grease between the contact surfaces improved the thermal conductance of a factor 3 for aluminum to an order of magnitude for copper contacts. This suggests that thermal conductivity of the bulk material plays an important role. It appears that conductance increases in a roughly logarithmic manner with increasing thermal conductivity of the bulk material.

Surface roughness and oxidation affects the thermal impedance [122]. Slight differences in surface preparation strongly influence the thermal impedance. If ultrasonic cleaning after grinding is eliminated, the resulting thermal impedance increases by an order of magnitude. The oxide present on contact surfaces has a relevant effect on the temperature dependence of thermal impedance. Oxidation can increase the thermal contact impedance by as much as a factor of 100.

